

Chapter-1

Introduction

1. 1. Supramolecular Chemistry:

The term “supramolecular chemistry” was created by Jean-Marie Lehn in 1978 was defined by him as “chemistry beyond the molecule, bearing on the structured entities of higher complexity that result from the association of two or more chemical species held together by intermolecular forces.”¹ Lehn’s definition is generally the most widely accepted and agrees with most other definitions. Two terms commonly encountered in supramolecular chemistry are self-assembly and self-organization. Lehn discussed these terms and other supramolecular terms extensively in his book.²

Supramolecular chemistry in its simplest sense would be defined as a noncovalent binding or complexation, i.e., host–guest chemistry. A well-known example of a host–guest type complexation is Fischer’s lock and key model for recognition of binding for proteins.³ Interest in this type of self-assembly chemistry has resulted in rapid growth of supramolecular chemistry since Pedersen’s discovery in 1967 that crown ethers complex with metal ions, e.g., 18-crown-6 complexed with a potassium ion.^{4,5} The role of “hosts” or receptors is usually played by cyclic molecules such as crown ethers, cryptands, cyclodextrins, cucurbiturils, calixarenes, amide based cycles, and Pillar[5]arenes. The “guests” can be a diverse group of molecules from small particles (inert gas atoms, metal ions, etc.) to larger molecules (ammonium salts, paraquats, fullerenes, etc.). Host – guest chemistry is the chemistry behind the synthesis of mechanically interlocked molecules (MIMs) such as pseudorotaxanes, polypseudorotaxanes, rotaxanes, polyrotaxanes, catenanes, polycatenanes, etc.

1. 1. 1 Pseudorotaxanes, Rotaxanes, Catenanes, and Borromean rings

A rotaxane, as one typical species of molecular machine, consists of one or more macrocycles encircling the rod portion of a dumbbell-like component, where the dissociation of a ring from an axis is hindered by two bulky terminals (stoppers). A rotaxane containing n components is usually called an $[n]$ rotaxane. Their counterparts that have the same structural characteristics except for an absence of bulky terminals are called pseudorotaxanes. However, some pseudorotaxanes can have some rotaxane-like character. Lüttringhaus et al. reported the first evidence supporting the synthesis of a pseudorotaxane in 1958.⁶ In 1961, the first concept of rotaxanes was published by Frisch and Wasserman.⁷ The first conclusive evidence for the existence of rotaxanes was reported in 1967 by Harrison and Harrison⁸ and Schill and Zöllenkopf.⁹ The area of supramolecular chemistry of pseudorotaxanes and rotaxanes has continued to grow rapidly since this pioneering work.

A catenane is a mechanically-interlocked molecular architecture consisting of two or more interlocked (entwined) macrocycles. The interlocked rings cannot be separated without breaking the covalent bonds of the macrocycles. Catenane is derived from the Latin *catena* meaning "chain". They are conceptually related to other mechanically-interlocked molecular architectures, such as rotaxanes, molecular knots or molecular Borromean rings. Recently the terminology "mechanical bond" has been coined that describes the connection between the macrocycles of a catenane.¹⁰ **Figure 1. 1** shows the cartoon representation of catenane, rotaxane, and Borromean ring. **Figure 1. 2** illustrating the formation of pseudorotaxane as vital precursor to either $[2]$ rotaxane or $[2]$ catenane.

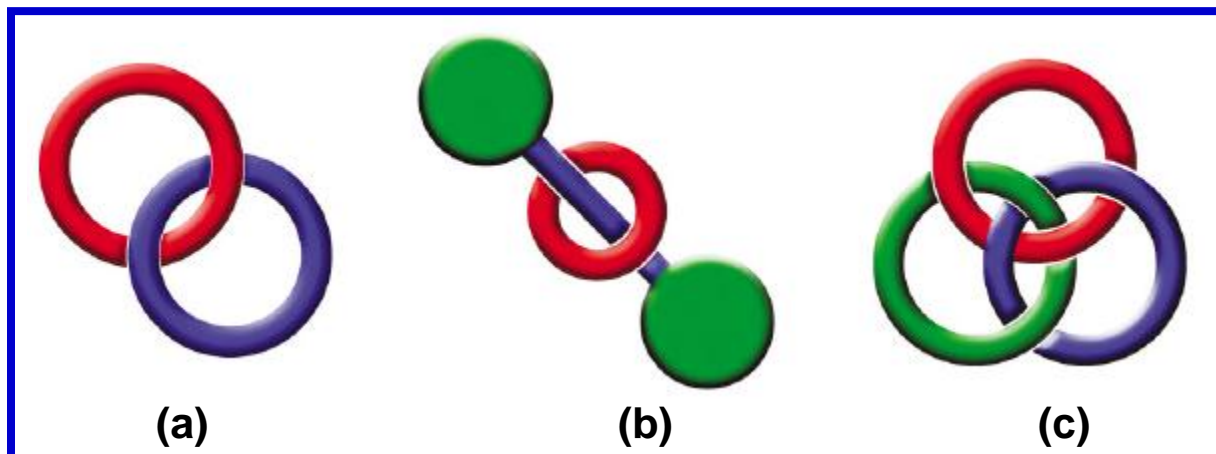


Figure 1. 1. Cartoon representation of (a) [2]Catenane, (b) [2]Rotaxane, and (c) Borromean ring.¹¹

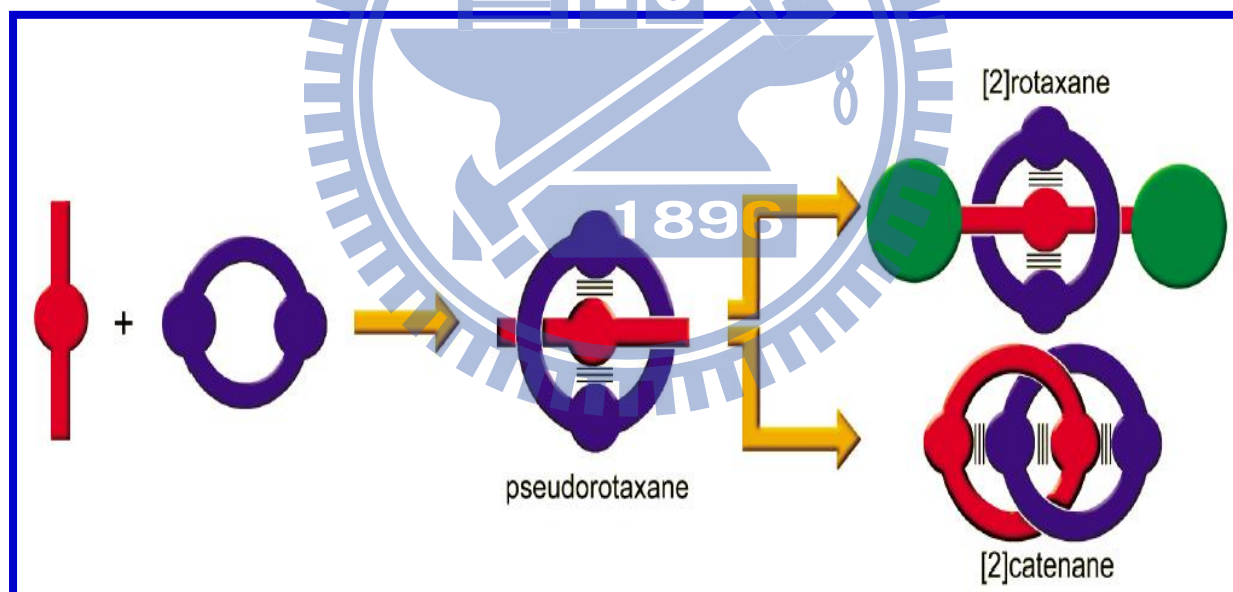


Figure 1. 2. Synthesis of [2]rotaxane and [2]catenane via the formation of a pseudorotaxane precursor.¹¹

1. 1. 2 Polyrotaxane architectures

Advanced supramolecular and mechanically interlocked polymers such as polyrotaxanes, polypseudorotaxanes, and polycatenanes have attracted considerable attention because the high degree of freedom of the mechanical bonding may strongly affect the physical and rheological properties of such polymers. In line with this idea, considerable effort has been expended in the synthesis of poly[2]rotaxanes^{12,13} that possess mechanical bonding in the main chains¹⁴. Most of the conventional approaches for poly[2]rotaxane synthesis relied on self-assembly, that is, polymerization accompanying the mechanical bond formation using the strong intermolecular attractive interaction between the components. Since the polymerization was carried out under thermodynamic control, these poly[2]rotaxanes exhibit labile mechanical bonding, and it was difficult to achieve a high degree of polymerization. A particular challenge in the synthesis of main-chain polyrotaxanes, for example, is achieving a combination of polymerization, threading or “clipping”, and end-capping to secure the overall interlocked nature of the ensemble—feats often executed in a stepwise fashion; inspired by elegant examples that have successfully accomplished these objectives, **Figure 1. 3.** exemplifying some of the main chain polyrotaxane architectures.

One class of polymeric rotaxanes consists of side chain polyrotaxanes and *polypseudorotaxanes*. Since side chain polyrotaxanes and *polypseudorotaxanes* are formed by host-guest interactions of polymer side chains with low molecular weight species or with other polymer side chains, these polyrotaxanes and *polypseudorotaxanes* can be considered as model systems for supramolecular complexes of biomacromolecules. Thus, side chain polyrotaxanes (**Figure 1. 4**) and *polypseudorotaxanes* are an important class of supramolecular complexes.^{15, 16}

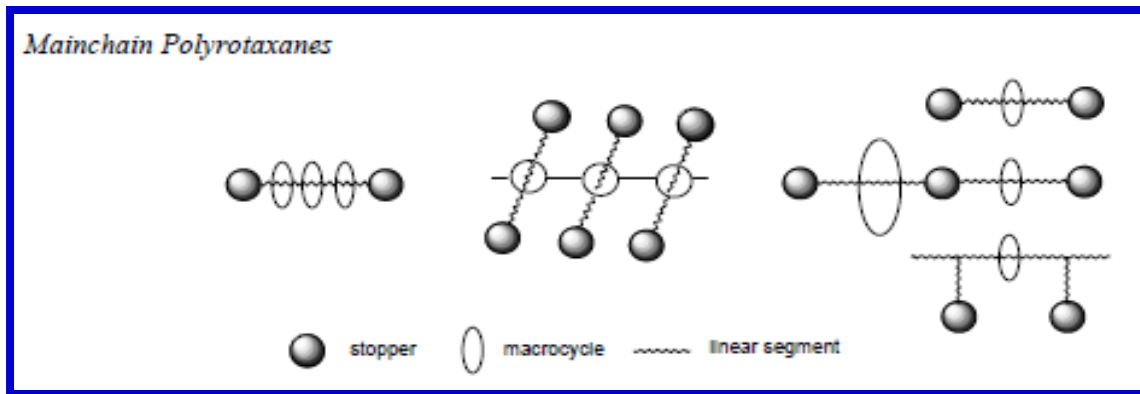


Figure 1. 3. Cartoon representation of some of main-chain polyrotaxanes.

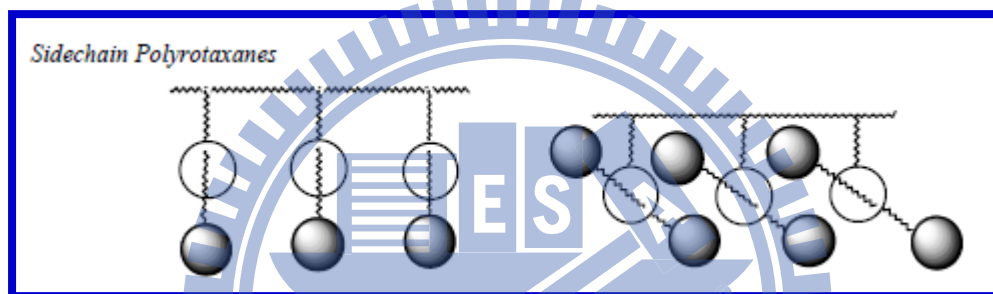


Figure 1. 4. Cartoon representation of some of side-chain polyrotaxanes.

Advantages of polyrotaxane architectures:

- Solubilities are altered
- Particular chance of improving and processibility of rigid rod polymers
- Glass transitions follow the Fox equation sometimes
- Glass transition sometimes remain distinct for each species
- Thermal stability can be enhanced
- New types of polymer chain compatibilisation for next generation application
- Insulated molecular wire approach and nano mechanical electronic memory devices
- Ideal drug delivery candidates
- Artificial molecular muscles

1. 1. 3 Early synthetic attempts to construct MIMs

Schill's epic contributions to the chemistry of MIMs were most unfortunately diminished due to the two key issues. One was that the synthetic chemistry involved numerous steps—commonly in excess of 20—and many of the reactions were daunting to perform and so their efficiencies were not all that high as illustrated in **Figure 1. 5**: the net outcomes were quite low overall yields of the catenanes, rotaxanes, and knots themselves. The other issue was the same as the one which had plagued the MIMs obtained by the statistical approach—namely, the lack of any specific interactions between their interlocked components, following cleavage of the covalent templates.^{17,18}

The long-term wait to create property-rich MIMs via practical synthetic approaches in an efficient way were first realized by Jean-Pierre Sauvage.^{19, 20} *“A new strategy has been developed for synthesizing catenanes. It is based on a generalized template effect. The first example of a novel class of molecules, the metallo-catenanes, has been obtained in good yield. It contains copper(I) and macrocyclic phenanthroline derivatives.”* In his seminal work Sauvage reported the two synthetic strategies based on the template effect induced by a transition metal. Functions f and g react to form links (fg). The molecular fragments f–f and g–g interact with the transition metal (m). This metal disposes the fragments perpendicular to one another as depicted in **Figure 1. 6** Although the Sauvage team's characterization of the first catenate and the derived catenand using spectroscopic techniques was totally convincing, an paper²¹ in Chemical Communications in 1985 was to illuminate the world with the very first X-ray crystal structures (**Figure 1. 7**) of a catenate and a catenand. These illustrations conveyed an important message namely, that in contrast with many complexing agents (receptors) which are preoriented in a stereoelectronic fashion appropriate to a good matching with a given metal (substrate), the

catenand has no geometrical analogy with the corresponding complex (catenate) although the stability and kinetic inertness of the catenate are extremely high.

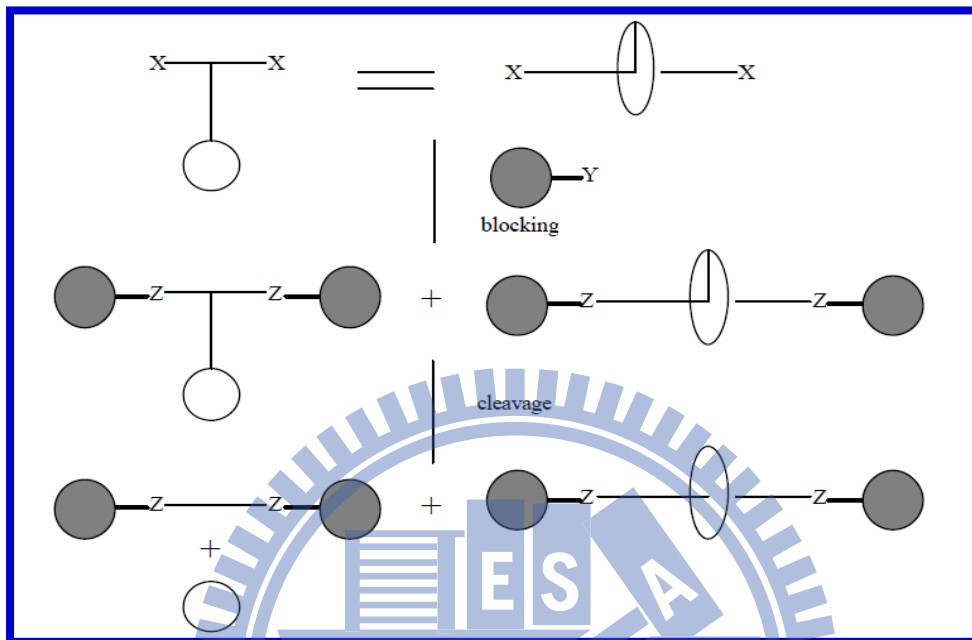


Figure 1. 5. Schill's chemical conversion rotaxane synthesis.

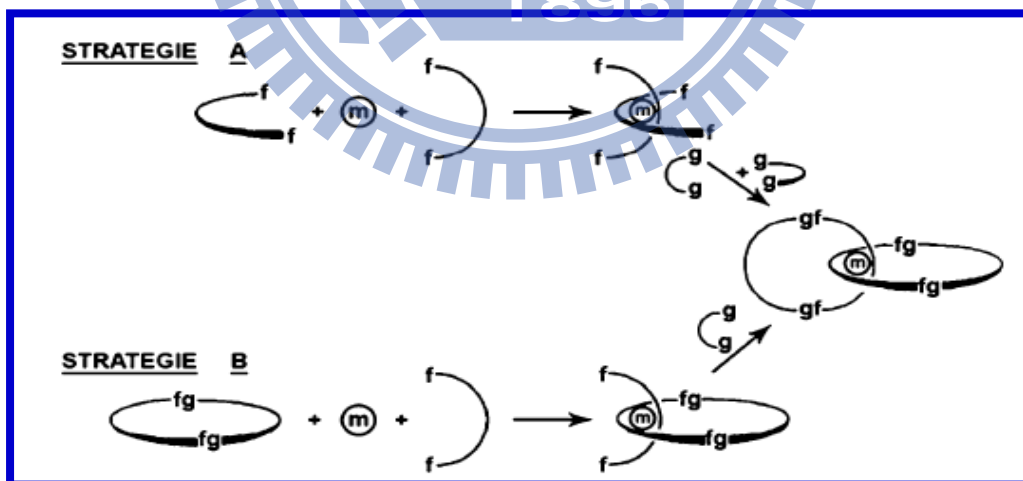


Figure 1. 6. Sauvage's passive copper(I) metal templated synthetic strategies A and B for [2]catenane.

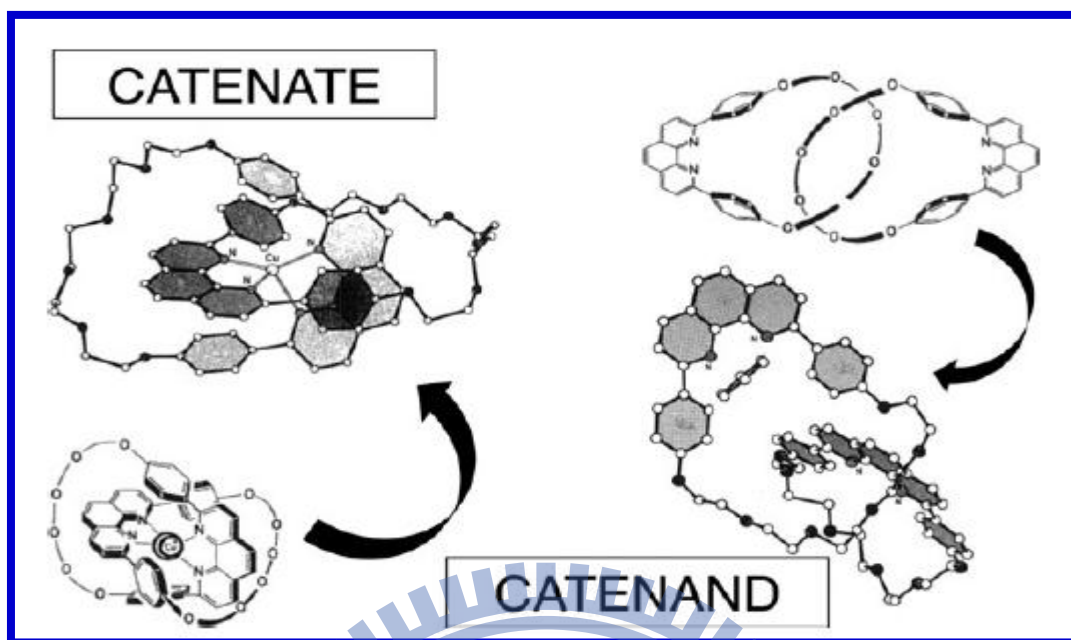


Figure 1. 7. The solid state structure of copper(I) catenate and the catenand derived from phenanthroline derivatives.

1. 1. 4 Principles to build MIMS and MIPAs

The synthetic challenge associated with the intriguing structure of rotaxanes has prompted numerous efforts to develop efficient synthetic methodologies to afford them. Three different principles known as *threading*, *slipping* and *clipping* were envisioned (**Figure 1. 8a–c**). In the case of *slipping*, a presynthesized size complementary ring and a dumbbell are assembled under the influence of an appropriate amount of thermal energy. In the *threading* principle, a preformed macrocycle is threaded onto the molecular axle at first, followed by the covalent attachment of the stoppers to the ends of the thread.²² Finally, in the *clipping* principle the macrocyclization of the ring-component is performed in the presence of the preformed dumbbell-component. The different strategies and methods can be combined according to their particular features. Thus, the statistical synthesis relies on the threading or slipping principle, while the directed method only

on the clipping one. The template method is more general, since it can make use of all the strategies. **Figure 1. 9** illustrating principle approaches for polyrotaxane assembly.

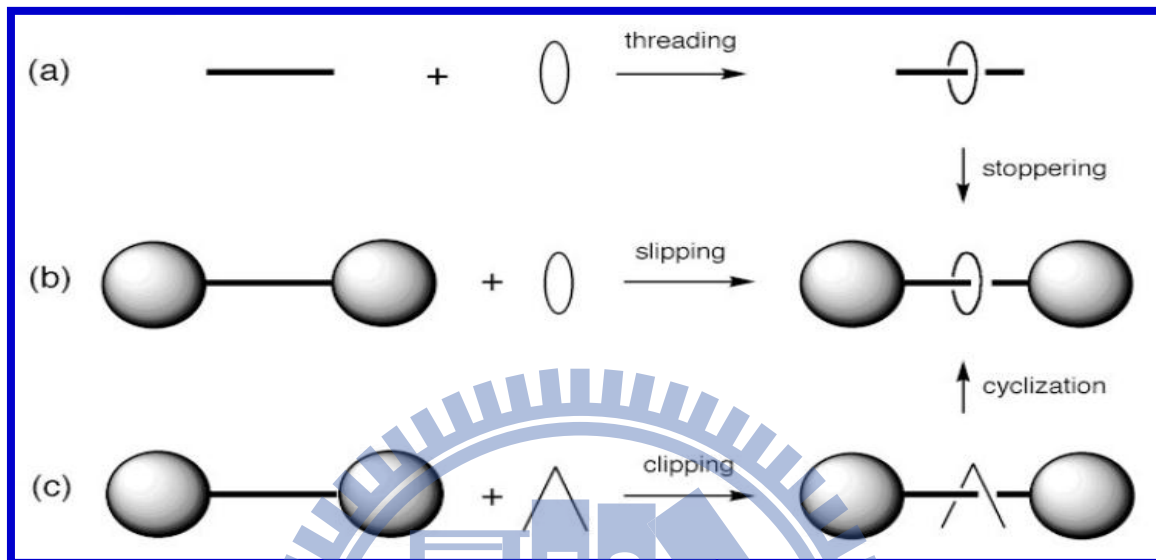


Figure 1. 8a-c. The three principles of rotaxane assembly.^{22, 23}

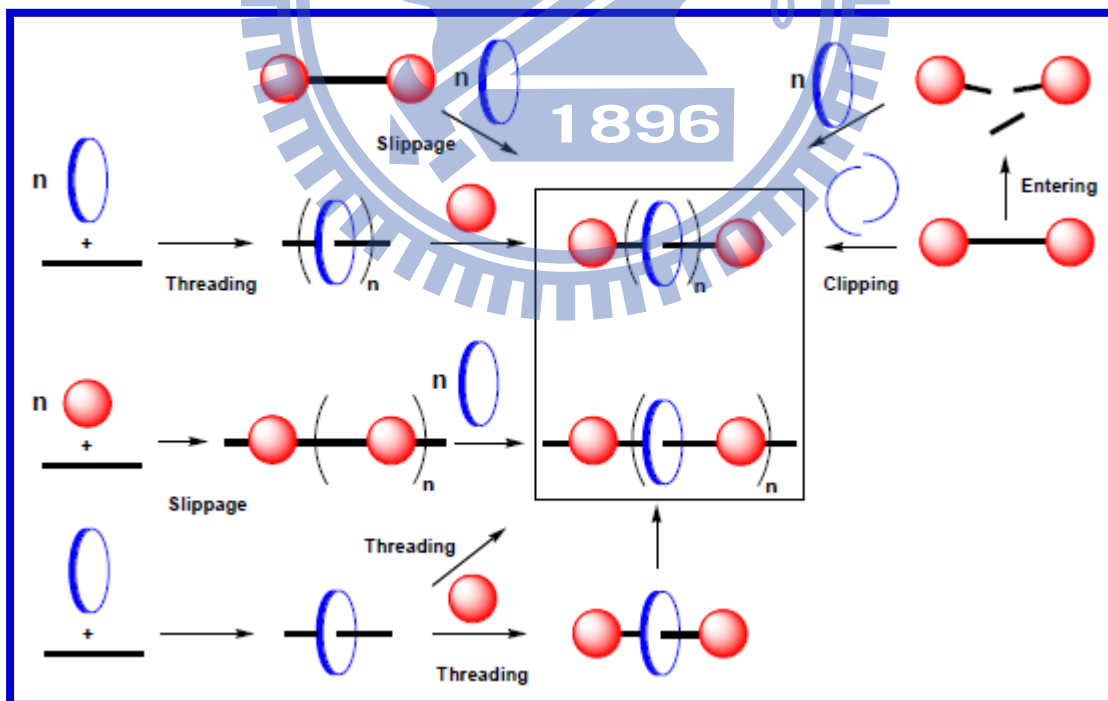


Figure 1. 9. Principle approaches of polyrotaxane assembly.

1. 1. 5 Modern supramolecular templating methodologies to create MIMs

The *template* method requires that the components interact through non-covalent bonds (*e.g.* van der Waals, hydrogen bonding, π - π stacking, metal–ligand interactions, electrostatic interactions, and hydrophobic-hydrophilic interactions) leading to the assembled prerotaxane. The synthetic methodology of rotaxanes based on coordination chemistry and supramolecular chemistry, in a broad sense, involves the existence of noncovalent interactions between the components of the rotaxane to be assembled. This approach was found to be highly efficient with regard to the previously developed directed and statistical approaches. Two main groups of synthetic template methods can be envisioned depending on the type of interactions: the first one comprises all the *organic* template methods and the second one includes the *transition metal* template methods. A rotaxane synthesis based on hydrogen bonding between amide groups of cyclic species and ammonium groups of linear species was published by Vogtle as shown in **Figure 1. 10**.²⁴

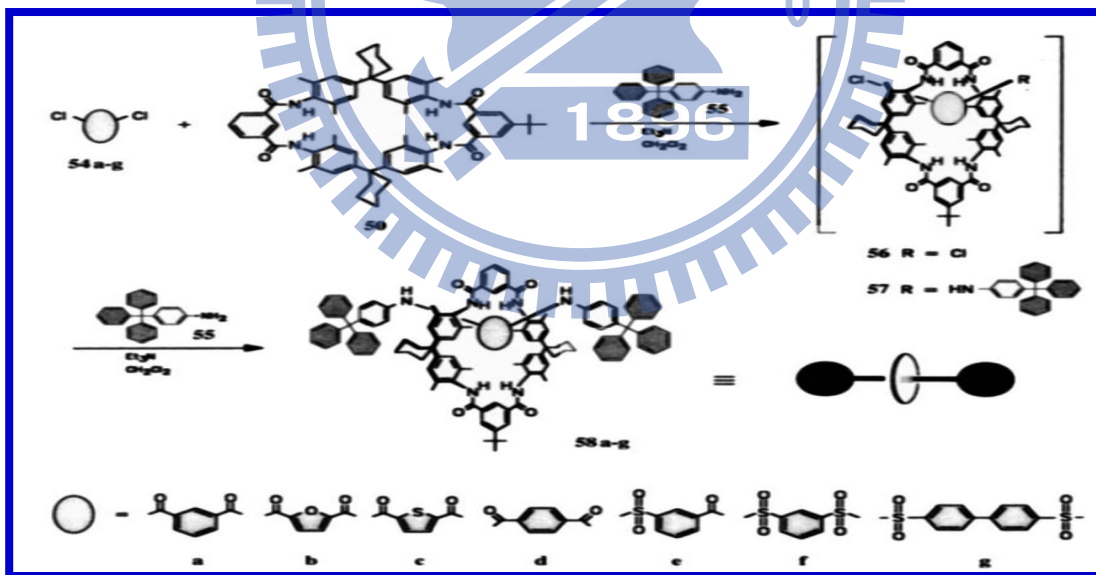


Figure 1. 10. Synthesis of the first amide linked [2]rotaxanes according to Vogtle et. al.

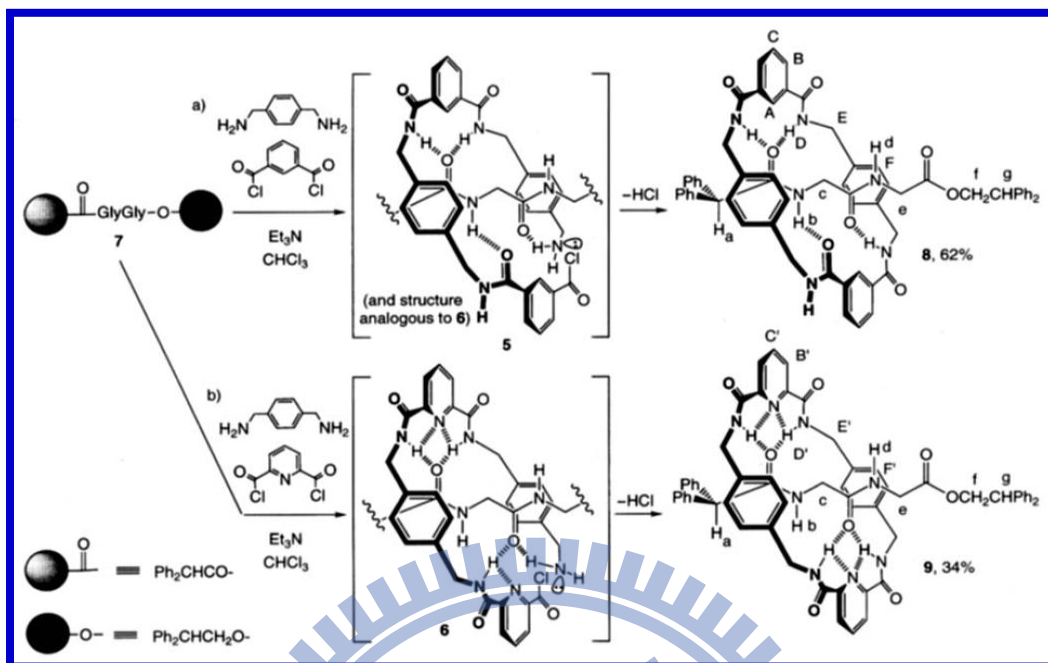


Figure 1. 11. The synthesis and mechanism of peptidorotaxanes by five molecules H-bond directed assembly.

Figure 1. 11 Illustrating the preparation of a Leigh et. al's synthetic peptide rotaxane by hydrogen bonding directed assembly between the amide NH and carbonyl oxygen groups.²⁵ Secondary stabilization is achieved through face to face and edge to face p-p stacking. Some rotaxanes are designed with π - π stacking as the main driving force for threading.²⁶

Stoddart has reported the synthesis of various rotaxanes based on secondary ammonium ions and crown ethers using hydrogen bonding.^{27, 28} This approach was used with the pyridine containing crown ether shown in **Figure 1. 12** Incorporation of nitrogen within the cavity of the crown ether introduces better binding sites. The nitrogen exhibits better hydrogen bonding with the linear guest. Stoddart used this crown to study the complexation with dibenzylammonium hexafluorophosphate and to form a [2]rotaxane.

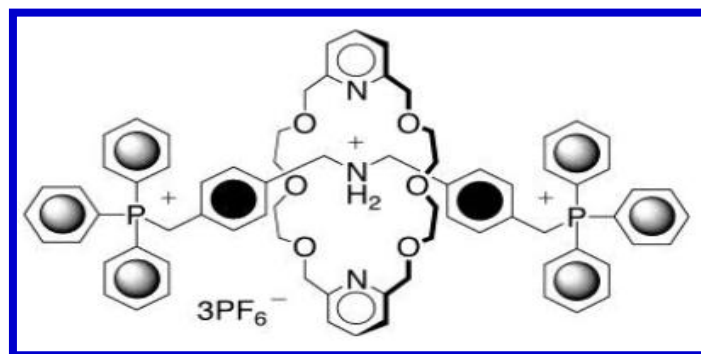


Figure 1. 12. Stoddart [2]rotaxane based on pyridine crownether and secondary ammonium salt via H-bonding.²⁹

Ogino reported the first rotaxane of cyclodextrins (CD) in 1981 using hydrophobic-hydrophilic inclusion complexation approach.³⁰ This pioneering approach led to revolutionary change in the field of host-guest or inclusion complex chemistry and complex self-assembled nanostructures and drug-delivery candidates based on CDs were later realized.

Rotaxanes have also been assembled using charge transfer complexation or Donor/Acceptor-based template. The majority of research conducted has involved complexation between linear or cyclic components containing bipyridinium moieties with bisphenylene crown ethers or linear units containing ethylene-oxy moieties. Stoddart and co-workers reported the first example of this type of rotaxane synthesis in 1987.³¹ Although the main driving force for the rotaxane formation is hydrogen bonding, charge transfer is an important secondary stabilizing factor. Other secondary stabilization occurs due to π - π aryl stacking and dipole-dipole interactions.

Beer et al presented a new general interweaving anion templation strategy for the formation of interpenetrated and interlocked architectures.³² **Figure 1. 13** depicting the formation of [2]rotaxane via Beer's anion templation and Grubbs ring closing metathesis methodologies.

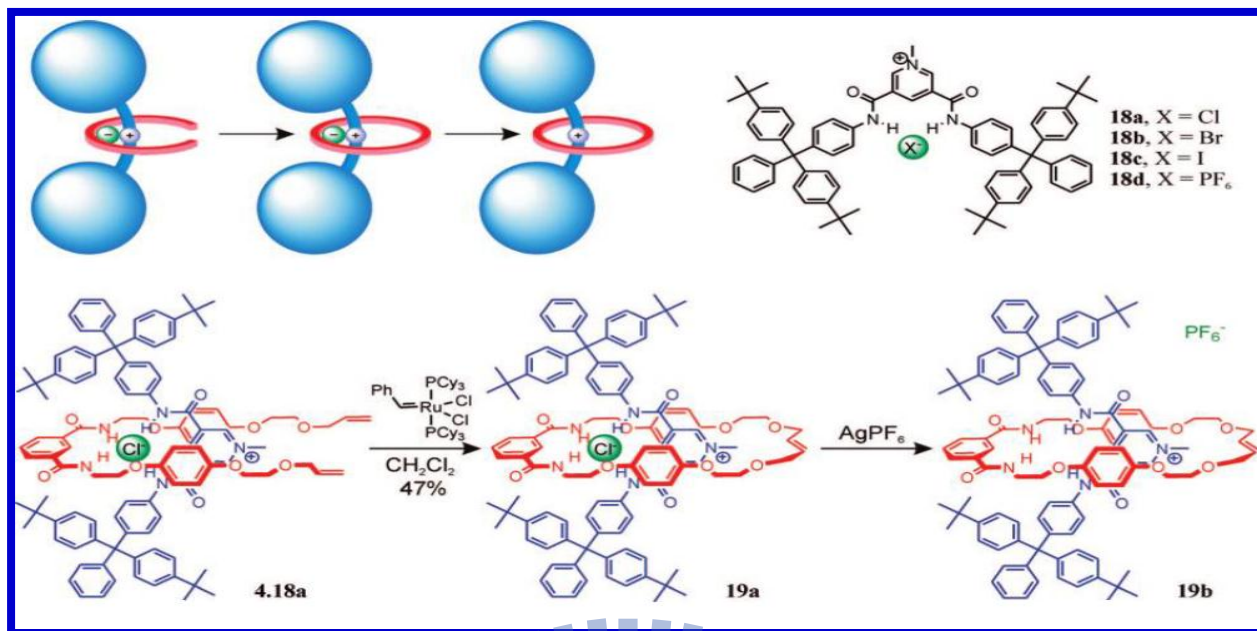


Figure 1. 13. Synthesis of [2]rotaxane via Beer's interweaving anion templating strategy.

A fundamental requirement for an interweaving template is the ability to direct two components in an orthogonal manner. Prominently the selection of appropriate anion coordination units and cationic guests are crucial in order to accomplish efficient pseudorotaxane formation.^{33, 34}

The active metal template approach relies on the use of a macrocycle which can bind a metal ion endotopically within its cavity. The metal ion is chosen such that it is capable of promoting covalent bond formation between two suitably functionalised "half-thread" units (rotaxane synthesis) or to effect ring closure of a precursor to a macrocycle (catenane synthesis). As the catalytic species is immobilised within the cavity of the macrocycle the metal ion selectively mediates the formation of new covalent bonds through the ring, leading to the formation of a new mechanical bond. This active metal template process is shown schematically in **Figure. 1. 14** in both stoichiometric (one equivalent of the template is required) and catalytic (the active template turns over during the reaction) variants.^{35, 36}

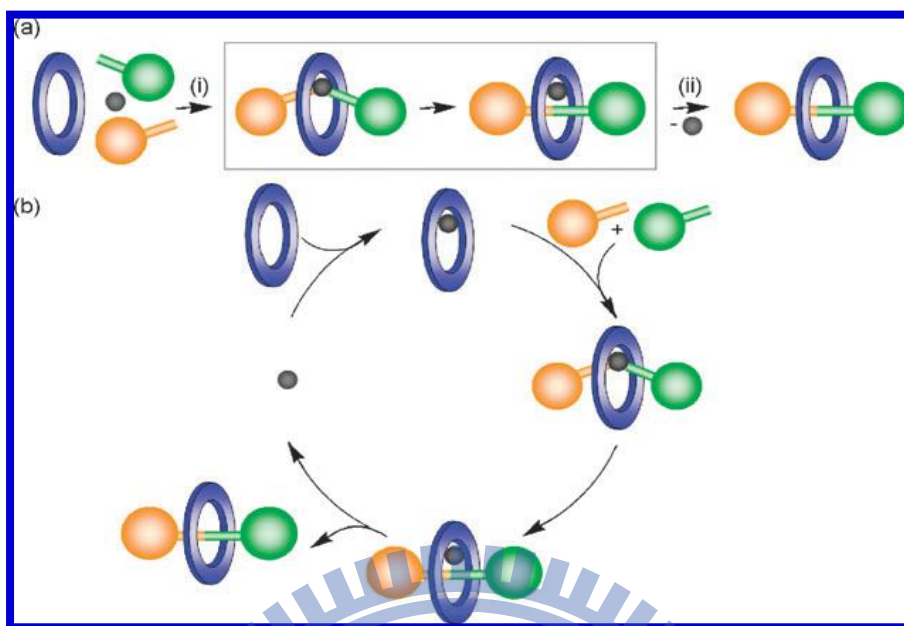


Figure 1. 14. Schematic illustration of the principles of active metal template synthesis. The formation of a covalent bond between the orange and green “half-thread” units to generate the rotaxane thread is promoted by a metal catalyst (shown in grey) and directed through the cavity of the macrocycle (shown in blue) by the metal ion coordination requirements. (a) Stoichiometric active metal template synthesis of a [2]rotaxane: (i) template assembly and covalent bond forming catalysis; (ii) subsequent demetallation. (b) Catalytic active metal template synthesis of a [2]rotaxane (only a sub-stoichiometric amount of the template is required as it turns over during the reaction).³⁷

There are several potentially attractive features of such a synthetic approach to mechanically interlocked architectures:

(i) the inherent efficiency and flexibility in having the macrocycle–metal complex perform multiple functions during the reaction.

(ii) the lack of requirement for permanent recognition elements on each component of the interlocked product, which increases the structural diversity possible in catenanes and rotaxanes and enables their formation to be ‘traceless’.

(iii) in some cases only sub-stoichiometric quantities of the active template may be required (i.e., the catalytic active metal template variant, **Figure 1. 14b**).

(iv) the strategy could prove applicable to many different types of well-known transition metal-catalyzed (and even organ catalytic) reactions.

(v) reactions that only proceed through a threaded intermediate could allow access to several currently inaccessible mechanically linked macromolecular architectures.

(vi) the coordination requirements during key stages of the catalytic cycle of active template reactions could provide insight into the mechanisms of the metal-catalyzed reactions.

1. 1. 6 Fluorescent chemo sensing applications of MIMS via molecular shuttle approach under external stimuli

A molecular shuttle in supramolecular chemistry is a distinctive type of molecular machine gifted of shuttling molecules or ions from one location to another as shown in **Figure 1. 15**. This field is of relevance to nanotechnology in its pursuit for nanoscale electronic components and also to biology where many biochemical functions are based on molecular shuttles. Academic interest also exists for synthetic molecular shuttles, the first prototype reported in 1991 based on a rotaxane.³⁸ since then the unique topological cavities of MIMs make them of great interest in molecular sensing field.³⁹

Mechanically interlocked molecules (MIMs) are a large part of supramolecular chemistry research due to the selective interactions between host and guest that are affected by external

stimuli. Their interlocked structures provide a basis to be used as shuttles, sensors, and switches at the molecular level. Molecular shuttling can be controlled chemically, electrochemically, photochemically, solvent polarity changes, acid/base (pH), counter ion changes. For switchable rotaxanes containing fluorophores, the switch of a rotaxane under external stimuli alters its internal conformation and the electron transfer process or the excited state and the luminescent properties of the fluorophores change subsequently. Since fluorescent signals provide many advantages mentioned above, many light-driven molecular machines employing fluorescent outputs have been built up in recent years. Either the enhancement⁴⁰ or the quenching⁴¹ of fluorescent signals could be utilized to indicate the shuttling conformations of rotaxanes.

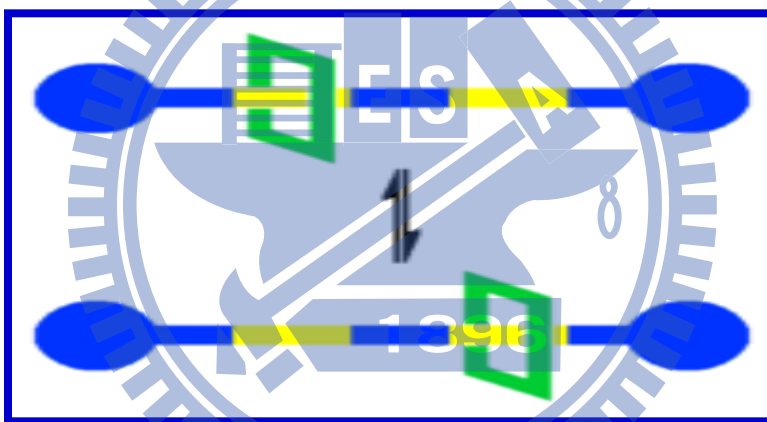


Figure 1. 15. Cartoon representation of molecular shuttle.

Co-conformational changes of switchable MIMs were mainly monitored by NMR, UV-vis, cyclic voltammetry, induced circular dichroism, Infrared spectroscopy, and fluorescence spectral techniques. In summarizing the driving forces and the monitoring methods of switchable MIMs, it can be found that an optical device, based on a light driven molecular machine with a fluorescent output, will be characterized by:^{42, 43}

- fast response.
- low-cost because the detection of photons can be easily carried out in a small space.

- highly sensitive output signal and furthermore, one which can be remotely detected thus allowing non-contact readout to be achieved.

By virtue of their structural aspects of MIMs such as rotaxanes, catenanes, pseudorotaxanes, and wide variety of macrocycles were offered an ideal chemo sensing platforms for various neutral, cationic, and anions guests. However, owing to their complex nature sensing mechanism via guest induced molecular shuttle approach; structurally MIMs were quite different from simple fluoroionophore systems. Although, the fundamental sensing mechanism in MIMS followed by many conventional principles such as intramolecular charge transfer (ICT), photo induced electron transfer (PET), photo induced charge transfer (PCT), fluorescence resonance energy transfer (FRET), electronic energy transfer (EET), and by change of noncovalent interactions (H-bonding, van der Waals, π - π stacking, anion- π , and hydrophobic-hydrophilic) MIMS treated as special constitutional parts of supramolecular chemistry. Herein, we discussed some MIMs based examples which were fall under these basic mechanisms via molecular shuttling.

Tian et. al. reported, a typical [2]rotaxane with dual fluorescence addresses contains an α -cyclodextrin (α -CD) macrocycle, an azobenzene unit, and two different fluorescent naphthalimide fluorophores, as shown in **Figure 1. 16**. The cis–trans photo-isomerization of the azobenzene unit resulted in the motion of the α -CD macrocycle on the thread. Because of the rigidity of the α -CD ring shifting close to the fluorophore, which hinders the vibration and rotation of the bonds in the methylene, the fluorescence intensities of the fluorophores nearer the CD rings increase, respectively. Because of the easy regulation and full reversibility of the fluorescence change of the two stopper units, this [2]rotaxane could be used as a molecular storage medium or switch with all-optical inputs and outputs.

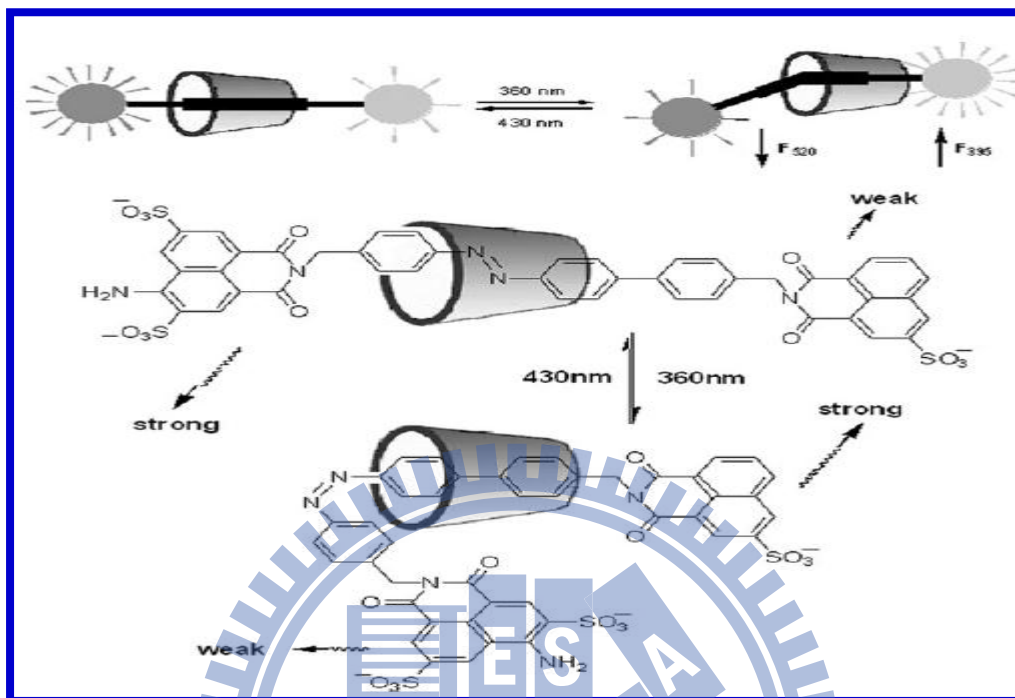


Figure 1. 16. Light driven naphthalimide [2]rotaxane molecular shuttle with dual fluorescence addresses.⁴⁴

A novel [2]rotaxane, containing pyrene and perylene bisimide as both stoppers and photoactive units, has been prepared by Zhu et. al. as showed in **Figure 1. 17**. The shuttling of the protonated macrocycle switched the energy transfer (EN) from a pyrene moiety to a perylene moiety, which resulted in changes of fluorescence of the perylene moiety.⁴⁵

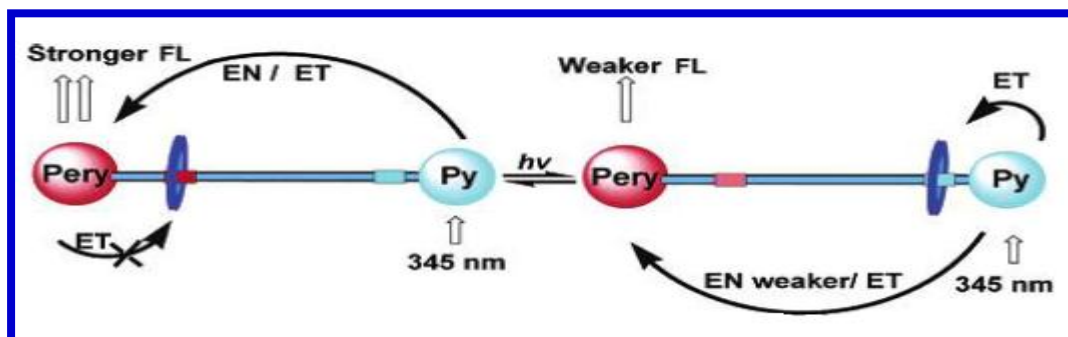


Figure 1. 17. Pyrene and perylene stoppered [2]rotaxane molecular shuttle under protonated cis-trans isomerization with energy transfer characteristics.

Brouwer and Vogtle investigated the wheel-chromophore interaction of fluorescent perylene [2]rotaxane by fluorescence dynamic, single molecule spectroscopy, and cyclic voltammetry methods.⁴⁶ **Figure 1. 18** representing the synthetic route of perylene [2]rotaxane.

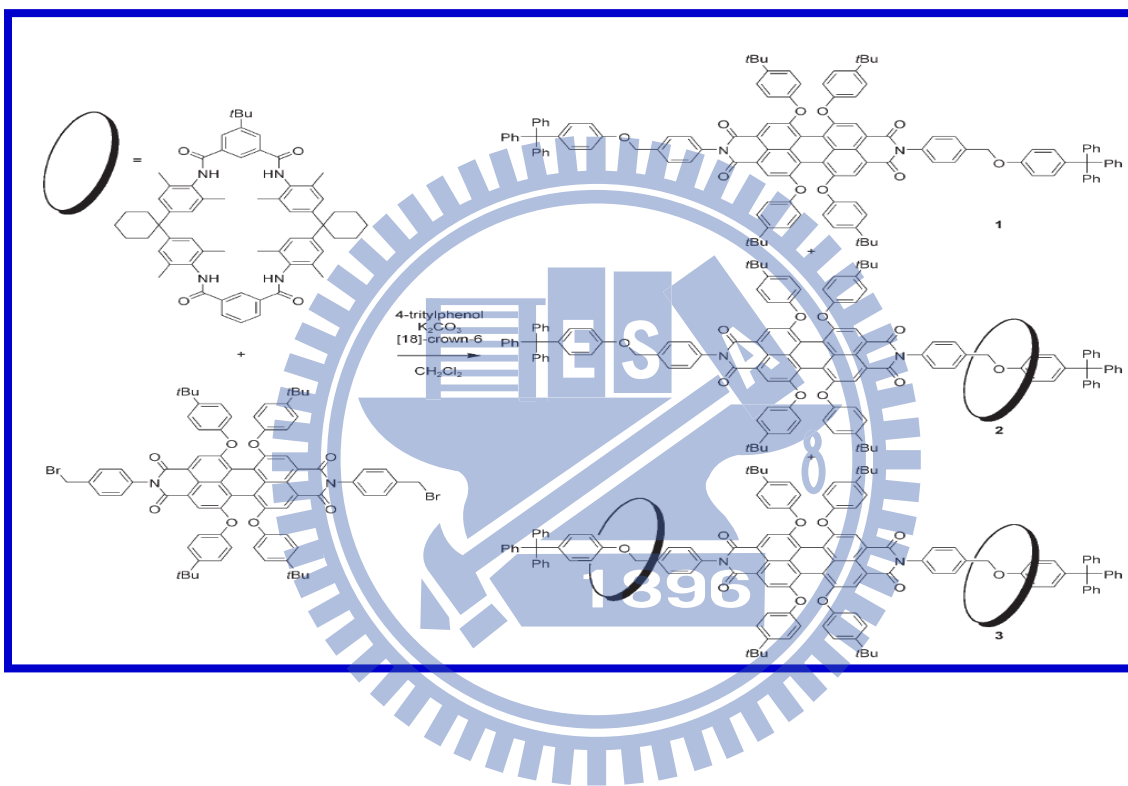


Figure 1. 18. Synthesis of perylene [2]rotaxane via Vogtle template method.

Smith et. al. reported the first example of squaraine based [2]rotaxane using Leigh amide-template protocol in two steps. The rotaxane exhibits photophysical properties that are similar to the precursor squaraine. The encapsulating macrocycle greatly increases the chemical stability of the squaraine thread and inhibits aggregation-induced broadening of its absorption spectrum as

shown in **Figure 1. 19**.⁴⁷ Later they developed squaraine-derived rotaxanes with improved properties for a wide range of photophysical, photochemical, and biomedical applications.⁴⁸

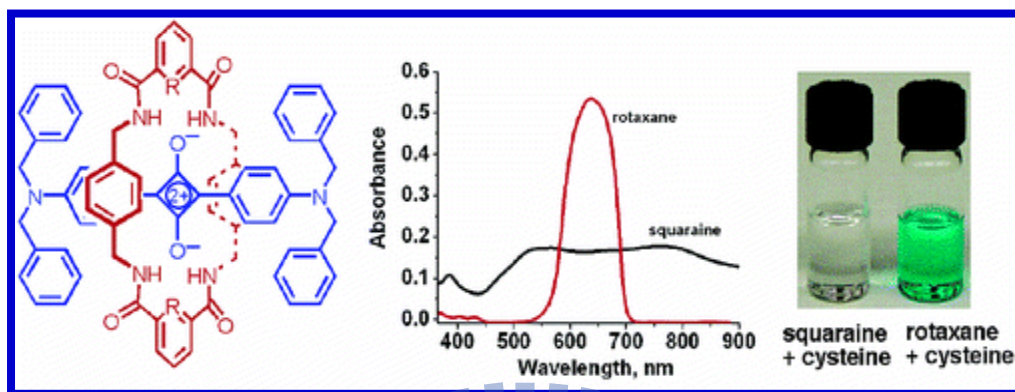


Figure 1. 19. Chemical structure and UV-vis spectra of squaraine derived [2]rotaxane.

Smithrud et al reported an astonishing intracellular drug delivery of fluoresceinated peptides by a host [2]rotaxane. As shown in **Figure 1. 20** the host [2]rotaxane enhanced the membrane permeability of fluoresceinated peptides of all polarities across the cell.⁴⁹

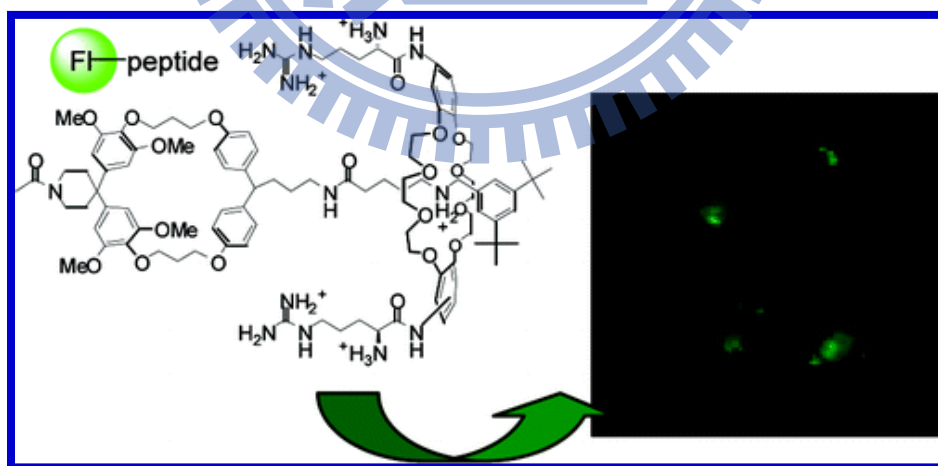


Figure 1. 20. Chemical structure and intracellular bio imaging of fluoresceinated peptides under [2]rotaxane host.

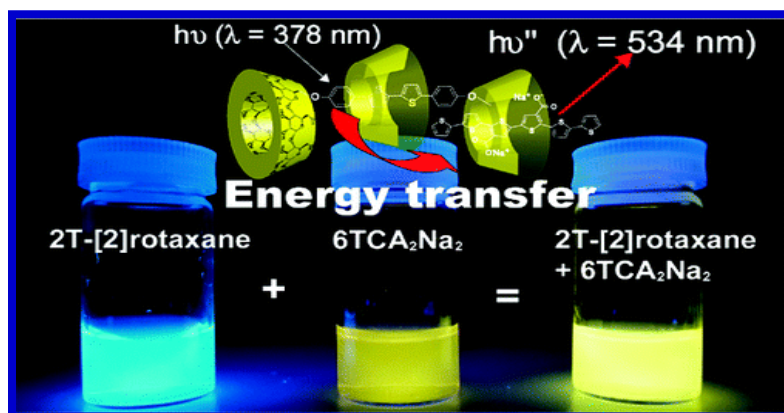


Figure 1. 21. PET process in a cyclodextrin-oligothiophene based 2T-[2] rotaxanes.⁵⁰

An Photo induced energy transfer (PET) process based MIMs was investigated using cyclodextrin–oligothiophene rotaxanes (2T-[2]rotaxane) by Harada et. al. The excited energy of 2T-[2]rotaxane is transferred to the sexithiophene derivative which is included in the cavity of β -CD stoppers of 2T-[2]rotaxane (**Figure 1. 21**).

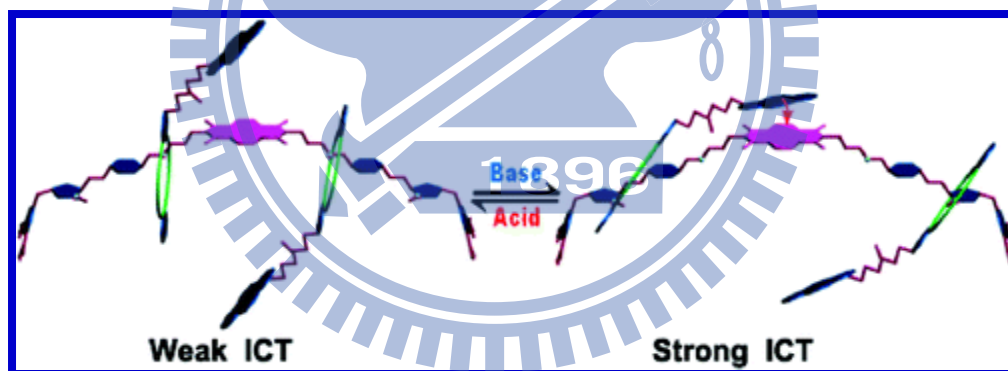


Figure 1. 22. Acid-base controllable NDI based [2]rotaxane molecular shuttle via ICT.⁵¹

Two [3]rotaxanes with an electron-rich pyrene moiety at the wheel and an electron-deficient naphthalenediimide (NDI) unit in the middle of the axle were prepared through “click chemistry”, in which the intramolecular charge-transfer (ICT) process occurred between the pyrene moiety and the NDI unit, and the addition of acid and/or base can adjust the intensity of ICT (**Figure 1. 22**).

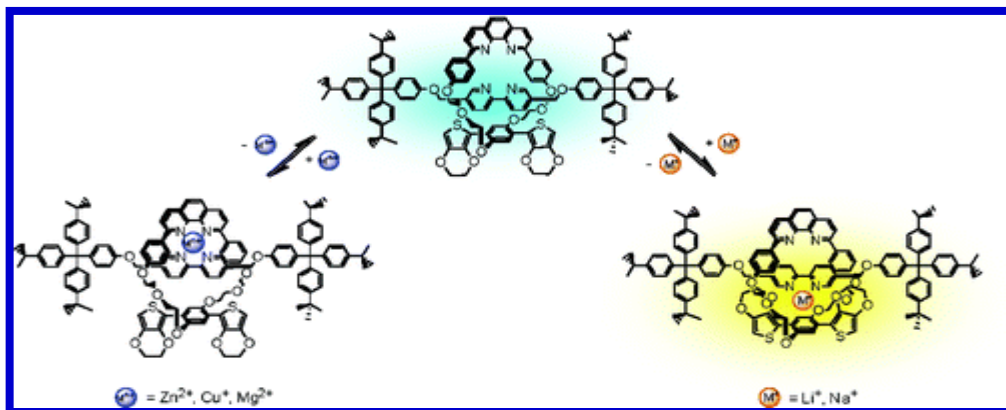


Figure 1. 23. Donor-acceptor based [2]rotaxane molecular shuttle via PCT and emission exciplex process.

Swager et. al reported first photo induced charge (PCT) and emission exciplex based donor-acceptor rotaxanes.⁵² The interlocked configuration of the rotaxane facilitates π orbital overlap of the excited state DA pair by keeping their center-to-center distance extremely small. This increased interaction between the DA pair significantly lowers the activation energy for exciplex formation (E_a) and helps stabilize the highly polar charge-transfer complex as shown in **Figure**

1. 23.

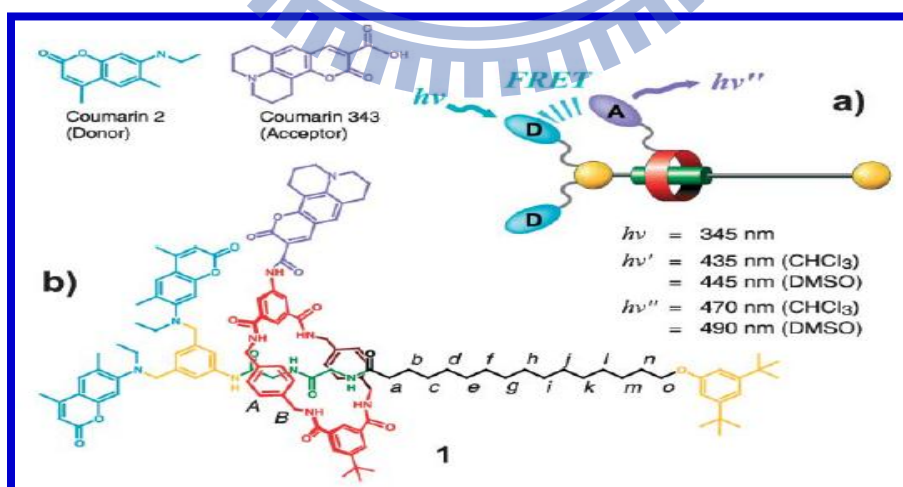


Figure 1. 24. FRET process across mechanical bond of a [2]rotaxane.⁵³

Rebek et. al studied FRET process across a donor-acceptor tagged rotaxane as illustrated in **Figure 1. 24**. Small co-conformational change of the rotaxane observed using fluorescent spectroscopy and ROESY NMR.

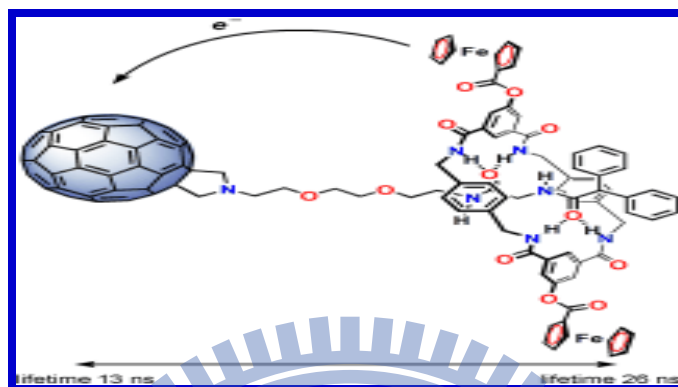


Figure 1. 25. Electron transfer process between ferrocenated wheel and fullerene stoppered H-bond templated [2]rotaxane.

A bistable fullerene-stoppered molecular shuttle equipped with two ferrocene electron donors on the macrocycle has been prepared.⁵⁴ A controlled positional change of the ferrocene groups along the thread results in different spatial arrangements of the electroactive units and allows the kinetics of the electron transfer and the lifetime of the charged-separated state to be modulated/fine-tuned (**Figure 1. 25**).

1. 2. Chemosensors: Principles and Mechanisms

Developing a novel chemo sensing platforms are vital owing to their implications in numerous fields, such as chemistry, biology, medicine and environmental studies.⁵⁵⁻⁵⁷ A chemosensor can be defined as a compound that can detect the analyte by invoking a change in one or more properties of the system, such as absorption, emission, or redox potential characteristics. Now, they are increasingly used in developmental biology and medicine because they allow us to spy on events in living cells and organisms, including humans, in real time and with high spatial resolution. The rapid and widespread usages of chemosensors were inevitable as this field witnessed emerging technological developments in the academic and industrial fronts. Recently many groups commercialized their seminal chemosensor technologies for quantitate detection of toxic, mutagenic, and carcinogenic neutral guests as well as cations, anions, and trace amount of gases.

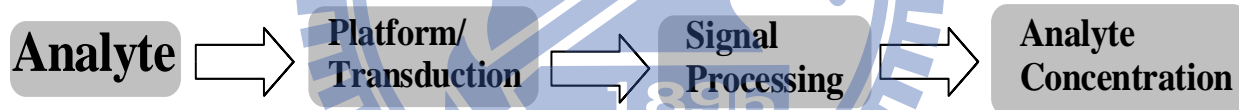


Figure 1. 26. Principal stages in the operation of a sensor.

Figure 1. 26 shows a schematic of a sensor system, illustrating the three main elements,⁵⁸ the sample (or analyte), transduction platform, and signal-processing step. Optical chemical sensors employ optical transduction techniques to yield analyte information. The most widely used techniques employed in optical chemical sensors are optical absorption and luminescence, but sensors based on other spectroscopies as well as on optical parameters, such as refractive index and reflectivity, have also been developed. However, among the numerous available analytical methods for the detection of cations, flame photometry, atomic absorption spectrometry, ion sensitive electrodes, electron microprobe analysis, neutron activation analysis, etc., are

expensive, often require samples of large size and do not allow continuous monitoring. In contrast, the methods based on fluorescent sensors offer distinct advantages in terms of sensitivity, selectivity, response time, local observation (e.g. by fluorescence imaging spectroscopy). Therefore, considerable efforts are being made to develop selective fluorescent sensors for various analytes detection.

1. 2. 1. Classification of chemosensors

The chemosensors can be classified into: (Figure 1. 27)

1. Fluorophores that are quenched upon collision with the analyte.
2. Fluorophores reversibly binding to the analyte with subsequent fluorescence quenching or enhancement.
3. Fluorophores that are linked to a receptor group by means of a spacer unit and the fluorescence is either quenched or enhanced upon analyte recognition at the receptor due to photo induced processes such as electron transfer, charge transfer, and energy transfer.

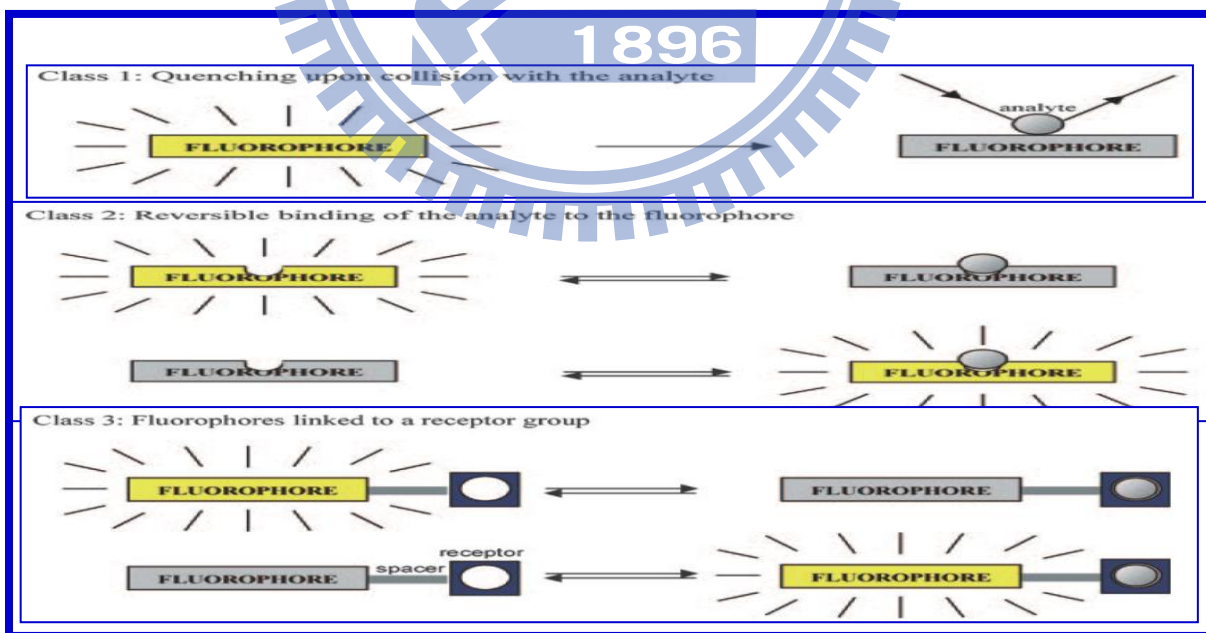


Figure 1. 27. Classification of fluoroionophore based chemosensors.⁵⁹

1. 2. 2. Intramolecular charge transfer (ICT)⁶⁰

Non-hydrocarbon (i.e., heteroatom containing) π -electron systems have very different dipole moments in their ground and lowest energy singlet excited states due to internal charge transfer (ICT). It is preferable to refer to ICT as internal rather than intramolecular charge transfer. The word intramolecular is poorly focused when supermolecules with multiple components are being addressed. On the other hand, the word internal can be restricted to a given fluorophore π -electron system. The influence of the solvent-solute dipole interaction on the various states of a sensor/switch is shown in Figures 1. 28 and 1. 29.

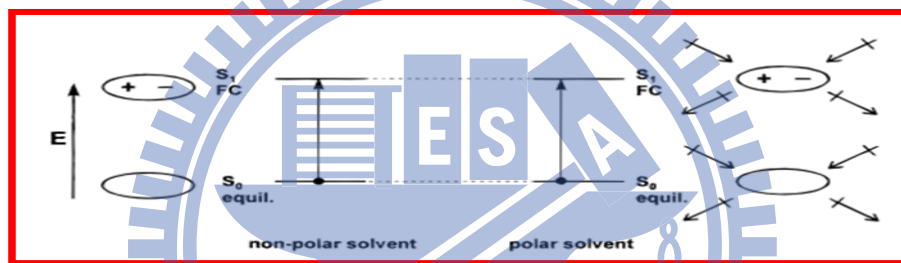


Figure 1. 28. Solvent effect on absorption spectral wavelength for a fluorophore with an ICT excited state. FC represents a Franck-Condon excited state. “Equil.” represents a thermally equilibrated electronic ground state. The dipole of the ground state is assumed to be small. S_0 and S_1 represent the electronic ground and lowest energy excited states, respectively.

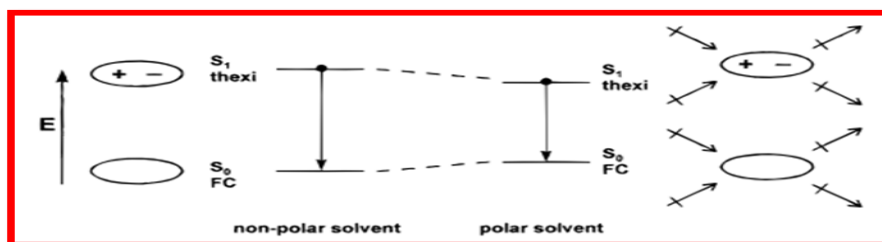


Figure 1. 29. Solvent effect on emission spectral wavelength for a fluorophore with an ICT excited state. “Thexi” represents a thermally equilibrated electronic excited state. The other terms are defined under **Figure 1. 28.**

For maximum clarity, we consider an extreme case where the ground state (S_0) has a much smaller dipole moment compared to that of the lowest energy singlet ICT excited state (S_1). The orientation of the solvent dipoles neighboring the thermally equilibrated S_0 state would therefore be distributed in an unbiased manner. Upon photon absorption, the Franck-Condon S_1 state is populated with the solvent dipole orientational distribution being conserved. Hence the solvent dipolar effects on the charge separation within the S_1 state largely cancel out within the timescale of the absorption experiment. In contrast, the longer time scale of the emission experiment means that the solvent dipoles can relax around the S_1 state in response to the charge separation. The field due to the oriented solvent dipoles is now non-zero and is responsible for perturbation of the thermally equilibrated S_1 and Franck-Condon S_0 states. The message we wish to take is that solvent or external effects can show up in emission even when they are hardly visible in absorption. Similarly, ions with their uncompensated charge can exert stronger electric effects. Most of the examples carry a receptor for the guest at the electron-rich terminal of the fluorophore.

1. 2. 3. Photoinduced electron transfer (PET)

Fluorescent PET sensors can be formalized as 'fluorophore-spacer-receptor' systems of modular structure. The photon- and guest-interaction sites can be chosen to cater for various excitation/emission wavelengths and for various concentration ranges of a given guest. This choice has several constraints, however and these constitute the design logic of fluorescent PET sensors. The energy stored in the fluorophore excited state upon photon absorption must be sufficient to, say, oxidize the guest-free receptor and to simultaneously reduce the fluorophore. In essence, this is the thermodynamic criterion for an exergonic trans-spacer PET process and

so far we and others have been blessed with fast PET rates which overwhelm the intrinsic emission of the fluorophore module. If we consider a canonic guest it is easy to frustrate the PET process since the oxidation potential of the guest-occupied receptor is significantly higher than that of the guest-free receptor. The excited state energy of the optically pumped fluorophore thus remains unused and is returned as a photon (**Figure 1. 30**). The cation entry is the second chemical command. Importantly, the spacer maintains the modularity of the system, which results in the additivity of component parameters, and is only violated by relatively long range forces. Fortunately for us, the PET process is of this type. Upon excitation of the fluorophore, an electron of the highest occupied molecular orbital (HOMO) is promoted to the lowest unoccupied molecular orbital (LUMO), which enables PET from the HOMO of the donor (belonging to the free cation receptor) to that of the fluorophore, causing fluorescence quenching of the latter. Upon cation binding, the redox potential of the donor is raised so that the relevant HOMO becomes lower in energy than that of the fluorophore; consequently, PET is not possible anymore and fluorescence quenching is suppressed. In other words, fluorescence intensity is enhanced upon cation binding.

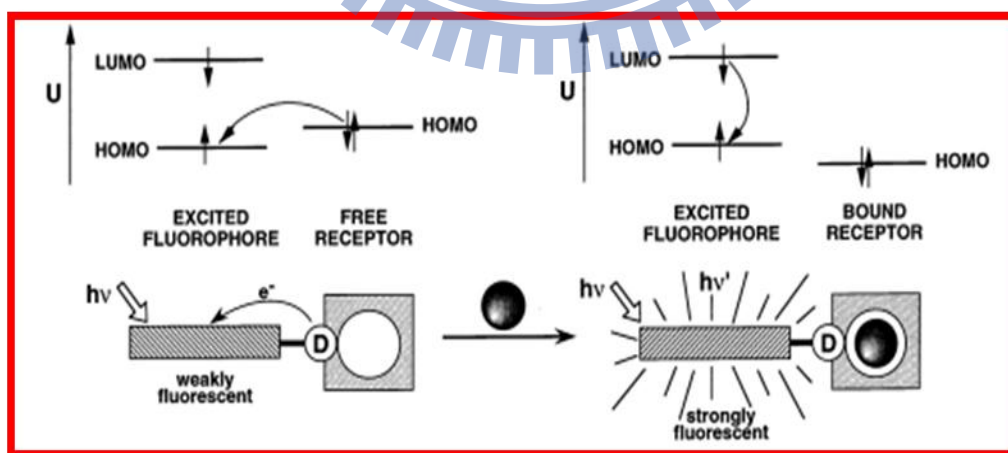


Figure 1. 30. Principle of analyte detection by fluorescent PET sensors.⁶¹

1. 1. 4. Photoinduced charge transfer (PCT)

When a fluorophore contains an electron-donating group (often an amino group) conjugated to an electron-withdrawing group, it undergoes intramolecular charge transfer from the donor to the acceptor upon excitation by light. The consequent change in dipole moment results in a Stokes shift that depends on the microenvironment of the fluorophore; polarity probes have been designed on this basis. It can thus be anticipated that cations in close interaction with the donor or the acceptor moiety will change the photophysical properties of the fluorophore because the complexed cation affects the efficiency of intramolecular charge transfer. When a group (like an amino group) playing the role of an electron donor within the fluorophore interacts with a cation, the latter reduces the electron-donating character of this group; owing to the resulting reduction of conjugation, a blue shift of the absorption spectrum is expected together with a decrease of the extinction coefficient. Conversely, a cation interacting with the acceptor group enhances the electron-withdrawing character of this group; the absorption spectrum is thus red-shifted and the molar absorption coefficient is increased. The fluorescence spectra are in principle shifted in the same direction as those of the absorption spectra. In addition to these shifts, changes in quantum yields and lifetimes are often observed. All these photophysical effects are obviously dependent on the charge and the size of the cation and selectivity of these effects are expected. The photophysical changes upon cation binding can also be described in terms of charge dipole interaction. Let us consider only the case where the dipole moment in the excited state is larger than that in the ground state. Then, when the cation interacts with the donor group, the excited state is more strongly destabilized by the cation than the ground state, and a blue shift of the absorption and emission spectra is expected (however the fluorescence spectrum undergoes only a slight blue shift in most cases; this important observation will be discussed below). Conversely,

when the cation interacts with the acceptor group, the excited state is more stabilized by the cation than the ground state, and this leads to a red shift of the absorption and emission spectra (Figure. 1. 31).

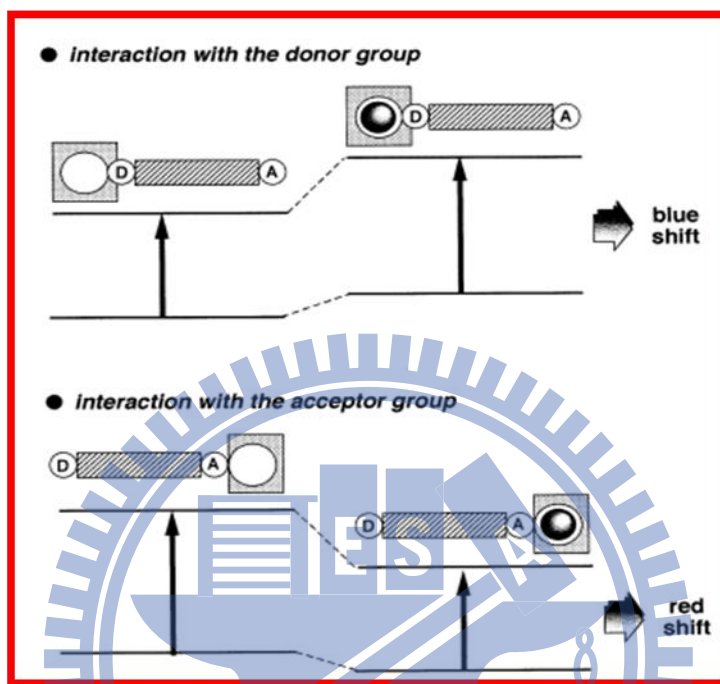


Figure 1. 31. Spectral displacements of PCT sensors resulting from interaction of a bound cation with an electron-donating or electron-withdrawing group.⁶²

1. 1. 5. Electronic energy transfer (EET)

The importance of EET within the photosynthetic reaction center has prompted its mimicry within smaller supramolecules. After photo excitation, energy absorbed by a molecule can be transferred efficiently over a distance of up to several tens of angstroms to another molecule by the process of electronic energy transfer (EET). The rate, or efficiency, of EET depends sensitively on the separation and geometric orientation of the donor and acceptor molecules. In other words, EET can be directed by the nanoscale organization of molecules; conversely, it can be used as a molecular-scale probe of such structures. By understanding the factors controlling

EET, it has been possible to explore and design natural and artificial antenna for the capture and energy conversion of light, to demonstrate amplification of fluorescence-based sensors, to optimize organic light-emitting diodes, and to measure structure in biology, even in living and moving systems. Nonlinear arrays of porphyrin/zinc(II)/metal-free porphyrin are also good candidates for EET and the mechanistic dilemmas are common because two or possibly three modes of EET are available to the larger supermolecules. Electron exchange, dipole-dipole coupling and emission-reabsorption are considered to be important at short-, medium-, and long-range respectively. Fluorescent signaling of ions via EET can also benefit from highly selective natural receptors. **Figure 1. 32** evidenced the Lindsey's porphyrin arrays which carry energy efficiently over large (~10 nm) distances can be fitted with redox switchable units to divert the productive EET into an energy sink upon command. The non-fluorescent porphyrinmagnesium (II) radical cation has such a low-energy excited state that it takeover as the ultimate destination for the excitation energy in the array. The possibility of PET at this stage

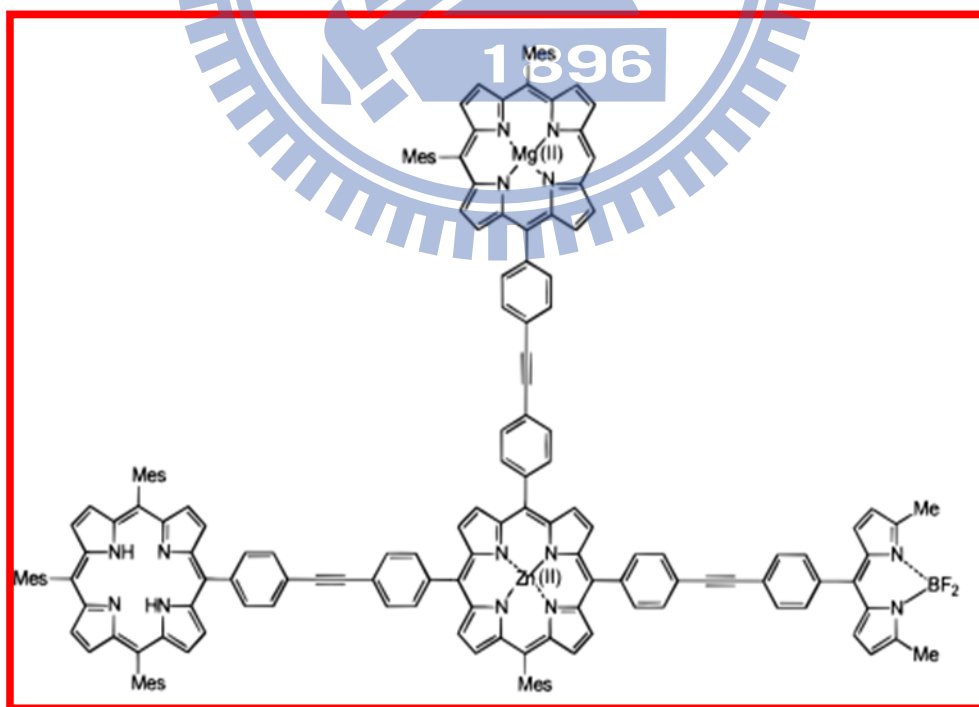


Figure 1. 32. Lindsey's porphyrin arrays for productive EET into an energy.⁶³

is yet to be evaluated. Of course, one electron reduction of this radical cation restores the ultimate energy acceptor status to the metal-free porphyrin which responds with strong fluorescence.

1. 1. 6. Fluorescence resonance energy transfer (FRET)

Fluorescence resonance energy transfer (FRET)⁶⁴ is a non-radiative energy transfer from the excited state of a donor (D) to an acceptor (A). FRET occurs when the emission spectrum of a fluorescent donor overlaps the absorption spectrum of an acceptor (**Figure 1. 33**). As a result, the donor lifetime is shortened and the acceptor fluorescence is sensitized. The distance between the donor and acceptor has to be in the range of 1-10 nm for FRET to occur. The idea of a nonradiative transfer of electronic excited energy was first proposed by J. Perrin in 1920. The model proposed by F. Perrin showed that energy could be transferred over hundreds or even thousands of angstroms. It was Th. Forster in 1946 that concluded that FRET could occur over distances up to 100Å. Galanin advanced the possibility of “inductive resonance” between molecules spaced at such a distance. Forster and Galanin observed a nontrivial fluorescence quenching in solutions containing mill molar levels of acceptor molecules. This nontrivial energy transfer could not be explained as occurring due to a trivial reabsorption of donor emission by acceptors. At these large concentrations the intermolecular distances are about 100Å or less, therefore the results proved that nonradiative transfer is possible when the donor and acceptors are within this distance range.

Two mechanisms could account for nonradiative energy transfer inductive resonance and exchange interaction. The inductive resonance mechanism is based on contributions from Coulomb interactions while the second is based on exchange interactions. The exchange

interactions are significant only for distances between donor and acceptor molecules that are smaller than 10\AA . The inductive-resonance mechanism is used to describe energy transfer over larger distances. Several phenomenological theories were developed to explain FRET. These theories consider donor-acceptor relations such as their spatial arrangement and their diffusion kinetics providing descriptive models of FRET. These theories also allow comparisons with experimental data. For a more detailed consideration, reference should be consulted. The dipole-dipole approximation applied by Th. Forster in his inductive-resonance theory is used exclusively to explain FRET.

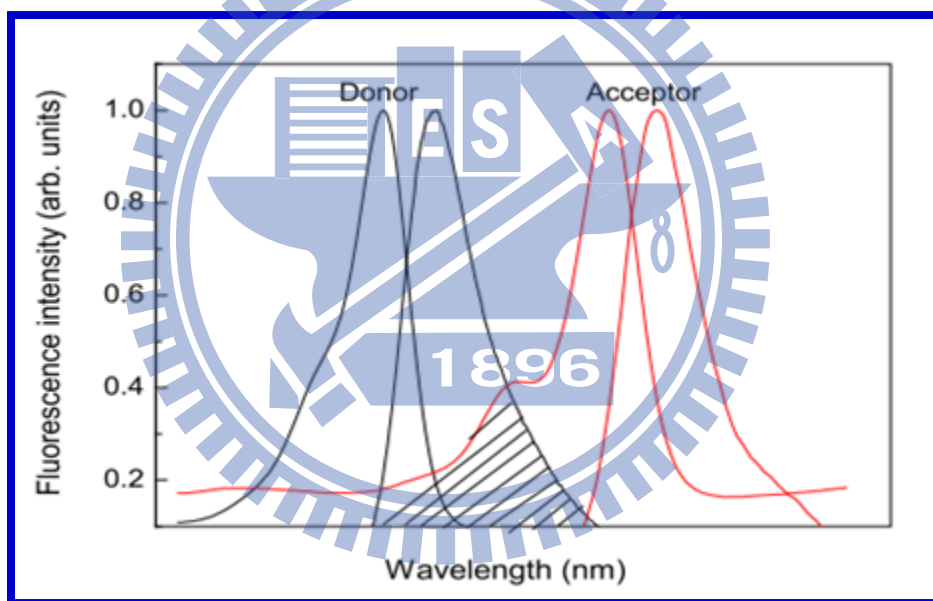


Figure 1. 33. A spectral overlap (marked in diagonal lines) between the donor emission and the acceptor absorption is required for fluorescence resonance energy transfer (FRET) between donor and acceptor fluorophores.

1. 1. 7. Ratiometric chemodosimeters

Apart from the above explained sensory mechanisms, recently, there has been immense interest in chemodosimeter based chemical sensing through a specific irreversible chemical reaction between dosimetric molecules and the target species, leading to a fluorescent/color change in the receptor. Chemodosimeter approach is often advantageous in compare to their simple fluorescent turn-off or turn-on sensors owing to their specificity towards the analyte of interest.

Despite advances in the development of new synthetic reagents, a limitation of intensity-based probes is that variabilities in excitation and emission efficiency, sample environment, and probe distribution pose potential problems for use in quantitative measurements. In contrast, ratiometric probes provide the practical advantage of builtin corrections for such variabilities by allowing simultaneous detection of two signals resulting from reacted and unreacted forms of the probe in the same sample.⁶⁵

Important analyte-recognition systems and strategies of modern chemodosimeters are mainly derived from chemosensors. Consequently, parallel to the characteristics of chemosensors, the changes in optical signals generated by dosimeters fall into two main types. One is fluorescence OFF-ON system. The free indicator is non-fluorescent (or fluorescent) and produces a fluorescent (or non-fluorescent) product after reacting with analyte. The other is the ratiometric system the indicator emit light at a certain wavelength; which is shifted after indicator reacts with an analyte.

Chemodosimeter mechanism can be divided into two main modes. (1) analytes react with the chemodosimeters, and the products show changed fluorescence signal; and (2) the analytes act as catalysts and the chemodosimeter acts as substrates of the catalyzed reactions. If the second

mechanism permits a great turn over, the fluorescence signal is much more amplified with a lower detection limit.⁶⁶ **Figure 1. 34** showed the two principles working modes of a fluorescent chemodosimeter.

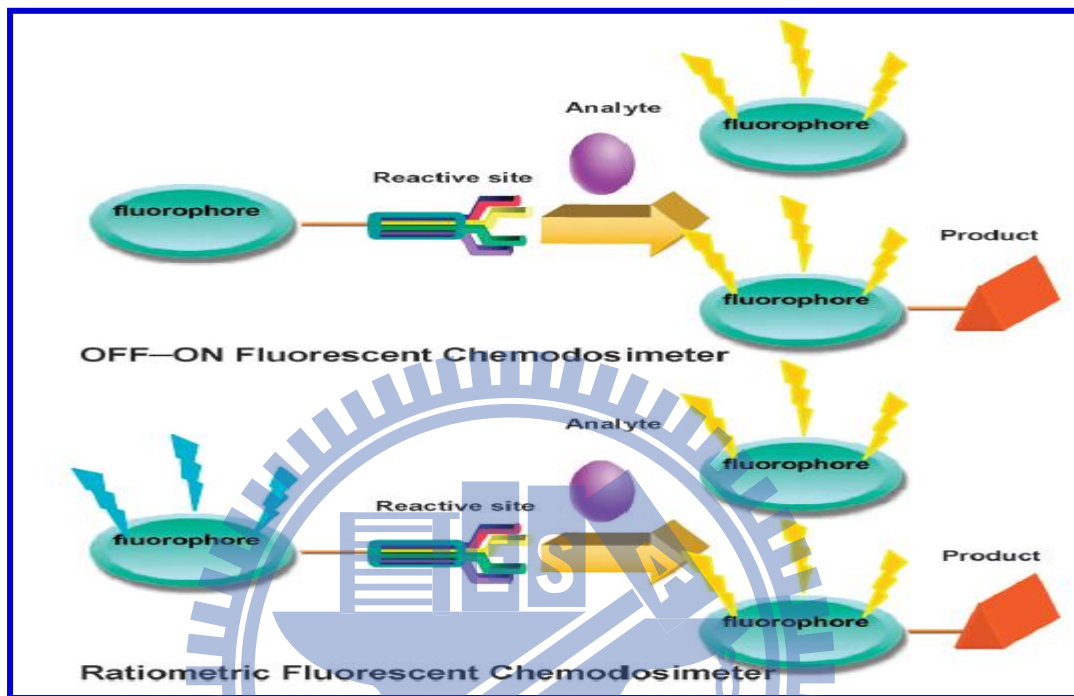


Figure 1. 34 Two principle working modes of a fluorescent chemodosimeter.

Figure 1. 35 illustrating a prototype example for specific H_2O_2 ratiometric detection based on ICT process modulated by reaction between boronate and H_2O_2 .

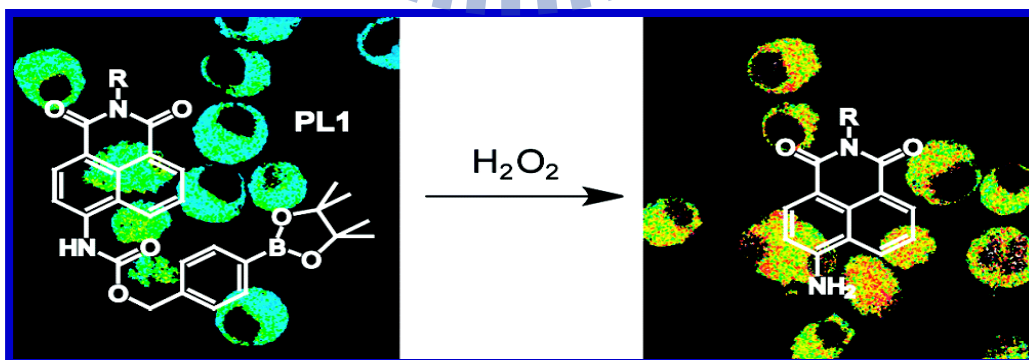


Figure 1. 35. A NDI and ICT based ratiometric Chemodosimeter for H_2O_2 .⁶⁷

1. 3. Literature Survey

1. 3. 1. Solvent and Anion Controllable [2]Rotaxane Molecular Shuttles

1. 3. 1. 1 (Solvent driven molecular shuttles)

(i) In response to a major change in the polarity of the environment of the shuttles (changing from halogenated solvents to DMSO- d_6),⁶⁸ the macrocycle stops shuttling between stations A and A' and instead spends nearly all of its time on the lipophilic station B of Leigh's peptide shuttle as shown in **Figure 1. 36**.

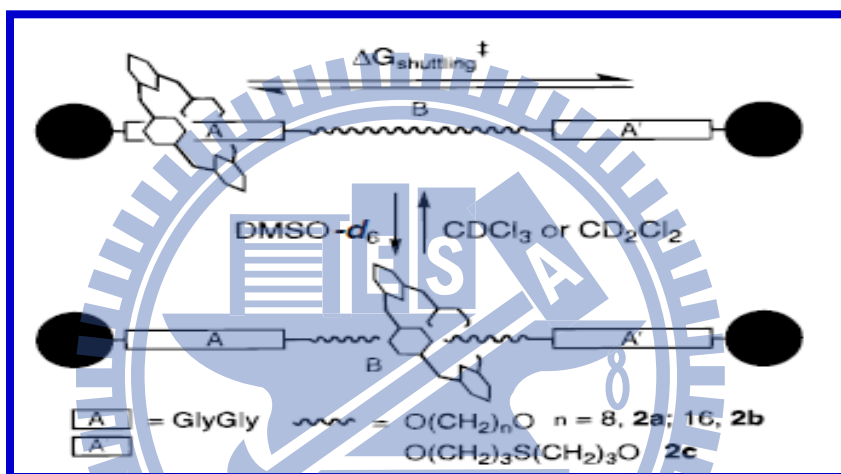


Figure 1. 36. Multistationed peptide-based molecular shuttles under solvent polarity.

(ii) A solvent-driven doubly threaded rotaxane dimer based on an amino-modified copillar[5]arene was prepared using bis(trifluoromethyl)phenyl isocyanate as stoppers by Huang and coworkers.⁶⁹ In CDCl₃, it was in a contracted state with a length of 31 Å. In DMSO- d_6 , it was in an extended state with a length of 37Å. Moreover, as the polarity of the solvent is changing, the length of the rotaxane dimer can change continuously as the contraction/stretching systems work in living organisms. It offered a basis for the construction of an environment responsive interlocked polymer that can mimic the biologic contraction/stretching process as portrayed in **Figure 1. 37**.

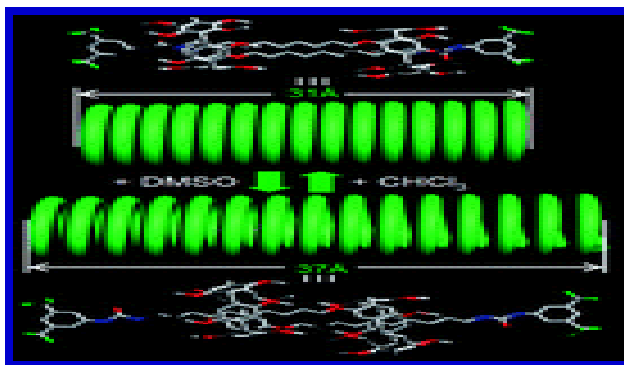


Figure 1. 37. Solvent driven copillar[5]arene based molecular spring.

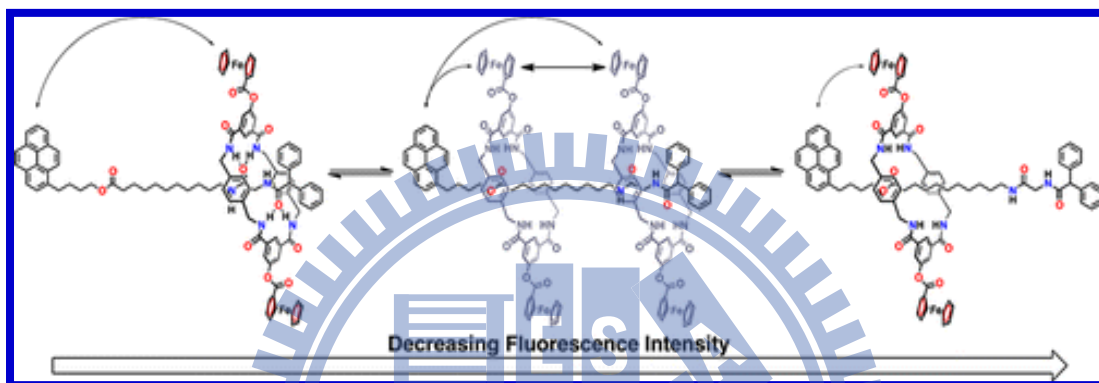


Figure 1. 38. Electronic/energy transfer between ferrocenated macrocycle and pyrene stopper [2]rotaxane with high contrast fluorescent molecular shuttle under solvent control.

(iii) Prato et. al. investigated electronic/energy transfer between ferrocenated macrocycle and pyrene stoppered [2]rotaxane, in which three different states, two nondegenerate and one degenerate, can be obtained in different solvents at room temperature as visualized in **Figure 1. 38**. This is accompanied by high contrast changes in fluorescence intensity of the pyrene stopper by the presence of the ferrocenyl moieties on the macrocycle, which quench the emission of pyrene more efficiently with proximity.⁷⁰

1. 3. 1. 2 (Anion driven molecular shuttles)

(i) Anion formation induces translocation of the macrocycle in a molecular shuttle (see **Figure 1. 39**). Shuttling only occurs in polar solvents and is unaffected by the nature of the counteraction or the presence of other anions.

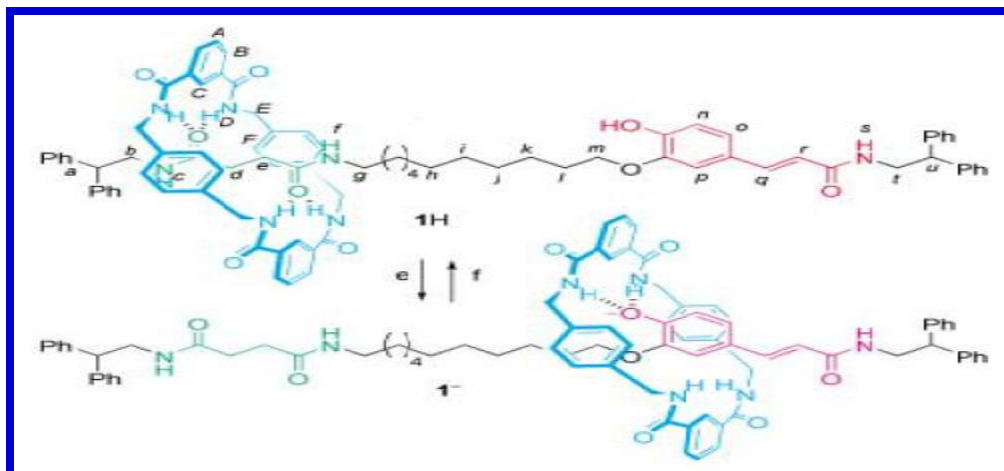


Figure 1. 39. Anion formation induced macrocycle translocation in Leigh peptide-based molecular shuttle.⁷¹

(ii) As Smith et. al. presented Cl^- binding to the interlocked [2]rotaxane induces macrocycle translocation away from the squaraine station and a reversible increase in red fluorescence emission (such as that depicted in **Figure 1. 40**). Immobilization of the rotaxane sensor creates a prototype dipstick system for fluorometric and naked-eye colorimetric detection of Cl^- in aqueous solution.

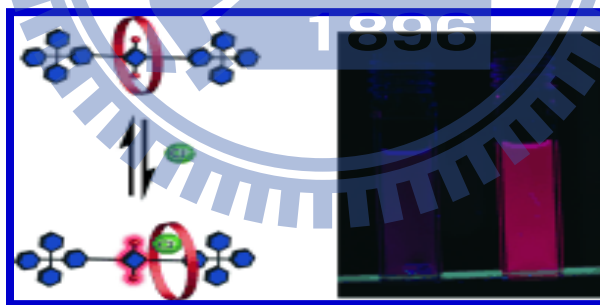


Figure 1. 40. Cl^- binding induced macrocycle translocation in squaraine based [2] rotaxane.⁷²

(iii) Chloride anion templation is used to synthesize novel rhenium(I) and ruthenium(II) bipyridyl appended [2]rotaxanes.⁷³ ^1H NMR spectroscopic titrations reveal the rotaxanes are capable of binding anions in competitive aqueous solvent mixtures, with the ruthenium rotaxane strongly complexing chloride in 30 % water. Photophysical investigations demonstrate the ability of the rotaxanes to sense anions in aqueous solvent mixtures (See **Figure 1. 41**).

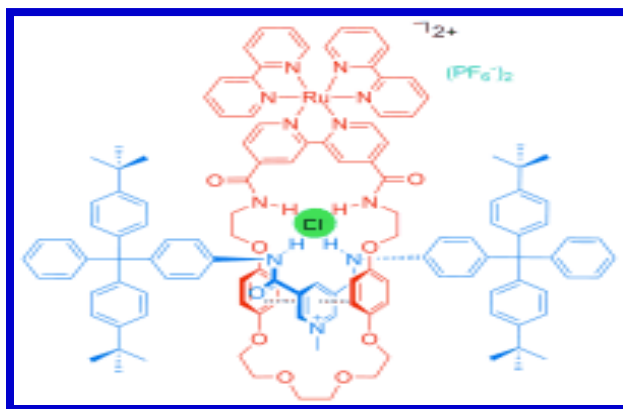


Figure 1. 41. Cl^- binding of a ruthenium complex appended [2]rotaxane molecular shuttle.

(iv) Beer et. al reported a chloride-templated synthesis of a novel [3]rotaxane, capable of binding anionic guests, and incorporating a naphthalene group for fluorescence sensing as shown in **Figure 1. 42.** Extensive ^1H NMR anion titration studies revealed the rotaxane to selectively recognize sulfate, by undergoing a conformational change to form a 1:1 stoichiometric sandwich-type complex, concomitant with significant quenching of the naphthalene emission.⁷⁴



Figure 1. 42. SO_4^{2-} binding of a naphthalene congaing [3]rotaxane molecular shuttle.

(v) Stepwise elongation and contraction of the linear threadlike component of a molecular-cage-based [2]rotaxane can be controlled in such a way that it mimics a two-stage retractable cable that can be operated in both push-button (free-selection) and rotary (continuous-change) modes, depending on the choice of operating reagents as shown in **Figure 1. 43.**

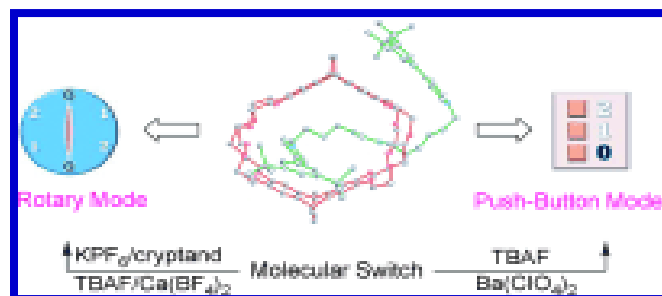


Figure 1. 43. TBAF triggered two-stage retractable functions of [2]rotaxane shuttle.⁷⁵

(vi) Chiu et. al. reported a molecular cage-based [2]rotaxane that functions as an artificial molecular muscle through the control of the addition and removal of fluoride anions as depicted in **Figure 1. 44**. The percentage change in molecular length of the [2]rotaxane is about 36% between the stretched and contracted states, which is larger than the percentage change (~27%) in human muscle.

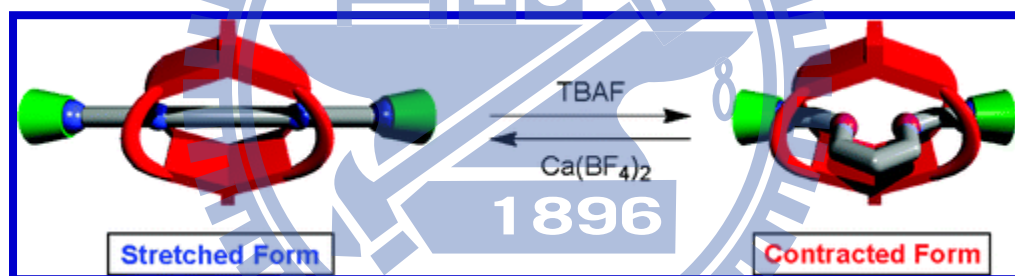


Figure 1. 44. TBAF driven reversible contracted and stretched forms of [2]rotaxane.⁷⁶

(vii) The shuttling motion of the ferrocene-functionalized macrocycle between the dibenzylammonium and the *N*-methyltriazolium recognition sites in a bistable [2]rotaxane, as well as the photo induced electron transfer process occurring between ferrocene units and the morpholin-naphthalimide fluorescent stopper, can be adjusted not only by acid–base stimuli but also addition–removal of the fluoride anion, along with remarkable, high-contrast fluorescent intensity changes as depicted in **Figure 1. 45**.

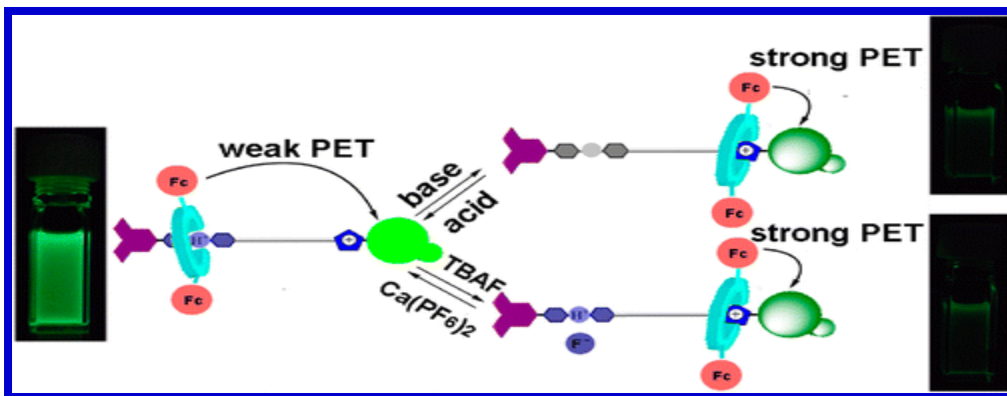


Figure 1. 45. TBAF and acid/base driven reversible morpholin-naphthalimide [2]rotaxane molecular shuttle.⁷⁷

1. 3. 2. Polyrotaxane Shuttles and their Controllable Self-assembly to form Hierarchical Nanostructures

1. 3. 2. 1 (Polyrotaxane shuttles)

(i) Swager et. al. reported two highly emissive conjugated polymers. Hydrogen bonding between acidic alcohols and *N*-heteroaromatic groups in the rotaxanes attenuated polymer fluorescence as shown in **Figure 1. 46**. In addition, the rotaxane groups create precise three-dimensional pockets for metal binding, which results in fluorescence quenching. Exposing thin films of Zn-doped polymers to alcohol vapors reverse the quenching up to 25%.

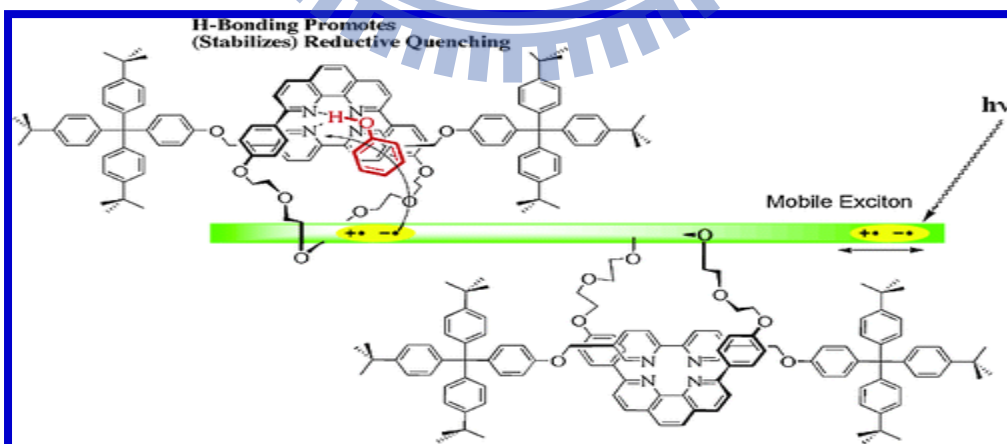


Figure 1. 46. Rotaxanated conjugated sensory polymer for acidic alcoholic vapors.⁷⁸

(ii) Yui et. al. developed a novel strategy for gene delivery using biocleavable polyrotaxanes, in which dimethylaminoethyl-modified α -cyclodextrins (DMAE- α -CDs) are threaded onto a poly(ethylene glycol) (PEG) chain capped with benzyloxycarbonyl-L-tyrosine via disulfide linkages (DMAE-SS-PRX), involves the formation of a stable polyanion complex (polyplex) against a counter polyanion and the intracellular plasmid DNA (pDNA) release from the polyplex accompanied by the supramolecular dissociation of DMAE-SS-PRXs as shown in **Figure 1. 47.**⁷⁹

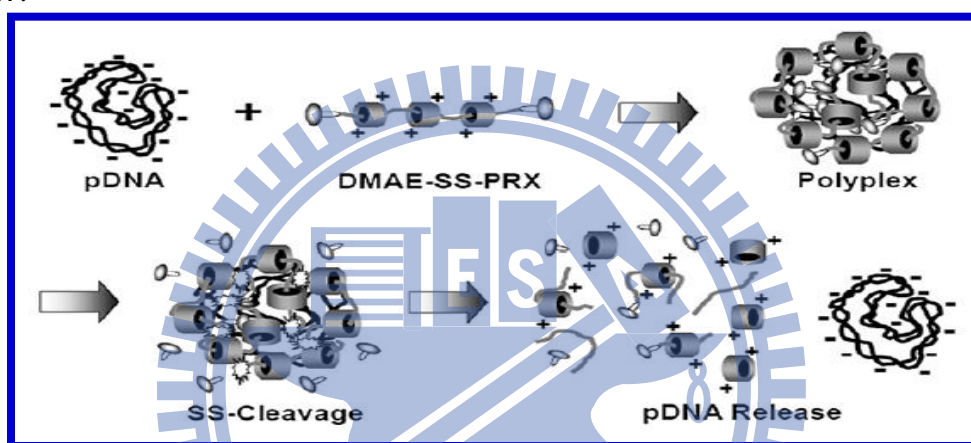


Figure 1. 47. Polyplex formation of DMAE-SS-PRX and its pDNA release by supramolecular dissociation.

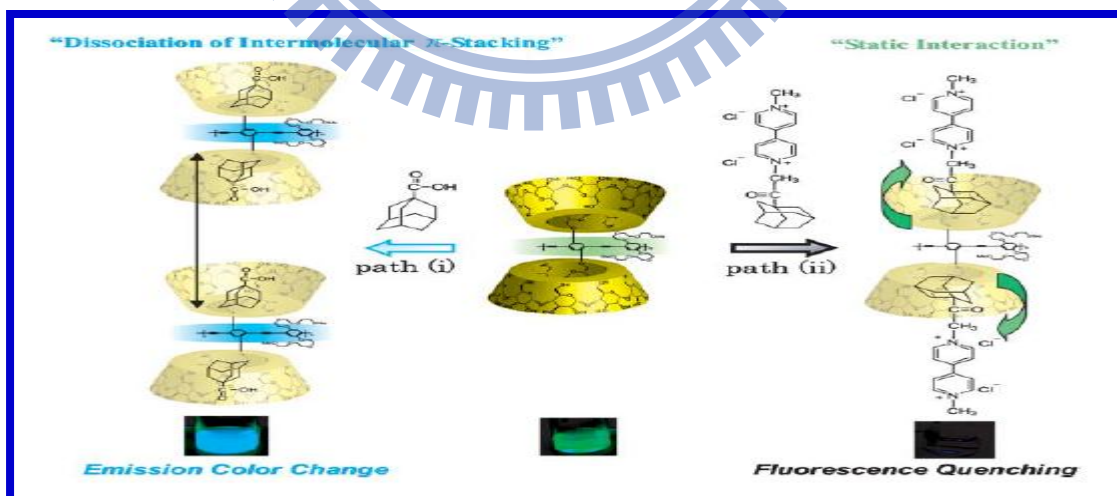


Figure 1. 48. Changes in fluorescence induced by host-guest complexes in a CD polyrotaxane.⁸⁰

(iii) Harada et. al. prepared water-soluble poly(phenylene ethylene) carrying β -cyclodextrin as shown in **Figure 1. 48**; the polymer exhibited a fluorescence color change or quenching, depending on the kind of guest.

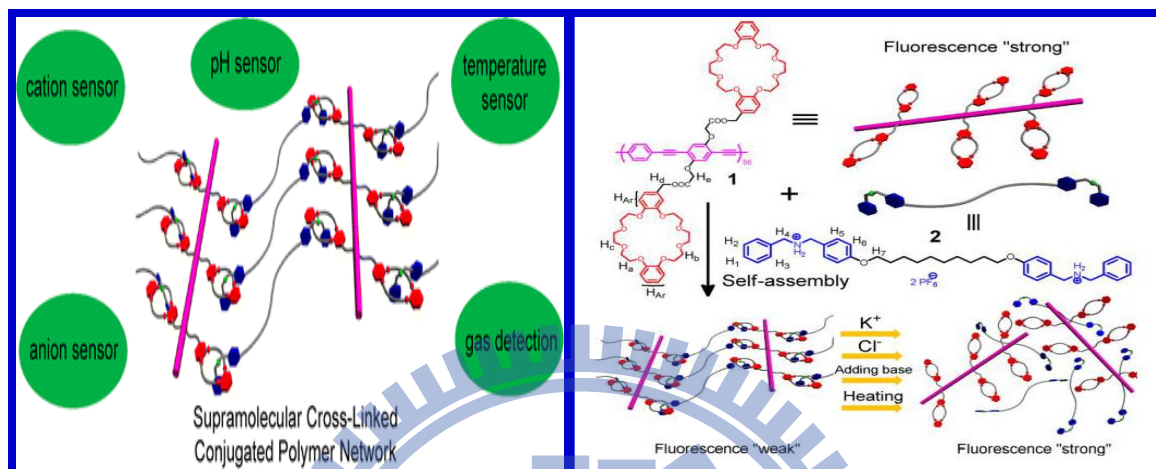


Figure 1. 49. A supramolecular cross-linked network as a multiple fluorescent sensor.⁸¹

(iv) Huang et. al have fabricated and demonstrated a supramolecular cross-linked network to act as multiple fluorescent sensor see **Figure 1. 49**. It was constructed from a fluorescent conjugated polymer and a bisammonium salt cross-linker driven by dibenzo[24]crown-8.secondary ammonium salt host-guest interactions. The fluorescence intensity of system can be enhanced by four types of signals including potassium cation, chloride ion, pH increasing, and heating in solution and film, hence current network acts as multiple sensors.

1. 3. 2. 2 (Controllable molecular self-assembly of polyrotaxanes and nanostructures)

(v) As inclusion complexes of poly(ethylene glycol)s (PEGs) and α -cyclodextrin (α -CD) had long been attracting as microtubular mimicking systems, Jeong and Kim et. al prepared a well-defined three dimensional nano structure of α -CD and PEGs by recrystallizing the resulted inclusion complex.⁸² Before recrystallization this system presented a plate-to-needle shaped

structure, however recrystallization in the presence of phosphate buffer yielded 3D- Hexagonal fiber as shown in the SEM image (**Figure 1. 50**).

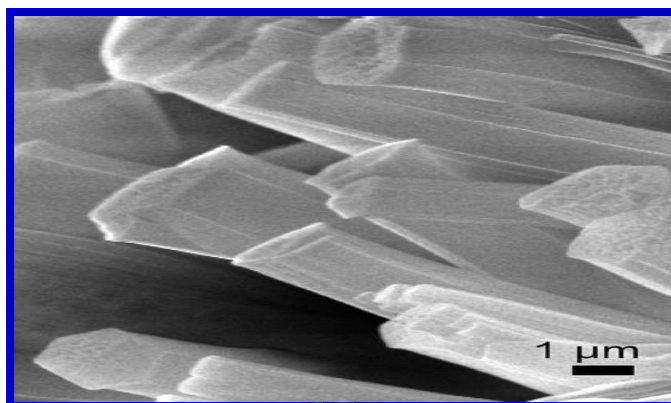


Figure 1. 50. SEM image presenting a 3D-hexagonal microfiber as drawn from a α -CD and PEG inclusion complex.

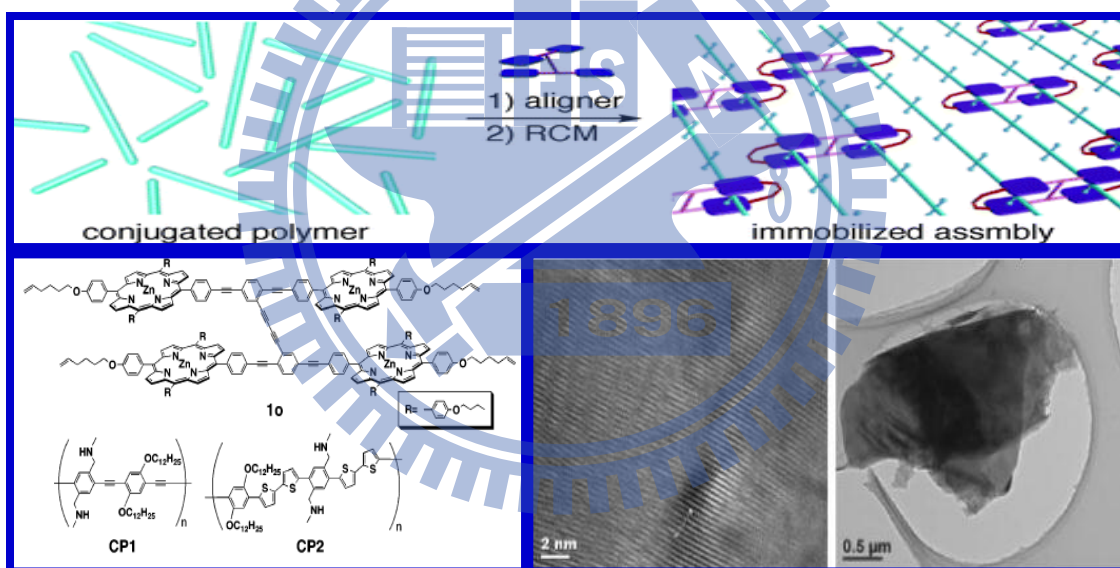


Figure 1. 51. Immobilized self-assembly of CP and aligner under RCM condition. TEM images denoting CP-aligner self-assembled structures before and after TFA treatment.

(vi) Shinkai et. al constructed aligned assemblies of conjugated polymers through supramolecular bundling and olefin metathesis.⁸³ HRTEM images (**Figure 1. 51**) showed 2.0 nm uniform periodicity self-assembled structures supramolecular bundles and their dissemble under acid treatment .

(vii) A bistable side-chain poly[2]catenane has been synthesized and found to form hierarchical self-assembled hollow superstructures of nanoscale dimensions in solution. Molecular electromechanical switching (see **Figure 1. 52**) of the material is demonstrated, and the ground-state equilibrium thermodynamics and switching kinetics are examined as the initial steps on the way to processible molecular-based electronic devices and nanoelectromechanical systems.⁸⁴

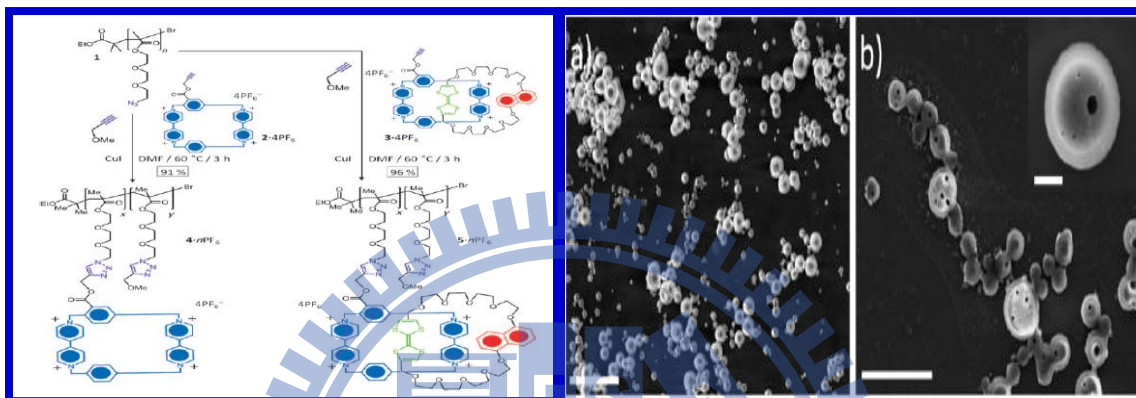


Figure 1. 52. Donor/acceptor based poly[2]catenane and its drop casted SEM self-assemble images.

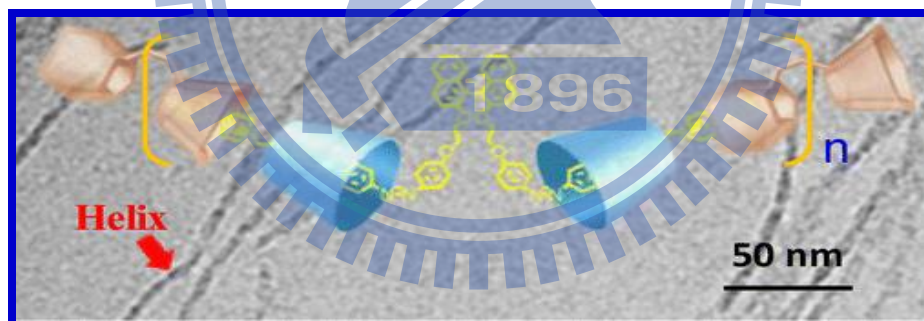


Figure 1. 53. Single helical nanostructure drawn from a calix[4]arene- α -CD based supramolecular chiral polyrotaxane.⁸⁵

(viii) Tian et. al constructed a light-driven, linear, chiral supramolecular polymer in water by host–guest molecular recognition between bis(*p*-sulfonatocalix[4]arene) and the α -cyclodextrin-based pseudo[3]rotaxane containing axially chiral 1,1'-binaphthyl and photoresponsive azobenzene moieties. More interestingly, dynamically self-assembled, light-driven, single-helical

linear supramolecular polymer molecules with lengths of hundreds of nanometers to micrometers in water were directly observed in their native state using cryo-TEM measurements as shown in **Figure 1. 53**.

1. 3. 3. Fluorescent Chemosensors for Hydrazine

(i) Chang et. al investigated chemosignaling of hydrazine by selective deprotection of levulinated coumarin. In the presence of hydrazine, levulinated coumarin was selectively deprotected, resulting in chromogenic and fluorescent turn-on type signaling as shown in **Figure 1. 54**. The selective naked-eye detectable signaling of hydrazine was possible in the presence of representative metal ions and common anions in an aqueous environment.⁸⁶

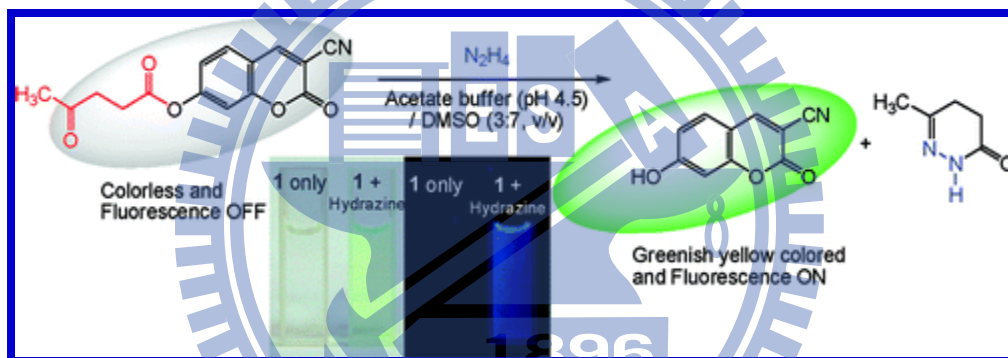


Figure 1. 54. Coumarin levulinated fluorogenic and chromogenic probe for selective detection of Hydrazine.

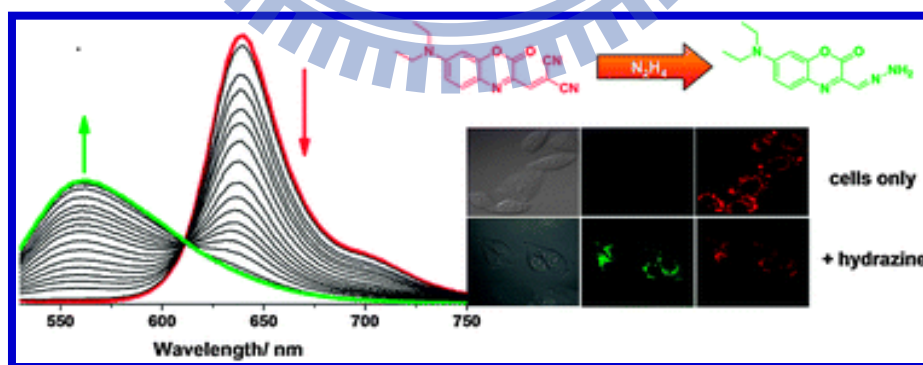


Figure 1. 55. 7-diethylamino-1,4-benzoxazine-2-one (DEAB) and ICT based ratiometric probe for Hydrazine.⁸⁷

(ii) Hydrazine is an important industrial chemical but also very toxic thus requiring rapid detection agents. Peng and Fan et. al successfully designed and demonstrated a ratiometric fluorescent probe that enables rapid low-limit and naked eye detection of hydrazine in solution and living cells (see **Figure 1. 55**).

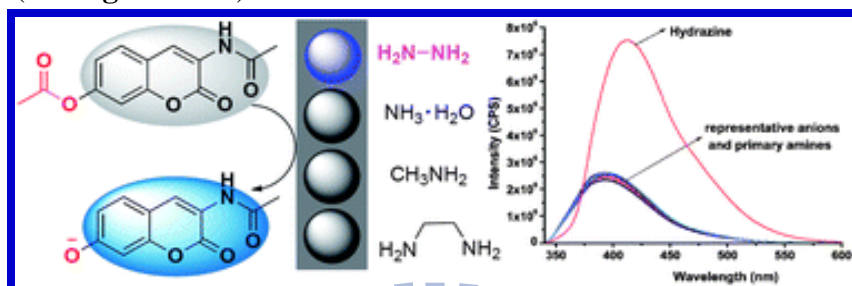


Figure 1. 56. Coumarin based chromogenic and ratiometric probe for Hydrazine.⁸⁸

(iii) Yu et. al presented a coumarin-based chromogenic and ratiometric probe for hydrazine, which could selectively detect hydrazine *via* an intramolecular charge transfer (ICT) mechanism with a red-shift of 21 nm as shown in **Figure 1. 56**. Importantly, the probe could selectively detect hydrazine over other primary amines.

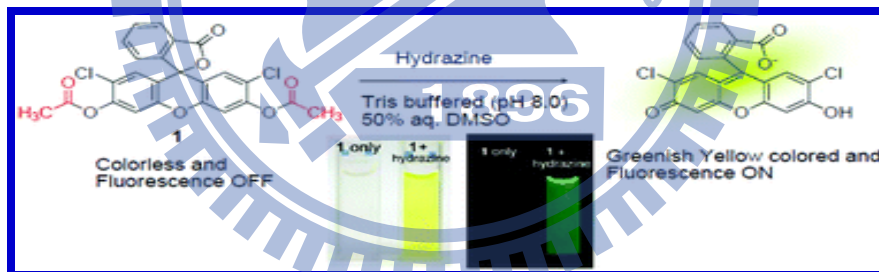


Figure 1. 57. Dichlorofluorescein and resorufin based dual signaling probe for Hydrazine.⁸⁹

(iv) Chang et. al investigated a highly selective chemosignaling behaviors for hydrazine by a reaction-based probe of dichlorofluorescein and resorufin acetates. Hydrazinolysis of latent dichlorofluorescein and resorufin acetate fluorochromes caused prominent chromogenic and fluorescent turn-on type signals as depicted in **Figure 1. 57**. Dichlorofluorescein and resorufin acetates selectively detected hydrazine with detection limits of 9.0×10^{-8} M and 8.2×10^{-7} M, respectively.

(v) Recently Peng et al have designed and synthesized cyanine dye derivative with a modulation of the conjugated polymethine π -electron system (Cy7A) with near-infrared ratiometric selective sensing for hydrazine (**Figure 1.58**). Cy7A can be selectively hydrazinolysized with great changes in its fluorescent excitation/emission profiles, which makes it possible to detect N_2H_4 in water samples and living cells and, for the first time, visualize N_2H_4 .⁹⁰

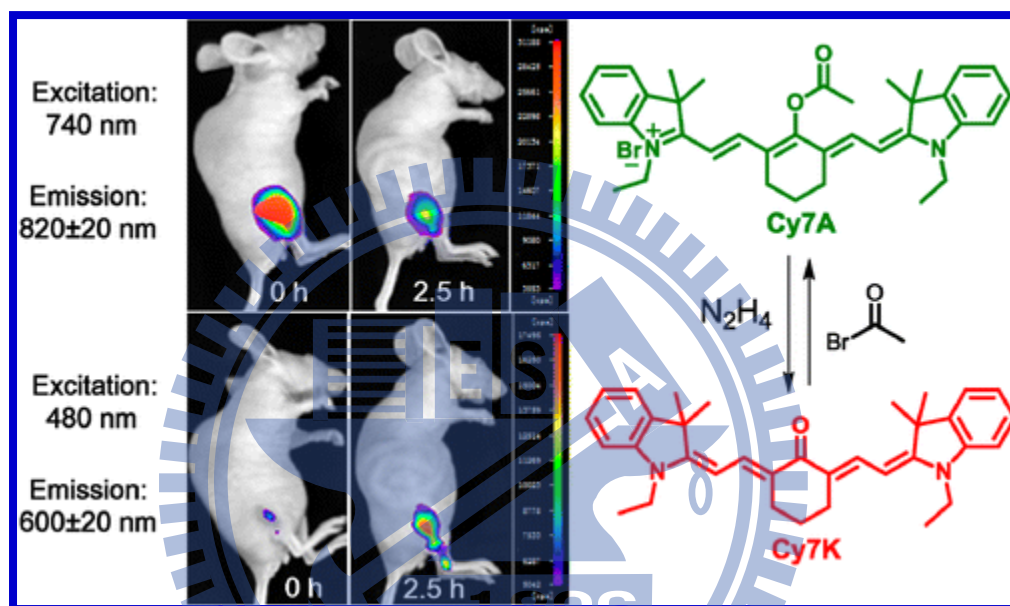


Figure 1. 58. Conjugated polymethine π -electron contained cyanine derivative (Cy7A) for selective ratiometric sensing of hydrazine in NIR-region.

1. 4 Research Motive

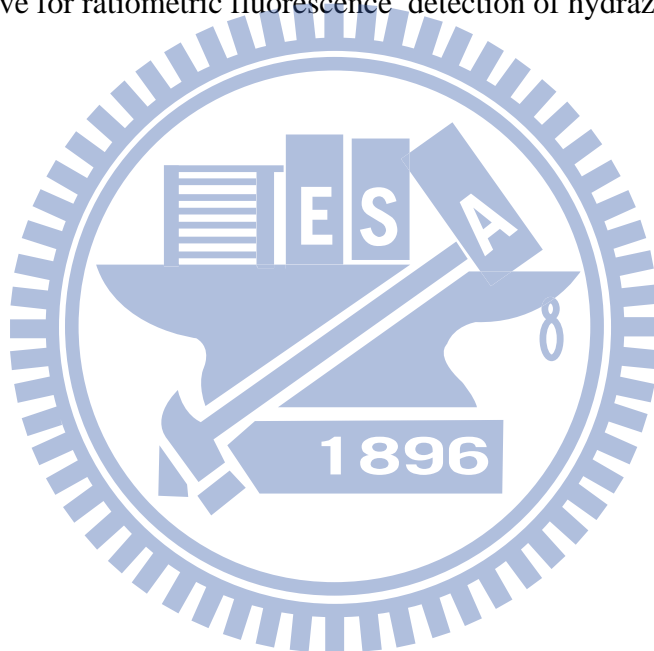
Mechanically interlocked molecules (MIMS) are archetype supramolecules as they involve almost all kinds of supramolecular interactions such as van der Waals interaction, dipolar and quadrupolar interactions, charge transfer and π - π interaction, metal coordination and hydrogen bonding, anion- π interactions, C-H- π interaction etc. supramolecular conception bearing noncovalent bond segments, e.g. H-bonds, was investigated and developed because of its functional properties and extensive availabilities by the molecular design of inter and intramolecular configurations.

Beyond their aesthetic appeal polymeric counterparts of MIMS such as MIPAs are now playing vital role in nanoscience and nanotechnology. Self-assembled phenomena through molecular recognition between complementary constituents have been explored in various areas such as nanoelectromechanical systems, insulated molecular wires, controlled drug release, artificial molecular muscles etc. Interestingly, supramolecular approaches have been employed in MIPAs to establish controllable hierarchical nano self-assembled superstructures. The unique molecular switchable functions of MIMS under various stimuli control have long been utilized to construct novel functional switches.

Rapid industrial growth and academic interests had long been creating great turmoil on environment and humans. Various small molecule guests, heavy metals, anions inherently releasing the ghastly toxic effects on environment and even accumulating in sea animal. So the need of realizing and design of molecular probes to detect the trace amounts various analytes is ever demanding interest around the scientific community. Fluorometric methods have been offering better and reliable paths in analyzing those guests owing to their easy functions. However, amending of the analytical techniques is promising area to realize novel sensor

molecules. All the key issues and attributes motivated us to design and study of molecular self-assembled structures as well as facile and efficient molecular probes.

Hence, we devoted to design the complex molecular architectures and reaction based molecular probes facile and efficient synthetic protocols having desired functions, which are presented in following section as three topics (Chapter 2-4): (1) Highly selective optical sensing of fluoride using a novel DPP based [2]rotaxane, (2) An Acid-Base controllable hierarchical nano self-assemble structure from a conjugated side-chain polyrotaxane, and (3) phthalimide appended naphthalimide derivative for ratiometric fluorescence detection of hydrazine .



Chapter-2

A Novel Diketopyrrolopyrrole (DPP)-Based [2]Rotaxane for Highly Selective Optical sensing of Fluoride

2. 1. Introduction

Developing bright and novel functional mechanically interlocked molecules (MIMs) with controlled topology for selective and sensitive anion binding and sensing is of current research interest in the field of anion supramolecular chemistry owing to their indispensable roles in biological and chemical processes.⁹¹ Due to its unique chemical properties and significant aspects in pharmacology, dental care, and treatment of osteoporosis, the fluoride ion is one of the most intriguing targets among all anions.⁹² It is thus imperative to develop MIM based probes for sensitive and selective sensing of fluoride. Controlled topology has been elegantly utilized by nature in recognition of anionic guests, inspired by many artificial anion receptors to be developed for the specific recognition of halides and other anions.⁹³ Myriads of molecular switches have been reported, due to their exquisite responsiveness to stimuli^{34b,44,45,51,53,78,94} and the handful of optical anion sensors;^{72,77,95} however, those switches often suffered in recognition of anionic guests in a discriminative fashion. To mimic this, we need a robust signaling unit (fluorophore) and a cavity with unique topological constraints formed in situ by virtue of mechanical bonding. Additionally pervasive advantages of chromogenic and fluorogenic molecular switches have been found because of their ease in responding to subtle guest interactions in microenvironments to perceivable outputs.⁹⁶

The exceptional thermal and light stabilities of 3,6-di(thiophen-2-yl)pyrrolo[3,4-c]pyrrole-1,4(2*H*,5*H*)-dione (DPP) and its derivatives along with remarkable photophysical properties make them expedient candidates in designing new functional MIMs.⁹⁷ Since fluoride ions have a

strong reactivity with receptor groups, such as amine, amide, lactam, urea, thiourea, and phenol, due to its high electronegativity and small ionic size, miscellaneous macrocyclic and tweezer-shaped receptors have been reported.⁹⁸ However, reports based on [2]rotaxanes with controllable topology under external stimuli having specific anionic guest binding abilities are still due.

Herein, we designed and synthesized a first example of a DPP stoppered [2]rotaxane **2-P** containing an orthogonal bifurcated pyridine-pyridine H-bonded motif. This design was found to be ideal for solvent induced shuttling and specific fluoride ion sensing with sensitive chromogenic and fluorogenic functions along with remarkable reversibilities (see **Figure 2. 1**).^{94a,99}

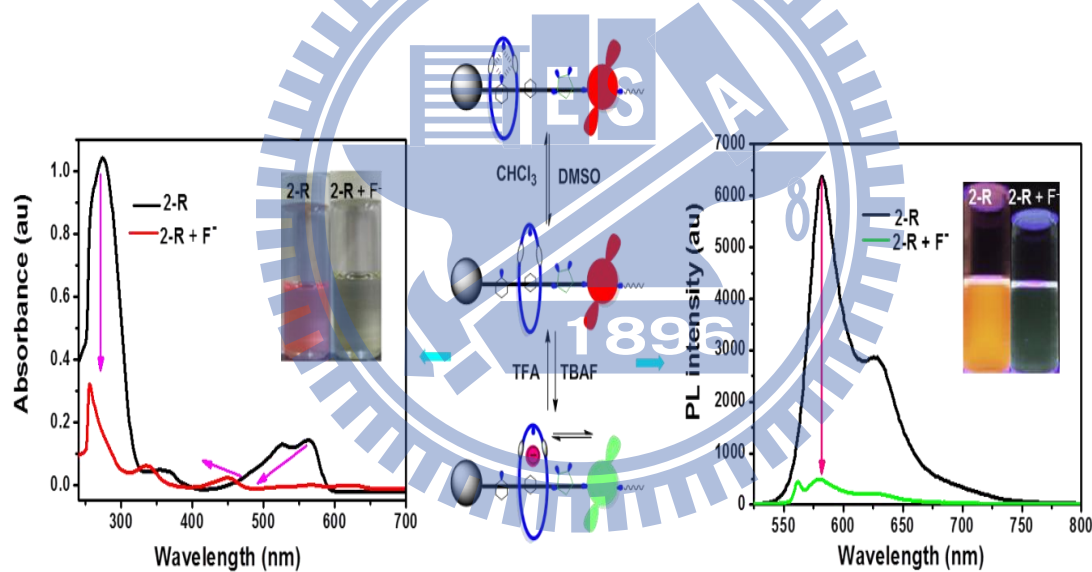


Figure 2. 1. Solvent polarity changes and anion tetrabutylammonium fluoride (TBAF) driven highly contrasted fluorescent DPP based reversible [2]rotaxane molecular shuttles.

2. 2. Experimental section

2. 2. 1. General methods and materials:

All the reactions and operations were carried out under an atmosphere of inert argon or nitrogen using Schlenk techniques unless otherwise stated. NMR spectra were recorded on Bruker DRX-300 Avance series or on a Varian Inova 400, Inova 500 and Inova 600 Series (^1H : 300, 400, 500 and 600 MHz; ^{13}C : 75, 100, 125 and 150 MHz) at a constant temperature of 298 K. Chemical shifts were reported in parts per million from low to high field and referenced to residual solvent (CDCl_3 $\delta = 7.26$ ppm and $\delta = 77.23$ ppm; $\text{DMSO-}d_6$ $\delta = 2.49$ ppm and $\delta = 39.56$ ppm respectively). Coupling constant (J) were reported in hertz (Hz). Standard abbreviations indicating multiplicity were used as follows: s = singlet, d = doublet, t = triplet, m = multiplet, br = broad. The detailed NMR assignments of final rotaxane were done with the aid of ^1H , ^{13}C , DEPT and 2D (COSY, HSQC, HMBC). UV-Vis spectra were recorded in different solvents from a Jasco UV-600 spectrophotometer using 1 cm quartz cuvette. Fluorescence measurements were conducted with HITACHI 4000 Series Spectrophotometer. All emission and excitation spectra were corrected for the detector response and the lamp output. Melting points were determined using a Fargo MP-2D apparatus and are uncorrected. Elemental analyses were conducted on HERAEUS CHN-OS RAPID elemental analyser. Time-resolved photoluminescence (TRPL) spectra were measured using a home built single photon counting system with excitation from a 525 nm diode laser (Picoquant PDL-200, 50 ps fwhm, 2 MHz). The signals collected at the excitonic emissions of all sample solutions were connected to a time-correlated single photon counting card (TCSPC, Picoquant Timeharp 200). The emission decay data were analyzed for **2-R/F** complex with biexponential kinetics, from which two decay components were derived; the lifetime values of (τ_1 , τ_2) and pre-exponential factors (A_1 , A_2) were determined. High resolution

mass spectroscopic measurements were performed using Bruker Daltonics Flex Series MALDI TOF/TOF instrument using α -cyano-4-hydroxycinnamic acid (CHC). ^{19}F NMR titrations were performed on (Varian Inova 400 MHz). Infrared spectroscopy data were collected using Perkin Elmer IR spectrophotometer. Solid sample were analysed using KBr pellet method and liquid sample data collected by forming neat thin film between two NaCl plates. CV measurements were conducted using (0.1 M TBAPF₆ (tetrabutylammonium hexafluorophosphate) as a supporting electrolyte at a scan rate of 0.1 Vs⁻¹; Carbon working electrode, Ag/AgCl reference electrode and Platinum wire as counter electrode) CHI661C CH Instruments Inc analyser.

All the reagents were purchased from commercial sources and used without further purification. All the solvents were HPLC grade; anhydrous solvents were obtained by passing through activated alumina column purification system, further dried by standard drying procedures. Solvents were degassed by freeze/thaw/pump cycle technique prior to use. Thin layer chromatographies (TLC) were performed on Glass plate coated with silica 60 F24 (Merck). The plates were visualized using ultra-violet light (256 nm) and developed using I₂ chamber. Flash chromatographies were performed on Merck silica gel 60 (230-400 mesh) under pressure using desired solvents.

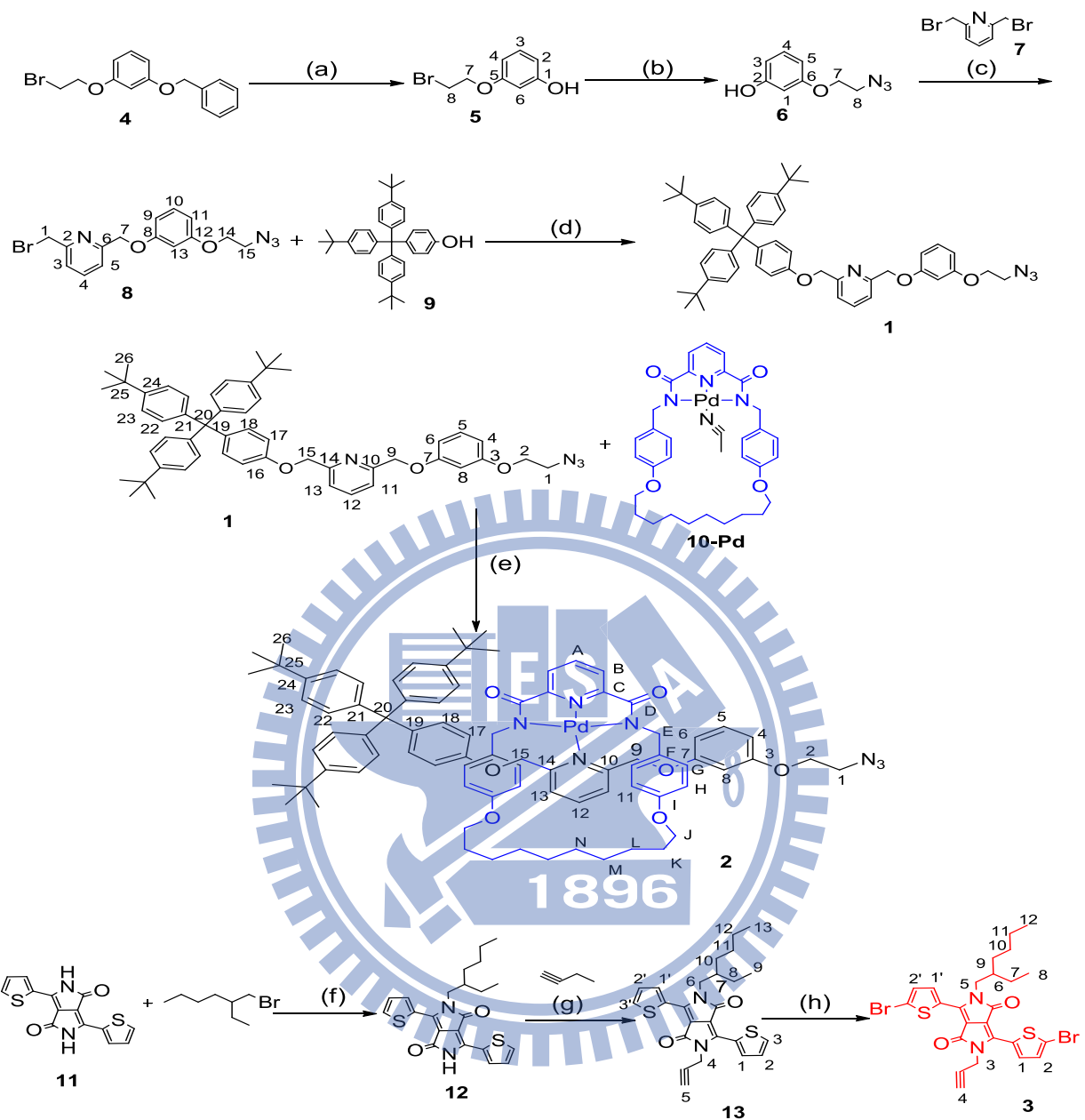
The following compounds were prepared according to literature procedures: 1-(benzyloxy)-3-(2-bromoethoxy)benzene **4**,¹⁰⁰ 2,6-bis(bromomethyl)pyridine **7**,¹⁰¹ stopper **9**,¹⁰² macrocycle **10-Pd**,¹⁰³ unsubstituted DPP **11**.¹⁰⁴

2. 2. 2. Stock solution preparation:

All the receptors (**1-C**, **2-M**, **2-P**, and **2-R**) solutions were prepared using dried and degassed solvents with a concentration of (100 μM in CH_2Cl_2 and DMSO) and all anion solutions (F^- , Cl^- , Br^- , I^- , AcO^- , NO_3^- , and H_2PO_4^-) were prepared from their respective TBA salts with concentration of (10 mM). Before titration studies receptors and anions were diluted to their desired volumes in respective solvents.

2. 2. 3. Synthesis of Compound 1, Compound 2, and DPP derivative 3:

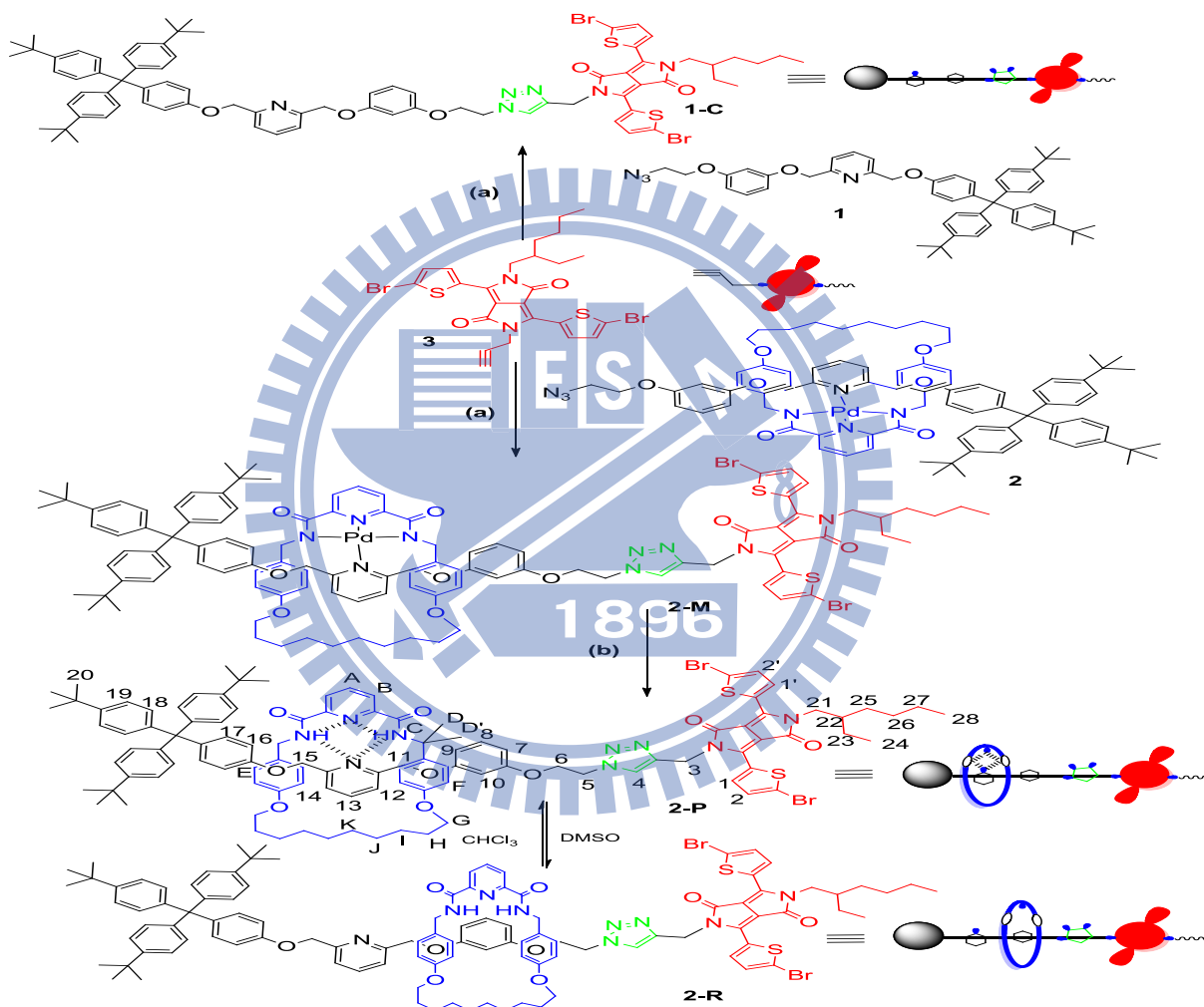
The key building blocks, i.e., pseudorotaxane **2** and asymmetric diketopyrrolopyrrole derivative **3**, were prepared in good yields. Compound **2** was synthesized from monodentate thread **1** and a preformed macrocycle-Pd tridentate ligand¹⁰⁵ using a palladium active metal template approach (see **Scheme 2. 1**). Novel asymmetric DPP derivative **3** was prepared from **11** in 3 steps. First, compound **11** was mono-alkylated with 2-ethylhexyl bromide to acquire compound **12**, which was further alkylated with propargyl bromide to afford **13**. Then, it was brominated by NBS to obtain asymmetric DPP derivative **3** as shown in **Scheme 2. 1**.



Scheme 2. 1. Synthesis of compounds **1**, **2**, and **3**; Reagents and conditions: (a) 10% Pd/C, H₂ (balloon), THF / EtOH (8/2), rt, 10 h, 91%; (b) NaN₃, DMF, 60 °C, 10 h, 91%; (c) K₂CO₃, CH₃CN, reflux, 24 h, 57%; (d) K₂CO₃, CH₃CN, reflux, 24 h, 91%, (e) CHCl₃ / CH₃CN (8/2), rt, 4 h, 87%; (f) *t*-BuOK, DMF, rt, 3 h; (g) *t*-BuOK, DMF, rt, 3 h, 54%; (h) NBS, CHCl₃, rt, 48 h, 76%.

2. 2. 4. Synthesis of Compound 1-C, [2]Rotaxane 2-M, and [2]Rotaxane 2-P:

The building blocks **2** and **3** were coupled by utilizing a click reaction strategy to afford metalated [2]rotaxane **2-M**, likewise control axle **1-C** was prepared. To manipulate guest binding capabilities, **2-M** was demetalated using potassium cyanide in $\text{CHCl}_3/\text{MeOH}$ to produce final [2]rotaxane **2-P** as depicted in **Scheme 2. 2**.



Scheme 2. 2. Synthesis of compounds **1-C**, **2-M**, and **2-P**; Reagents and conditions: (a) $\text{CuSO}_4 \cdot 5\text{H}_2\text{O}$, Sodium ascorbate, THF / H_2O (1/1), rt, 6 h; yields of **1-C** (76%) and **2-M** (73%). (b) KCN, $\text{CHCl}_3/\text{MeOH}$, rt, 2 h, 64%.

2. 2. 5. Synthetic procedures:

Synthesis of 3-(2-bromoethoxy)phenol-(5):

1-(benzyloxy)-3-(2-bromoethoxy)benzene **4** (3.25 g, 10.58 mmol, 1.0 equiv) was weighed in a 100 ml dried round bottomed flask and was added degassed mixture of THF/EtOH (8/2, 50 ml). The round bottomed flask was evacuated by 3 freeze-thaw-pump cycle. To the above solution was added carefully 10% Pd/C (0.325 g, 10 w %) then further evacuated by a freeze-thaw-pump cycle. H₂-gas was applied through balloon and the reaction stirred at room temperature for 10 h. The solution was filtered through celite bed and washed with (40 ml) of THF. The organic layer was dried over MgSO₄ after filtration the solvent was evaporated under reduced pressure to give a (2.1 g, 9.67 mmol, 91%) of pale brown liquid **5**. Chemical formula: C₈H₉BrO₂, Molecular weight: 217.06

¹H NMR (300 MHz, CDCl₃, 298 K): δ (ppm) = 7.14 (t, J_t = 8.0 Hz, 1H, 3), 6.50-6.41 (m, 3H, 2, 4, and 6), 5.26 (s, br, 1H, OH), 4.26 (t, J_t = 6.30 Hz, 2H, 7), 3.63 (t, J_t = 6.30 Hz, 2H, 8); ¹³C NMR (100 MHz, CDCl₃, 298 K): δ (ppm) = 159.1 (5), 156.4 (1), 130.2 (3), 108.6 (4), 107.0 (2), 102.4 (6), 67.7 (7), 29.1 (8); MS (+EI): (m/z): Calcd for C₈H₉BrO₂; 217.06; found: 217.06 [M]⁺, 218 [M+2]⁺; IR (wave number cm⁻¹) = 3041, 2974, 2866, 1608, 1470, 1287.

Synthesis of 3-(2-azidoethoxy)phenol-(6):

To a solution of 3-(2-bromoethoxy)phenol **5** (2.00 g, 9.21 mmol, 1.0 equiv) in DMF (40 ml) was added NaN₃ (1.79 g, 27.64 mmol, 3.0 equiv) and the suspension stirred at 60 °C for 10 h at which time the suspension was cool down to room temperature. The suspension was poured into a beaker containing Et₂O (400 ml) and H₂O (400 ml) and the layers separated. The organic phase was washed with H₂O (2 x 200 ml) and followed by brine solution (2 x 200 ml). The Et₂O solution was dried over (MgSO₄) after filtration the solvent removed in vacuum. The crude

residue was subjected to column chromatography (silica gel, Hexane/ EtOAc: 9/1 to 6/4). A brown liquid **6** was recovered (1.51 g, 8.42 mmol, 91%). Chemical formula: C₈H₉N₃O₂, Molecular weight: 179.18.

¹H NMR (300 MHz, CDCl₃, 298 K): δ (ppm) = 7.16 (t, J_t = 8.1 Hz, 1H, 3), 6.53-6.45 (m, 3H, 2, 4, and 6), 5.10 (s, br, 1H, OH), 4.12 (t, J_t = 4.95 Hz, 2H, 7), 3.58 (t, J_t = 4.95 Hz, 2H, 8); **¹³C NMR** (100 MHz, CDCl₃, 298 K): δ (ppm) = 159.1 (5), 156.5 (1), 130.1 (3), 108.4 (4), 106.6 (2), 102.1 (6), 66.6 (7), 49.8 (8); **MS (+EI)**: (m/z): Calcd for C₈H₉N₃O₂; 179.18; found: 179 [M]⁺, 180 [M+H]⁺, 151 [M-OH-N₃]⁺; **IR** (wave number cm⁻¹) = 3028, 2942, 2876, 2119 (azide), 1601, 1497, 1295, 1157.

Synthesis of 2-((3-(2-azidoethoxy)phenoxy)methyl)-6-(bromomethyl)pyridine-(8):

To a solution of 3-(2-azidoethoxy)phenol **6** (0.80 g, 4.46 mmol, 1.0 equiv) in Acetonitrile (30 ml) was added K₂CO₃ (7.40 g, 53.57 mmol, 12.0 equiv) and the suspension was stirred for 20 min at 60 °C at which time 2,6-bis(bromomethyl)pyridine **7** (3.60 g, 13.61 mmol, 3.05 equiv) in Acetonitrile (20 ml) was added slowly over a period of 10 min and the suspension was stirred under reflux for 24 h. After cooling, the mixture was filtrated and the residual solid washed with EtOAc. The filtrate was evaporated under reduced pressure and the crude residue was subjected to column chromatography (silica gel hexane/ EtOAc: 9/1). A pink solid **8** was recovered (925 mg, 2.54 mmol, 57%). Chemical formula: C₁₅H₁₅BrN₄O₂, Molecular weight: 363.21.; mp. 63.5-65.3 °C

¹H NMR (300 MHz, CDCl₃, 298 K): δ (ppm) = 7.70 (t, J_t = 7.78 Hz, 1H, 4), 7.44 (d, J_d = 7.74 Hz, 1H, 3 or 5), 7.34 (d, J_d = 7.65 Hz, 1H, 3 or 5), 7.18 (t, J_t = 8.08 Hz, 1H, 10), 6.62-6.52 (m, 3H, 9,11, and 13) 5.16 (s, 2H, 1), 4.54 (s, 2H, 7), 4.10 (t, J_t = 4.96 Hz, 2H, 14), 3.55 (t, J_t = 4.96 Hz, 2H, 15); **¹³C NMR** (100 MHz, CDCl₃, 298 K): δ (ppm) = 159.3 (8 or 12), 159.2 (8 or 12),

157.0 (2 or 6), 156.0 (2 or 6), 137.7 (4), 129.9 (10), 122.2 (3 or 5), 120.3 (3 or 5), 107.4 (9 or 11), 107.2 (9 or 11), 101.8 (13), 70.2 (7), 66.7 (14), 49.9 (15), 33.5 (1); **MS (+EI)**: (m/z): Calcd for C₁₅H₁₅BrN₄O₂; 363.21; found: 363 [M]⁺, 365 [M+2]⁺; **IR** (KBr, cm⁻¹) = 23042, 3001, 2953, 2095(azide), 1591, 1352, 1177; **Anal. Calcd. for** C₁₅H₁₅BrN₄O₂: C, 49.60; H, 4.16; N, 15.43, found: C, 49.68; H, 4.18; N, 15.40.

Synthesis of 2-((3-(2-azidoethoxy)phenoxy)methyl)-6-((4-(tert-butyl)phenyl)methyl)phenoxy)methylpyridine-(1):

To a stirred solution of 4-(tris(4-(tert-butyl)phenyl)methyl)phenol **9** (0.50 g, 0.99 mmol, 1.0 equiv) in Acetonitrile (45 ml) in a 100 ml round bottomed flask was added K₂CO₃ (1.64 g, 11.88 mmol, 12.0 equiv) and the suspension stirred at 60 °C for 20 min. To above suspension was added 2-((3-(2-azidoethoxy)phenoxy)methyl)-6-(bromomethyl)pyridine **8** (0.36 g, 0.99 mmol, 1.0 equiv) in Acetonitrile (5 ml) over a period of 10 min at which time the suspension refluxed for 24 h. After cooling, the mixture was filtrated and residual solid washed with EtOAc. The filtrate was evaporated under reduced pressure and the crude residue was subjected to column chromatography (silica gel, Hexane/ EtOAc: 9/1). A white solid **1** was recovered (0.71 g, 0.90 mmol, 91%). Chemical formula: C₅₂H₅₈N₄O₃, Molecular weight: 787.04.; mp. 174-176 °C.

¹H NMR (300 MHz, CDCl₃, 298 K): δ (ppm) = 7.77 (t, J_t = 7.77 Hz, 1H, 12), 7.49-7.47 (m, 2H, 13 or 11), 7.29-7.26 (m, 7H, 23 and 5), 7.14-7.13 (m, 8H, 22 and 18), 6.91-6.88 (m, 2H, 17) 6.67-6.55 (m, 3H, 6,4, and 8), 5.23 (s, 4H, 9 and 15), 4.14 (t, J_t = 5.01 Hz, 2H, 2), 3.59 (t, J_t = 4.99 Hz, 2H, 1), 1.35 (s, 27H, 26); **¹³C NMR** (100 MHz, CDCl₃, 298 K): δ (ppm) = 159.5 (3), 159.3 (7), 156.9 (16), 156.5 (10), 156.2 (14), 148.2 (24), 144.0 (21), 140.0 (19), 137.5 (12), 132.2 (18), 130.6 (22), 130.0 (5), 124.0 (23), 120.1 (13), 120.0 (11), 113.2 (17), 107.6 (4), 107.3 (6), 102.0 (8), 70.5 (9), 70.4 (15), 66.8 (2), 63.0 (20), 50.0 (1), 34.2 (25), 31.3 (26); **MS (+ESI)**:

(m/z): Calcd for $C_{52}H_{58}N_4O_3$; 787.04; found: 788 $[M+H]^+$; **IR** (KBr, cm^{-1}) = 3113, 3020, 2935, 2864, 2102(azide), 1597, 1352, 1201; **Anal. Calcd. for** $C_{52}H_{58}N_4O_3$: C, 79.35; H, 7.43; N, 7.12, found: C, 79.21, H, 7.46; N, 7.13.

Synthesis of pseudorotaxane-(2):

Azide end-capped pyridine derivative **1** (0.416 g, 0.52 mmol, 1.0 equiv) was taken in to a 50 ml of a round bottomed flask containing a mixture of anhydrous $CHCl_3/CH_3CN$ (8/2, 20 ml) solvent. The solution was purged with argon for 5 min. The pre-formed macrocycle ligand complex **10-Pd** (0.349 g, 0.52 mmol, 1.0 equiv) was added to the above solution and stirred for 4 h at room temperature. After completion of pseudorotaxanation the solution was evaporated under reduced pressure. The crude residue was subjected to column chromatography (silica gel, DCM/MeOH: 9.9/0.1). A yellow solid **2** was recovered (0.65 g, 0.46 mmol, 87%). Chemical formula: $C_{83}H_{93}N_7O_7Pd$, molecular weight: 1407.09.; mp. 170-172 °C (decomp).

1H NMR (600 MHz, $CDCl_3$, 298 K): δ (ppm) = 8.03 (t, $J_t = 7.83$ Hz, 1H, 12), 7.81-7.79 (m, 3H, A, B, and C), 7.36 (d, $J_d = 7.68$ Hz, 1H, 13 or 11), 7.30 (d, $J_d = 7.8$ Hz, 1H, 13 or 11), 7.17 (d, $J_d = 8.52$ Hz, 7H, 23 and 5), 7.07 (d, $J_d = 8.82$ Hz, 2H, 18), 7.03 (d, $J_d = 8.5$ Hz, 6H, 22), 6.72 (d, $J_d = 8.8$ Hz, 2H, 17), 6.53-6.50 (m, 3H, 4, 6, and 8), 6.30 (d, $J_d = 8.2$ Hz, 4H, G or H), 6.22 (d, $J_d = 8.5$ Hz, 4H, G or H), 5.22 (s, 2H, 9 or 15), 5.02 (s, 2H, 9 or 15), 4.27 (d, $J_d = 14.42$ Hz, 2H, E), 4.07 (t, $J_t = 4.8$ Hz, 2H, 2), 3.95 (d, $J_d = 14.43$ Hz, 2H, E), 3.67- 3.64 (m, 4H, J), 3.52 (t, $J_t = 4.5$ Hz, 2H, 1), 1.51- 1.49 (m, 4H, K), 1.28- 1.18 (m, 39H, 26+N+L+M); **^{13}C NMR** (150 MHz, $CDCl_3$, 298 K): δ (ppm) 171.3 (D), 159.3 (3), 159.2 (7), 158.5 (10), 158.0 (14), 157.5 (I), 154.9 (16), 152.5 (C), 148.2 (A), 143.8 (24), 141.1 (21), 140.7 (19), 139.0 (12), 132.3 (18), 132.1 (F), 130.5 (22), 130.1 (5), 127.9 (G), 124.9 (B), 124.0 (23), 121.7 (11), 121.6 (13), 114.5 (H), 114.1 (17), 108.3 (4), 107.7 (6), 103.1 (8), 69.9 (9), 69.4 (15), 67.0 (J), 67.0 (2), 63.0 (20), 50.1 (1),

49.8 (E), 34.1 (25), 31.2 (26), 29.1 (K), 28.3 (L+M), 25.3 (N); **MS (+LR-FAB)**: (m/z): Calcd for $C_{83}H_{93}N_7O_7Pd$; 1407.09; found: 1407.0 [M]⁺, 787.0 [M-macrocycle]⁺, 620.10 [macrocycle-Pd(CH₃CN)]⁺; **IR** (KBr, Cm⁻¹) = 3642, 3430, 3209, 3058, 2955, 2871, 2108(azide), 1617, 1362, 1172, **Anal. Calcd. for** $C_{83}H_{93}N_7O_7Pd$: C, 70.85, H, 6.66; N, 6.97, found: C, 70.68; H, 6.69; N, 7.01.

Synthesis of 2-(2-ethylhexyl)-3,6-di(thiophen-2-yl)pyrrolo[3,4-c]pyrrole-1,4(2H,5H)-dione (12):

To a 100 ml round bottomed flask containing anhydrous DMF (50 ml) was added 3,6-di(thiophen-2-yl)pyrrolo[3,4-c]pyrrole-1,4(2H,5H)-dione **11** (1.00 g, 3.32mmol, 1.0 equiv) the resulting suspension was purged with argon for 20 min at which time *t*-BuOK (0.97 g, 8.65 mmol, 2.6 equiv) was added and the suspension stirred for 20 min (an immediate color change from red to violet was observed). To above violet suspension was added 2-ethylhexylbromide (0.96 g, 0.89 ml, 4.96 mmol, 1.5 equiv) and the resulting solution stirred at room temperature for 3 h under argon atmosphere. The solution was poured into a beaker containing H₂O (100 ml) and stirred for 1h. The solution was filtrated off, the residual solid washed with DCM/hexane (6/4, 2 x 200ml) to remove any di-alkylated product. The red solid was dried under vacuum at 60 °C for 5 h and directly used without further purification in the next reaction. Chemical formula: $C_{22}H_{24}N_2O_2S_2$, Molecular weight: 412.57.

Synthesis of 2-(2-ethylhexyl)-5-(prop-2-yn-1-yl)-3,6-di(thiophen-2-yl)pyrrolo[3,4-c]pyrrole-1,4(2H,5H)-dione-(13):

To a 100 ml round bottomed flask containing anhydrous DMF (50 ml) was added mono alkylated crude product **12** (1.00 g, 2.42 mmol, 1.0 equiv) the resulting suspension was purged with argon for 20 min at which time *t*-BuOK (0.70 g, 6.30 mmol, 2.6 equiv) was added and the

suspension stirred for 20 min (an immediate color change from red to violet was observed). To above violet suspension was added propargyl bromide 80% solution in toluene (0.57 g, 0.72 ml, 4.84 mmol, 2.0 equiv) and the resulting suspension stirred at room temperature for 3 h under argon atmosphere. The solution was poured into a beaker containing H₂O (100 ml) and stirred for 1 h. The solution was filtrated off, the residual solid was subjected to column chromatography (silica gel, Hexane/EtOAc: 9.8/0.2). A red solid **13** was recovered (0.82 g, 1.82 mmol, 54% over all two steps yield). Chemical formula: C₂₅H₂₆N₂O₂S₂, Molecular weight: 450.62.; mp. 102.5-104.0 °C.

¹H NMR (300 MHz, CDCl₃, 298 K): δ (ppm) = 8.86 (dd, *J* = 1.01 Hz, *J* = 3.91 Hz, 1H, 1 or 1'), 8.70 (dd, *J* = 1.01 Hz, *J* = 3.87 Hz, 1H, 1 or 1'), 7.65-7.62 (m, 2H, 2 or 2'), 7.25-7.23 (m, 2H, 3 or 3'), 4.81 (d, *J*_d = 2.27 Hz, 2H, 4), 4.01-3.98 (m, 2H, 6), 2.28 (t, *J*_t = 2.1 Hz, 1H, 5), 1.82-1.79 (m, 1H, 7), 1.33-1.20 (m, 8H, 8,10,11, and 12), 0.86- 0.81 (m, 6H, 9 and 13); **¹³C NMR** (100 MHz, CDCl₃, 298 K): δ (ppm) = 161.4, 160.0, 141.0, 138.1, 135.3, 133.8, 130.8, 130.7, 129.3, 129.2, 128.2, 128.1, 107.9, 106.7, 78.1, 72.4, 45.5, 38.7, 31.3, 29.8, 27.9, 23.1, 22.7, 13.6, 10.1; **MS (+ESI)**: (m/z): Calcd for C₂₅H₂₆N₂O₂S₂; 450.62; found: 450.20 [M]⁺, 451.19 [M+H]⁺, 452.17 [M+2]⁺, **IR** (KBr, cm⁻¹) = 3329, 3054, , 2893, 2851, 2139, 1642, 1545, 1398, 1308, 1265; **Anal. Calcd. for** C₂₅H₂₆N₂O₂S₂: C, 66.63; H, 5.82; N, 6.22, found: C, 66.35; H, 5.85; N, 6.24.

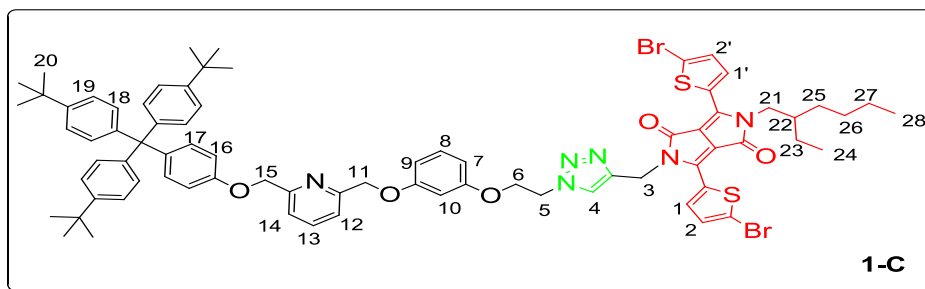
Synthesis of 3,6-bis(5-bromothiophen-2-yl)-2-(2-ethylhexyl)-5-(prop-2-yn-1-yl)pyrrolo[3,4-c]pyrrole-1,4(2H,5H)-dione-(3):

Asymmetric di alkylated diketopyrrolopyrrole derivative **13** (0.70 g, 1.55 mmol, 1.0 equiv) was added into a 100 ml round bottomed flask containing anhydrous CHCl₃ (56 ml) protected with aluminium foil. To above solution was added N-bromosuccinimide (0.58 g, 3.26 moll, 2.1 equiv) in a portion wised over a period of 30 min at room temperature and the reaction stirred under

argon atmosphere for 48 h at which time the solution was diluted with H₂O (100 ml). The layers were separated and the organic phase was washed with H₂O (2 x 50 ml) followed by brine solution (2 x 50 ml). The solution was dried over MgSO₄ after filtration the solution evaporated under reduced pressure the crude residue was subjected to column chromatography (silica gel, Hexane/EtOAc: 9.9/0.1). A maroon solid **3** was recovered (0.72 g, 1.18 mmol, 76%). Chemical formula: C₂₅H₂₄Br₂N₂O₂S₂, Molecular weight: 608.41.; mp. 178.2-180.1 °C.

¹H NMR (300 MHz, CDCl₃, 298 K): δ (ppm) = 8.65 (dd, *J* = 1.1 Hz, *J* = 4.1 Hz, 1H, 1 or 1'), 8.44 (dd, *J* = 1.1 Hz, *J* = 4.1 Hz, 1H, 1 or 1'), 7.24-7.22 (m, 2H, 2 and 2'), 4.75 (d, *J*_d = 2.4 Hz, 2H, 3), 3.93- 3.89 (m, 2H, 2H, 5), 2.35 (t, *J*_t = 2.1 Hz, 1H, 4), 1.81- 1.79 (m, 1H, 6), 1.34- 1.25 9 (m, 8H, 7, 9,10, and 11), 0.90- 0.85 9 (m, 6H, 8 and 12): ¹³C NMR (100 MHz, CDCl₃, 298 K): δ (ppm) = 161.3, 159.9, 140.1, 137.2, 135.7, 134.1, 131.5, 131.4, 131.1, 130.8, 119.7, 119.6, 108.2, 106.9, 78.0, 73.2, 45.9, 39.0, 31.5, 30.1, 28.2, 23.4, 22.9, 13.9, 10.4; **MS (+LR-FAB)**: (m/z): Calcd for C₂₅H₂₄Br₂N₂O₂S₂; 608.41; found: 608.0 [M]⁺, 610.0 [M+2]⁺; **IR (KBr, cm⁻¹)** = 3307, 3087, 2978, 2905, 2859, 2142, 1661, 1554, 1402, 1311, 1252, 1117; **Anal. Calcd. for C₂₅H₂₄Br₂N₂O₂S₂**: C, 49.35; H, 3.98; N, 4.60, found: C, 49.49; H, 4.00; N, 4.58.

Synthesis of 3,6-bis(5-bromothiophen-2-yl)-2-(2-ethylhexyl)-5-((1-(2-(3-((6-((4-(tris(4-(tert-butyl)phenyl)methyl)phenoxy)methyl)pyridin-2-yl)methoxy)phenoxy)ethyl)-1H-1,2,3-triazol-4-yl)methyl)pyrrolo[3,4-c]pyrrole-1,4(2H,5H)-dione-(1-C):

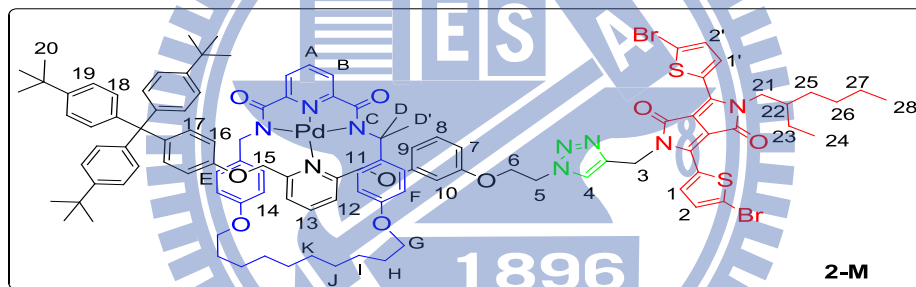


To a 50 ml of round bottomed flask was added a mixture of azide ended thread **1** (0.15 g, 0.19 mmol, 1.0 equiv) and alkyne ended asymmetric diketopyrrolopyrrole derivative **3** (0.12 g, 0.20 mmol, 1.05 equiv) containing a mixture of solvent THF/H₂O (12/3, ml) and then flask was evacuated by freeze-pump-thaw cycle. To the suspension was added a separately degassed CuSO₄ · 5H₂O (0.047 g, 0.19 mmol, 1.0 equiv) in H₂O (5 ml). An immediate color change was observed from maroon solution to violet at which time a separately degassed sodium ascorbate (0.075 g, 0.38 mmol, 2.0 equiv) solution in H₂O (4 ml) was added at room temperature slowly and further degassed by freeze-pump-thaw and stirred for 6 h room temperature. THF was evaporated under reduced pressure to the resulted aqueous solution was added DCM (200 ml) and 17% aqueous ammonia solution (200 ml) and stirred at room temperature for 30 min to remove the excess Cu as [Cu(NH₃)₃]⁺ salts. The DCM layer was separated and washed with H₂O (2 x 100 ml) followed by brine solution (2 x 100 ml) and dried over MgSO₄. After filtration the organic solution was evaporated under reduced pressure and the crude residue was subjected to column chromatography (silica gel, Hexane/EtOAc: 9/1 to 8/2). A red crystalline powder **1-C** was recovered (0.201 g, 0.14 mmol, 76%). Chemical formula: C₇₇H₈₂Br₂N₆O₅S₂, Molecular weight: 1395.45.; mp. 110-113 °C.

¹H NMR (600 MHz, CDCl₃, 298 K): δ (ppm) = 8.53 (dd, *J* = 1.01 Hz, *J* = 4.13 Hz, 1H, 1 or 1'), 8.37 (dd, *J* = 1.01 Hz, *J* = 1.01 Hz, *J* = 4.13 Hz, 1H, 1 or 1'), 7.71 (s, 1H, triazole CH, 4), 7.66 (t, *J*_t = 7.76 Hz, 1H, 13), 7.40 (t, *J*_t = 7.73 Hz, 1H, 12 or 14), 7.33 (t, *J*_t = 7.67 Hz, 1H, 12 or 14), 7.15 (m, 7H, 19 + DPP 2 or 2'), 7.08 (dd, *J* = 1.01 Hz, *J* = 4.13 Hz, 1H, DPP 2 or 2'), 7.04-6.99 (m, 9H, 18, 8, and 17), 6.78 (d, *J*_d = 8.81 Hz, 2H, 16), 6.48 (dd, *J* = 1.82 Hz, *J* = 8.2 Hz, 1H, 9), 6.42-6.41 (m, 1H, 10), 6.33 (dd, *J* = 1.82 Hz, *J* = 8.2 Hz, 7), 5.17 (s, 2H, 15 or 11), 5.10 (s, 2H, 15 or 11), 5.05 (s, 2H, 3), 4.61 (t, *J*_t = 4.98 Hz, 2H, 6), 4.22 (t, *J*_t = 5.34 Hz, 2H, 5), 3.84-3.81 (m,

2H, 21), 1.74-1.72 (m, 1H, 22), 1.22-1.18 (m, 35H, 20, 23, 25, 26, 27), 0.80-0.77 (m, 6H, 24 and 28); ^{13}C NMR (150 MHz, CDCl_3 , 298 K): δ (ppm) = 161.4, 161.0 159.5, 158.9, 156.9, 156.4, 156.1, 148.2, 144.0, 143.8, 140.0, 140.0, 138.0, 137.6, 135.4, 134.2, 132.3, 131.6, 131.4, 131.0, 130.9, 130.6, 130.1, 124.2, 124.0, 120.1, 120.0, 119.7, 119.4, 113.2, 108.1, 107.6, 107.4, 107.3, 101.9, 70.4, 70.3, 66.1, 63.0, 49.7, 45.9, 39.0, 38.0 34.2, 31.3, 30.0, 29.6, 28.2, 22.9, 14.0, 10.4, **MS (MALDI-TOF): matrix (CHC):** (m/z): Calcd for $\text{C}_{77}\text{H}_{82}\text{Br}_2\text{N}_6\text{O}_5\text{S}_2$; 1395.45; found: 1395.24 $[\text{M}]^+$, 1414.21 $[\text{M}+\text{Na}]^+$, 1433.21 $[\text{M}+\text{K}]^+$; **IR** (KBr, cm^{-1}) = 3133, 3041, 3030, 2959, 2887, 1664, 1551, 1459, 1255, 1459, 1255, 1091; **Anal. Calcd. for $\text{C}_{77}\text{H}_{82}\text{Br}_2\text{N}_6\text{O}_5\text{S}_2$:** C, 66.27; H, 5.92; N, 6.02, found; C, 66.09; H, 5.95; N, 5.99.

Synthesis metalated rotaxane-(2-M):



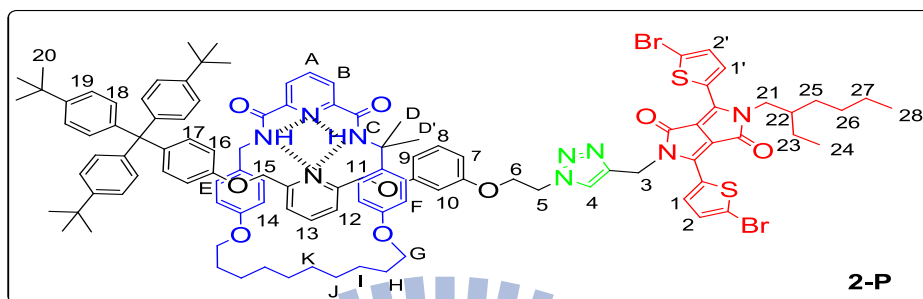
To a 100 ml of round bottomed flask was added a mixture of azide ended pseudorotaxane ended thread **2** (0.40 g, 0.28 mmol, 1.0 equiv) and alkyne ended asymmetric diketopyrrolopyrrole derivative **3** (0.181 g, 0.29 mmol, 1.05 equiv) containing a mixture of solvent THF/ H_2O (18/4.5, ml) and then flask was evacuated by freeze-pump-thaw cycle. To the suspension was added a separately degassed $\text{CuSO}_4 \cdot 5\text{H}_2\text{O}$ (0.0701 g, 0.28 mmol, 1.0 equiv) in H_2O (7.5 ml). An immediate color change was observed from maroon solution to violet at which time a separately degassed sodium ascorbate (0.112 g, 0.56 mmol, 2.0 equiv) solution in H_2O (6 ml) was added at room temperature slowly and further degassed by freeze-pump-thaw and stirred for 6 h room temperature. THF was evaporated under reduced pressure, to the resulted aqueous solution was

added DCM (250 ml) and 17% aqueous ammonia solution (250 ml) and stirred at room temperature for 30 min to remove the excess Cu as $[\text{Cu}(\text{NH}_3)_3]^+$ salts. The DCM layer was separated and washed with H_2O (2 x 150 ml) followed by brine solution (2 x 150 ml) and dried over MgSO_4 . After filtration organic solution was evaporated under reduced pressure and the crude residue was subjected to column chromatography (silica gel, DCM/MeOH: 9.9/0.1 to 9.8/0.2). A red crystalline powder **2-M** was recovered (0.422 g, 0.209 mmol, 73%). Chemical formula: $\text{C}_{108}\text{H}_{117}\text{Br}_2\text{N}_9\text{O}_9\text{PdS}_2$, Molecular weight: 2015.5.; mp. 152-155 °C.

^1H NMR (600 MHz, CDCl_3 , 298 K): δ (ppm) = 8.51 (dd, $J = 1.01$ Hz, $J = 4.19$ Hz, 1H, 1 or 1'), 8.39 (dd, $J = 1.01$ Hz, $J = 4.13$ Hz, 1H, 1 or 1'), 8.04 (t, $J_t = 7.88$ Hz, 1H, A), 7.81-7.78 (m, 3H, 13 and B), 7.75 (s, 1H, triazole CH, 4), 7.38 (d, $J_d = 7.73$ Hz, 1H, 12 or 14), 7.29 (d, $J_d = 7.79$ Hz, 1H, 12 or 14), 7.17 (d, $J_d = 9.6$ Hz, 6H, 19), 7.14 (dd, $J = 1.01$ Hz, $J = 4.19$ Hz, 1H, 2 or 2'), 7.10 (m, 2H, 8 and DPP 2 or 2'), 7.06 (d, $J_d = 8.75$ Hz, 2H, 17), 7.03 (d, $J_d = 8.51$ Hz, 6H, 18), 6.70 (d, $J_d = 8.81$ Hz, 2H, 16), 6.54-6.53 (m, 1H, 9), 6.44-6.43 (m, 2H, 7, and 10), 6.28 (d, $J_d = 8.22$ Hz, 4H, E or F), 6.21 (d, $J_d = 8.46$ Hz, 4H, E or F), 5.24 (s, 2H, 15 or 11), 5.18 (s, 2H, 15 or 11), 4.96 (s, 2H, 3), 4.66 (t, $J_t = 5.15$ Hz, 2H, 6), 4.34 (d, $J_d = 14.39$ Hz, 2H, D), 4.30 (t, $J_t = 5.21$ Hz, 2H, 21), 3.85 (d, $J_d = 12.47$ Hz, 2H, D'), 3.82-3.80 (m, 2H, 21), 3.64-3.63 (m, 4H, G), 1.74-1.73 (m, 1H, 22), 1.65-1.62 (m, 4H, H), 1.48-1.46 (m, 4H, I), 1.25-1.18 (m, 43H, 20, J, K, 10, 25, 26, and 27), 0.81-0.78 (m, 6H, 24 and 28); **^{13}C NMR** (150 MHz, CDCl_3 , 298 K): δ (ppm) = 171.3, 161.4, 161.0, 159.6, 159.0, 158.6, 157.9, 157.5, 154.9, 152.6, 148.3, 143.9, 143.8, 141.2, 140.8, 140.0, 139.0, 138.0, 135.4, 134.2, 132.4, 132.2, 131.6, 131.4, 131.1, 130.9, 130.6, 130.3, 128.0, 125.0, 124.2, 124.0, 121.9, 121.7, 119.7, 119.4, 114.6, 114.2, 108.4, 108.2, 108.2, 107.3, 103.3, 70.2, 69.4, 67.0, 66.3, 63.1, 49.8, 49.7, 45.9, 39.0, 38.0, 34.2, 31.3, 30.1, 29.6, 29.2, 28.4, 28.2, 25.4, 23.4, 23.0, 14.0, 10.4; **MS (MALDI-TOF): matrix (CHC):** (m/z): Calcd for

$C_{108}H_{117}Br_2N_9O_9PdS_2$; 2015.5; found: 2015.341 $[M]^+$, 2037.331 $[M+Na]^+$, 2053.331 $[M+K]^+$; **IR** (KBr, cm^{-1}) = 3079, 3052, 2978, 2917, 2863, 17171, 1676, 1602, 1492, 1398, 1262; **Anal.** **Calcd. for** $C_{108}H_{117}Br_2N_9O_9PdS_2$: C, 64.36; H, 5.85; N, 6.25, found: C, 64.22; H, 5.88; N, 6.22.

Synthesis of diketopyrrolopyrrole stoppered [2]rotaxane-(2-P):



To Pd-templated [2]rotaxane **2-M** (0.350 g, 0.173 mmol, 1.0 equiv) in anhydrous $CHCl_3$ (15 ml) and anhydrous MeOH (15 ml) was added KCN (0.180 g, 2.778 mmol, 16.0 equiv) in MeOH (5 ml). The solution was stirred for 2 h at room temperature and then heated gently to reduce the overall volume to less than 10 ml. The resulting mixture was portioned between DCM (60 ml) and H_2O (60 ml). The organic phase was collected and aqueous phase further extracted with DCM (2 x 100 ml). The organic extracts were combined and washed with H_2O (100 ml) followed by brine solution (100 ml) and then dried over $MgSO_4$. After filtration the organic layer was evaporated under reduced pressure and the crude residue was subjected to flash column chromatography (Silica gel DCM/MeOH: 9.9/0.1). A red solid **2-P** was recovered (0.215 g, 0.112 mmol, 64%). Chemical formula: $C_{108}H_{119}Br_2N_9O_9S_2$, Molecular weight: 1911.09.; mp. 101.0-104.0 °C.

1H NMR (600 MHz, $CDCl_3$, 298 K): δ (ppm) = 9.22 (t, $J_t = 12.17$ Hz, 2H, macrocycle NH, C), 8.50 (dd, $J = 1.01$ Hz, $J = 4.13$ Hz, 1H, 1 or 1'), 8.43 (dd, $J = 1.01$ Hz, $J = 4.13$ Hz, 1H, 1 or 1'), 8.31 (d, $J_d = 7.85$ Hz, 2H, B), 7.91 (t, $J_t = 7.82$ Hz, 1H, A), 7.54-7.53 (m, 2H, triazole CH, 4 and 13), 7.18-7.16 (m, 7H, 19 and DPP 2 or 2'), 7.10 (m, 2H, 12 and 14), 7.07 (dd, $J = 1.1$ Hz, $J =$

4.19 Hz, 1H, DPP 2 or 2'), 7.02 (d, $J_d = 8.51$ Hz, 6H, 18), 6.94 (d, $J_d = 8.87$ Hz, 2H, 17), 6.91 (t, $J_t = 8.33$ Hz, 1H, 8), 6.52 (d, $J_d = 8.45$ Hz, 4H, E or F), 6.39 (d, $J_d = 8.87$ Hz, 2H, 16), 6.24-6.22 (m, 2H, 7, and 9), 6.18 (d, $J_d = 8.57$ Hz, 4H, E or F), 6.12 (m, 1H, 10), 5.08 (s, 2H, 15 or 11), 4.62 (s, 2H, 15 or 11), 4.54 (dd, $J = 7.6$ Hz, $J = 7.0$ Hz, 2H, D or D'), 4.38 (t, $J_t = 5.21$ Hz, 2H, 6), 4.26 (s, 2H, 3), 3.94 (t, $J_t = 5.27$ Hz, 2H, 5), 3.87-3.79 (m, 4H, D or D', and 21), 3.63-3.62 (m, 4H, G), 1.73-1.71 (m, 1H, 22), 1.58-1.56 (m, 4H, H), 1.35-1.33 (m, 4H, I), 1.22-1.18 (m, 43H, 20, J, K, 23, 25, 26, and 27), 0.80-0.77 (m, 6H, 24 and 28); $^{13}\text{C NMR}$ (150 MHz, CDCl_3 , 298 K): δ (ppm) = 163.6, 161.4, 161.1, 159.1, 158.7, 157.7, 156.3, 155.9, 155.6, 149.0, 148.2, 144.0, 143.5, 140.1, 138.7, 138.0, 137.2, 135.3, 134.2, 132.0, 131.6, 131.3, 131.0, 130.9, 130.6, 130.5, 130.0, 129.5, 128.6, 125.3, 124.2, 124.1, 120.2, 120.1, 119.8, 119.6, 113.8, 112.9, 108.1, 107.4, 107.3, 106.9, 101.6, 69.4, 68.7, 66.7, 65.7, 63.0, 49.4, 45.9, 42.5, 39.0, 37.9, 34.2, 31.3, 30.1, 29.2, 28.3, 28.3, 28.2, 25.4, 23.4, 22.9, 14.0, 10.4; **MS (MALDI-TOF): matrix (CHC):** (m/z): Calcd for $\text{C}_{108}\text{H}_{119}\text{Br}_2\text{N}_9\text{O}_9\text{S}_2$: 1911.09; found: 1911.399 $[\text{M-Pd}]^+$, 1932.390 $[\text{M-Pd+Na}]^+$, 1948.382 $[\text{M-Pd+K}]^+$; **IR** (KBr, cm^{-1}) = 3466, 3355, 3078, 3015, 2959, 2841, 1678, 1575, 1496, 1393, 1251, 1101; **Anal. Calcd. for** $\text{C}_{108}\text{H}_{119}\text{Br}_2\text{N}_9\text{O}_9\text{S}_2$: C, 67.88; H, 6.28; N, 6.60, found: C, 67.75; H, 6.30; N, 6.58.

Rotaxane 2-R Characterization data:

$^1\text{H NMR}$ (400 MHz, d_6 -DMSO, 298 K): δ (ppm) = 9.57 (t, 2H, macrocycle proton NH, C), 8.47-8.43 (m, 2H, 1 and 1'), 8.16 (d, 2H, B), 7.98-7.93 (m, 2H, A + triazole 4), 7.68(t, 1H, 13), 7.48 (d, 1H, 12 or 14), 7.46 (d, 1H, 12 or 14), 7.26-7.21 (m, 7H, 19 and 2 or 2'), 7.14 (m, 1H, 2 or 2'), 6.98-6.94 (m, 7H, 18 and 8), 6.75-6.72 (m, 6H, 17 and E or F), 6.49(d, 2H, 16), 6.39 (d, 1H, 10), 6.25-6.23 (m, 2H, 7 and 9), 6.14 (d, 4H, e or F), 5.13 (s, 2H, 15 or 11), 4.82 (s, 2H, 15 or 11), 4.67 (dd, 2H, D or D'), 4.39 (t, 2H, 6), 4.27 (s, 2H, 3), 4.06 (t, 2H, 5), 4.01-3.97 (dd, 2H, D or

D'), 3.88-3.79 (m, 2H, 21), 3.57-3.54 (m, 4H, G), 1.65-1.61 (m, 1H, 22), 1.47-1.45 (m, 4H, H), 1.22-1.10 (m, 47H, I, 20, J, K, 23, 25, 26, and 27), 0.78-0.76 (m, 6H, 24 and 28); ^{13}C NMR (100 MHz, d_6 -DMSO, 298 K): δ (ppm) = 162.7, 160.4, 160.0, 159.0, 158.7, 157.1, 156.2, 155.6, 155.4, 148.6, 147.4, 144.0, 142.4, 138.7, 138.6, 137.9, 137.1, 134.6, 134.2, 131.9, 131.8, 130.8, 130.7, 130.5, 130.1, 129.7, 128.2, 124.2, 123.9, 123.7, 120.3, 120.2, 119.2, 119.0, 114.5, 113.7, 113.3, 107.1, 107.0, 106.9, 101.5, 69.7, 69.2, 66.2, 65.6, 65.5, 62.4, 48.6, 44.9, 41.4, 38.3, 38.1, 33.9, 29.4, 28.8, 27.8, 27.5, 24.9, 24.4, 22.3, 13.7, 10.1; **MS (ESI +ve mode):** (m/z): Calcd for $\text{C}_{108}\text{H}_{119}\text{Br}_2\text{N}_9\text{O}_9\text{S}_2$; 1911.09; found: 1911.1 $[\text{M}]^+$, 1932.6 $[\text{M}+\text{Na}]^+$.

2. 3. Results and Discussion

Investigation of mechanical interlocking and solvent polarity/anion (TBAF) induced molecular shuttlings in DPP based [2]rotaxane by ^1H & ^{19}F NMR spectroscopy:

2. 3. 1. ^1H NMR titration studies:

The ^1H NMR spectra of [2]rotaxane **2-P**, control axle **1-C**, and macrocycle were compared in CDCl_3 (**Figure 2. 2**). Upfield shifts for axle pyridyl protons (12, 13, and 14) and macrocycle protons (E and F) along with 1.5 ppm downfield shift for macrocycle amide protons C indicated the existence of an overwhelming interlocked nature through an orthogonal bifurcated pyridine-pyridine H-bonding between axle and wheel. Moreover, in relative polar solvent d_6 -DMSO the observed upfield shifts for resorcinol protons (7 and 9) along with downfield shifts for pyridyl protons (12, 13, and 14) and macrocycle amide protons C suggested that the cycle was translocated to the resorcinol unit as the H-bonding basicity was increased (**Scheme 2. 1** and **Figure 2. 3**). Thus, [2]rotaxane presents two translational isomers under different solvent

polarities in which the macrocycle resides on the pyridine unit in CDCl_3 (translational isomer **2-P**) and on the resorcinol unit in DMSO (translational isomer **2-R**).^{68,69,70,106}

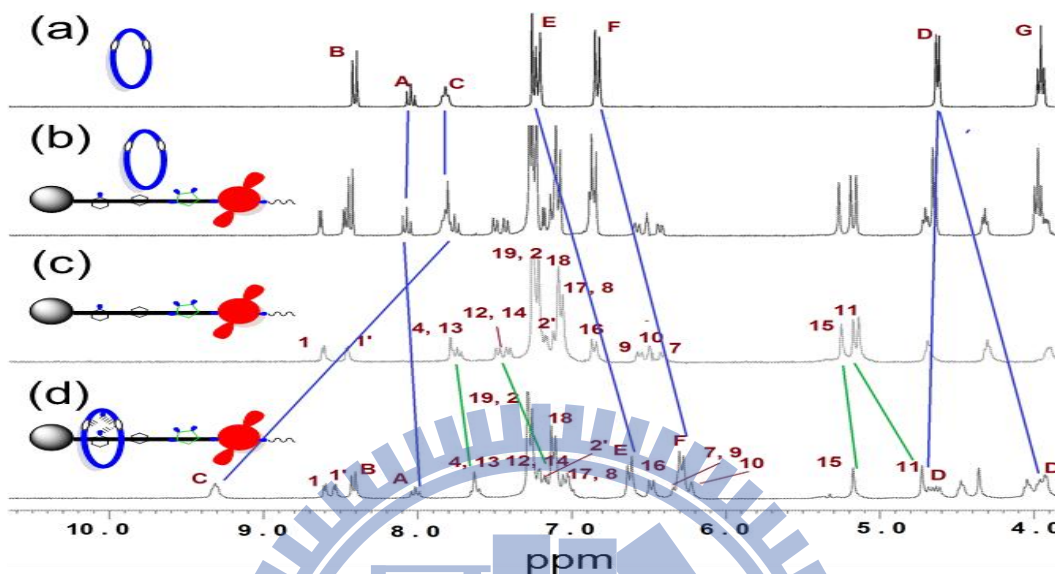


Figure 2. 2. ^1H NMR spectra (CDCl_3 , 300 MHz, 298 K): (a) macrocycle, (b) 1:1 mixture of control axle **1-C** and macrocycle, (c) **1-C**, (d) **[2]rotaxane 2-P**. The assignments correspond to the lettering shown in **Scheme 2. 2.** (numerical and alphabetical lettering indicating dumbbell part and macrocycle, respectively).

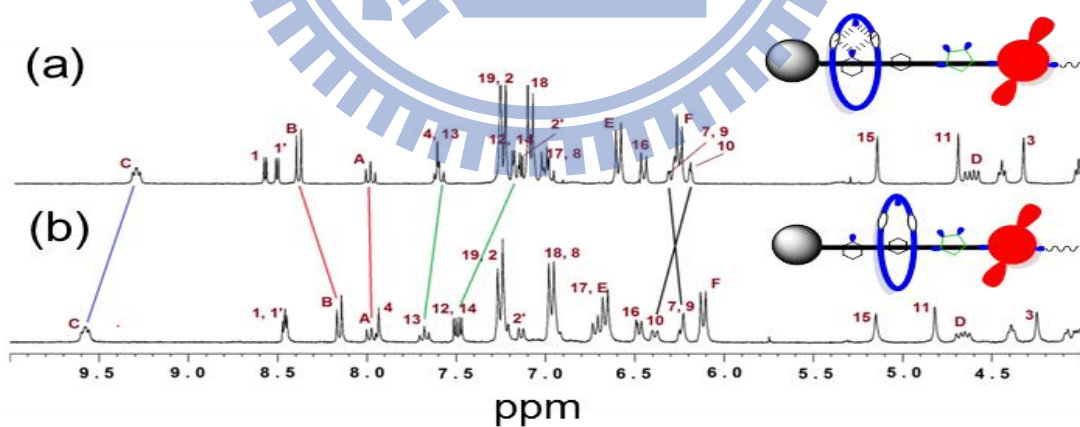


Figure 2. 3. ^1H NMR spectra (300 MHz, 298 K): (a) **[2]rotaxane translational isomer 2-P** in CDCl_3 , (b) **[2]rotaxane translational isomer 2-R** in $d_6\text{-DMSO}$. The assignments correspond to the lettering shown in **Scheme 2. 2.**

To probe the anion recognition affinities of [2]rotaxane, we employed ^1H NMR titrations of **2-P** in CDCl_3 over a range of anions, such as F^- , Cl^- , Br^- , I^- , AcO^- , NO_3^- , and H_2PO_4^- , with 3 equiv of respective tetrabutylammonium salts (**Figure 2. 4**).

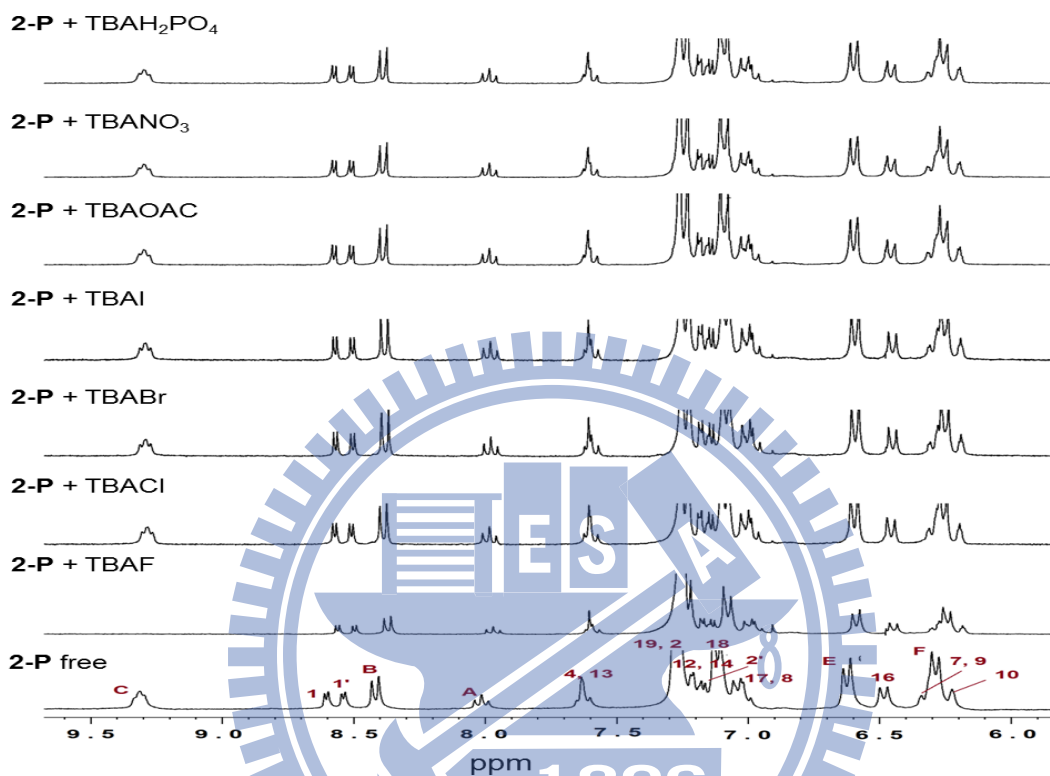


Figure 2. 4. ^1H NMR (CDCl_3 , 300 MHz) spectral changes of [2]rotaxane **2-P** (3 mM) with the addition of 3 equiv different anions (F^- , Cl^- , Br^- , I^- , AcO^- , NO_3^- , and H_2PO_4^-) as tetrabutylammonium salts. The assignments correspond to lettering shown in the main **Scheme 2. 2**.

Interestingly, no other anions showed any significant spectroscopic changes except F^- . Taking this vivid spectroscopic clue, further titrations were conducted with F^- . Upon the progressive addition of F^- , significant upfield shifts were observed for cavity and thread protons along with disappearance amide NH protons at 1 equiv of F^- . On further addition, no obvious changes were

observed as shown in **Figure 2. 5**. Importantly, the [2]rotaxane precursors, such as **1-C** and **2-M**, could not show observable changes with the addition of 3 equiv of F^- (**Figure 2. 6**).

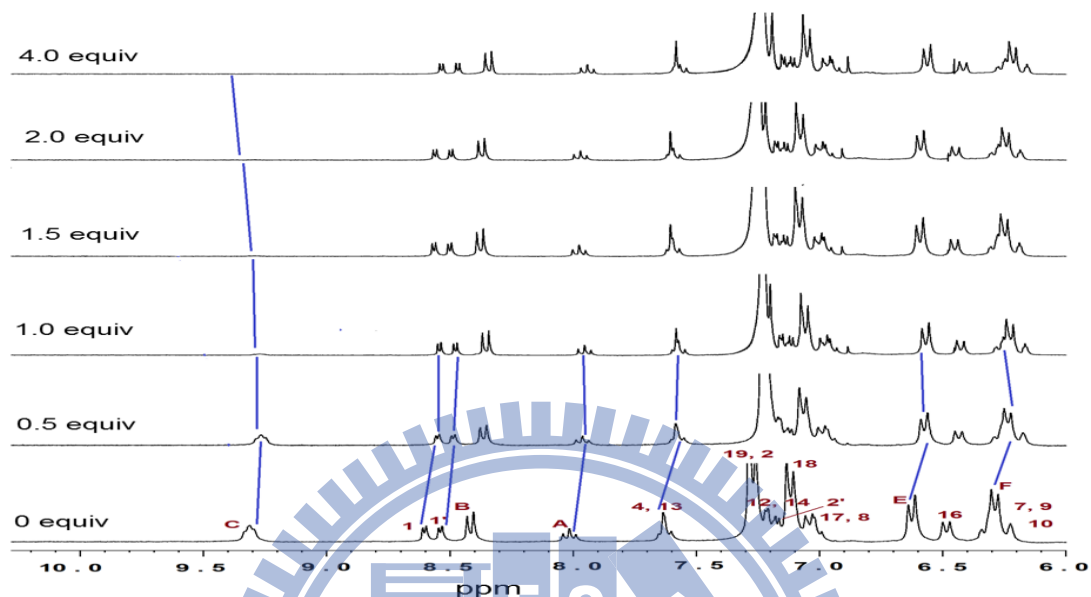


Figure 2. 5. Changes in the 1H NMR spectrum of [2]rotaxane **2-P** (3 mM) during titration with TBAF (0-4 equiv) ($CDCl_3$, 300 MHz, 298 K). The assignments correspond to lettering shown in the main **Scheme 2. 2**.

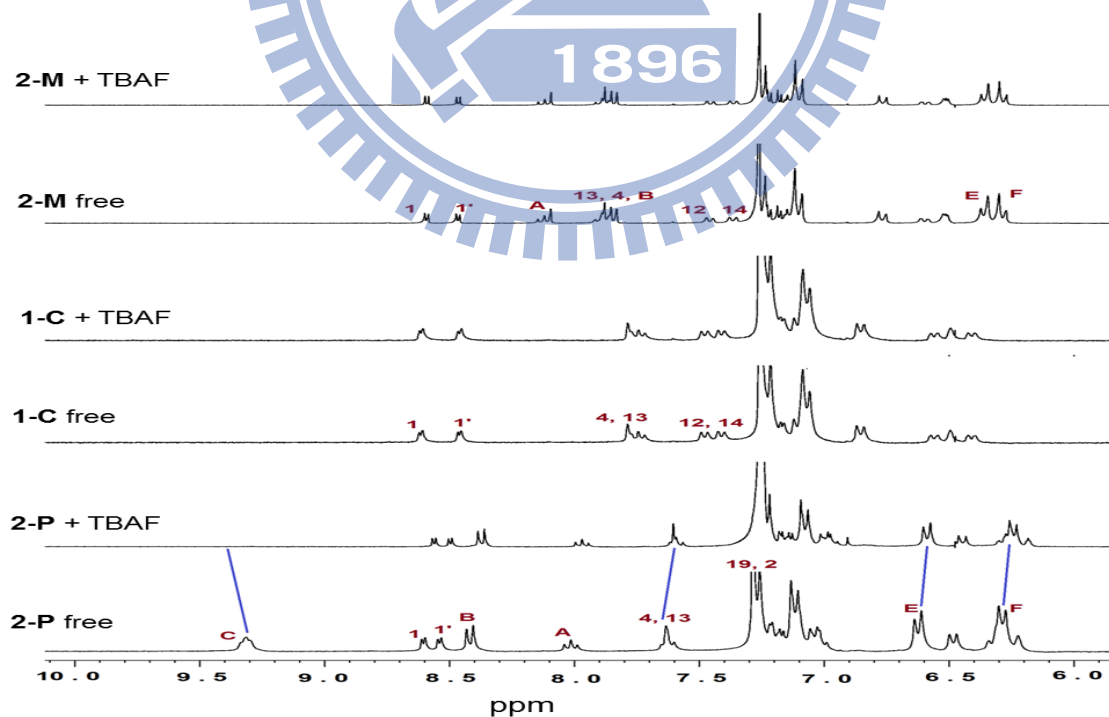


Figure 2. 6. Changes in the ^1H NMR spectrum of [2]rotaxane **2-P** (3 mM) , control axle **1-C** (3 mM), and metalated [2]rotaxane **2-M** (3 mM) with the addition of 3 equiv TBAF (CDCl_3 , 300 MHZ, 298 K). The assignments correspond to lettering shown in the main **Scheme 2. 2**.

Furthermore, ^1H and ^{19}F NMR titrations were conducted in polar solvent DMSO to appreciate the sensing ability of [2]rotaxane and to attain a better insight into the binding interaction of **2-R**/ F^- . The ^1H NMR spectrum of **2-R** showed significant changes upon the addition of F^- . As the addition of F^- reached 1 equiv, the cavity and thread protons, such as pyridine and the resorcinol unit, showed upfield shifts. On further addition the spectrum became broad as well as the amide NH proton C completely disappeared and formed a strong HF_2^- peak at 4 equiv of F^- (**Figure 2. 7**).

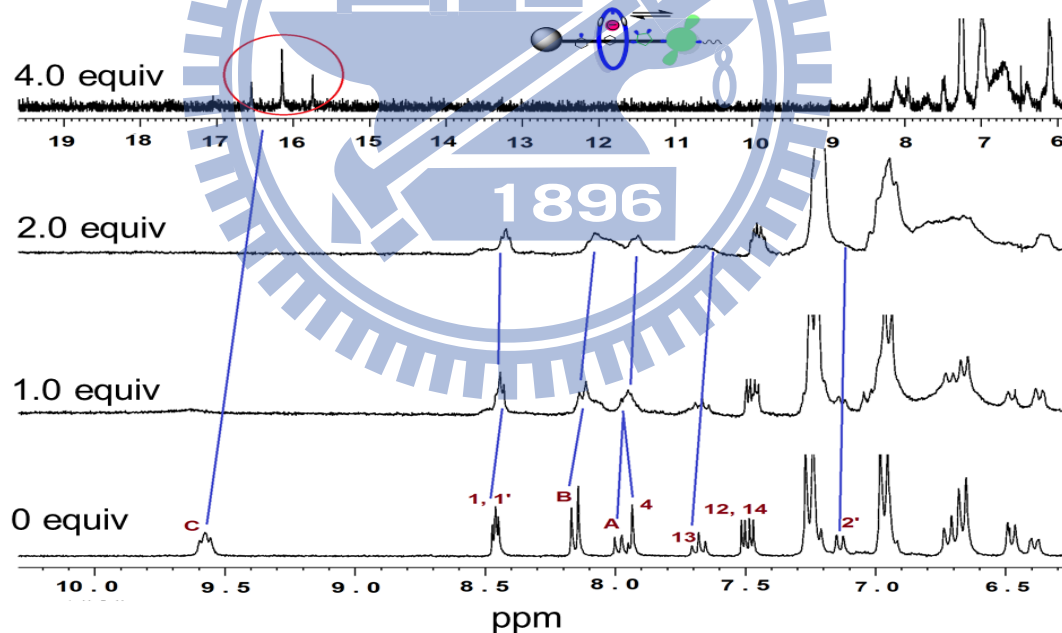


Figure 2. 7. Changes in ^1H NMR (300 MHz, d_6 -DMSO, 298 K) spectrum of [2]rotaxane **2-R** (3 mM) during titration with TBAF (0-4 equiv). Red circled region indicating the formation of HF_2^- ion. The assignments correspond to the lettering shown in **Scheme 2. 2**.

2. 3. 2. ^{19}F NMR titration studies:

Delightfully, the binding mode was clearly revealed by ^{19}F NMR titrations in DMSO, in which the sharp singlet corresponding to free TBAF at -102.5 ppm was upfielded to -103.8 ppm ($\Delta\delta = 1.3$ ppm) upon the addition of **2-R** solution (3 equiv) to TBAF. Moreover, the weak doublet corresponding to HF_2^- at -143.1 ppm was gradually raised in its intensity with a declined triplet intensity of DF_2^- at -143.5 ppm simultaneously as depicted in **Figure 2. 8**.^{97a} Importantly the binding process of **2-R**/ F^- was completely reversible upon the addition of CF_3COOH (TFA, 5 equiv) and provided a spectrum identical to the original rotaxane (**Figure 2. 9**). Thus, [2]rotaxane **2-R** selectively recognized F^- through a non-covalent interaction due to a positive cooperativity between 2,6-dicarboxyamidopyridine receptor (in macrocycle) and F^- , and further guest equiv would deprotonate the amide cleft and induce a macrocycle shuttling.

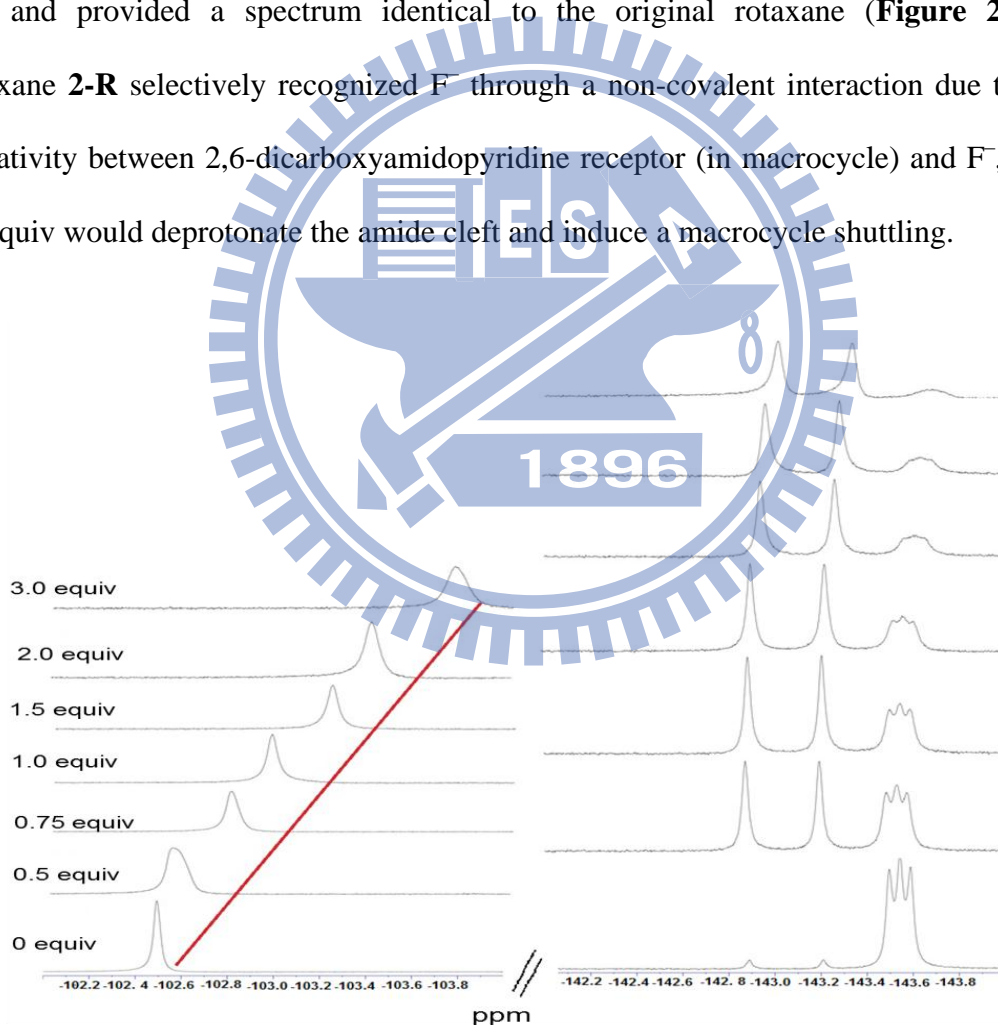


Figure 2. 8. Changes in ^{19}F NMR spectrum of TBAF (in Ar-Saturated d_6 -DMSO) upon gradual addition of [2]rotaxane **2-R** solution in Ar-Saturated d_6 -DMSO.

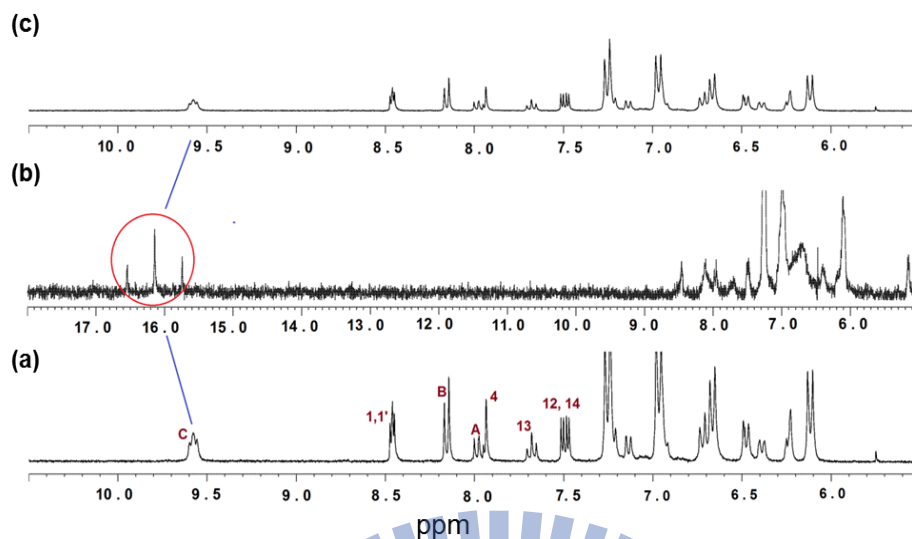


Figure 2. 9. ^1H NMR spectrum (d_6 -DMSO, 300 MHz, 298 K); (a) [2]rotaxane **2-R**; (b) deprotonation with the addition 4 equiv of TBAF to sample (a); (c) recovered the [2]rotaxane sample back with the addition of 5 equiv of TFA to sample (b). The assignments correspond to lettering shown in the main **Scheme 2. 2**.

2. 3. 3. UV-vis & Fluorescence titration studies:

Next, we focused on the photophysical properties of **1-C**, **2-M**, and **2-R** under the influence of chemical stimuli (solvent and anionic guests). To escalate future aqueous soluble functional MIMs, we further carried out all photophysical measurements in DMSO. Both absorption and fluorescence intensities of [2]rotaxane were sharply decreased in the relative polar solvent DMSO (**Figure 2. 10**), which lucidly indicated the translocation of wheel from pyridine to the resorcinol unit as the H-bond formed between pyridine and wheel was disrupted, which is consistent with our above ^1H NMR observations as well as previous reports.^{53,70}

UV-vis and fluorescence measurements were explored to probe the optical anion sensing abilities of **2-R**, and significant absorption changes in the absorption maxima of DPP (564 and 525 nm) and non fluorogenic axle part (274 nm) were observed. As depicted in **Figure 2. 11a**, upon the

gradual addition of TBAF (0-40 equiv), the original absorption maxima of DPP decreased with two emerging new peaks at 257 and 451 nm. Simultaneously, the emission maximum of **2-R** at 582 nm ($\lambda_{\text{ex}} = 525$ nm) was gradually quenched (**Figure 2. 11b**). Since the titration patterns of absorption and ^1H NMR were complex, we employed fluorescence titrations to determine the stoichiometry and binding constant. Unambiguously, the results established a 1:1 stoichiometry of the **2-R**/ F^- complex and yielded a binding constant of $2.65 \times 10^4 \text{ M}^{-1}$ (see **Figures 2. 12a** and **2. 12b**).^{107,108}

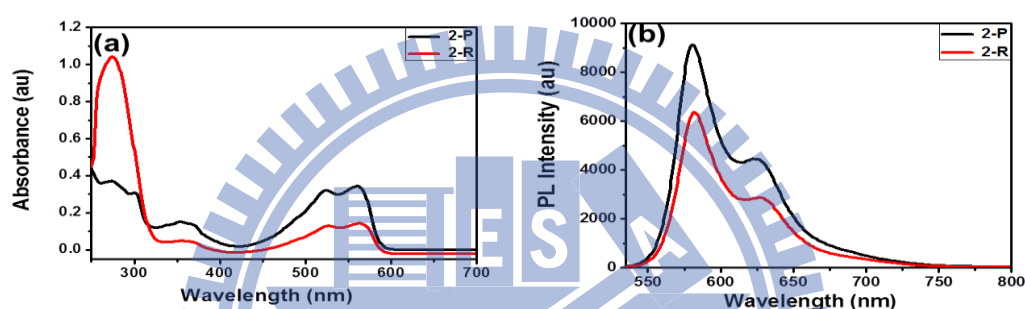


Figure 2. 10. Changes in photophysical properties of [2]rotaxane under solvent stimuli; (a) UV-vis absorption of translational isomer **2-P** ($1 \times 10^{-5} \text{ M}$ in DCM) and translational isomer **2-R** ($1 \times 10^{-5} \text{ M}$ in DMSO); (b) fluorescence of translational isomer **2-P** (in DCM) and translational isomer **2-R** (in DMSO). ($\lambda_{\text{ex}} = 525 \text{ nm}$).

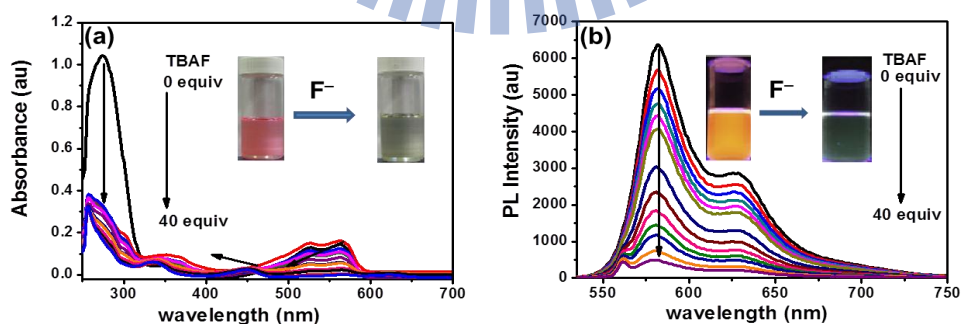


Figure 2. 11. (a), (b) UV-Vis and fluorescence spectral changes of **2-R** ($1 \times 10^{-5} \text{ M}$ in DMSO) upon the addition of TBAF in DMSO (0-40 equiv), respectively. Inset pictures in (a) and (b)

indicating naked eye color changes as well as fluorescence changes under UV light (365 nm) upon the addition of TBAF, respectively. ($\lambda_{\text{ex}} = 525 \text{ nm}$).

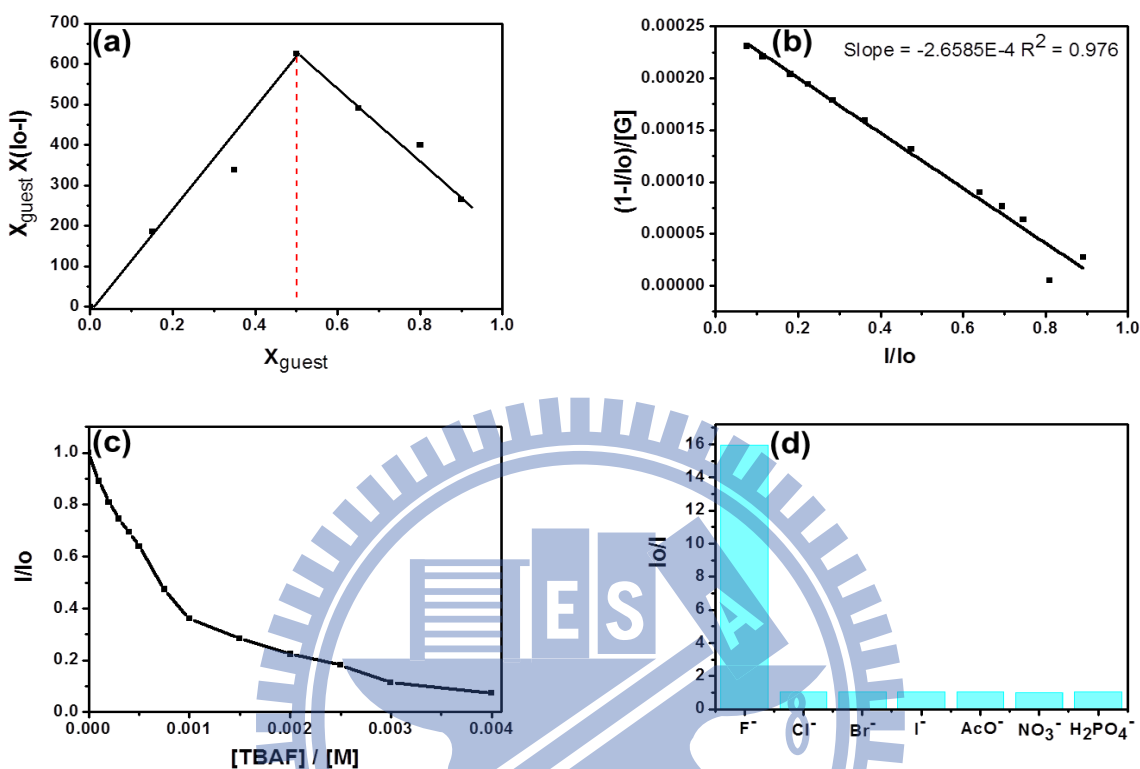


Figure 2. 12. (a) Fluorescence spectral responses of **2-R** were utilized in determining the stoichiometry for **2-R**/ F^- complex, change in the fluorescence intensity multiplied by guest mole fraction was plotted against guest mole fraction. Indicating 1:1 binding stoichiometry for the **2-R**/ F^- complex (total concentration $200 \mu\text{M}$); (b) calculation of binding constant for **2-R**/ F^- complex using Connors method; (c) Stern-Volmer plot of I/I_0 ($\lambda_{\text{em}} = 582 \text{ nm}$) vs $[F^-]$; (d) histograms representing the fluorescence spectral changes of [2]rotaxane **2-R** with the addition of 40 equiv of different anions.

Further selectivity of the [2]rotaxane host system was verified by titrations of anions, such as Cl^- , Br^- , I^- , AcO^- , NO_3^- , and $H_2PO_4^-$. Importantly, none of the above anions could show noticeable changes in either the absorption or emission spectra. Moreover, to strengthen the selectivity of

[2]rotaxane, we did control titrations on its precursors **1-C** and **2-M**. However, their responses were trivial under similar conditions (see **Figures 2.13a- 2.13f**).

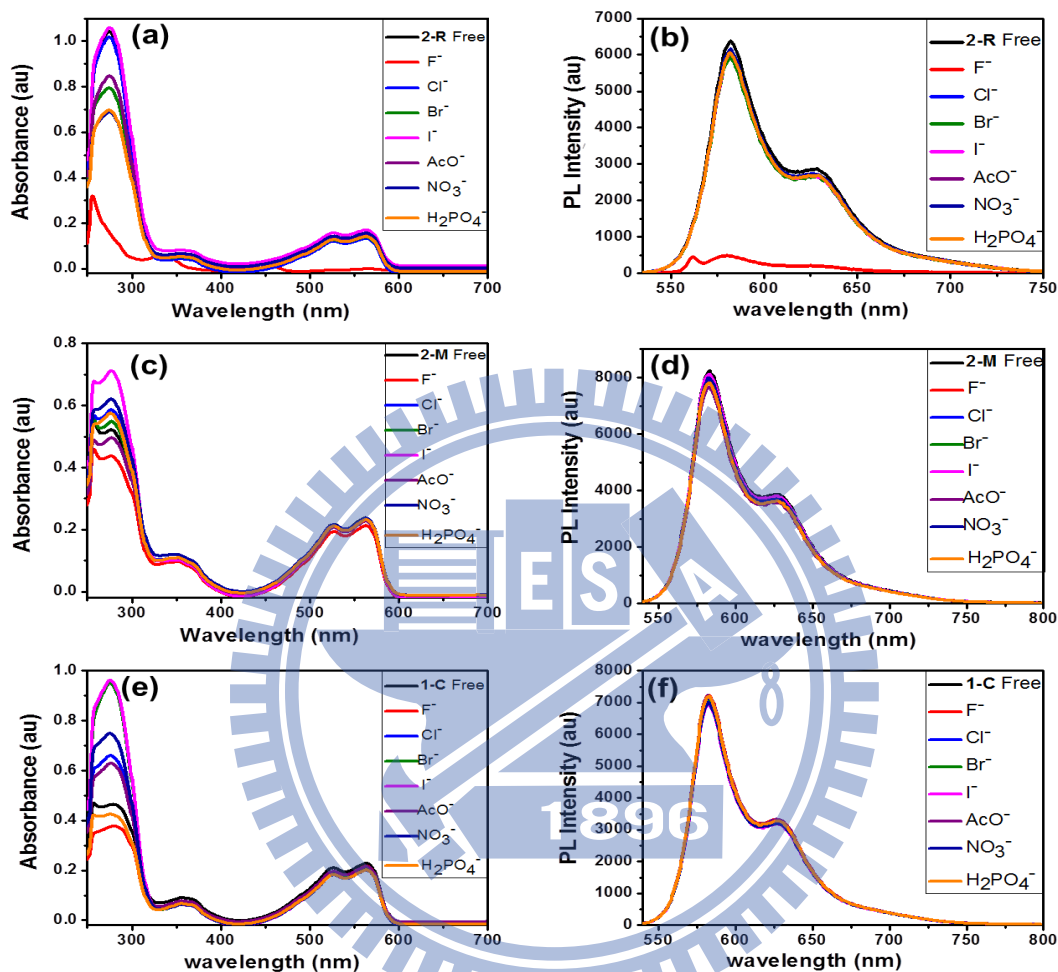


Figure 2. 13. UV-vis absorption and fluorescence spectral changes of **2-R**, **2-M**, and **1-C** (all receptors concn = 1×10^{-5} M, DMSO) with the addition of 40 equiv of different anions as TBAX ($X = F^{-}$, Cl^{-} , Br^{-} , I^{-} , AcO^{-} , NO_3^{-} , and $H_2PO_4^{-}$); (a), (b) UV-Vis absorption and fluorescence spectral changes of **2-R**, respectively; (c), (d) UV-Vis absorption and fluorescence spectral changes of **2-M**, respectively; (e), (f) UV-vis absorption and fluorescence spectral changes of **1-C**, respectively. (for all the samples fluorescence was monitored at their respective emission maxima by exciting at 525 nm).

The observable naked eye color change of **2-R** from pink to pale green upon the addition of TBAF was consistent with our absorption trends. Other anions could not change the color as their sizes were too large to interact with the cavity. Moreover, **1-C** and **2-M** did not show any obvious color changes with all anions (see **Figures 2. 14a-2. 14f**). Remarkably, the on-off-on fluorescence etiquette of the **2-R**/ F^- complex was successfully achieved via the alternative addition of F^- and TFA up to four cycles, which proved the excellent chromogenic and fluorogenic functions along with reversibility of this novel functional molecular switch.

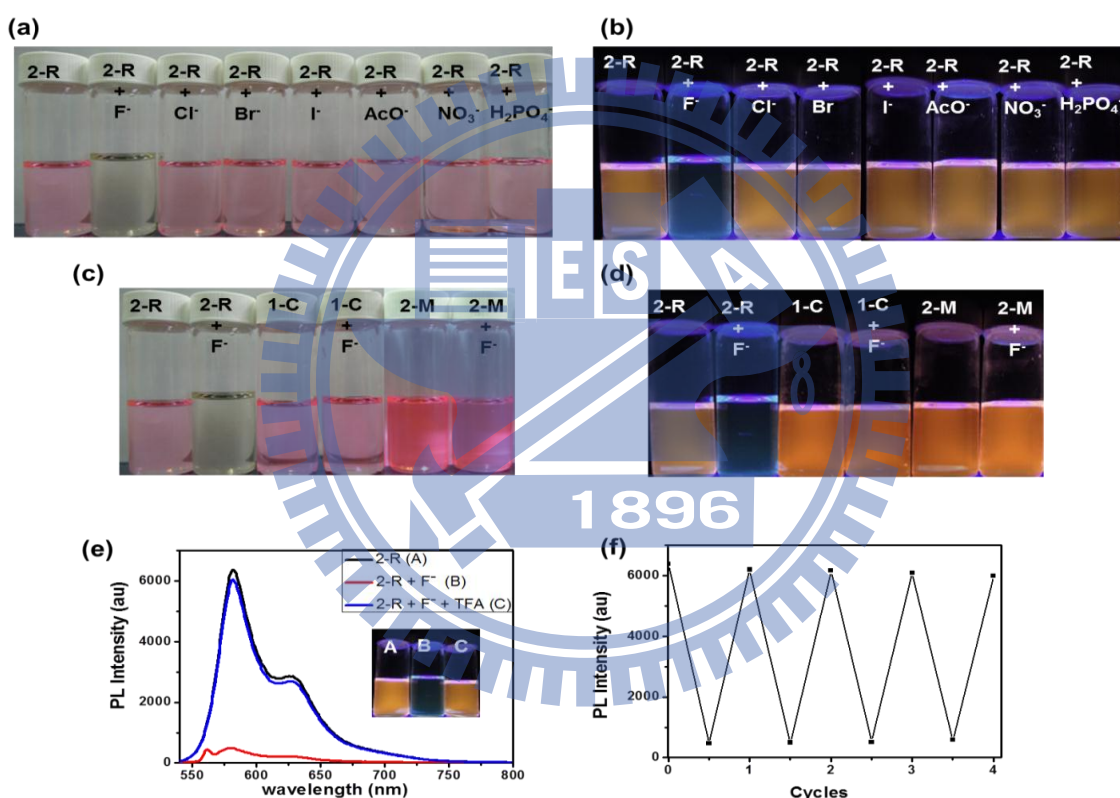


Figure 2. 14. (a) Naked eye color changes of [2]rotaxane **2-R** (1×10^{-5} M, DMSO) with the addition of various anions (30 equiv in DMSO); (b) fluorescence changes of samples mentioned in (a) under UV light (365 nm); (c) naked eye color changes of **2-R** and its precursors **1-C** and **2-M** with the addition of 30 equiv TBAF; (d) fluorescence changes of samples mentioned in (c); (e) as depicted in the inset picture of **2-R** fluorescence spectra , fluorescence changes of (A) **2-R**

free, (B) after addition of TBAF to sample (A), and (C) is recovered sample with the addition of TFA to sample (B) under UV light (365 nm); (f) fluorescence intensity changes of **2-R** (1×10^{-5} M, DMSO) at 582 nm under addition of alternate compounds (TBAF and TFA) for four cycles ($\lambda_{\text{ex}} = 525$ nm).

2. 3. 4. Electrochemical titrations:

To verify the dramatic color change and fluorescence quenching of DPP molecule, we further carried out electrochemical titrations of **2-P** with F^- (see **Figures 2. 15a and 2. 15b**). A dramatic cathodic shift of $\Delta E_{1/2} = 450$ mV at 1 equiv of F^- was observed, and a further addition of F^- showed a steady cathodic perturbation, which is consistent with our ^1H NMR and UV-Vis titration trends. Based on these results, we infer that the smallest anion F^- could be easily percolated into the macrocycle to form H-bonding with the 2,6-dicarboxyamidopyridine unit, and further guest equiv would deprotonate the amide cleft to induce the shuttling of charged wheel over the thread and to close the proximity of DPP in relative polar solvent DMSO. Eventually, this process facilitates the supramolecular electronic coupling between DPP and **2-R/F** complex and thus to affects the photophysical properties of the current functional MIM.^{94c,109}

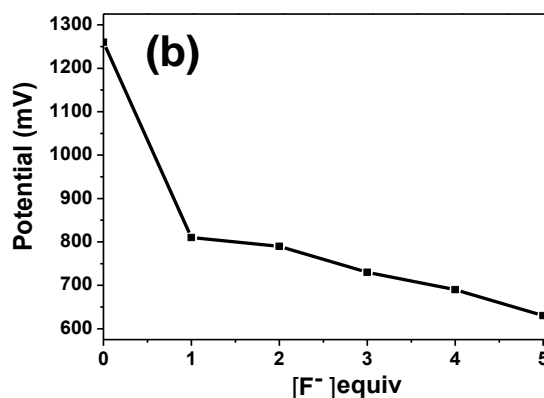
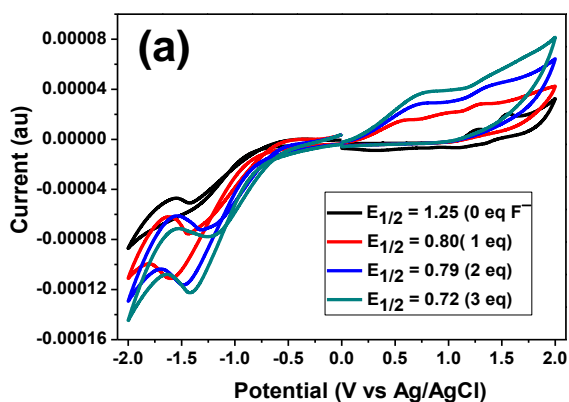


Figure 2. 15. Electrochemical titration studies of **2-P** (3 mM) using 0.1M TBAPF₆ supporting electrolyte at a scan rate of 0.1Vs⁻¹ in CHCl₃: a) changes in electrochemical potential of **2-P** with TBAF (30 mM) upon progressive addition from 0-3 equiv (for clarity in picture we depicted 3 equiv upto 3 equiv only); b) plot of potential change in mV against fluoride equiv.

2. 3. 5. Time resolved photo luminescence studies:

To corroborate the above observations, time resolved fluorescence measurements were carried out for the **2-R** and **2-R/F⁻** complex probed at 582 nm (excited at 525 nm). Significantly, as shown in **Figure 2. 16**, time resolved fluorescence became a biexponential decay with the life time of (τ_1) 5.71 ns (69.21%) and (τ_2) 2.19 ns (30.79%) from the original mono-exponential decay with a life time of (τ_1) 5.56 ns. The shorter value can be attributed to the charged wheel (amide deprotonation by F⁻) and the longer value represents the intrinsic fluorescence of the DPP fluorophore. However, the life time values of **1-C** and **2-M** remained constant from their original mono-exponential decay even in the presence of F⁻ (see **Figures 2. 17a** and **2. 17b**).

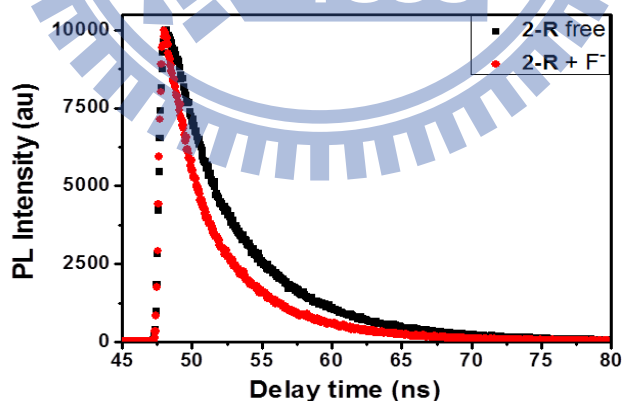


Figure 2. 16. Time resolved fluorescence spectral changes of [2]rotaxane **2-R** before and after the addition of TBAF.

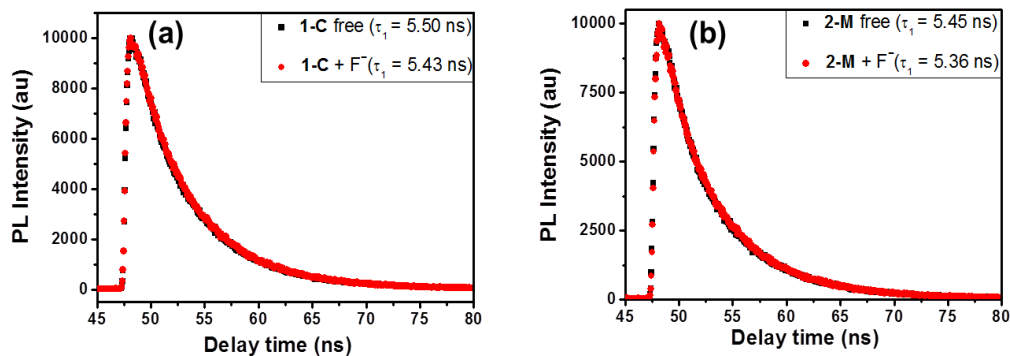


Figure 2. 17. Time resolved fluorescence spectral responses for **1-C** and **2-M** before and after addition of TBAF.

2. 4. Conclusions

In summary, a bright DPP functionalized [2]rotaxane was synthesized and well characterized. The pre-organized cavity formed in rotaxane by virtue of mechanical bond enhanced stimuli-responses towards solvent and F^- via noncovalent interactions. It was demonstrated spectroscopically that the [2]rotaxane **2-R** host could selectively recognize F^- with remarkable chromogenic, fluorogenic, and reversible functions. A Prevailing time resolved fluorescence profile proved the sensitivity of **2-R** in contrast to its precursors. As the complex quenching mechanism was coupled with both charged macrocycle shuttling and chemical stimuli, the electron or energy transfer between macrocycle and fluorophore could not be easily differentiated. Further kinetic and transient absorption studies are currently underway in our laboratory, which will be reported in due course. Hence, this design of functional MIMs could be an ideal for developing future allosteric anion sensors.

Chapter-3

An Acid-Base Controllable Hierarchical Nanostructure from a NIR-Absorbing Conjugated Polyrotaxane-Based Optical Molecular Switch

3. 1. Introduction

The quest for developing novel and creative mechanically interlocked polymeric architectures (MIPAs) stimulated us, since these architectures had been found potential applications in fields like nanoelectromechanical systems (NEMS),¹¹⁰ insulated molecular wires (IMWs),¹¹¹ and controlled drug release.¹¹² During the last two decades, rotaxanes and catenanes have been experienced revolutionary changes in their synthetic protocols,¹¹³ thus their convenient and modular fashioned approaches allowed to realize complex macromolecular architectures. In this context, conjugated polymers with mechanically interlocked units either in main-chains¹¹⁴ or side-chains¹¹⁵ have drawn a special attention among materials and supramolecular chemists. Unique optical and semiconducting properties of π -conjugated polymers have long been motivated to construct novel optoelectronic devices.¹¹⁶ In addition to this molecular self-assembly properties of copolymers, π -conjugated structures have created a new dimension for these polymers.¹¹⁷

Supramolecular complex architectures, such as polyrotaxanes, polycatenanes, and daisy chain polymers, have often been offering unique properties in contrast to their single ensemble counterparts.¹¹⁸ Enormous strides have long been made in the field of MIPAs to the realization of precise molecular mechanics in imparting the unusual photophysical properties to the π -conjugated polymers at molecular level. Swager and co-workers have reported how the optical properties of conjugated main-chain polymers were affected by the rotaxane exciplex.¹¹⁹ Stoddart and co-workers have extensively investigated bistable MIPAs and developed molecular

electronic memory devices with cross-sections even smaller than a white blood cell.¹²⁰ They suggested that the unique degrees of freedom and controlled molecular motions of mechanical bonds altered the photophysical properties of MIPAs; however, most of these reports were associated with macrocycle units, such as cyclodextrins,¹²¹ cucurbiturils,¹²² and crown ethers.¹²³ Nevertheless, there is no such example of polyrotaxane architecture contains an orthogonal H-bonded macrocycle unit.

Self-assembled bilayer membrane nanostructures of phospholipids have been elegantly utilized by the nature to compartmentalize vital biological reactions, inspired by many artificial synthetic amphiphilic receptors to be developed for specific drug delivery¹²⁴ and ion-channel transportation.¹²⁵ The nanostructures and their morphological changes were dependent on individual intermolecular interactions which were controllable by the concentrations, polarities, pH values, functional groups, and geometries of the units. Thus, the remarkable stimuli responsiveness of these nanostructures combined with switchable rotaxane units make them expedient candidates in designing novel and functional MIPAs.^{110b,117b} Moreover, synthetic amphiphilic receptors possessing extended conjugations close to the infrared region are highly demanding, as this region provides the diminished Rayleigh-Tyndall scattering of light which is suitable for most of the biological specimen imaging.⁴⁹

From the viewpoint of creating novel hierarchical nanostructures, the orthogonal hydrogen-bonded [2]rotaxane units in conjunction with polymeric structures might provide interesting MIPAs. However, to the best of our knowledge, such systems have not been investigated previously. To mimic this, we need a bottom-up approach with an amphiphilic synthetic receptor that possesses a unique topologically controlled H-bonded macrocycle unit tethered to an extended π -conjugated planar polymeric backbone. We have recently developed a novel

diketopyrrolopyrrole-based [2]rotaxane architecture with an orthogonal H-bonded macrocycle unit, which showed remarkable stimuli responsiveness and selective anion sensing capability.¹²⁶ With the aim of utilizing unique topological cavities of MIPAs in stimuli controlled macromolecular self-assembled nanostructures, which could not be attained previously, we extended our efforts to create novel and functional MIPAs and to study the effects of rotaxanation on the thermal and optical properties, as well as the self-assembly process of MIPAs.

In this study, we synthesized a series of new polymers by copolymerizing the 9-alkylidene-9H-fluorene (**A1**) monomer unit with various monomers, including the diketopyrrolopyrrole tethered with dumbbell (**1-c**), metalated [2]rotaxane (**2-a**), demetalated [2]rotaxane (**2-b**), and simple alkyl chain monomers (**1-d**), by Suzuki coupling strategy to afford copolymers **P1**, **P2**, **P3**, and **P4**, respectively. We employed these new MIPAs in the host-guest chemistry, in which orthogonal H-bonded pendant [2]rotaxanated **P3** showed a selective and reversible optical response towards the trifluoroacetic acid (TFA) in comparison with the other polymers (**P1**, **P2**, and **P3**). We explored the effects of a topological H-bonding on the optical and self-assembled properties of the π -conjugated main-chain polymer **P3**. Furthermore, we carried out computational density functional theory (DFT) and Parameterized Model number 3 (PM3) calculations to understand the basic molecular interactions and electron absorption properties of MIPAs. Macromolecular self-assembled nanostructures were examined by using various microscopic analyses (AFM, SEM, and TEM) and dynamic light scattering (DLS) studies (see **Figure 3. 1**). Herein, we provide a novel and yet a simple paradigm of MIPAs that showed a sensitive controllable and reversible acid-base sensing as well as molecular self-assembly properties.

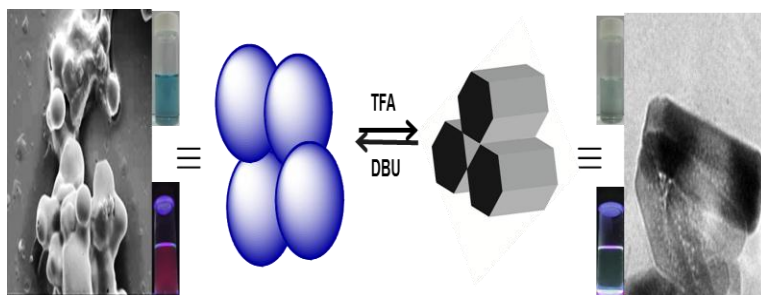


Figure 3. 1. Acid-base driven reversible molecular shuttling process in a conjugated side-chain polyrotaxane having an orthogonal topological cavity and its controllable hierarchical nanostructure formation mechanism along with high contrast optical functions.

3. 2. Experimental section

3. 2. 1. General methods and materials:

All the reactions and operations were carried out under an atmosphere of inert argon using Schlenk techniques unless otherwise stated. NMR spectra were recorded on Varian Inova 400, and Inova 600 Series (^1H : 400 and 600 MHz; ^{13}C : 100 and 150 MHz) at a constant temperature of 298 K. Chemical shifts were reported in parts per million from low to high field and referenced to residual solvent (CDCl_3 $\delta = 7.26$ ppm and $\delta = 77.23$ ppm). Coupling constant (J) were reported in hertz (Hz). Variable temperature NMR experiments were carried out by NMR services of NCTU Taiwan (Varian Inova 500 MHz, with VT-gas 10 LPM flow-rate and cooling gas 16 LPM flow-rate using FTS system). 2D-diffusion order NMR spectroscopy 2D-DOSY experiments were acquired on Varian Inova 600 MHz. UV-Vis spectra were recorded in different solvents from a Jasco UV-600 spectrophotometer using 1 cm quartz cuvette. Fluorescence measurements were conducted with HITACHI 7000 Series Spectrophotometer. All emission and excitation spectra were corrected for the detector response and the lamp output. Melting points were determined using a Fargo MP-2D apparatus and are uncorrected. Elemental analyses were conducted on HERAEUS CHN-OS RAPID elemental analyser. Infrared spectroscopy data were

collected using Perkin Elmer IR spectrophotometer. Solid sample were analysed using KBr pellet method and liquid sample data collected by forming neat thin film between two NaCl plates. CV measurements were conducted using (0.1 M TBAPF₆ (tetrabutylammonium hexafluorophosphate) as a supporting electrolyte at a scan rate of 0.1 Vs⁻¹; Carbon working electrode, Ag/AgCl reference electrode and Platinum wire as counter electrode) CHI661C CH Instruments Inc analyser. The number and weight average molecular weights of polymers were determined through gel permeation chromatography (GPC) using Waters chromatography interfaced with Waters 2414 differential refractometer, polystyrene standards, and THF as the eluent.

Thermal properties of polymers were probed using thermo gravimetric analysis (TGA) TA Instruments Q500 apparatus at a temperature flow rate of 10 °C for min. Powdered XRD studies were conducted on Bruker AXS D2 Phaser using LENXEYE detector and CuK α radiation source. Nano-assembled superstructures morphology were probed using atomic force microscopy (AFM) in tapping mode using Bruker diInnova Scanning Microscope, field-emission Scanning electron microscope (FE-SEM) JEOL JSM-6500F and Transmission electron microscopy JEOL JEM-2100 Microscope (TEM) were used in analysing size and shape of controllable nano superstructures. Furthermore, dynamic light scattering measurements were carried out using MALVERN Nano-ZS90 Zetasizer DLS instrument to assembled samples particle size in solution.

All the reagents were purchased from commercial sources and used without further purification. All the solvents were HPLC grade; anhydrous solvents were obtained by passing through activated alumina column purification system, further dried by standard drying procedures.

Solvents were degassed by freeze/thaw/pump cycle technique prior to use. The following compounds were prepared according to literature procedures: 1-a¹²⁷ and 1-b¹²⁸.

3. 2. 2. Sample Preparation:

Stock solutions of polymers, monomers (10 μ M), and TFA (10 mM) were prepared (using freshly distilled and degassed solvents, further diluted to their desired volumes before experiments). Polymer solutions were spin-coated at 1500 rpm on 2 x 2 cm² glass plates for solid state UV-vis to NIR absorption measurements. Solutions were sonicated and filtered through fine micron filter prior to dynamic light scattering analysis. For microscopic experiments, such as AFM and FE-SEM, freshly prepared solutions were drop-cast on 1 x 1 cm² SiO₂/Si substrates, and gold coatings were used in FE-SEM sample analysis. Furthermore, the samples were drop-cast on carbon coated Cu-grids in TEM analysis. All samples were evaporated in a vacuum oven prior to analysis.

3. 2. 3. Calculation methods:

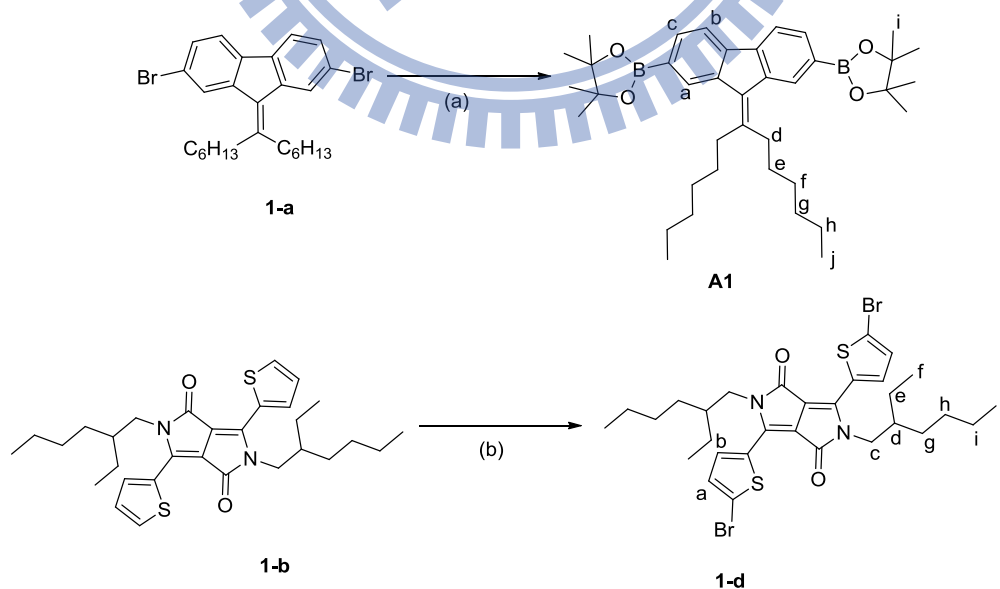
We carried out density functional theory (DFT) calculations to elucidate the complex nature of interaction in repeating polymer units, starting from smaller model units because a full large unit calculation is too extensive and lengthy. The calculations, including the simple asymmetric propargyl unit substituted diketopyrrolo pyrrole (**D1**), **A1**, and 9-alkylidene-9*H*-fluorene connecting to an asymmetric triazole substituted diketopyrrolopyrrole unit (**D2**), were explored by quantum chemical calculations using the Gaussian09 software package.¹²⁹ Geometry optimization of the ground state structures was carried out with DFT at the tHCTHhyb¹³⁰ level of theory using the 6-31+G(2d,p) basis set. The excitation energies of the low lying excited states and oscillator strengths were predicted using the time dependent density functional theory (TD-DFT) with Handy's gradient-corrected correlation functionals at the HCTH147/6-31+G(2d,p)

level.¹³¹ The orthogonal H-bonded strengths with and without the acid of demetalated [2]rotaxane monomer **2-b** were examined using the semi-empirical PM3¹³² method to understand the controlled nanostructure formation of the **P3**.

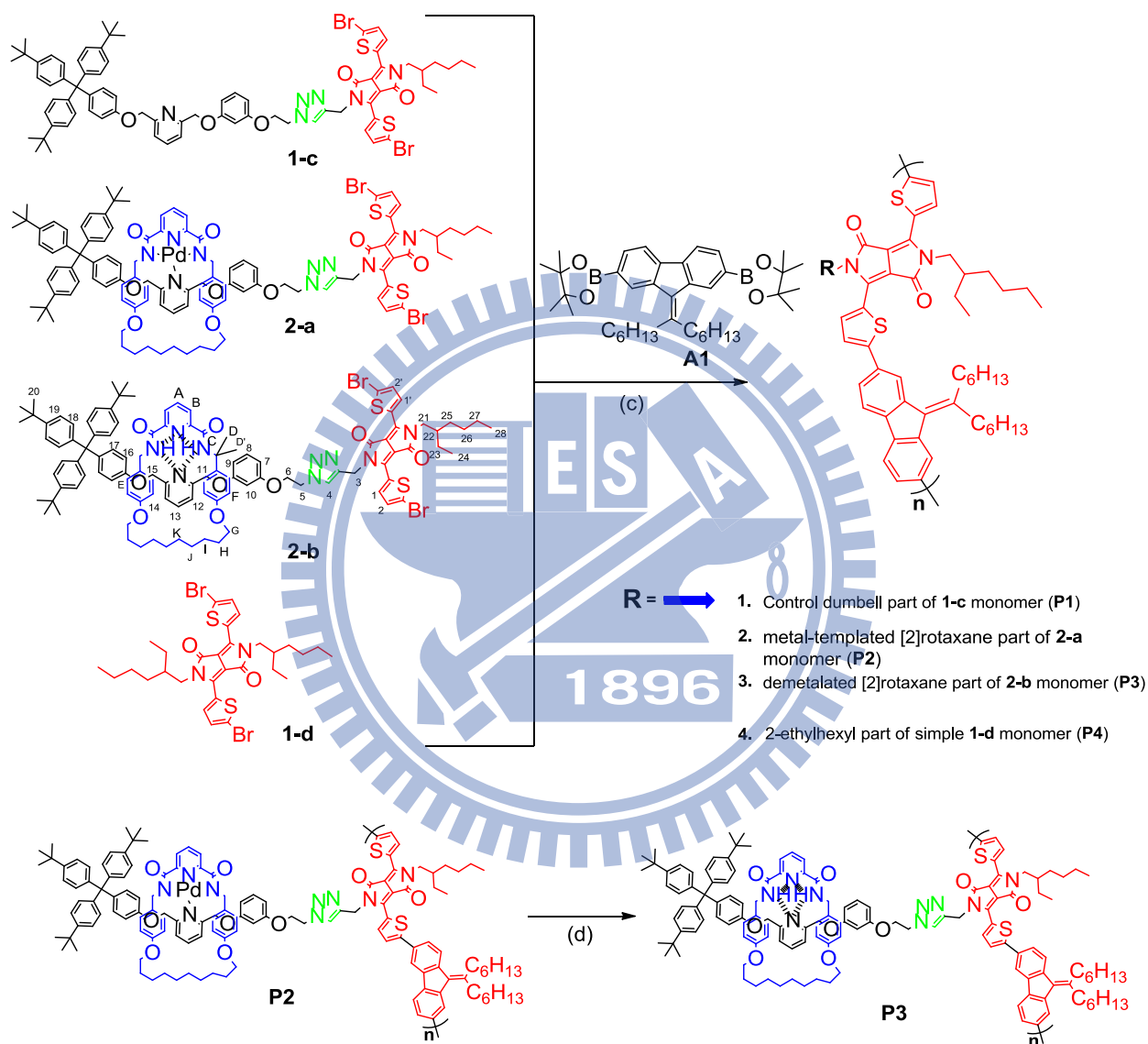
3. 2. 4. Molecular design:

It is expected that the introduction of unique topological cavities formed in situ by the virtue of mechanical bond into pendants of the polymeric architectures could be an ideal choice to realize the superior material processibility.^{110b,78} Several merits, including the unique optical properties, flexible self-assembled nature of diketopyrrolopyrrole,¹³³ and better coplanar structured 9-alkylidene-9H-fluorene donor unit,¹³⁴ (**Scheme 3. 1**) inspired us to accomplish the aforementioned task (**Scheme 3. 2**). The complete chemical structures of these polymers were depicted in **Scheme 3. 3** and the monomers **1-c**, **2-a**, and **2-b** were prepared according to our previous protocol.¹²⁶ The synthetic procedures and characterization data of all these polymers are provided in the Supporting Information.

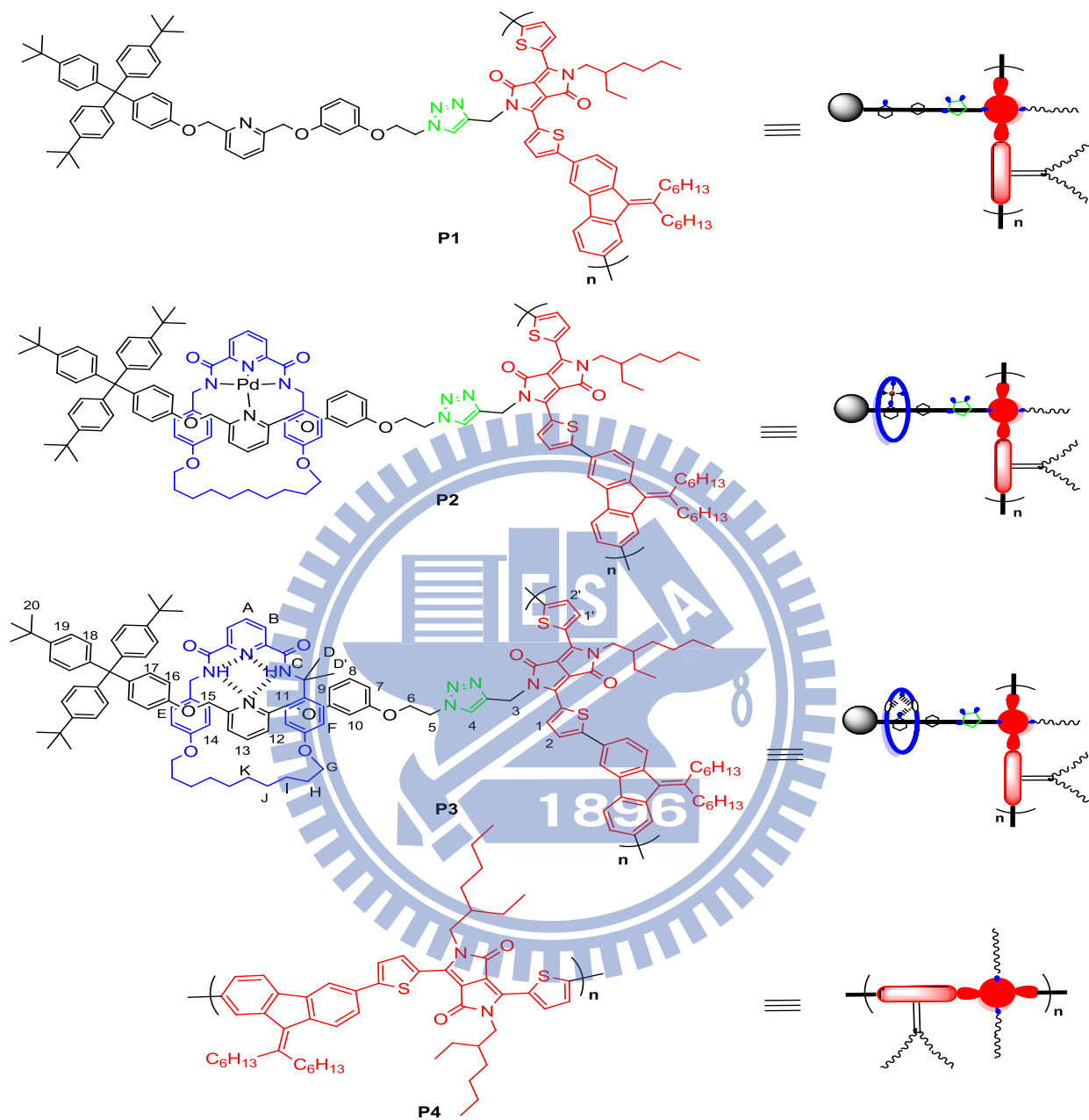
3. 2. 5. Synthesis of AKF donor, DPP derivative, and rotaxanated copolymers:



Scheme 3. 1. Synthesis of compounds **A1** and **1-d**; Reagents and conditions: (a) 1, 4-dioxane, KOAc, bispinacolato diboron, PdCl₂(dppf): DCM complex, 90 °C, 48 h, 82%, (b) NBS, CHCl₃/AcOH, rt, 48 h, 84%.



Scheme 3. 2. Synthesis of rotaxanated copolymers; Reagents and conditions: (c) toluene, THF, K₂CO₃ aq Solution, Pd(PPh₃)₄, 80 °C, 48 h, yields of **P1** (63%), **P2** (73%), **P3** (60%), and **P4** (52%), respectively (d) CHCl₃/MeOH, KCN, 60 °C, 4 h, 52%.



Scheme 3. 3. Chemical structures of polymers **P1**, **P2**, **P3**, and **P4**.

3. 2. 6. Synthetic procedures:

synthesis of 2,2'-(9-(tridecan-7-ylidene)-9H-fluorene-2,7-diyl)bis(4,4,5,5-tetramethyl-1,3,2-dioxaborolane) (A1):

To a 100 ml oven dried round bottomed flask was added a mixture of 2,7-dibromo-9-(tridecan-7-ylidene)-9H-fluorene (0.50 g, 0.99 mmol, 1.0 equiv), bis pinacolatodiboron (0.75 g, 2.97 mmol, 3.0 equiv), KOAc (0.78 g, 7.93 mmol, 8.0 equiv) and PdCl₂(dppf)₂DCM complex (0.040 g, 0.049 mmol, 0.05 equiv) the flask was evacuated by freeze-pump-thaw cycle. To this mixture was added a separately degassed 1,4-dioxane (50 ml) and further degassed by freeze-pump-thaw cycle the reaction was stirred at 90 °C for 48 h. After cooling, the reaction mixture was filtrated through celite and H₂O (100 ml) was added for extraction with AcOEt (2 x 100 ml). The organic phase was washed with brine solution (2 x 100 ml) and dried over (MgSO₄). After filtration the solution was evaporated under reduced pressure and the crude residue was subjected to column chromatography (silica gel, PE/AcOEt: 9/1 to 8/2). A yellow solid was recovered further recrystallization in a mixture of Et₂O/hexane gave a pale yellow crystalline solid (0.49 g, 0.81 mmol, 82.0%). Chemical formula: C₃₈H₅₆B₂O₄, Molecular weight: 598.47; mp. 125-128 °C

¹H NMR (400 MHz, CDCl₃, 298 K): δ (ppm) = 8.30 (s, 2H, a), 7.86 (d, J_d = 7.5 Hz, 2H, b), 7.81 (d, J_d = 7.5 Hz, 2H, c), 2.90-2.85 (m, 4H, d), 1.82-1.78 (m, 4H, e), 1.74-1.69 (m, 4H, f), 1.66-1.47 (m, 8H, g and h), 1.40 (s, 24H, i), 1.01-0.97 (m, 6H, j); ¹³CNMR (100 MHz, CDCl₃, 298 K): δ (ppm) = 152.19, 142.02, 138.33, 132.67, 131.38, 130.94, 119.03, 83.57, 37.88, 31.71, 29.80, 28.29, 24.90, 22.78, 14.11; IR (KBr, cm⁻¹): 2975, 2938, 2873, 1594, 1475, 1345, 1262, 1132, 956; MS (+EI): (m/z): Calcd for C₃₈H₅₆B₂O₄; 598.47; found: 598.0 [M]⁺, 599.0 [MH]⁺,
Anal. Calcd. for C₃₈H₅₆B₂O₄: C, 76.26; H, 9.43, found; C, 76.11; H, 9.40.

Synthesis of 3,6-bis(5-bromothiophen-2-yl)-2,5-bis(2-ethylhexyl)pyrrolo[3,4-c]pyrrole-1,4(2H,5H)-dione (1-d):

2,5-bis(2-ethylhexyl)-3,6-di(thiophen-2-yl)pyrrolo[3,4-c]pyrrole-1,4(2H,5H)-dione **1-b** (0.75 g, 1.42 mmol, 1.0 equiv) was added into a 250 ml round bottomed flask containing anhydrous CHCl_3 (56 ml) and 5 drops of AcOH covered with aluminum foil to protect from ambient sun light. To above solution was added NBS (0.52 g, 2.93 mmol, 2.05 equiv) in a portion wise over a period of 30 min at room temperature and the reaction stirred under argon atmosphere for 48 h at which time the solution was poured into beaker containing MeOH (200 ml). The resulting solution was filtered and the solid washed with hot MeOH and H_2O . The crude residue was subjected to flash column chromatography (silica gel, Hexane/EtOAc: 9.9/0.1). A reddish brown solid **1-d** was recovered (0.82 g, 1.20 mmol, 84%). Chemical formula: $\text{C}_{30}\text{H}_{38}\text{Br}_2\text{N}_2\text{O}_2\text{S}_2$, Molecular weight: 682.57.; mp. 169.5-171.5 °C.

$^1\text{H NMR}$ (400 MHz, CDCl_3 , 298 K): δ (ppm) = 8.64 (d, $J_d = 8.2$ Hz, b), 7.22 (d, $J = 8.2$ Hz, a), 3.94-3.91 (m, 4H, c), 1.37-1.23 (m, 16H, e, g, h and i), 0.91- 0.86 (m, 12H, f and j); $^{13}\text{C NMR}$ (100 MHz, CDCl_3 , 298 K): δ (ppm) = 161.5, 139.5, 135.5, 131.5, 131.3, 119.1, 108.1, 46.1, 39.2, 30.3, 28.4, 23.7, 23.1, 14.1, 10.6; **MS (+LR-FAB)**: (m/z): Calcd for $\text{C}_{30}\text{H}_{38}\text{Br}_2\text{N}_2\text{O}_2\text{S}_2$; 682.57; found: 682.0 $[\text{M}]^+$, 684.0 $[\text{M}+2]^+$; **IR** (KBr, cm^{-1}): 3307, 3087, 2978, 2905, 2859, 2142, 1661, 1554, 1402, 1311, 1252, 1117; **Anal. Calcd.** for $\text{C}_{30}\text{H}_{38}\text{Br}_2\text{N}_2\text{O}_2\text{S}_2$: C, 52.79; H, 5.61; N, 4.10, found: C, 52.61; H, 5.63; N, 4.08.

3. 2. 7 General Polymerization method and Polymers data:

Rotaxane monomer/axle monomer and simple monomer **1-d** (1.0 equiv), alkyldiene fluorene monomer (1.0 equiv) and dried K_2CO_3 (20.0 equiv) was taken in 50 ml flame dried round bottomed flask equipped with reflux condenser and a septum. The reaction flask was evacuated by freeze-thaw-pump cycle and filled with argon. To the above dried solid monomers was added a separately degassed THF (10 ml), Toluene (10 ml) and H_2O (3 ml) via dried hypodermic cannula. The septum of the flask was briefly removed and catalyst $Pd(PPh_3)_4$ (0.05 equiv) was added and the septum was replaced immediately. The above reaction solution was further evacuated by freeze-thaw-pump cycle and degassed for 5 minutes by argon purging. The reaction was stirred at $80\text{ }^\circ\text{C}$ for 36 h at which time phenylboronic acid (10 mg) and catalyst (4 mol%) were added to the reaction, and then 4 h later iodobenzene (120 μl) was added and the reaction was stirred for another 8 h at which time the reaction flask was cooled to room temperature slowly and H_2O (5 ml) was added. The reaction solution was added drop wise to MeOH (250 ml) to precipitate the polymer. The polymer solution was carefully filtered through 0.5- μm fine micron polytetrafluoroethylene (PTFE) filter and washed with excess of hexane, acetone and H_2O . The crude polymer was purified by soxhlet extraction using hexane (250 ml), Acetone (250 ml) to remove catalyst and other oligomer impurities. Finally soxhlet extraction was done with $CHCl_3$ (250 ml) and the $CHCl_3$ layer was reduced to overall volume less than (10 ml). The $CHCl_3$ layer was poured slowly into a MeOH (250 ml) to precipitate the polymer, after filtration the polymer was dried under high vacuum for overnight to afford dark blackish-green solid.

Protic demetalation method: Alternatively **P2** was demetalated using potassium cyanide in $CHCl_3/MeOH$ to prove the efficient and preserved interlocked nature during polymerization. The blackish green **P2** (0.025 g , 0.011 mmol, 1.0 equiv) solid was added to a $CHCl_3/MeOH$ (1:1) 8

ml solution of KCN (0.022 g, 0.34 mmol) in a 25 ml round bottomed flask equipped with argon and the resultant solution was stirred at 60 °C for about 4 h. The red fluorescent solution cooled down to room temperature and diluted with CHCl₃ (25 ml) further washed with aqueous brine solution 2 x 15 ml then dried over MgSO₄ and evaporated under vacuum to minimum volume of (5 ml). The resulted CHCl₃ layer was slowly poured in to beaker containing 100 ml of MeOH, the precipitated solid was filtered via fine micron filter and dried overnight under vacuum to yield **P3** (0.012 g, 52%).

Data for Polymers: (P1): monomer **1-c** (0.12 g, 0.085 mmol, 1.0 equiv) and monomer **A1** (0.051 g, 0.085 mmol, 1.0 equiv) were polymerized according above protocol. ¹H NMR (600 MHz, CDCl₃, 298 K): δ (ppm) = 8.98, 8.94, 8.75, 8.03, 7.98, 7.92, 7.73, 7.71, 7.58, 7.38, 7.36, 7.18, 6.76, 6.40, 6.31, 5.31, 5.21, 5.03, 4.99, 4.61, 4.23, 4.07, 2.78, 1.95, 1.77, 1.52, 1.21, 0.84 (all broad peaks); **IR** (KBr disc, cm⁻¹): 3423, 3064, 2971, 2867, 1663, 1524, 1443, 1130; **Yield** (0.085 g, 63%); **Anal. Calcd.** for C₁₀₃H₁₁₄N₆O₅S₂: C, 78.29; H, 7.27, N, 5.32; found; C, 77.86; H, 7.36, N, 5.24; **GPC** (PS standards) *M*_w = 17505 g/mol; polydispersity = 1.32

Data for P2: monomer **2-a** (0.12 g, 0.059 mmol, 1.0 equiv) and monomer **A1** (0.036 g, 0.059 mmol, 1.0 equiv) were polymerized according above protocol. ¹H NMR (600 MHz, CDCl₃, 298 K): δ (ppm) = 9.09, 8.92, 8.76, 8.02, 7.88, 7.78, 7.18, 7.02, 6.65, 6.62, 6.59, 6.49, 6.44, 6.26, 6.19, 5.31, 5.25, 4.88, 4.81, 4.66, 4.52, 4.42, 4.30, 4.01, 3.61, 2.79, 1.95, 1.60, 1.56, 1.22, 0.84 (all broad peaks); **IR** (KBr disc, cm⁻¹): 3492, 3381, 2960, 2856, 1686, 1607, 1418, 1246; **Yield** (0.095 g, 73%); **Anal. Calcd.** for C₁₃₄H₁₄₉N₉O₉PdS₂: C, 73.15; H, 6.83, N, 5.73; found; C, 72.74; H, 6.76, N, 5.64; **GPC** (PS standards) *M*_w = 17700 g/mol; polydispersity = 1.24.

Data for P3: monomer **2-b** (0.10 g, 0.052 mmol, 1.0 equiv) and monomer **A1** (0.031 g, 0.052 mmol, 1.0 equiv) were polymerized according above protocol. $^1\text{H NMR}$ (600 MHz, CDCl_3 , 298 K): δ (ppm) = 9.18, 8.88, 8.81, 8.39, 8.26, 8.24, 8.18, 7.99, 7.82, 7.72, 7.50, 7.47, 7.36, 7.18, 7.02, 6.52, 6.41, 6.19, 6.13, 5.335.22, 4.66, 4.60, 4.33, 4.26, 3.87, 3.80, 2.78, 1.96, 1.78, 1.51, 0.86 (all broad peaks); **IR** (KBr, cm^{-1}): 3496, 3394, 3051, 2952, 2863, 1668, 1579, 1516, 1461, 1243, 1144, 1006; **Yield** (0.066 g, 60%); **Anal. Calcd.** for $\text{C}_{134}\text{H}_{151}\text{N}_9\text{O}_9\text{S}_2$: C, 76.79; H, 7.26, N, 6.01; found; C, 76.34; H, 7.34, N, 5.93; **GPC** (PS standards) $M_w = 18246$ g/mol; polydispersity = 1.25.

Data for P4: monomer **1-d** (0.15 g, 0.22 mmol, 1.0 equiv) and monomer **A1** (0.131 g, 0.22 mmol, 1.0 equiv) were polymerized according above protocol. $^1\text{H NMR}$ (600 MHz, CDCl_3 , 298 K): δ (ppm) = 9.03-8.97 (1H, br), 8.63-8.61(1H, br), 8.06-7.95 (2H, br), 7.71-7.61 (2H, br), 7.54-7.38 (4H, br), 4.07 (4H, br), 3.75 (2H, br), 2.87 (2H, br), 1.86-1.83 (2H, br) 1.59 (16H, br), 1.40-1.26 (16H, br), 0.92-0.85 (18H, br); **IR** (KBr disc, cm^{-1}): 3327, 3239, 3051, 2942, 2873, 1658, 1569, 1421, 1224, 1095; **Yield** (0.100 g, 52%); **Anal. Calcd.** for $\text{C}_{56}\text{H}_{70}\text{N}_2\text{O}_2\text{S}_2$: 77.55; H, 8.14, N, 3.13; found; C, 77.08; H, 8.06, N, 3.21; **GPC** (PS standards) $M_w = 120964$ g/mol; polydispersity = 2.1.

3. 3. Results and Discussion

3. 3. 1. Gel Permeation Chromatography (GPC) and 2D-DOSY NMR Characterization of MIPA:

The molecular weights, polydispersity indexes (PDI), and self-assembled natures of these MIPAs were examined by GPC. In contrast to the polymer retention volume (19.9 ml) of simple **P4**, supramolecular polymer **P3** showed a higher retention volume (22.1 ml) as shown in **Figure 3. 2**. Moreover, **P3** revealed a narrower PDI value of 1.24 than **P4** with a PDI value of 2.10. In contrast to **P4**, the interesting escalation of the retention volume in **P3** with a higher molar mass [2]rotaxane unit was observed. It clearly suggested that a smaller molecular weight of **P3** was obtained in contrast to **P4**, which was due to a lower degree of polymerization of **P3** induced by its larger pendent group. Additionally, a larger retention volume could also be evolved in **P3** via the more folded conformation during its macromolecular self-assembly owing to the strong intermolecular H-bonding and π - π stacking interactions as also suggested by Stoddart *et al.*¹³⁵ However, the broad PDI of simple polymer **P4** indicated a linear fashioned assembly through the π - π stacking interactions.

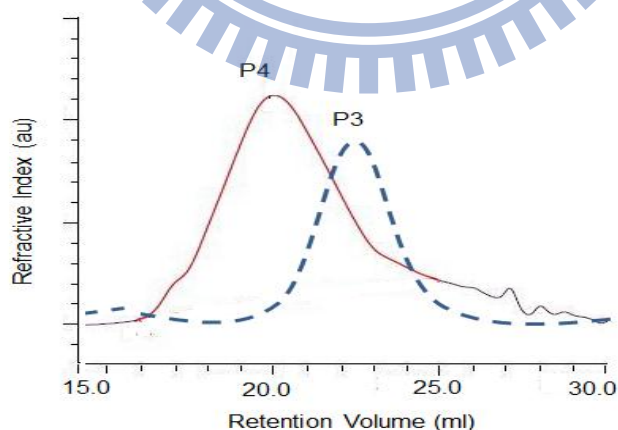


Figure 3. 2. Gel permeation chromatographs of polymers **P4** and **P3**.

To study the supramolecular polymerization, we compared the ^1H NMR spectra of both monomer **2-b** and polyrotaxane **P3** as shown in **Figure 3. 3a**, in which broad peaks of **P3** than those of **2-b** clearly suggested that mechanically interlocked nature of **P3** was maintained during polymerization. To confirm further the interlocked nature, we did protic demetalation of **P2** in $\text{CHCl}_3/\text{MeOH}$ with potassium cyanide which gave **P3** identical to that of obtained directly from monomer **2-b**. Furthermore, 2D-DOSY experiments were probed to confirm the mechanically interlocked nature of **P3** as depicted in **Figure 3. 3b**, where the marked diffusion rate of **P3** ($1.8 \times 10^{-10} \text{ m}^2/\text{s}$) was clearly distinctive from the diffusion rate of free monomer **2-b** ($4.7 \times 10^{-10} \text{ m}^2/\text{s}$). To further fortify the preserved mechanical interlocking nature of polymer **P3**, we conducted a 2D-DOSY experiment on the metalated polymer (**P2**) with the same degree of polymerization of **P3**. As shown in **Figure 3. 4**, polymer **P2** demonstrated a higher diffusion rate of $3.1 \times 10^{-10} \text{ m}^2/\text{s}$ in contrast to polymer **P3** ($1.8 \times 10^{-10} \text{ m}^2/\text{s}$). The slow diffusion rate¹²³ of polymer **P3** in comparison with the analogous monomer unit (**2-b**) as well as the metalated polymer (**P2**) lucidly supported the mechanically interlocked nature of the polymer through the strong orthogonal H-bonded interactions. This result clearly denoted the well preserved mechanical interlocking of **P3** with globule-like assembly structures.

3. 3. 2. ^1H NMR Spectroscopic Studies:

To explore the stimuli-based host-guest properties of these polymers, we carried out a series of ^1H NMR studies on the respective monomers of polymers. Upon adding TFA to monomer **2-b**, the wheel amide NH protons showed a downfield shift along with thread pyridyl protons (12, 13, and 14) as shown in **Figure 3. 5**. However, a downfield shift for proton E was observed during the titration of **2-b** with TFA. Upon further addition no significant effects were evidenced, which clearly

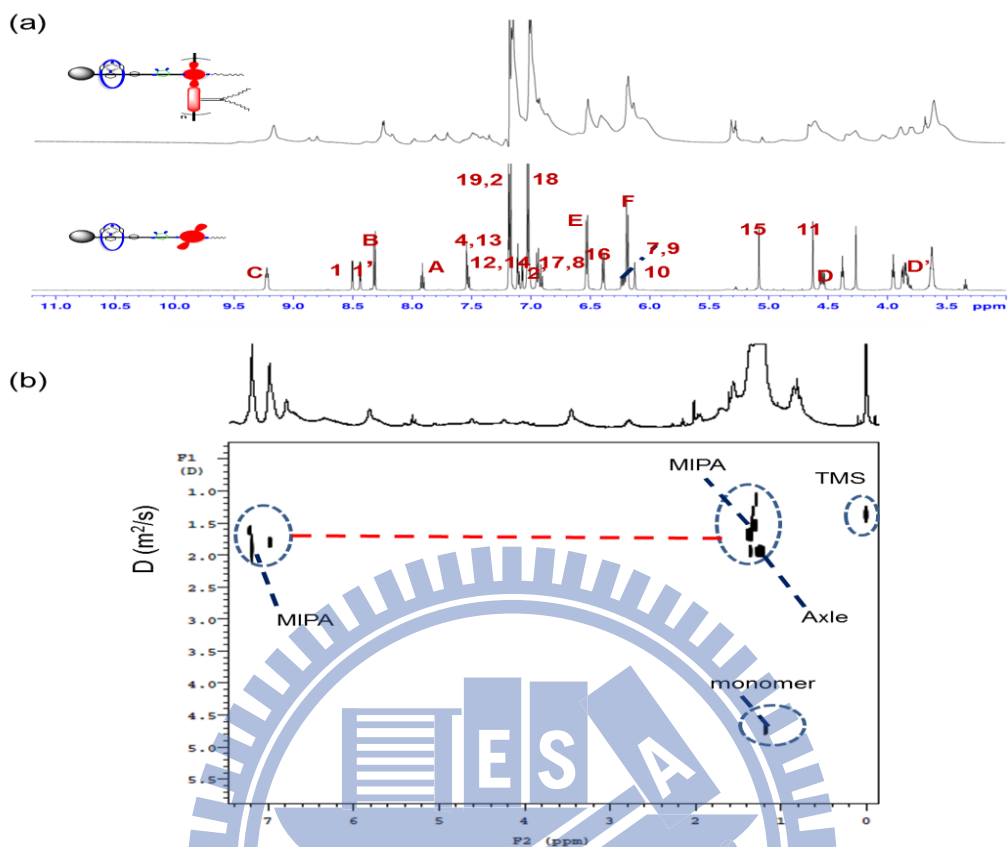


Figure 3. 3. (a) ^1H NMR (600 MHz, CDCl_3 , 298 K) stock plot of monomer **2-b** and polymer **P3** and (b) 2D-DOSY (600 MHz, CDCl_3 , 298 K) NMR spectra of **P3** at a concentration of 12 mg/ml. Diffusion coefficient of MIPA, axle part, and free monomer were marked with circles. The assignments correspond to the lettering shown in Scheme 1.

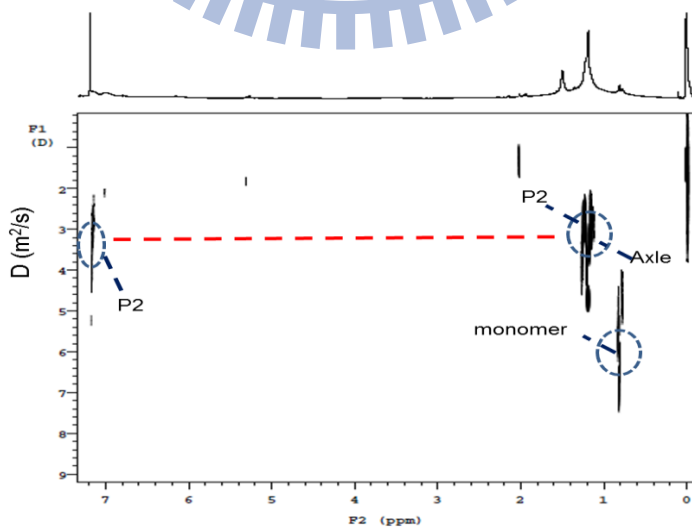


Figure 3. 4. 2D-DOSY (600 MHz, CDCl₃, 298 K) NMR spectra of **P2** at a concentration of 12 mg/ml. Diffusion coefficient of **P2**, axle part, and monomer were marked with circles.

illustrated that TFA was deprotonated by the axle unit to induce a strong H-bonded complex with the resulting trifluorocarboxylate anion. To further confirm the binding interactions, we verified the ¹H NMR spectrum of the dumbbell monomer **1-c** with TFA; the noticeable downfield shifts for pyridyl protons 12, 13, and 14 supported the deprotonation of TFA by the pyridine station. Unambiguously, the job plot analysis of **2-b** by drawing the chemical shift changes against the mole fractions of TFA yielded a 1:1 stoichiometry as represented in **Figure 3. 6**. Importantly, the acid-mediated host-guest interactions were completely reversible upon adding the base DBU as depicted in **Figure 3. 7**, which proved the potential molecular switch ability of the mechanically interlocked polymeric architecture in polyrotaxane **P3**.

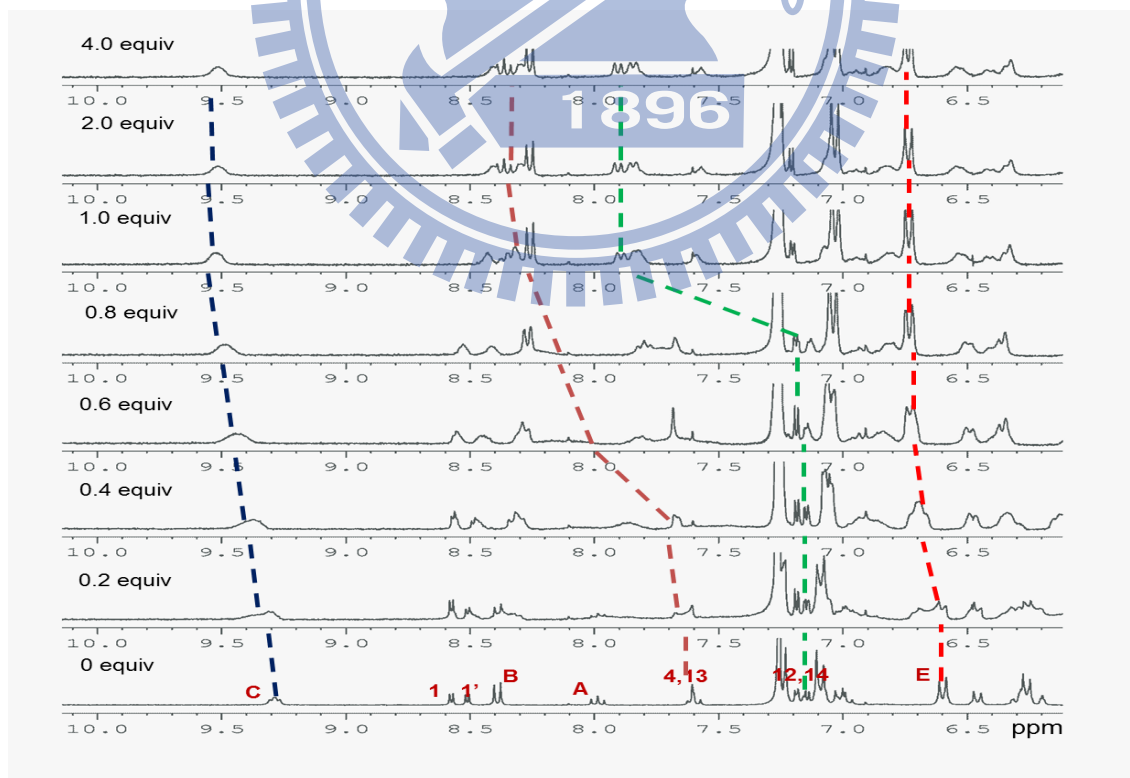


Figure 3. 5. Changes in ^1H NMR (300 MHz, CDCl_3 , 298 K) spectrum of [2]rotaxane **2-b** (3 mM) during titration with TFA (0-4 equiv). The assignments correspond to the lettering shown in **Main Scheme 1**.

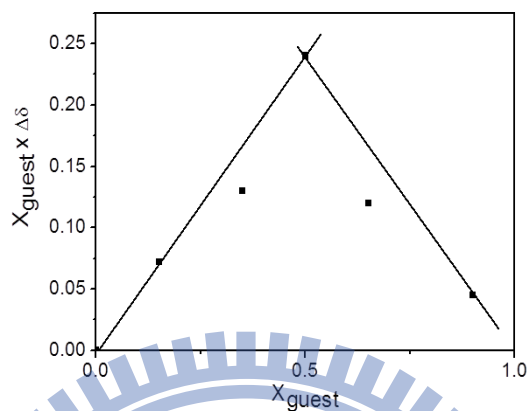


Figure 3. 6. Job plot between monomer **2-b** and TFA obtained by plotting $\Delta\delta$ in chemical shift for **2-b** pyridine proton (13) observed by ^1H NMR against the change in mole fraction of guest

$X_{\text{guest}} \cdot 10^7$

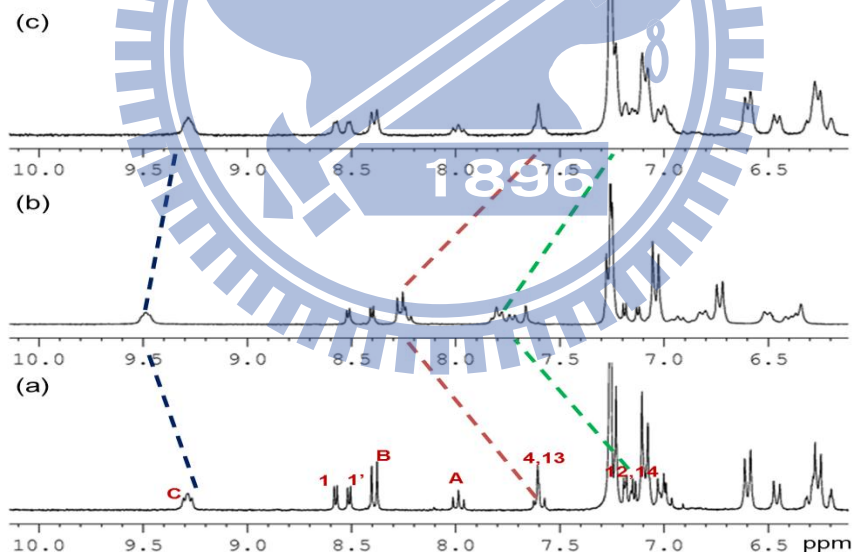


Figure 3. 7. ^1H NMR (CDCl_3 , 300 MHz): **2-b** (CDCl_3 , $c = 3$ mM); TFA (CDCl_3 , $c = 30$ mM): (a) free monomer **2-b**. (b) **2-b** + TFA 1.0 eq. (c) TFA containing monomer **2-b** recovered with the addition of DBU.

To further shed light on the acid mediated dynamic self-assembly of MIPAs, variable temperature NMR (VT NMR) experiments of complex **2-b-TFA** were conducted. When the temperature cooled down to 233 K the ^1H NMR spectrum of **2-b-TFA** showed the splitted resonances for amide protons C and pyridyl protons 12, 13, and 14 along with aliphatic protons with broad peaks in contrast to that at 298 K as shown in **Figure 3. 8**. However, when the solution of **2-b-TFA** was heated to 323 K close to *d*-chloroform boiling point, interestingly the amide protons and pyridyl protons showed marginal upfield shifts. Moreover, **2-b-TFA** presented downfield shifts for amide and pyridyl protons along with aliphatic splitting at 323 K in comparison with free monomer **2-b** at 298 K. Prominently, **2-b-TFA** showed coalescence for the complex proton resonances at 298 K and represented that the self-assembly process of MIPAs could be evolved through folding and unfolding of individual rotaxane units. These observations plug to a positive cooperative effect of the thermally-controllable folded conformation of the MIPA system. Furthermore, the kinetically stable self-assembly process through a continuous π - π stacking in MIPAs was attributed to the steric demand of the polyrotaxane system with the inter-convertible intermolecular orthogonal H-bonded interactions, strong anion- π , and hydrophobic interactions along with high energy unfolding of more individual MIPA units.

Orthogonal H-bonded interactions were further probed by the IR spectroscopy for rotaxane monomer **2-b** and complex **2-b-TFA**, where the vivid and strong H-bonded interactions could be visualized from **Figure 3. 9** with amide band at 3346 cm^{-1} . The IR spectrum of **2-b-TFA** presented a newly originated medium band at 2620 cm^{-1} with an amide strong band at 3331 cm^{-1} . Moreover, the band at 1915 cm^{-1} corresponding to pyridine carboxylic acid type H-bonding band was shifted marginally to 1924 cm^{-1} . The shift in the amide band along with a new band lucidly

suggested a strong H-bonded interaction between **2-b** and TFA. We reasoned that the new band at 2620 cm^{-1} was instigated owing to the H-bonded interactions of pyridinium-trifluorocarboxylate anion.

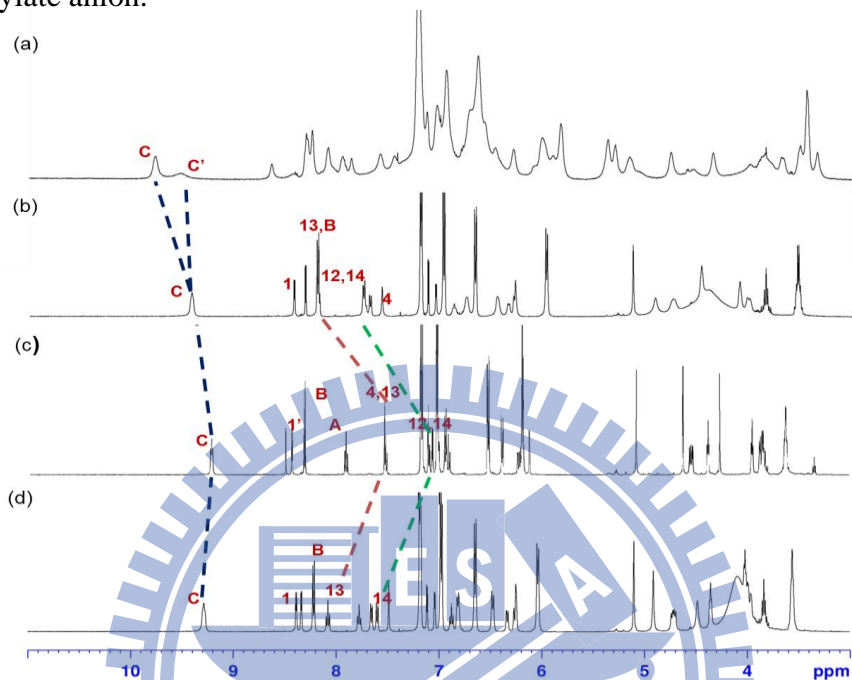


Figure 3. 8. VT-NMR (500 MHz, CDCl_3) Stock plot of monomer **2-b** in the presence of TFA; (a) **2-b** + TFA (1.0 equiv), 233 K. (b) **2-b** + TFA (1.0 equiv), 298 K. (c) free **2-b**, 298 K. (d) **2-b** + TFA (1.0 equiv), 323 K. The assignments correspond to the lettering shown in Scheme 1.

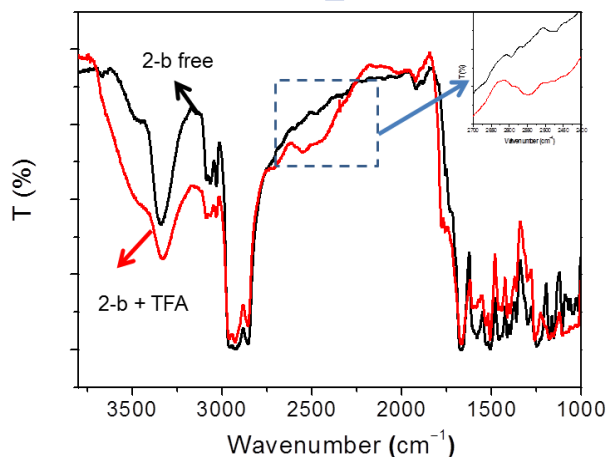


Figure 3. 9. IR-chromatographs of monomer **2-b** (marked black) and complex **2-b-TFA** (marked red). Inset picture is showing a noticeable new band for complex **2-b-TFA** indicating strong H-bonded interactions.

3. 3. 3 Optical and Electrochemical Measurements:

The photophysical properties of MIPAs were ideally measured to realize future optoelectronic devices and the absorption spectra in the UV-vis to NIR regions of these polymers in solution and solid films are shown **Figures 3. 10a** and **3. 10b**, respectively. Interestingly, the polymers with rotaxane and dumbbell units (i.e., **P3**, **P2**, and **P1**) presented two bands, which illustrated one peak in the UV-vis region and another one in the NIR region in contrast to a single band in simple **P4**. Polymers **P3** and **P4** in solution and solid films showed the absorption maximum values at 642,725(solution)/664,746(solid) nm and 622(solution)/643(solid) nm. An obvious red shift (20 nm) from solution to films for **P3** and **P4** were observed; however, both shifts from solution to films in **P1** and **P2** were trivial. This typical behavior of polymers in the film case could be ascribed to a proliferation in the effective conjugation length due to a better coplanar geometry of both polymer backbones in the solid state. On the other hand, in contrast to simple **P4**, the prominent absorption band in the NIR region for rotaxanated polymers demonstrated that the pendant dumbbell and [2]rotaxane units enabled effective molecular packing and intramolecular charge transfer interactions, and thus to lead to extended conjugations in these MIPAs.

Encouraged by the excellent photophysical properties of rotaxanated conjugated polymers, we decided to explore acid-mediated host-guest complexation by UV-vis and PL titrations as shown in **Figure 3. 11a**. The two absorption maxima values at 525 and 554 nm of **2-b** (10 μ M) became a single broad absorption with an incremental trend, simultaneously the emission intensity at 580

nm of **2-b** was gradually decreased (**Figure 3. 11b**) during the titration with TFA (0-10 equiv) in dichloromethane. Additionally, it can be confirmed by a perceptible naked eye and fluorescence color changes as illustrated in the insets of **Figures 3. 11a** and **3. 11b**.

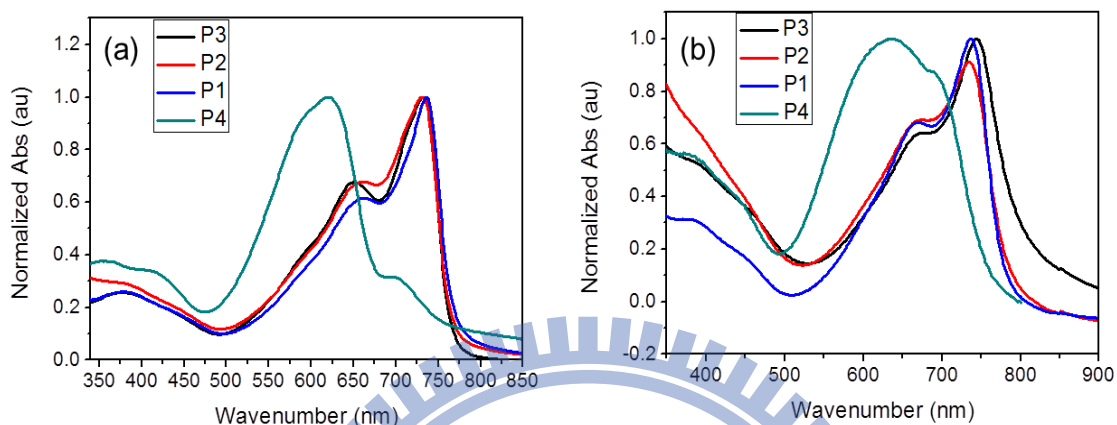


Figure 3. 10. UV-vis to NIR absorption spectra of polymers **P1**, **P2**, **P3**, and **P4** (a) in chloroform solution; (b) films on quartz plates.

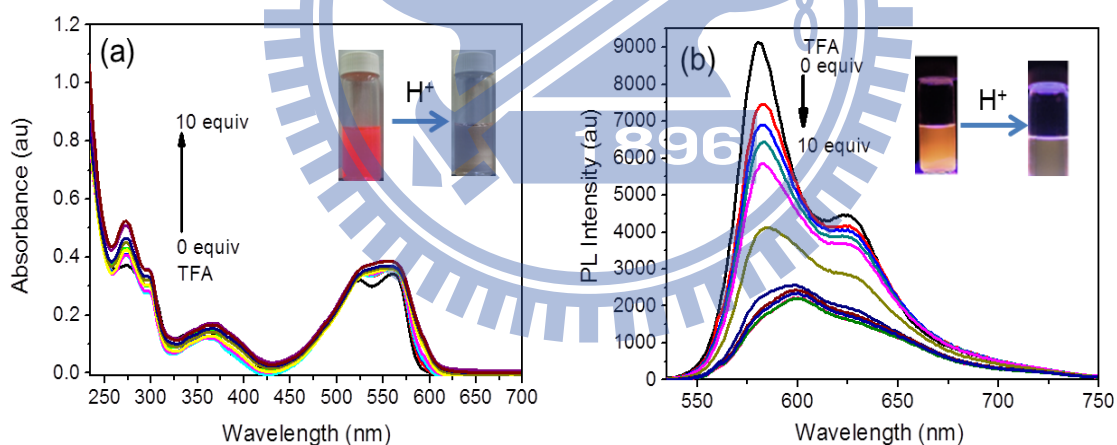


Figure 3. 11. (a) and (b) UV-vis and fluorescence spectral changes of **2-b** ($10 \mu\text{M}$ in DCM) upon the addition of TFA in DCM (0 - 10 equiv), respectively. Insets: pictures in (a) and (b) indicate naked eye color changes as well as fluorescence changes under UV light (365 nm) upon the addition of TFA, respectively ($\lambda_{\text{ex}} = 525 \text{ nm}$).

These observations were attributed to a deprotonation of TFA by **2-b** (pyridine site) and in situ formation of a strong H-bonded complex between the resulting trifluorocarboxylate anion, 2-6-biscrabaxyamidopyridine, and pyridinium part of dumbbell. Unlike the monomer case, polyrotaxane **P3** (10 μM) provided exclusively different absorption patterns during the titration with TFA (0-8 equiv) in THF, the absorption bands of polyrotaxane **P3** at 642 and 725 nm gradually decreased in their intensities as displayed in **Figure 3. 12a**. Similarly, the fluorescence emission maxima at 766 nm decreased concurrently as shown in **Figure 3. 12b**. During the titration with TFA, the absorption peak at 642 nm was completely vanished while 8 equiv of TFA was added in **P3**. As a result, a noticeable naked eye color change was observed as presented in the inset of **Figure 3. 12a**.

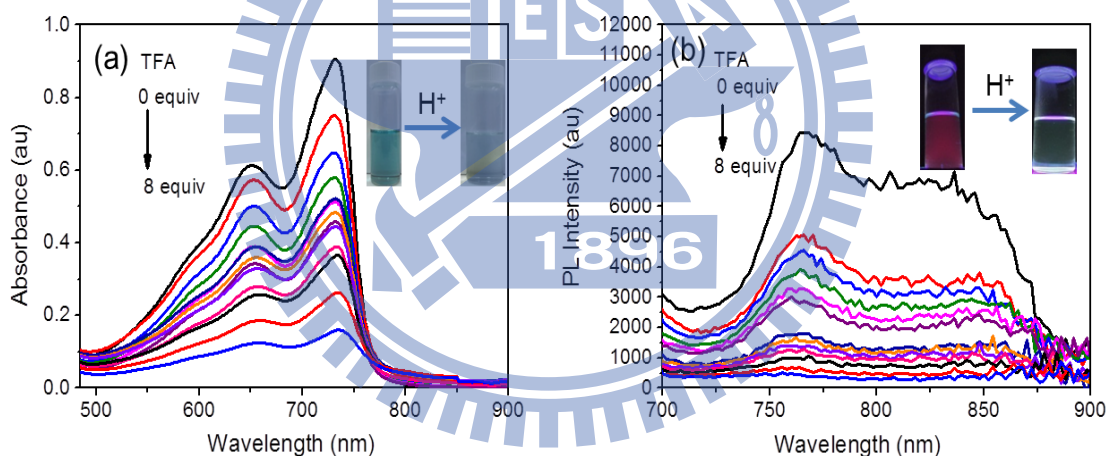


Figure 3. 12. (a) and (b) UV-vis and fluorescence spectral changes of **P3** (10 μM in THF) upon the addition of TFA in THF (0 - 8 equiv), respectively. Insets: pictures in (a) and (b) indicate naked eye color changes as well as fluorescence changes under UV light (365 nm) upon the addition of TFA, respectively ($\lambda_{\text{ex}}=720$ nm).

The binding constants of **2-b** and **P3** with TFA were calculated to be *ca.* $9.9 \times 10^3 \text{ M}^{-1}$ and $1.22 \times 10^5 \text{ M}^{-1}$, respectively, as shown in **Figures 3. 13a** and **3. 13b**. Compared with monomer **2-b**, the

drastically improved binding constant of polyrotaxane **P3** clearly indicated an enhanced interaction of acid with polymer has more binding sites to augment the supramolecular electronic energy transfer between the polymer backbone and binding cavity.^{78,109} Moreover, to fortify the selectivity of the orthogonal H-bonded cavity in **2-b** and **P3**, control experiments were conducted on other monomers and polymers. However, their responses were trivial under similar conditions (see **Figures 3. 14a-3. 14d**).

Delightfully, the complexation of TFA with the orthogonal H-bonded unit in **2-b** and **P3** was completely reversible upon adding the excess of base DBU. The on-off-on fluorescence etiquette for both **2-b** and **P3** was successfully achieved via an alternate addition of acid and base up to four cycles as shown in **Figures 3. 13c-3. 13f**. Hence, the absorption patterns in polyrotaxane **P3** can be assigned to more mobile H-bonded interactions between inter-layered polymer axle pyridinium units and trifluorocarboxylate anion along with anion- π interactions, thus the pendant rotaxane imparting unique photophysical properties to the π -conjugated backbones of MIPAs.

The electrochemical properties of monomers and polymers were evaluated by cyclic voltammetry (CV) measurements. Both polyrotaxane **P3** and monomer **2-b** exhibited the quasi-reversible redox process as shown in **Figures 3. 15a** and **3. 15b**. The energy levels of highest occupied molecular orbital (HOMO) and lowest unoccupied molecular orbital (LUMO) of **P3** were compared with those of its precursor monomer **2-b**. It was found that **P3** possessed a higher HOMO level (-5.19 eV) than **2-b** (-5.35 eV) and a lower LUMO level (-3.45 eV) than **2-b** (-3.17 eV), which suggested a narrower bandgap acquired in polyrotaxane **P3**. These energy level changes for **P3** could be ascribed to the extended conjugation length in the polymer with the addition of electron rich **A1** unit. Detailed optical and electrochemical data are summarized in **Table 3. 1**.

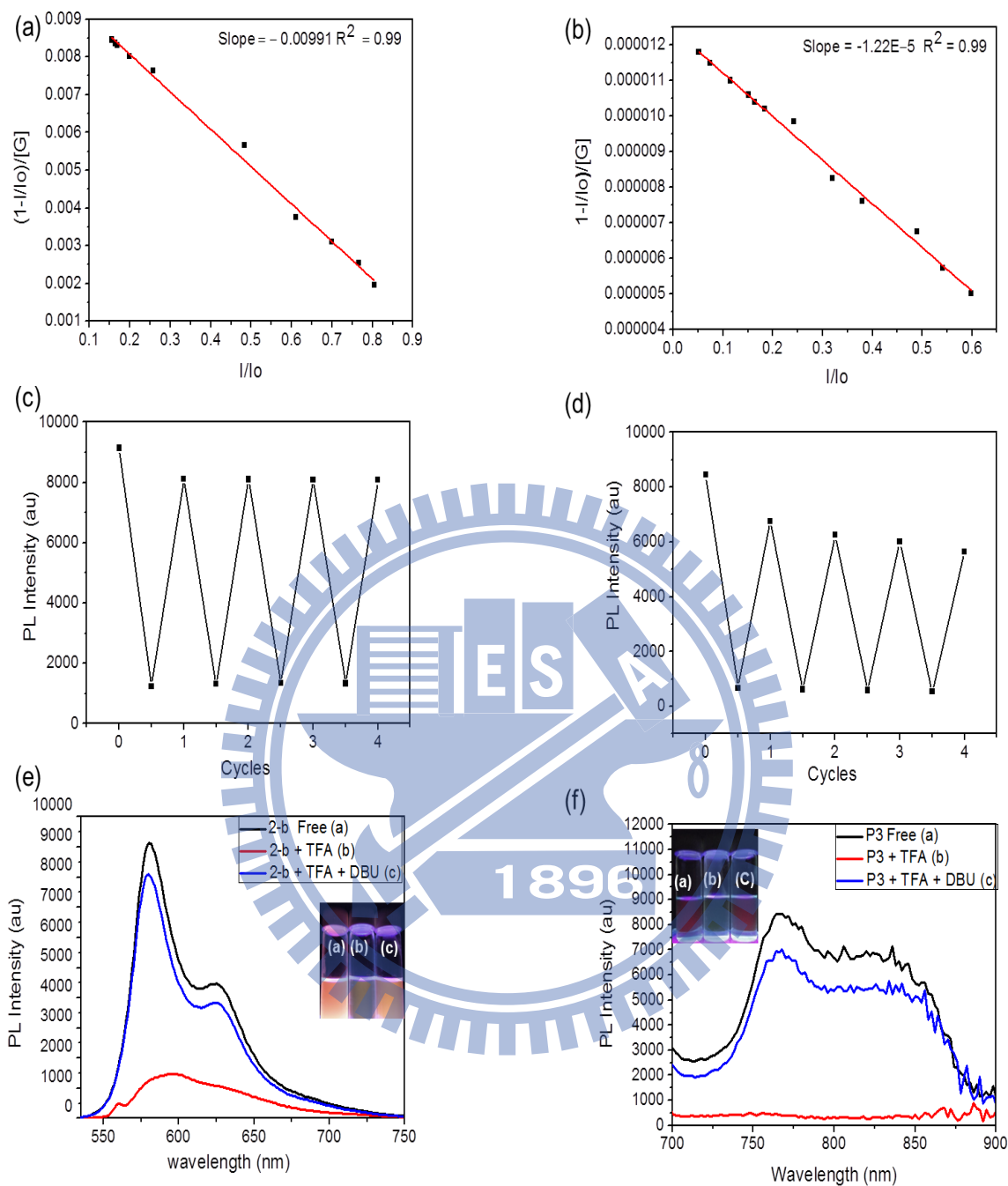


Figure 3.13. (a) and (b) calculation of binding constants for **2-b-TFA** and **P3-TFA** using Connors method,¹⁰⁸ respectively; (b) and (d) fluorescence intensity changes of **2-b** and **P3** (10 μ M, DCM) at 580 and 766 nm under addition of alternate compounds (TFA and DBU) for 4 cycles with ($\lambda_{ex} = 525$ and 720 nm), respectively. (e) and (f) fluorescence changes without acid

(a), with acid (b), and recovered fluorescence by addition of DBU (c) of **2-b** and **P3**, respectively. Insets denoting their respective fluorescence changes under UV light (365 nm).

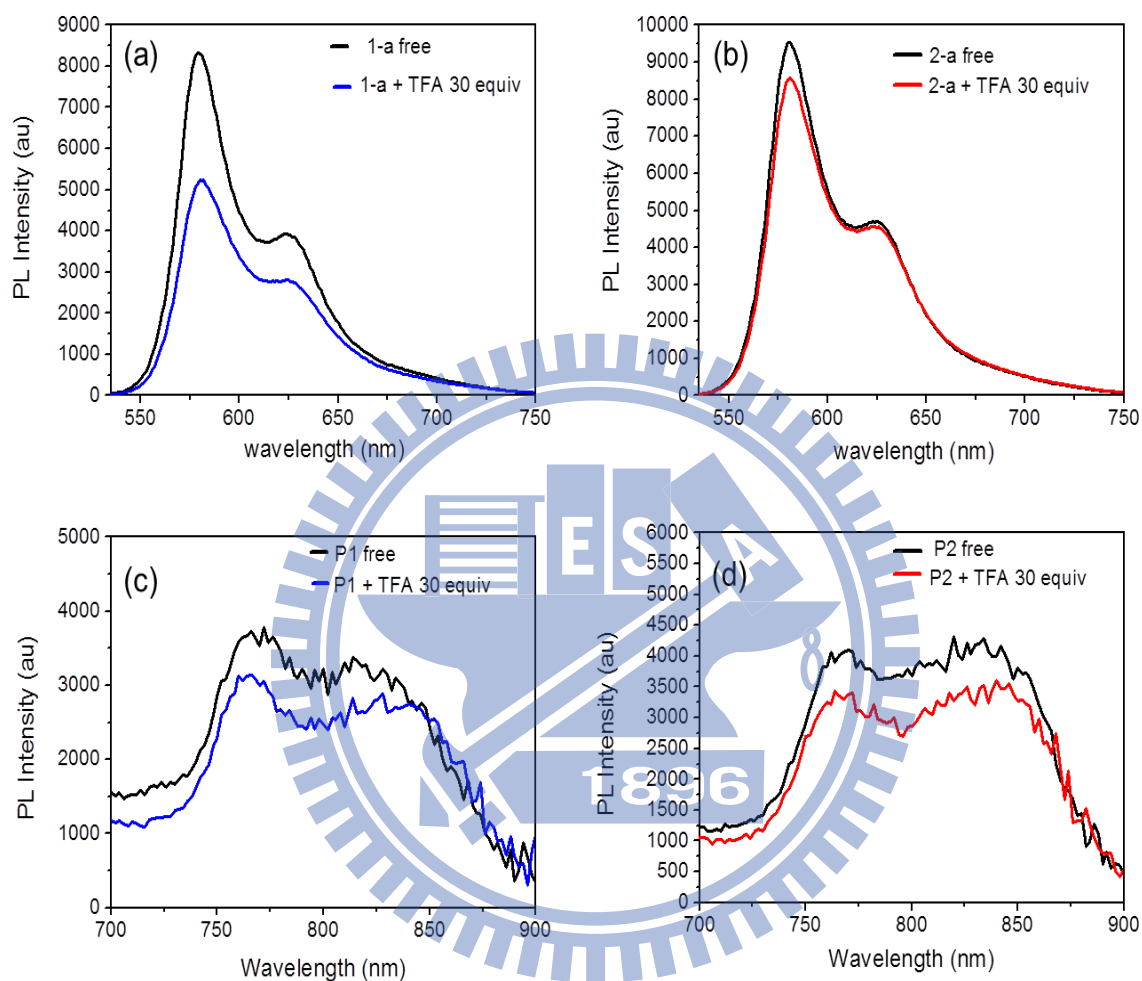


Figure 3. 14. (a) and (b) fluorescence changes of monomers **1-a** and **2-a** ($10 \mu\text{M}$ in DCM) without acid and with the addition of (TFA, 30 equiv), respectively. (c) and (d) fluorescence changes of polymers **P1** and **P2** ($10 \mu\text{M}$ in THF) without acid and with the addition of (TFA, 30 equiv), respectively.

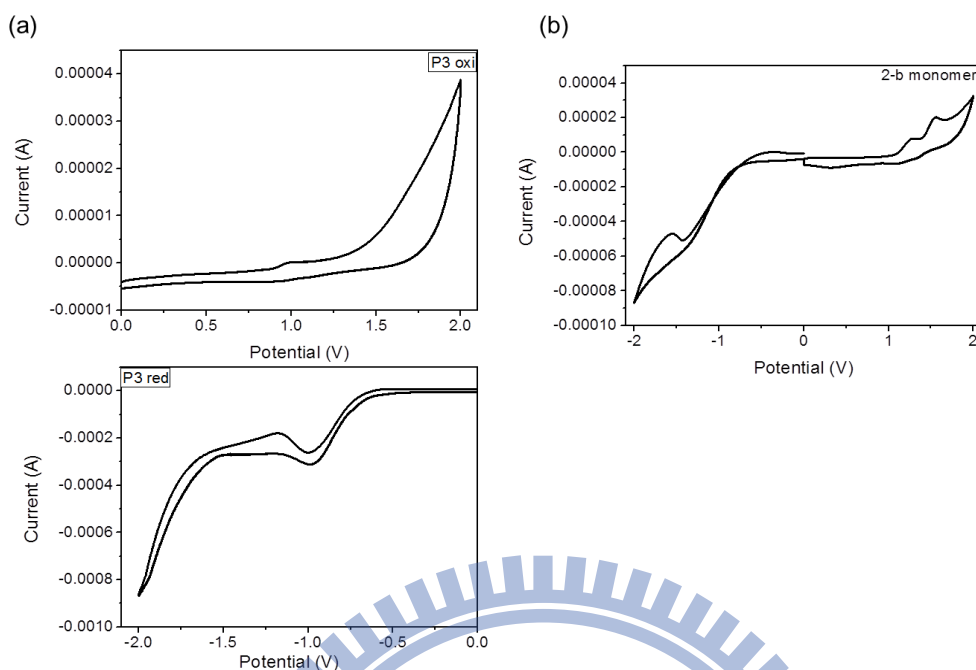


Figure 3. 15. (a) and (b) cyclic voltammograms of **P3** and **2-b** (3 mM) using 0.1M TBAPF₆ supporting electrolyte at a scan rate of 0.1Vs⁻¹ in CHCl₃, respectively. For clarity in Figure (a) both the oxidation and reduction voltammograms were separated.

Table 3. 1. UV-vis to NIR absorption and electrochemical data of monomer **2-b** and polymers **P1**, **P2**, **P3**, and **P4**, respectively.

Compound	$\lambda_{\text{ons}}^{\text{a}}$ nm	$\lambda_{\text{max,abs}}$ nm (solution)	$\lambda_{\text{max,abs}}$ nm (film)	$E_{\text{HOMO}}^{\text{HOMO}}$ eV	$E_{\text{LUMO}}^{\text{LUMO}}$ eV	$E_{\text{g}}^{\text{ece}}$ eV	$E_{\text{g}}^{\text{opt}}$ eV
2-b	602	525/554	534/566	-5.35 ^c	-3.17	2.18 ^d	2.06 ^b
P1	772	656/735	662/738	-5.30	-3.37	1.93	1.60
P2	778	658/728	664/733	-5.28	-3.43	1.85	1.59
P3	805	642/725	664/746	-5.19	-3.45	1.74	1.54
P4	740	622	643	-5.25	-3.41	1.84	1.68

^a optical edge onset value of absorption spectrum in long wavelength direction. ^b optical band gap $E_{\text{g}}^{\text{opt}} = 1240/\lambda_{\text{ons}}$. ^c $E_{\text{HOMO}} = [-(E_{\text{oxionset}} - 0.45) - 4.8]$ eV. ^d electrochemical band gap. $E_{\text{onset(FC/FC+ vs. Ag/Ag+)}} = 0.45$ eV

3. 3. 4 Theoretical Calculations:

To corroborate the experimental observation of the polymers and to provide a better insight into fundamental orthogonal H-bonded cavity and TFA binding interaction with a subtle change of macromolecular architecture, theoretical calculations were carried out as described above. For the sake of dealing with the H-bonded interactions in polyrotaxane **P3**, its precursor monomer **2-b** was used in this study by replacing the 2-ethylhexyl unit with a methyl group. PM3 optimized energy minimized geometry of **2-b** ([2] rotaxane monomer) is given in **Figure 3. 16a**, illustrating that the macrocycle in free **2-b** monomer was tilted with an angle of 26° to avoid inter component pyridyl lone pair interactions with an unsymmetrical inter-component hydrogen-bonded distances of 2.8 Å and 3.2 Å in a twisted chair-conformation. However, when TFA was added to **2-b**, the cycle displaced from central pyridine station relative to the free **2-b** as shown in **Figure 3. 16b** with a tilt angle of 45° .

A further Mulliken charge analysis clearly revealed that the axle pyridine deprotonated the TFA (axle pyridinium NH^+ N(1) = 0.43 e , H = 0.2 e , O(2) = -0.45 e , and O(1) = -0.64 e , where e is the magnitude of the charge on an electron), forming a strong inter-component hydrogen-bonded complex **2-b-TFA** with the resulting trifluorocarboxylate with distances of N1-H---O1 = 1.67 Å, N2-H---O2 = 2.56 Å, and N3-H---O2 = 2.77 Å, respectively. The evolution of molecular orbital delocalization for the HOMO and LUMO orbital density states in **2-b** showed that in both these density states electron delocalization is mainly residing on the diketopyrrolopyrrole units in the free **2-b** as shown in **Figures 3. 17a** and **3. 17b**. We envisioned that the addition of TFA might change the electronic distribution such that the HOMO corresponded to the diketopyrrolopyrrole part and the LUMO corresponded to the **TFA-2-b** interaction site. Indeed, we found this to be the case as shown in **Figures 3. 17c** and **3. 17d**. These two prevailing theoretical observations

were consistent with our above ^1H NMR and optical measurements as well as the previous report.¹³⁶

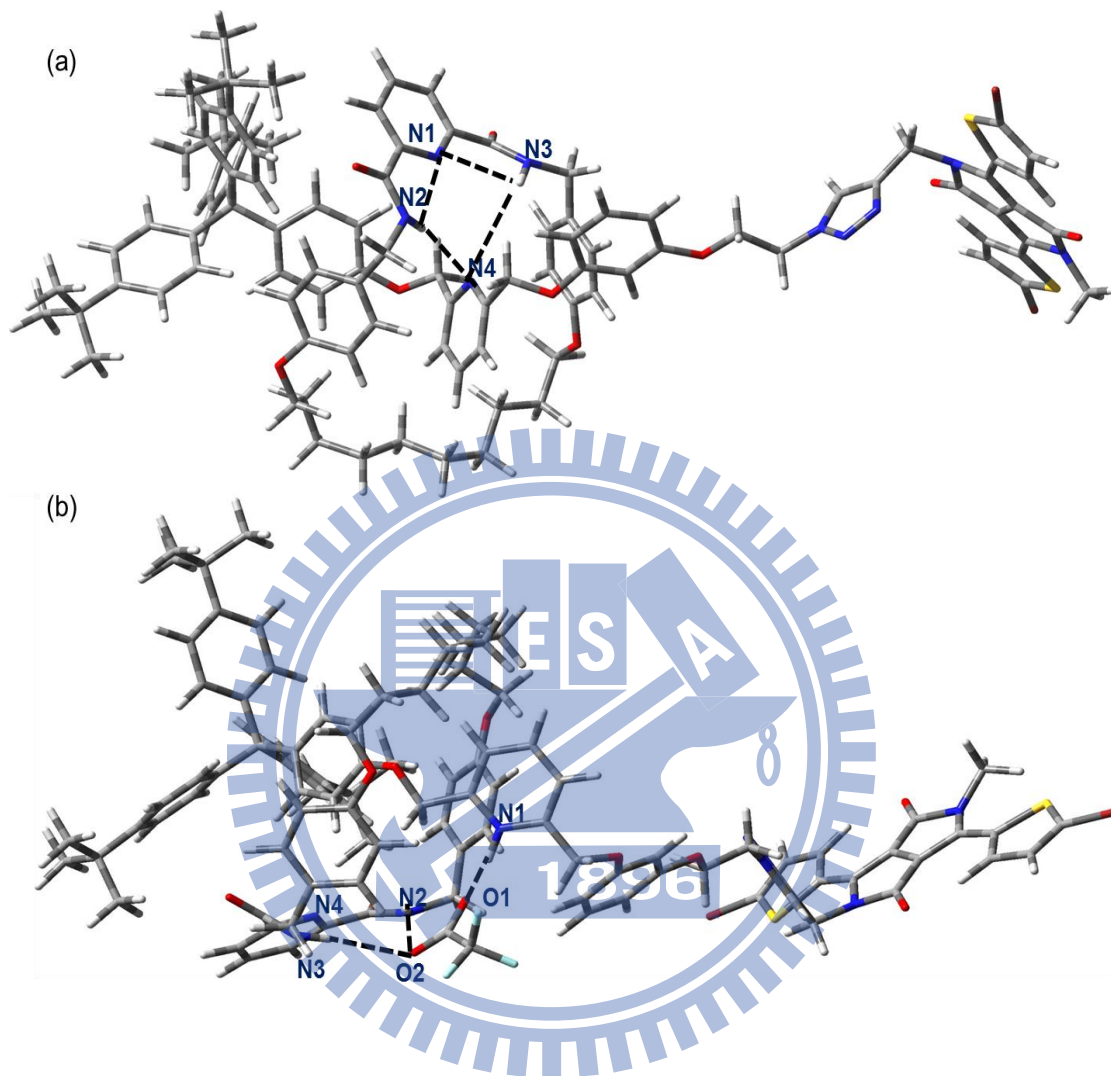


Figure 3. 16. (a) and (b) PM3 optimized chemical structures of monomer **2-b** and complex **2-b-TFA**, respectively. Selected H-bonded lengths [\AA] for **2-b**: N4---N3-H= 3.42 \AA ; N4---N2-H= 2.88 \AA ; N1---N2-H= 2.52 \AA ; N1---N3-H= 2.65 \AA ; for complex **2-b-TFA**: N1-H---O1= 1.67 \AA ; N2-H---O2= 2.56 \AA ; N3-H---O2= 2.77 \AA .

To provide the further clue about the origin of extended conjugations in these polymers, we employed the DFT and TD-DFT calculations. The predicted absorption wavelengths ($\lambda_{\text{abs, cal}}$), oscillator strengths (f), and the configuration description of the lowest two singlet excited states

are shown in Table 1. To establish the role of individual units on the effective π -conjugations in these polymers, we optimized the simple **A1** and **D1** units first, the energy minimized planar structures and the electronic delocalizations of the frontier molecular orbitals (FMOs) for **A1** and **D1** can be visualized in **Figures 3. 18** and **3. 19**, respectively.

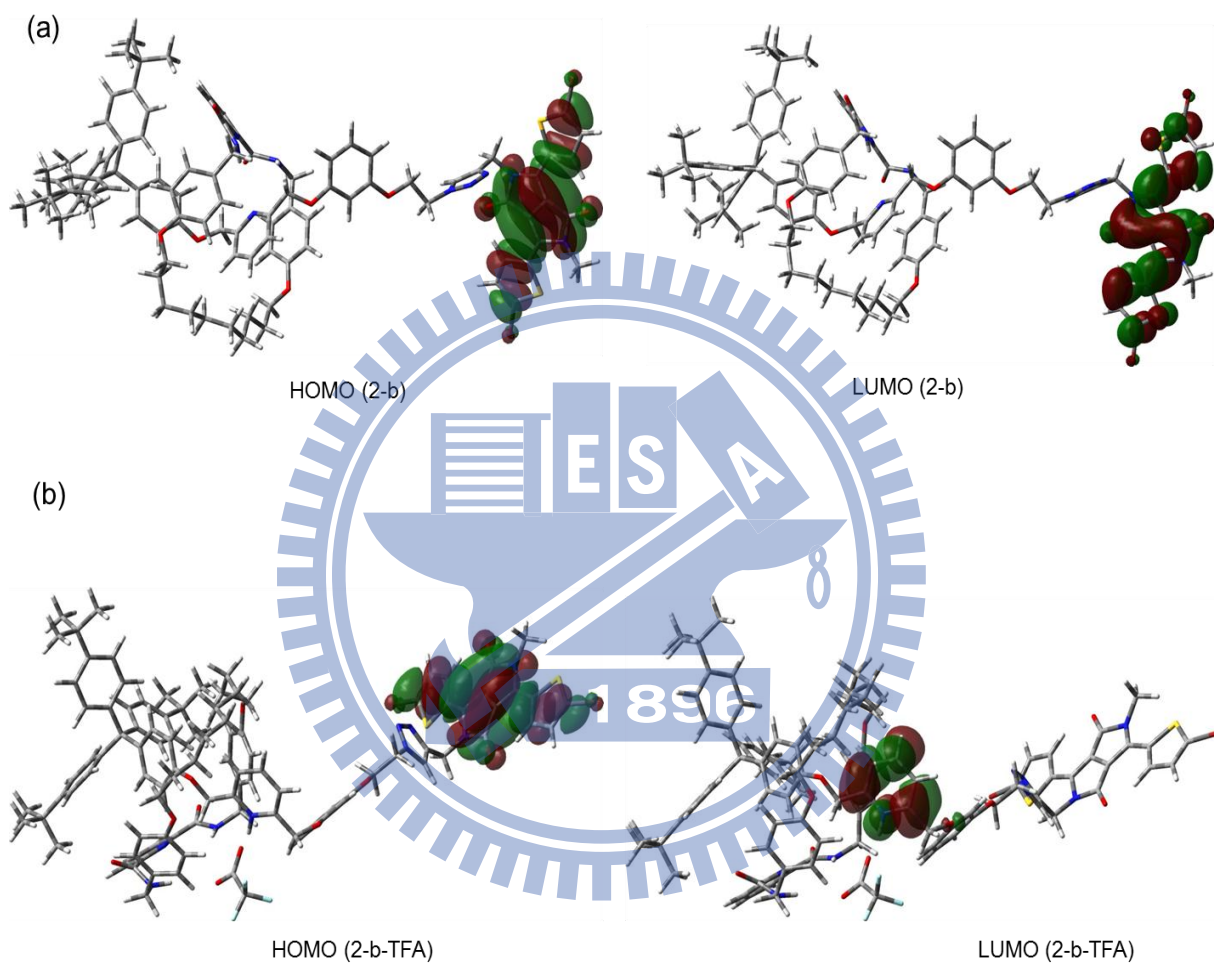


Figure 3. 17. (a) and (b) PM3 optimized chemical structures of monomer **2-b** and complex **2-b-TFA**, and the molecular orbital distribution plots of their HOMO and LUMO states, respectively in the ground state.

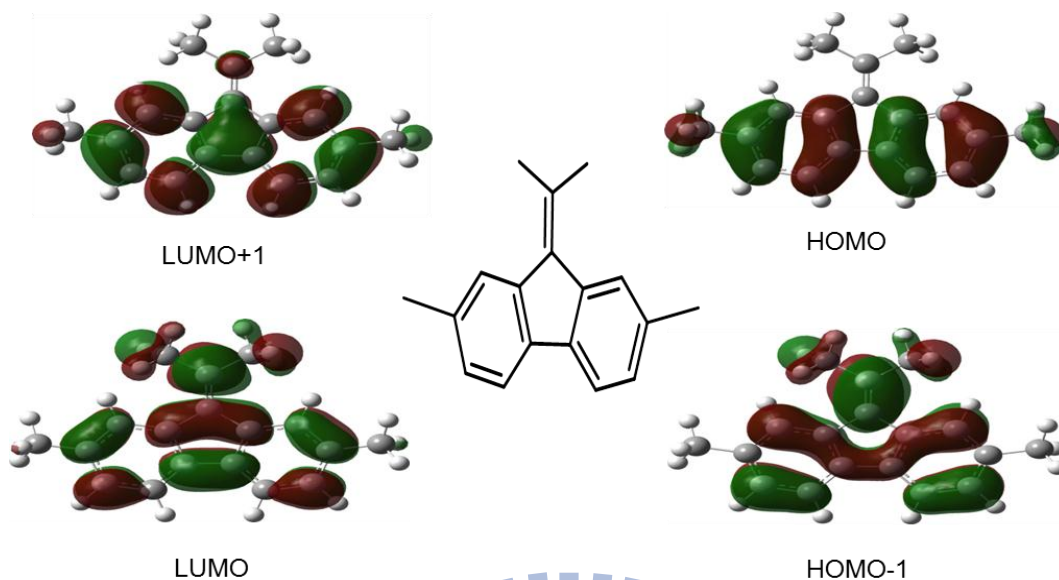


Figure 3. 18. TD-DFT optimized stable chemical structures of monomer A1. Molecular orbital distribution plots of the HOMO and LUMO states, respectively, in the ground state and their corresponding HOMO-1 and LUMO+1 plots in the excited state.

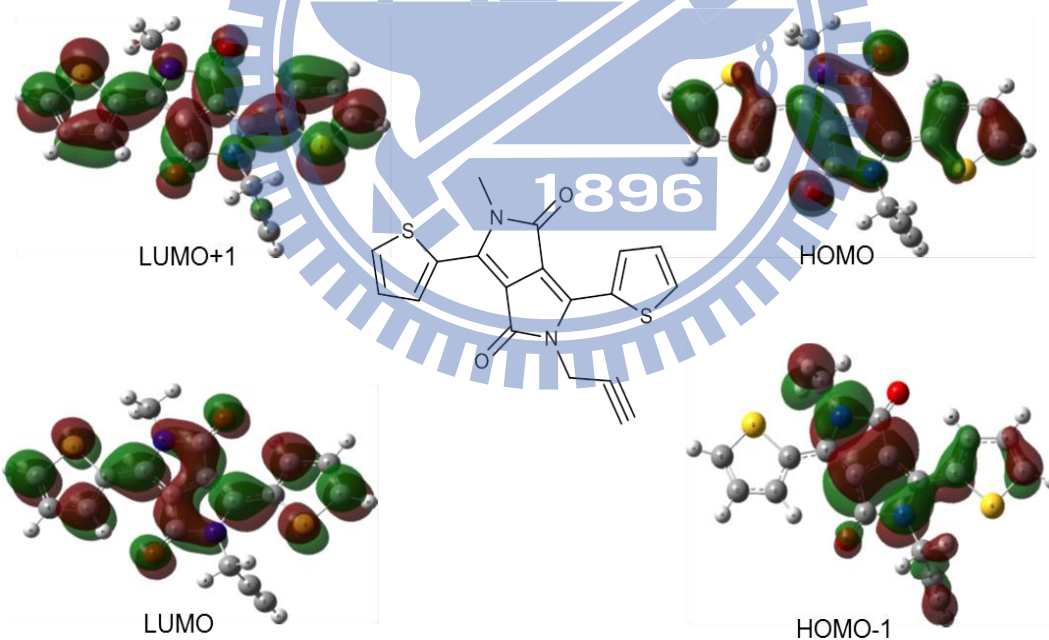


Figure 3. 19. TD-DFT optimized stable chemical structures of monomer D1. Molecular orbital distribution plots of the HOMO and LUMO states, respectively, in the ground state and their corresponding HOMO-1 and LUMO+1 plots in the excited state.

For both **A1** and **D1** units, their lowest energy singlet transitions are mainly from HOMO to LUMO. However, in the next excited state, we noticed a major highest energy singlet transition in **D1** from HOMO to LUMO+1 and in the **A1** from HOMO-1 to LUMO as well as HOMO-1 to LUMO+1. For both units FMOs were delocalized over the entire molecule. To substantiate the above observations and the trend, we carried out the TD-DFT calculations. We noticed a remarkable incremental shift in the oscillator strength (f) of **A1** from the ground state to the next excited state (0.016 to 0.142), whereas the f of **D1** was noted to decrease from 0.431 to 0.001 as shown in **Table 3. 2**.

These observations suggested that both molecules possessed a strong π -character and gave a clue that the assembly of these two units could enable better intramolecular charge transfer transitions. Taking this vivid theoretical clue, we further connected the triazole substituted asymmetric diketopyrrolopyrrole and **A1** units to afford the **D2** unit (via the Suzuki coupling strategy) as well as to model the ground and excited states to investigate the consequential electronic properties of these polymers.

The optimized coplanar conformation of **D2** and FMO delocalizations of HOMO and LUMO are presented in **Figure 3. 20**. For the **D2**, the two units were almost fully coplanar while the pendant substituted triazole unit demonstrated a model of the dumbbell units presenting a twist angle of 56° against the **D1** unit as shown in **Figure 3. 21**. Moreover, the inserted triazole substitution was coplanar with the **D1** unit, the main chain became distorted between the **D1** and **A1** units with a twist angle of 24° . The analysis of FMO energy levels revealed that the major energy transition in the ground state of **D2** was mainly from HOMO to LUMO; however, in the next excited state the major energy transition contribution resulted from HOMO to LUMO+1. Due to the enhanced

main-chain conjugation length by the connection of the **D1** and **A1** units in **D2**, the HOMO energy level raised to ca. 0.29 eV while the LUMO dropped by 0.11 eV.

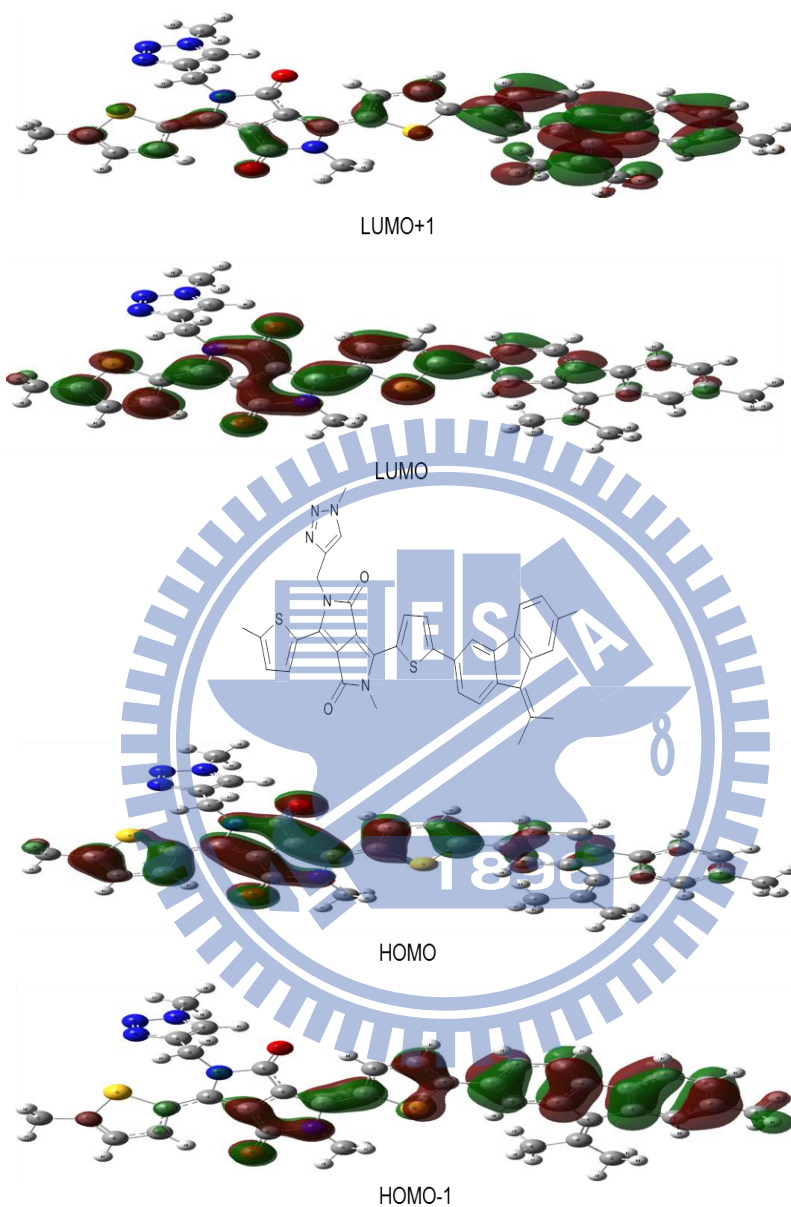


Figure 3. 20. TD-DFT optimized stable chemical structures of monomer **D2** modeled for the polymer in this study. Molecular orbital distribution plots of HOMO and LUMO states in the ground state and their corresponding HOMO-1 and LUMO+1 plots in the excited state.

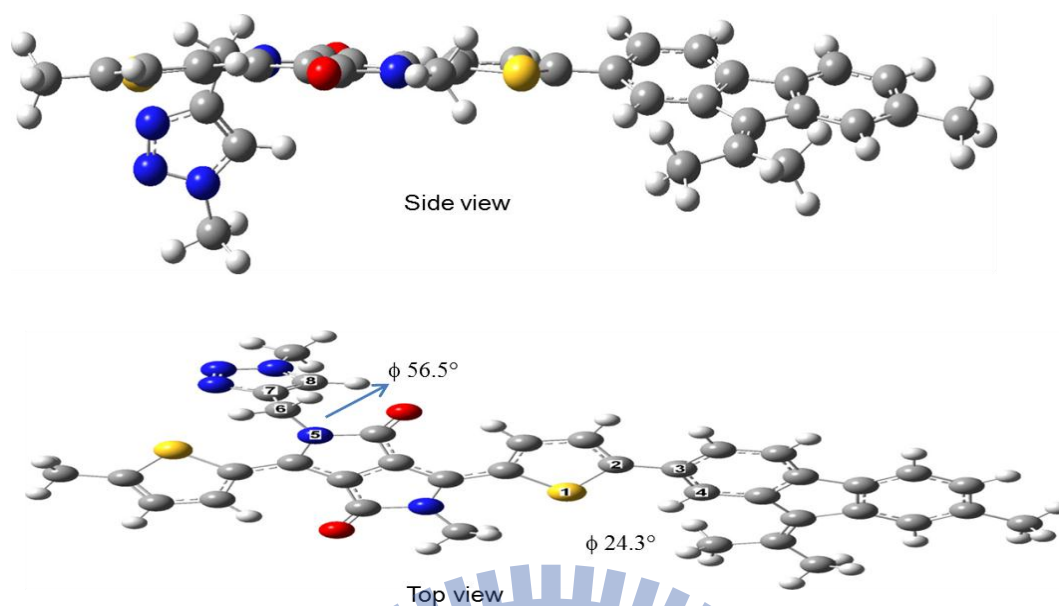


Figure 3. 21. DFT optimized stable chemical structures of monomer **D2** modeled for the polymer in this study and its side and top views, respectively. Dihedral angles between DPP and AKF ($\Phi = 24.3^\circ$) along with main chain triazole units ($\Phi = 56.5^\circ$) are presented in the top view picture of **D2**.

These results strongly indicated that the enriched intramolecular charge transfer transitions facilitated the marginal destabilization of the HOMO and the stabilization of the LUMO, and thus narrowing the band gap for **D2** with red shifts in all of these polymers. Moreover, the NIR absorption band in the case of polyrotaxane **P3** may be ascribed to an effective molecular packing and unperturbed backbone π -conjugation owing to its controlled topological bonding. Based on these theoretical results, we can infer that the introduction of a topological bond in the π -conjugated polymers may expedite the effective backbone conjugation by the enhanced molecular packing which was mainly governed by the orthogonal H-bonding and the π - π stacking interactions offered by the controlled topological cavities.

Table 3. 2. TD-DFT calculated HOMO, LUMO, HOMO-LUMO gap (HLG), wavelength (λ_{\max}), and oscillator strength (f) for **D1**, **D2**, and **A1**.

Compound	HOMO (eV)	LUMO (eV)	HLG ^a (eV)	TD-DFT calculated transition data ^b				
				Excited State	$\lambda_{\text{abs,cal}}$ ^b (nm)	f ^c	Configu- ration ^d	Weight ^e (%)
D1	-5.19	-3.01	2.18	S1	566	0.431	H → L	96
				S2	433	0.001	H-1 → L	38
							H → L+1	48
D2	-4.90	-2.90	2.00	S1	666	0.790	H → L	72
							H → L+1	27
				S2	602	0.373	H → L+1	60
							H → L	22
							H-1 → L	16
A1	-5.53	-1.75	3.78	S1	409	0.016	H → L	97
				S2	330	0.142	H-1 → L	53
							H-1 → L+1	36

^aHOMO, LUMO and HOMO-LUMO Gaps are calculated with the tHCTHhyb/6-31+G(2d,p) method. ^bAbsorption energies are calculated with the TDDFT method at the HCTH147/6-31+G(2d,p) level. ^cOscillator strength. ^dH and L stand for the predicted HOMO and LUMO, respectively. The second highest occupied and lowest unoccupied molecular orbitals denoted as H-1 and L+1, respectively. ^eOnly configurations with 5% or greater contribution are included.

Thermal properties of these polymers were probed by thermogravimetric analysis (TGA). The 5% weight loss temperatures (T_{d5}) of polymers **P4** and **P3** were 320 °C and 344 °C, respectively

as shown in **Figure 3. 22**. The high thermal stability of polyrotaxane **P3** was attributed to its folded nature presumably caused by flexible topological cavities of pendant rotaxane unit in **P3**.

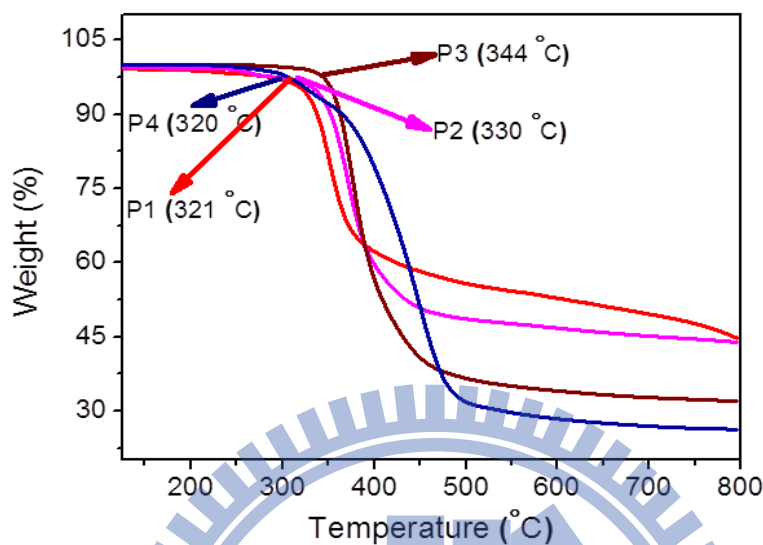


Figure 3. 22. Thermogravimetric (TGA) analyses of polymers **P3**, **P1**, **P2**, and **P4**. 5% weight loss temperature (T_{d5}) of each polymer was denoted.

To understand the effect of the orthogonal H-bonded rotaxane on macromolecular architecture packings and crystalline properties, powdered X-ray diffraction patterns of these polymers were evaluated. The polymer **P4** X-ray diffractogram showed a characteristic reflection at $2\theta = 6.27^\circ$ (d -spacing = 14.08 \AA) referenced to the interlayered distance between polymer chains and $2\theta = 24.81^\circ$ ($d = 3.58 \text{ \AA}$) which denoted the π - π stacking interactions of the polymer units (see **Figure 3. 23**). However, in the case of polyrotaxane **P3**, these reflections were shifted to $2\theta = 9.46^\circ$ (d -spacing = 9.33 \AA) and $2\theta = 18.41^\circ$ (d -spacing = 4.81 \AA), respectively. Moreover, in the case of **P3**, the degree of crystallinity was reduced and eventually enhanced the organic solubility of this polymer in relative to other polymers in this study. Thus, gave a strong evidence that the introduction of a pendant orthogonal H-bonded [2]rotaxane was regulating the π -

conjugated backbone polymer molecular arrangement. This result is consistent with our above theoretical observations as well as the other previous reports.^{114c,14c}

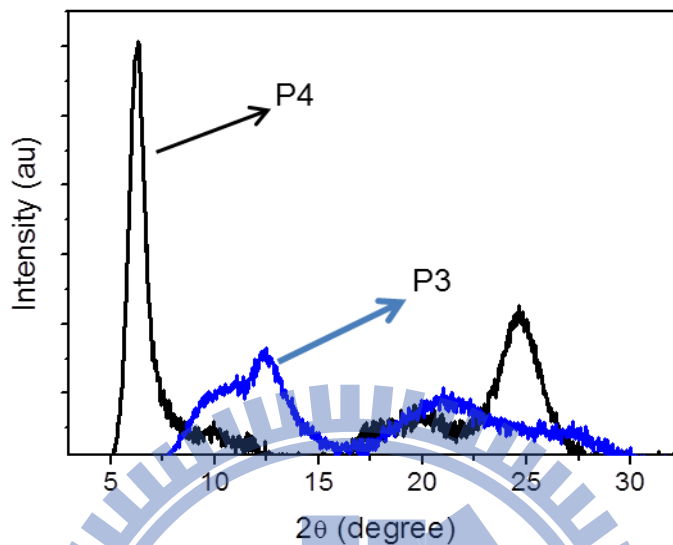


Figure 3. 23. Powder XRD patterns of polymers **P4** and **P3**.

3. 3. 5 Microscopic and DLS Monitoring of Controllable Hierarchical Nano-Self-Assemblies of MIPAs:

Cyclodextrin- and cucurbituril-based molecular self-assemblies of polyrotaxanes were extensively researched.¹³⁷ However, the studies based on pendant orthogonal H-bonded rotaxane copolymers are due owing to their complexities in attaining the well-organized molecular packing at molecular level. We have primarily conducted atomic force microscopy experiments to study the preserved mechanical interlocking nature of polymer **P3** and the effect of the pendant rotaxane unit on the polymer backbone. The optimized dilute solutions (100 μM) of polymers **P2** and **P3** in THF were used to avoid possible inter-chain aggregation behavior as shown in **Figures 3. 24a** and **3. 24c**, respectively. We noticed a change in the morphology from the buddle-like structure with the root mean square roughness (S_q) of 1.7 nm in **P2** to the globule-like structure with $S_q = 0.6$ nm in **P3**. Moreover, the rendered 3D images of both **P2** and

P3 showed the smooth and well aligned surfaces in **Figures 3. 24b** and **3. 24d**, respectively. Cross-sectional analyses of these polymers further confirmed the morphological evolution from the metalated rotaxane polymer to demetalated rotaxane polymer as shown in **Figure 3. 25**. Furthermore, we recorded the AFM images of the simple polymer **P4** and MIPA (**P3**). As shown in **Figure 3. 26a**, **P4** illustrated a higher roughness ($Sq = 16.1$ nm with an average cross sectional height of 35 nm) than **P3** ($Sq = 0.6$ nm with an average cross sectional height of 1.5 nm).

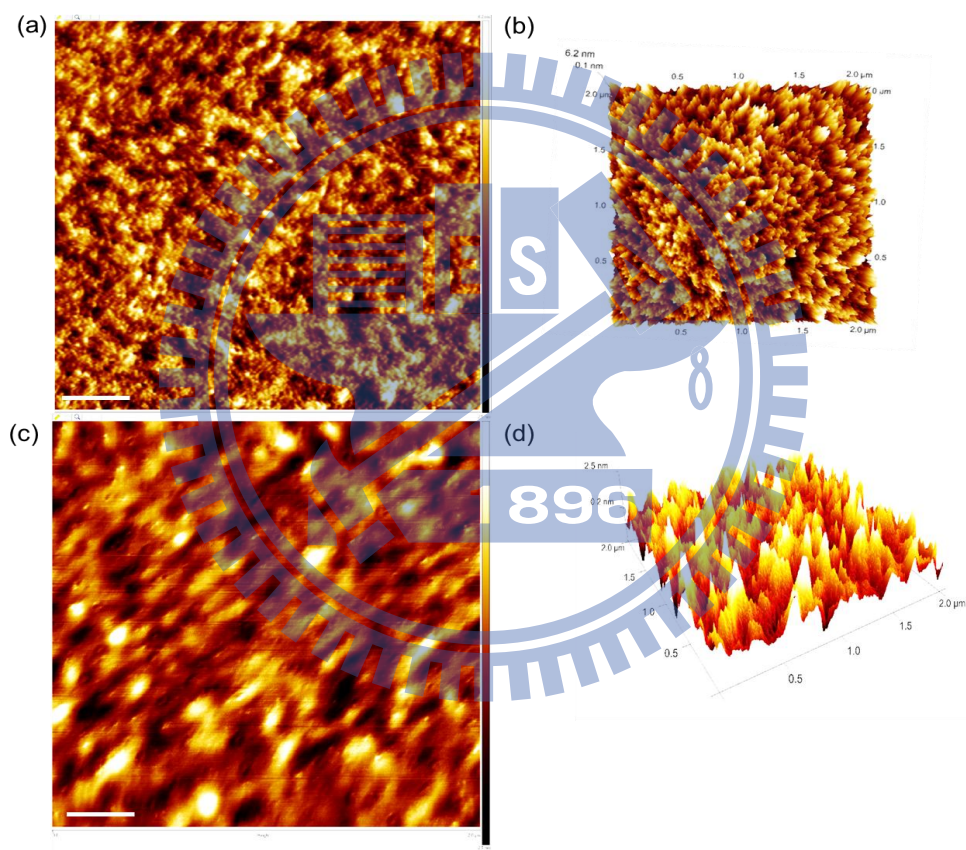


Figure 3. 24 (a) and (c) AFM-images of polymers **P2** and **P3**, respectively. (b) and (d) rendered AFM-3D images of (a) and (b), respectively. Scale bar (a) and (b) = $2 \mu\text{m}$; z-scale (a) = 6.2 nm and (c) = 2.5 nm.

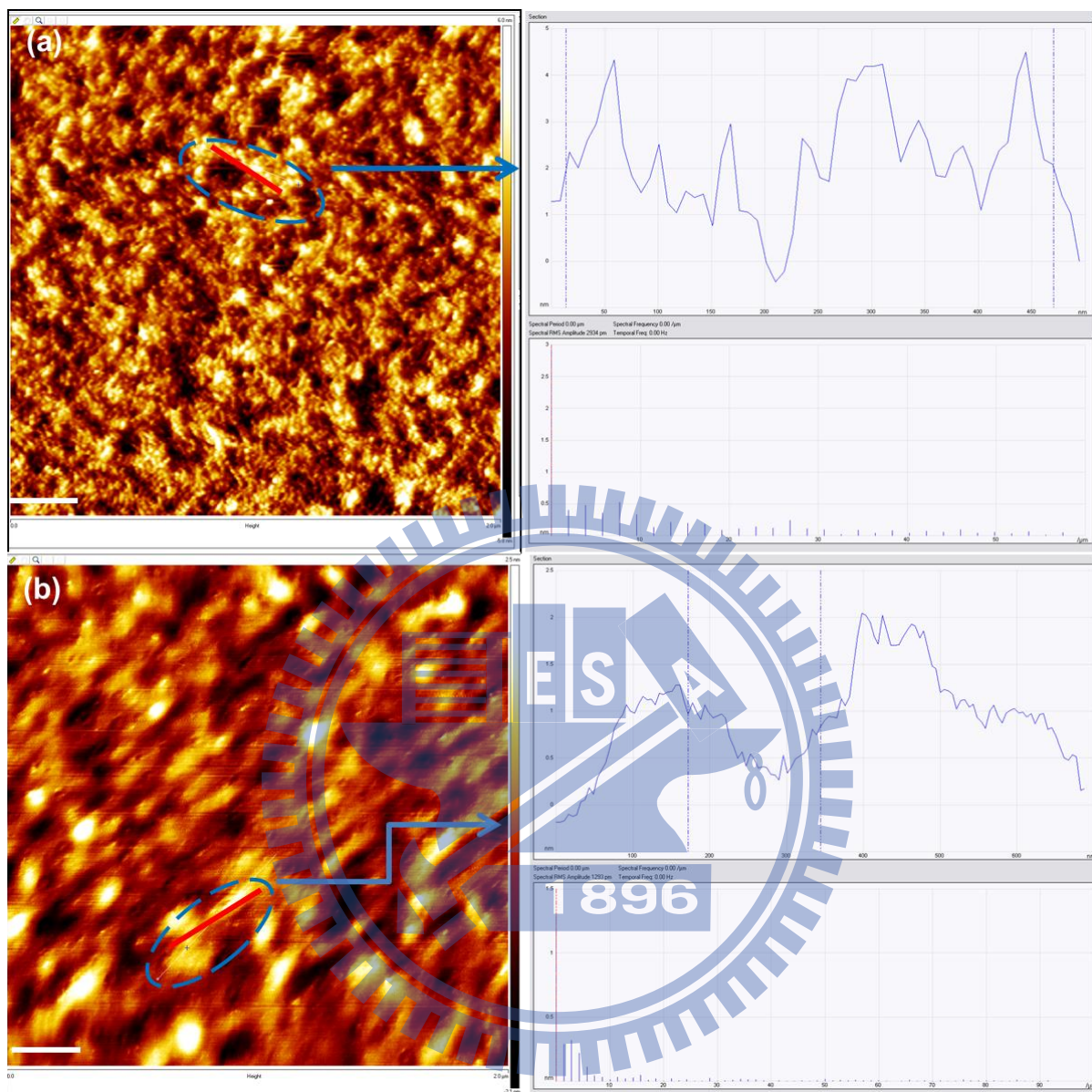


Figure 3. 25. (a) and (b) AFM cross-sectional analysis of polymers **P2** and **P3**. Marked region analyses clearly denoting noticeable changes in their average height from 4.2 nm of **P2** to 1.5 nm of **P3** confirmed the preserved interlocking nature as well as twisted geometry in MIPA. (scale bar = 2 μm ; z-scale (a) = 6.2 nm and (b) = 2.5 nm).

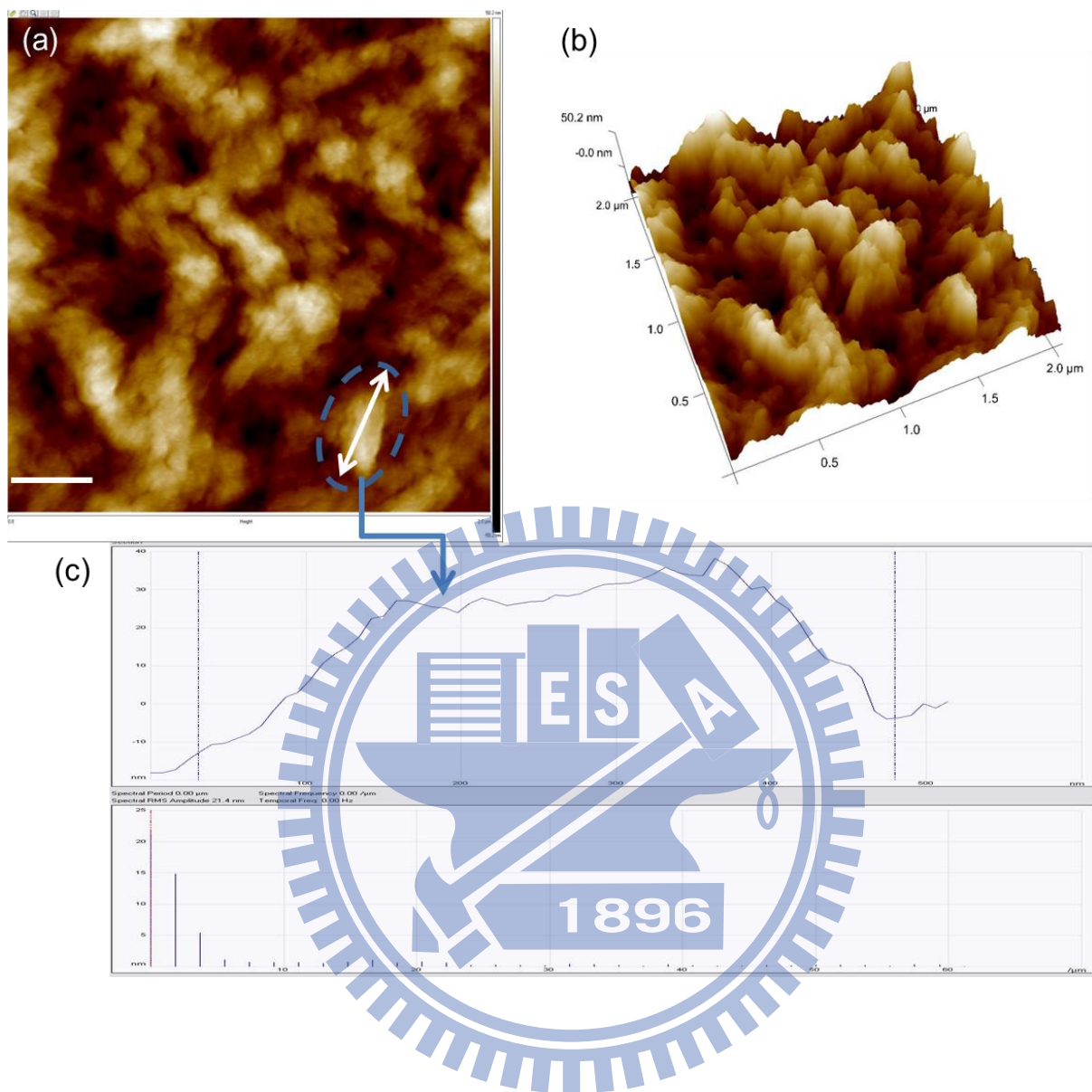


Figure 3. 26 Polymer **P4**. (a) AFM-image,(b) Rendered AFM-3D image, and (c) AFM cross-sectional analysis. The average height of **P4** was about 35 nm, however the average height of **P3** was about 1.5 nm, this distinctive low height of **P3** was plausibly arose from its twisted geometry in compare to **P4** with strong π - π interactions. (Scale bar = 2 μm ; z-scale (a) = 50.2 nm).

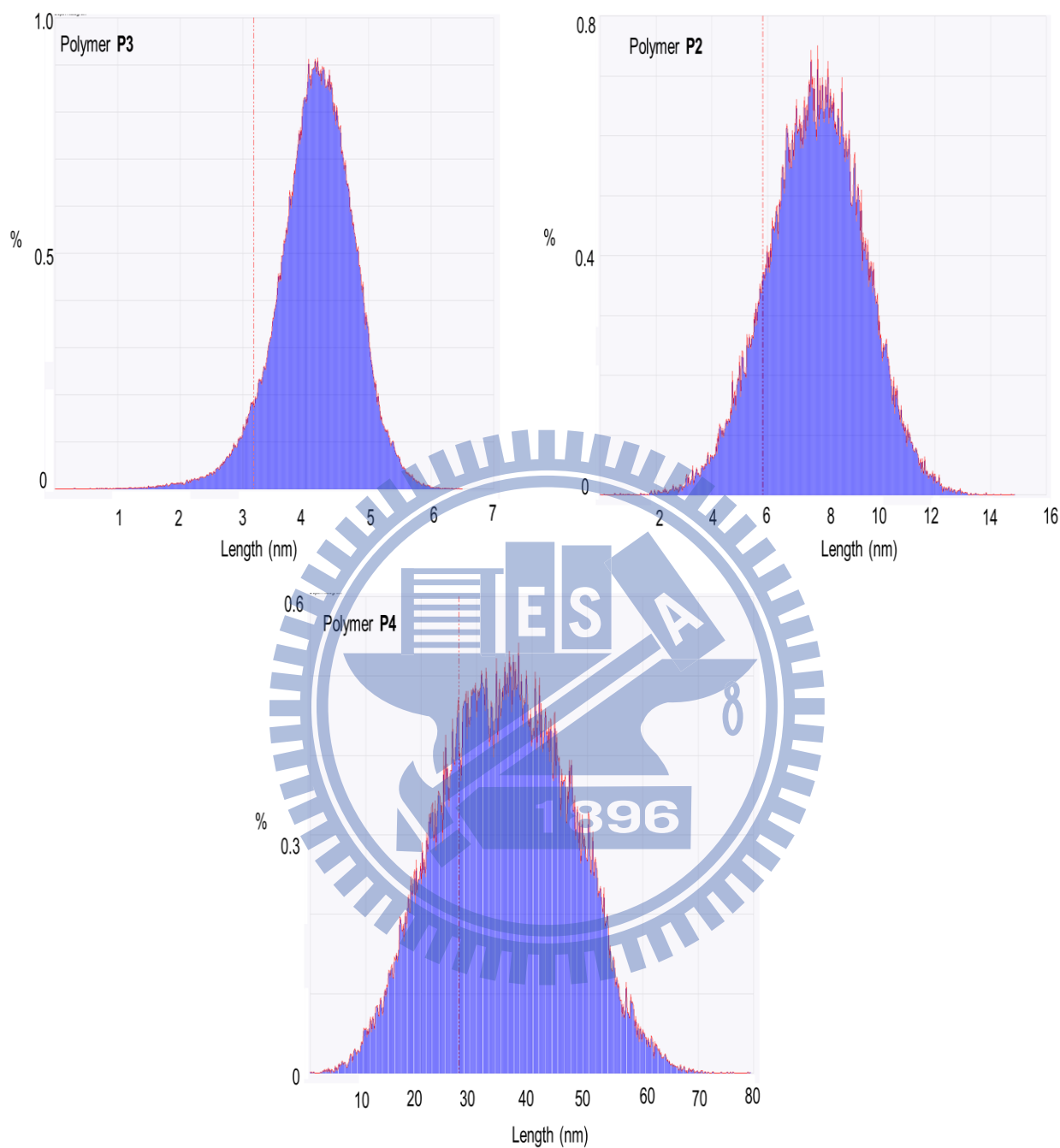


Figure 3. 27. AFM image based depth analyses polymer **P3**, **P2**, and **P4**. Variation in the structural and molecular dimension lengths in these MIPAs denoted that orthogonal H-bonded polymer **P3** could be oriented in folded fashion.

As shown in **Figure 3. 27**, the structural length and depth analyses of polymers showed a smaller average height (4.2 nm) in polymer **P3** in contrast to **P2** (8.3 nm) and **P4** (38 nm). Thus, this result indicated that compared with **P4**, the pendant orthogonal H-bonded unit in polyrotaxane **P3** has an ability not only to form inter-convertible H-bonding with the other units in the polymer but also to affect the self-assembly of the conjugated backbone. More prominently these results indicated that the mechanical bond of **P3** was well preserved during the demetalation and polymerization processes via H-bonding, π - π stackings,¹³⁸ and hydrophobic interactions. Both the finite radius of the probe tip and loading force applied to the sample preserve a stable controlled feedback and eventually control the structural and molecular dimensions of this MIPA.¹³⁹

We are intrigued in exploring the controlled self-assembly structures of MIPAs as well as the pivotal issue of the external stimuli (acid-base) effect in a reversible manner on the self-assembly of polymer **P3**. The SEM images revealed spherical vesicular type particles that appeared to be flattened and bloated due to the sample preparation as displayed in **Figure 3. 28a**. However, protonated form presented a distinctive flacks as well as nano fibers structures and the average size of the nano fibers is estimated to be 460 nm (**Figure 3. 28b**). Moreover, the huge-sized (μm) spherical vesicles could be inevitable owing to its inherent folded globules geometry as well as the process of surface energy minimization^{84,140} during the self-assembly process.

To substantiate such an expedient phenomenon further we devoted to study the effect reversibility of these MIPAs. One could imagine that the protonation of the orthogonal H-bonded unit in **P3** would strongly influence the morphology as suggested by our above VT-NMR, photophysical, and theoretical studies. Delightfully, a drastic change in morphology was indeed observed after protonation of polyrotaxane **P3** by TFA (1 M, 10 equiv) as shown in **Figure 3.**

29b, which formed a flack-like structure as well as nano fiber structures in contrast to its spherical vesicles of free **P3**. Fairly, the reversible molecular switch ability was achieved by treating **P3-TFA** with DBU base as shown in **Figure 2. 29c**, which is almost identical to its spherical vesicles shape as displayed in **Figure 3. 29a**. The acid-base controllable morphological changes were reasonable as the protonation of the axle unit in **P3** by TFA disrupted the self-assembly process due to the electrostatic repulsions. However, to minimize such repulsions, complex **P3-TFA** would reorient themselves in an elongated nucleation growth fashion to present hierarchical stacks with strong π - π stacking interactions.

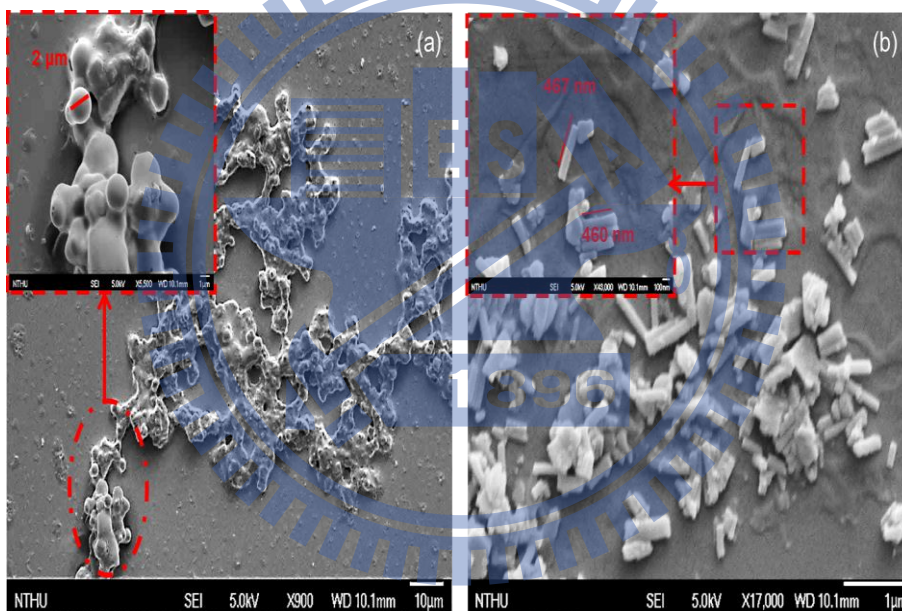


Figure 3. 28. FE-SEM images of polymer **P3** (a) in free state and (b) in protonated state with the addition of TFA (1 M, 10 equiv in THF). Insets: the corresponding enlarged portions of (a) and (b), respectively. (scale bar (a) = 10 μm and (b) = 1 μm, insets: scale bar (a) = 1 μm and (b) = 100 nm).

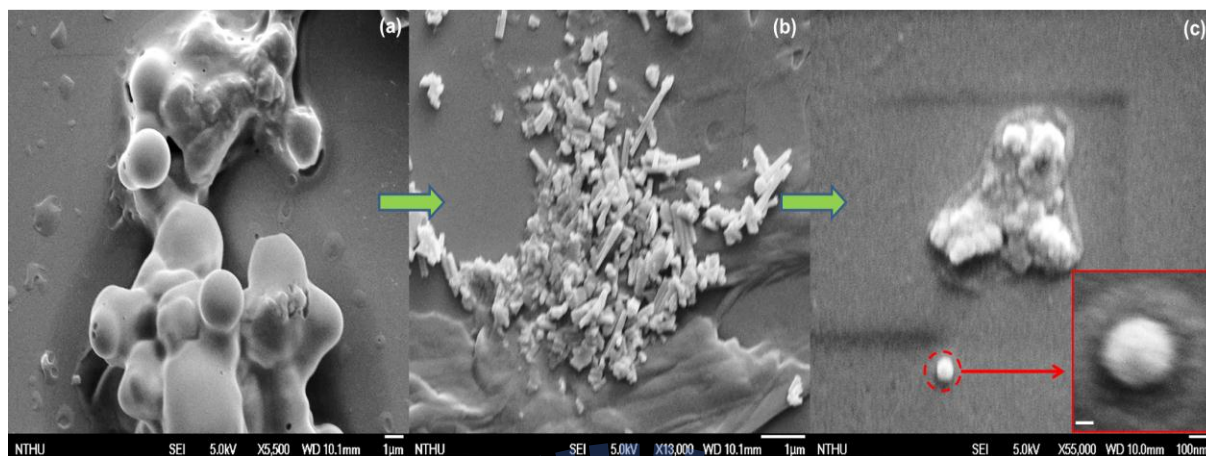


Figure 3. 29. FE-SEM images of polymer **P3**. (a) in free state, (b) in the protonated state with the addition of TFA (1 M, 10 equiv), and (c) in the recovered state by neutralization with DBU. Inset in (c) magnified portion of spherical vesicle. (scale bar (a), (b) = 1 μm , and (c) = 100 nm; inset of (c) = 100 nm).

Superior to SEM, we recorded the TEM images to get rough insights into the sizes and shapes of these hierarchical nano self-assembled structures. The TEM image (**Figure 3. 30a**) of polyrotaxane **P3** showed spherical vesicular type particles comparable to SEM images as we noticed earlier, where the size of vesicular type particle was estimated to be an average size of 120 nm from **Figure 3. 31a**. Exclusively, the TEM image revealed the picture lucidly in the case of protonated **P3** which presented the multi-layered hexagonal-shaped nano-sheets⁸² as shown in **Figure 3. 30b**. We attempted to disclose the sizes and shapes of the individual sheets to understand the assembly mechanism. However, the TEM image depicted that the individual sheets looked to be embedded in to multi-layered hierarchical hexagonal nano-superstructures, where the average size of the nano-sheets was estimated to be 260 nm (with a height of 120 nm, see **Figure 3. 31b**).

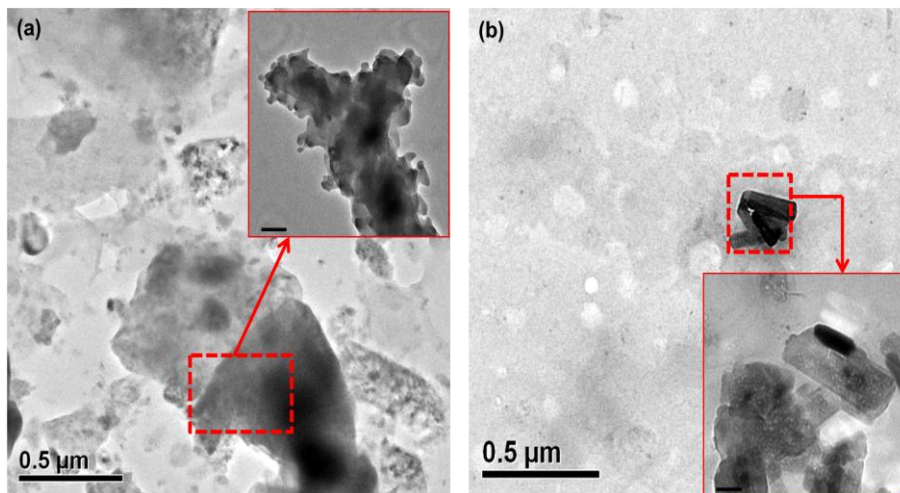


Figure 3. 30. TEM images of polymer **P3** (a) in free state and (b) in protonated state with the addition of TFA (1 M, 10 equiv in THF). Insets: the corresponding enlarged portions of (a) and (b), respectively. (scale bar (a) and (b) = 500 nm, insets: scale bar (a) = 200 nm and (b) = 100 nm).

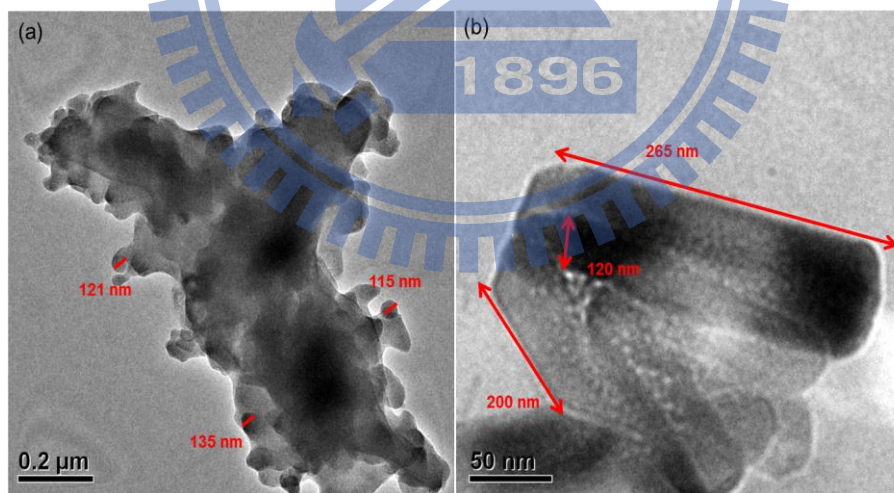


Figure 3. 31. (a) TEM image of polymer **P3** in free form and estimated size of vesicle type particles during its nano self-assembly process. (b) TEM image of **P3** upon the addition of TFA

and its transformation in to hierarchical nano hexagonal sheets and estimated sizes of an individual hexagonal sheet. (Scale bar (a) = 200 nm and (b) = 50 nm).

Both force and electron microscopy images indicated that such a pronounced size of these vesicular and hexagonal sheets seemed to well surface-adhered and flattened upon evaporation of solvents from their cavities.¹⁴¹ Furthermore, we carried out DLS measurements of **P3** in THF solution which revealed an average hydrodynamic diameter of vesicles ca. 140 nm and hexagonal sheets ca. 440 nm in its free and protonated forms, respectively (**Figure 3. 32**). These results are in excellent agreement with the above morphologies of SEM and TEM observations. More importantly, upon adding base to the protonated **P3** it morphed back into the vesicle state (from sheet state) with an average diameter of 150 nm, which showed a marginal difference in the average diameter owing to the precipitated salts during neutralization.

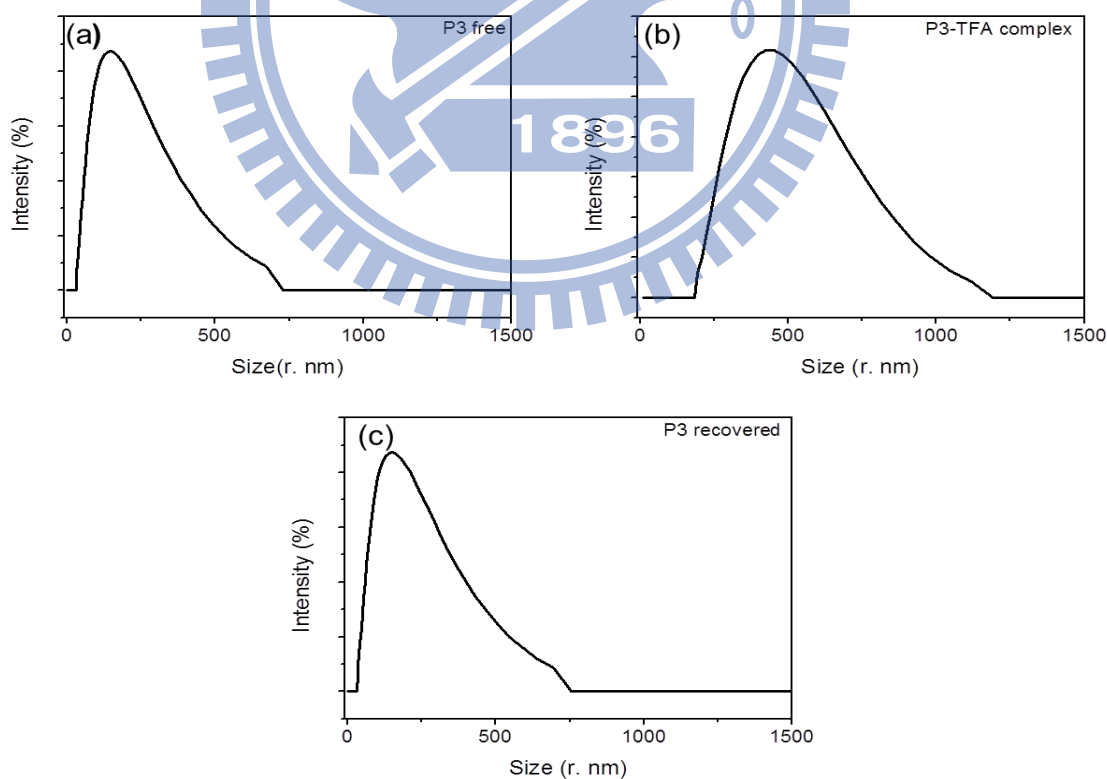


Figure 3. 32. Variation in the hydrodynamic diameter of the polymer **P3**. (100 μM solution in THF) (a) **P3** without TFA. (b) **P3** with the addition of TFA (1 M, 10 equiv). (c) Recovered sample by neutralization with DBU.

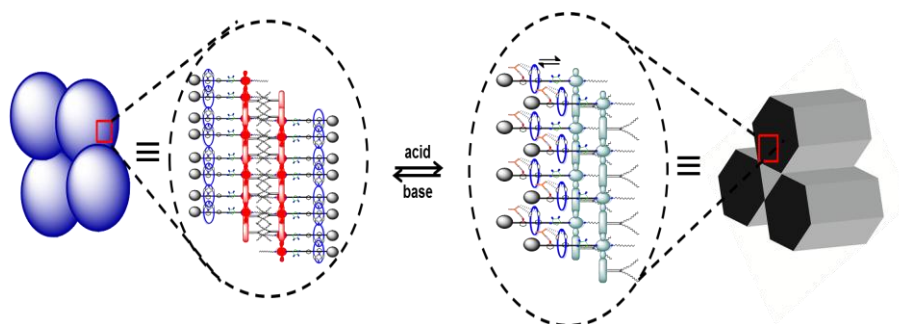


Figure 3. 33. Graphical representation of plausible hierarchical nano-self-assembly process of MIPAs into bilayer vesicles and its acid driven transformation into hexagonal nano-sheets and fibers in a reversible fashion. For legibility of the self-assembly process we denoted simple repeating monomer unit of supramolecular polymer **P3**.

Therefore, based on these concrete evidences we deduced that the pendant orthogonal H-bonded cavity in **P3** adopted folded geometry by virtue of mechanical bond and prone to self-assemble into the bimolecular-layered structure in tail-to-tail fashion, where the rotaxane units were stacked exteriorly via the π - π stacking and larger alkyl chains oriented interiorly owing to their hydrophobic interactions as shown in **Figure 3. 33**. Moreover, upon adding TFA to **P3** it tended to reorganize to minimize the local electrostatic repulsions between protonated axle parts as well as to stack further in layer-by-layer fashion to form hierarchical nano-sheets and fibers with lateral π - π stackings along with an inevitable cooperative interlayered anion- π interactions. Eventually, the orthogonal H-bonds in **P3** not only presented controllable hierarchical nano-self-assembly but also induced a better material processibility relative to the other polymers (**P1**, **P2**, and **P4**).

3. 4. Conclusions

In this study, we have developed a novel polymer with the mechanically interlocked polymeric architecture by polymerization of 9-alkylidene-9*H*-fluorene with a diketopyrrolopyrrole tethered with an orthogonally H-bonded macrocycle unit, which successfully illustrated the effects of orthogonal H-bonded unit on the photophysical properties as well as nano-self-assembly process of the conjugated main-chain polymer (**P3**). It was demonstrated spectroscopically and microscopically that the mechanically interlocked nature of polyrotaxane **P3** was well preserved during the polymerization. Benefited from its unique topological cavities formed in **P3**, it showed enriched material properties, such as extended conjugations, narrow bandgaps, and unique self-assembled structures, in contrast to the other polymers in this study. Remarkably, the fluorescence on-off-on reversible acid-base controllable molecular switch ability in NIR region for the first time has been fruitfully attained by supramolecular electronic energy transfer between the polymeric backbone and pendent topological cavities. We were able to show that the orthogonal H-bonded unit in **P3** induced the hierarchical nanostructures, first into vesicle-shaped particles in its free form, which further morphed into hexagonal nano-sheets and fibers in its protonated form. The formation of vesicle-type nanostructures was mainly governed by π - π stackings and hydrophobic interactions by virtue of its folded geometry. Moreover, this polymer in protonated state was reoriented to elude local electrostatic repulsions, and augmented positive cooperative anion- π interactions between embedded inner layers were also allowed to form hierarchical multilayered hexagonal nano-sheets and fibers. Therefore, we developed the first prototype design of a polyrotaxane architecture and set a stage to realize previously unattainable macromolecular architectures with orthogonally H-bonded topological cavities in a reversible fashion. Hence, this design of functional molecular switchable MIPAs will lead to a new bottom-up approach for the future optoelectronic applications of nano-materials.

Chapter-4

A Facile Ratiometric Fluorescent Chemodosimeter for Hydrazine and its Applications in Living Cells

4. 1. Introduction

Amending of facile and sensitive analytical techniques for the detection of small molecule based analytes is of pivotal research interest owing to their ghastly toxic effects on humans and environment.¹⁴² Hydrazine is a strong reducing agent and highly reactive base;¹⁴³ moreover, its widespread usage is inevitable due to its vital roles in chemical, pharmaceutical, and agricultural industries involving catalysts, corrosion inhibitors, and pesticides.¹⁴⁴ Hydrazine is a well-known high-energy fuel in rocket propulsion and missile systems due to its better detonable properties.¹⁴⁵ However, hydrazine is extremely toxic and easily absorbed by oral, dermal, and inhalation exposure routes. Previous studies on laboratory animals suggested that hydrazine is highly neurotoxin, mutagenic, and carcinogenic.¹⁴⁶ Thus, developing reliable and real-time fluorometric detection methods for specific detection of hydrazine is highly demanding.

Conventionally, hydrazine was analyzed by electrochemistry¹⁴⁷ and gas chromatography¹⁴⁸ methods. However, those methods were often suffered in detecting hydrazine with low sensitivities. Despite their ease in detections with a trace amount of analytes by fluorometric methods possessing high sensitivity and selectivity functions; however, only a limited number of fluorescent small molecule based probes for hydrazine have been reported. Chang et al. developed a selective detection of hydrazine by deprotection of a levulinate group.⁸⁶

Developing ratiometric and reaction specific fluorescent chemodosimeters are often beneficial due to their specificity and built-in correction for quantitative measurement by the ratio of fluorescence intensities at two different wavelengths.¹⁴⁹ Chemodosimeters appended with

specific protection groups for selective detections via target specific deprotection for various analytes have often been utilized effectively.^{150,66a,89,151} However, till date there are only two reported ratiometric probes based on hydrazine mediated ester deprotection⁸⁸ and hydrazone formation.⁸⁷ However, to the best of our knowledge a renowned NH_2 functional group synthon phthalimide¹⁵² has never been explored yet in the specific ratiometric detection of hydrazine. Excellent photophysical properties and outstanding intramolecular charge transfer (ICT) structures of hydrophilic 4-aminonaphthalimide make them expedient candidates in designing novel fluorescent probes.¹⁵³

Herein, we developed a novel phthalimide protected 4- amino naphthalimide for the specific and sensitive ratiometric detection of hydrazine via Ing-Manske hydrozinolysis method,¹⁵⁴ a second key step in Gabriel amine synthesis¹⁵⁵ and thus, enabling ICT as well as living cell permeability as shown in **Fig 4. 1**.

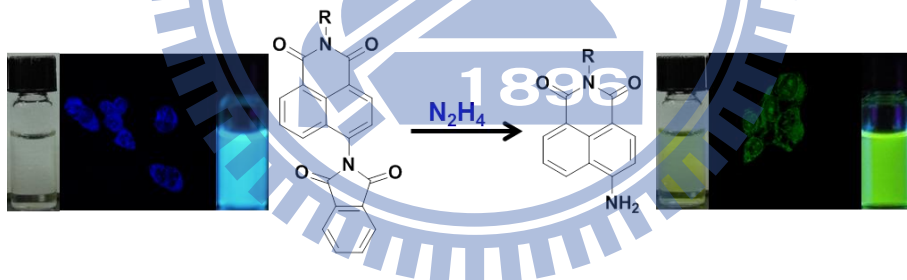


Figure 4. 1. Hydrazine triggered phthalimide deprotection with a fluorescent ratiometric response of phthalimide appended hydroxyl 4-naphthalimide derivative.

4. 2. Experimental section

4. 2. 1. General methods and materials:

NMR spectra were recorded on Bruker Avance DRX300 Series (^1H : 300 MHz; ^{13}C : 75 MHz) at a constant temperature of 298 K. Chemical shifts were reported in parts per million from low to high field and referenced to residual solvent (CDCl_3 , d_6 -DMSO $\delta = 7.26, 2.49$ ppm and $\delta = 77.23, 39.52$ ppm, respectively). Coupling constant (J) were reported in hertz (Hz). UV-Vis spectra were recorded on the Jasco UV-600 spectrophotometer using 1 cm quartz cuvette. Fluorescence measurements were conducted with HITACHI 7000 Series Spectrophotometer. All emission and excitation spectra were corrected for the detector response and the lamp output. Melting points were determined using a Fargo MP-2D apparatus and are uncorrected. Elemental analyses were conducted on HERAEUS CHN-OS RAPID elemental analyser. Infrared spectroscopy data were collected using Perkin Elmer IR spectrophotometer. Solid sample were analysed using KBr pellet method. Confocal imaging was carried out using Olympus FV1000-IX81 confocal fluorescence microscope, confocal fluorescence imaging with 100 \times objective lens. Semi-empirical PM3 calculations were calculated using Gaussian-09 suite.

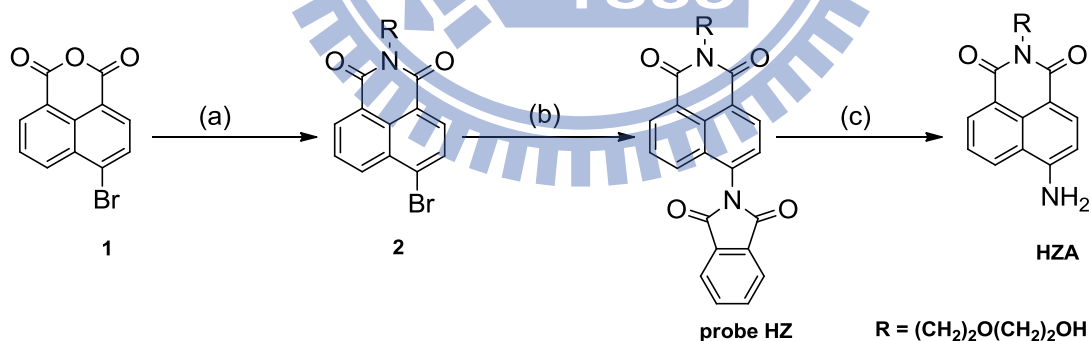
Materials: All the reagents were purchased from commercial sources and used without further purification. All the solvents were HPLC grade; anhydrous solvents were obtained by passing through activated alumina column purification system, further dried by standard drying procedures. Solvents were degassed by freeze/thaw/pump cycle technique prior to use. 6-bromo-2-(2-(2-hydroxyethoxy)ethyl)-1*H*-benzo[de]isoquinoline-1,3(2*H*)-dione was prepared with a slight modification of previous literature.¹⁵⁶

4. 2. 2. Stock Solutions:

Standard solution of probe **HZ** (100 μM) were prepared in (1:9, v/v) in a mixture of water and ethanol solution. Prior to analysis the stock solution was diluted and pH of the solution was adjusted to about 7.2 using phosphate buffer saline (PBS) solution to deliver the final concentration of the probe (5 μM , pH = 7.2,) in PBS-EtOH (1:9, v/v) solution. Hydrazine, other primary amines, metal ions, and anion stock solutions with concentration of (10 mM) were prepared, respectively in water. Before the titrations analytes were diluted to their desired volumes.

4. 2. 3. Design strategy:

Probe **HZ** was synthesized by appending phthalimide group via CuI promoted aryl halide nucleophilic substitution of compound **2** with potassium phthalimide in high boiling dimethylacetamide (DMA) solvent in a moderate yield as depicted in **Scheme 4. 1**. The detailed synthetic procedures and characterization data of all compounds are outlined in the following pages.



Scheme 4. 1. Reagents and Conditions: (a) 2-(2-aminoethoxy)ethanol, EtOH, reflux, 4 h, 88%; (b) potassium phthalimide, CuI, DMA, reflux, 1 day, 55%; (c) Hydrazine (N_2H_4), EtOH/ H_2O , 15 min, 70%.

4. 2. 4. Synthetic Procedures:

Synthesis of 6-bromo-2-(2-(2-hydroxyethoxy)ethyl)-1H-benzo[de]isoquinoline-1,3(2H)-dione (Compound 2):

A mixture of 6-bromobenzo[de]isochromene-1,3-dione (**1**, 2.0 g, 7.22 mmol, 1.0 equiv) and 2-(2-aminoethoxy)ethanol (0.79 g, 7.58 mmol, 1.05 equiv) in 60 ml of ethanol was reflux for 4 h, and slowly cooled down to room temperature. The solution further cooled overnight in a freezer and the precipitated compound was filtered and dried for overnight to get the compound **2** (2.31 g, 6.34 mol, 88%). Chemical formula: C₁₆H₁₄BrNO₄, Molecular weight: 364.19; m.p.140.9-142.4°C

¹H NMR (300 MHz, CDCl₃, 25 °C): δ (ppm) = 8.65 (d, J_d = 8.9 Hz, 1H), 8.55 (d, J_d = 8.9 Hz, 1H), 8.40 (d, J_d = 8.9 Hz, 1H), 8.03 (d, J_d = 8.9 Hz, 1H), 7.83 (t, J_t = 9.0 Hz, 1H), 4.43 (t, J_t = 6.1 Hz, 2H), 3.86 (t, J_t = 6.1 Hz, 2H), 3.68 (t, J_t = 6.0 Hz, 4H), 2.51 (br, 1H, OH); ¹³C NMR (75 MHz, CDCl₃, 298 K): δ (ppm) = 163.7, 133.2, 132.1, 131.3, 131.0, 130.4, 128.7, 128.0, 122.7, 121.9, 72.4, 68.3, 61.8, 39.7; IR (KBr, cm⁻¹): 3513, 3081, 2908, 2865, 1692, 1588 ; MS (+ESI-MS) : (m/z): Calcd for C₁₆H₁₄BrNO₄; 364.19; found: 364.0 [M]⁺, 366.0 [M+2]⁺, 386 [M+Na]⁺, [M+Na+2]⁺; Anal. Calcd. for C₁₆H₁₄BrNO₄: C, 52.77; H, 3.87, N, 3.85 found; C, 52.68; H, 3.85, N, 3.86

Synthesis of 6-(1,3-dioxoisindolin-2-yl)-2-(2-(2-hydroxyethoxy)ethyl)-1H-benzo[de]isoquinoline-1,3(2H)-dione (Probe HZ):

A mixture of compound **2** (1.0 g, 2.74 mmol, 1.0 equiv), potassium phthalimide (0.53 g, 2.88 mmol, 1.05 equiv), and CuI (0.575 g, 3.00 mmol, 1.1 equiv) were taken in over dried 100 ml RBF, and the mixture was applied to 3 freeze-thaw-pump cycles. A freshly degassed DMA (60 ml) was added to the compound mixture and further degassed under argon atmosphere for 5 min, then reflux for 1 day. The solution was slowly cooled down to room temperature and poured into

a beaker containing 200 g of crushed ice and stirred for 30 min, the resulted yellowish orange precipitate was filtered. The crude cake was dissolved in 400 ml of DCM and washed with brine solution 2 x 80 ml. The resulting solution was dried over MgSO_4 and evaporated under vacuum. The crude product was subjected to flash column chromatography (silica gel, Hexane/EA: 8/2 to 6/4) to yield a pure yellow colored final probe **HZ** (0.65 g, 1.51 mmol, 55%). Chemical formula: $\text{C}_{24}\text{H}_{18}\text{N}_2\text{O}_6$, Molecular weight: 430.12; m.p. 256.8-258.2 °C

$^1\text{H NMR}$ (300 MHz, CDCl_3 , 25 °C): δ (ppm) = 8.72 (d, $J_d = 8.9$ Hz, 1H), 8.66 (d, $J_d = 7.3$ Hz, 1H), 8.05-8.00 (m, 3H), 7.91-7.88 (m, 2H), 7.79-7.73 (m, 2H), 4.47 (t, $J_t = 5.9$ Hz, 2H), 3.86 (t, $J_t = 5.8$ Hz, 2H), 3.67 (t, $J_t = 3.9$ Hz, 4H), 2.47 (br, 1H, OH); $^{13}\text{C NMR}$ (75 MHz, CDCl_3 , 298 K): δ (ppm) = 167.1, 164.2, 163.8, 135.1, 134.4, 132.1, 131.8, 131.2, 129.5, 129.3, 128.9, 127.9, 127.8, 124.4, 123.5, 123.2, 72.4, 68.4, 61.9, 39.8; **IR** (KBr, cm^{-1}): 3515, 3091, 2942, 2863, 1727, 1609, 1401, 1224, 1046; **MS (+ESI-MS)**: (m/z): Calcd for $\text{C}_{24}\text{H}_{18}\text{N}_2\text{O}_6$; 430.12; found: 431.1 $[\text{M}+1]^+$, 453.1 $[\text{M}+\text{Na}]^+$; **Anal. Calcd.** for $\text{C}_{24}\text{H}_{18}\text{N}_2\text{O}_6$: C, 66.97; H, 4.22 N, 6.51, found; C, 66.90; H, 4.20, N, 6.53.

Synthesis of 6-amino-2-(2-(2-hydroxyethoxy)ethyl)-1H-benzo[de]isoquinoline-1,3(2H)-dione (Compound HZA):

In an oven dried 25 ml RBF, probe **HZ** (0.050 g, 0.11 mmol, 1.0 equiv) was taken and dissolved in 8 ml of $\text{H}_2\text{O}/\text{EtOH}$ (1/9, v/v) solution. Hydrazine (0.008 g, 0.24 mmol, 2.1 equiv, 0.5 M) solution was added in portion, an immediate color change from deep yellow to pale yellow was observed. The reaction was continued for 15 min, at which time TLC showed complete deprotection of phthalimide. The resulted deep fluorescent solution was evaporated under vacuum, then 25 ml DCM was added to the crude product and stirred for 30 min, the resulted precipitate filtered through fine micron filter. The crude product was dissolved in minimum

amount (4 ml) of MeOH and pentane (100 ml) was added and left under stirring for overnight. The resulted fine orange precipitate was filtered through fine micron filter and dried for overnight under vacuum to yield the final HZA product (0.024 g, 0.079 mmol, 70%). Chemical formula: C₁₆H₁₆N₂O₄, Molecular weight: 300.31; m.p. 204.6-206.0 °C

¹H NMR (300 MHz, d₆-DMSO, 25 °C): δ (ppm) = 8.60 (d, J_d = 8.9 Hz, 1H), 8.42 (d, J_d = 8.9 Hz, 1H), 8.18 (d, J_d = 8.9 Hz, 1H), 7.64 (t, J_t = 8.9 Hz, 1H), 7.45(s, 2H, NH₂), 6.83 (d, J_d = 8.1 Hz, 1H), 4.56 (s, 1H, OH), 4.19 (t, J_t = 6.0 Hz, 2H), 3.60 (t, J_t = 6.0 Hz, 2H), 3.44 (s, 4H); ¹³C NMR (75 MHz, d₆-DMSO₃, 298 K): δ (ppm) = 164.3, 163.3, 153.2, 134.5, 131.5, 130.2, 129.8, 124.4, 122.1, 119.8, 108.6, 107.8, 72.5, 67.5, 60.6, 38.8; IR (KBr, cm⁻¹): 3425, 3351, 3201, 2962, 2879, 1665, 1564, 1119; MS (+ESI-MS): (m/z): Calcd for C₁₆H₁₆N₂O₄; 300.31; found: 301.3 [M+1]⁺, 323.1 [M+Na]⁺; Anal. Calcd. for C₁₆H₁₆N₂O₄: C, 63.99; H, 5.37 N, 9.33, found; C, 63.89; H, 5.35, N, 9.31.

4. 3. Results and Discussion

4. 3. 1. UV-Vis and Fluorescence-based sensing studies of probe HZ:

We primarily assessed the spectroscopic properties of the probe **HZ** in a mixture of phosphate buffer saline (PBS, pH = 7.2, 10 mM) and EtOH (1:9, v/v). The probe **HZ** (5 μM) without hydrazine exhibited a moderate UV-vis absorption band and a fluorescence emission band at 344 and 467 nm, respectively, owing to the electron withdrawing phthalimide protection group. However, upon the addition of hydrazine (20 μM, 4.0 equiv) we noticed an immediate naked eye color change from colorless (344 nm) to yellow color (439 nm) with a noticeable red-shift in the absorption band (**Figure 4. 2**). Concomitantly, a selective red-shift from 467 nm (blue) to 528 nm (yellowish green) was evidenced in the fluorescence emission spectra (see **Figure 4. 3**). The

perceptible red-shifts in both UV-vis and fluorescence cases could be ascribed to the hydrazine promoted phthalimide deprotection with the release of electron donating amino grouped compound **HZA**. Prominently, these observations indicated that the current probe **HZ** would be acted as a sensitive ratiometric sensor under the physiological condition.

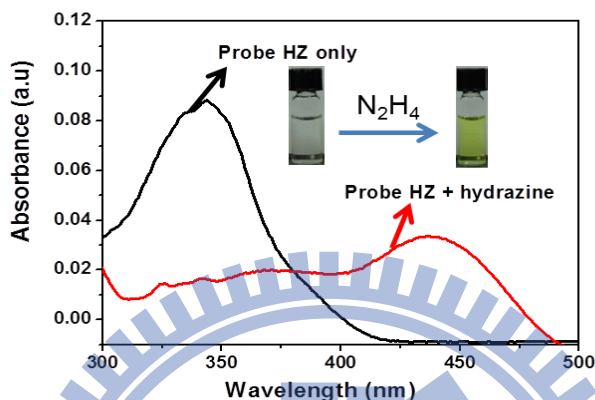


Figure 4. 2. UV-vis absorption spectra change of probe **HZ** (5 μ M) upon addition of the hydrazine (20 μ M) in a mixture of PBS buffer (PBS, pH 7.2, 10 mM) and EtOH (1:9, v/v) solution, Inset pictures depicting perceivable naked eye color change of probe **HZ** upon hydrazine addition.

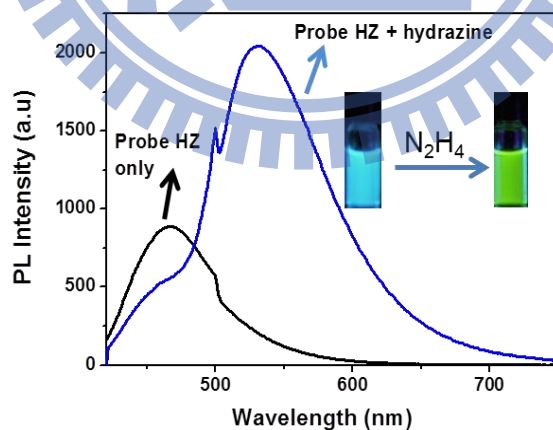


Figure 4. 3. Fluorescence spectra change of probe **HZ** (5 μ M) upon addition of the hydrazine (20 μ M) in a mixture of PBS buffer (PBS, pH 7.2, 10 mM) and EtOH (1:9, v/v) solution, Inset

pictures depicting perceivable fluorescence color change (under UV lamp $\lambda = 365$ nm) of probe **HZ** upon hydrazine addition. $\lambda_{\text{ex}} = 405$ nm, Slits: 5 nm/ 5 nm.

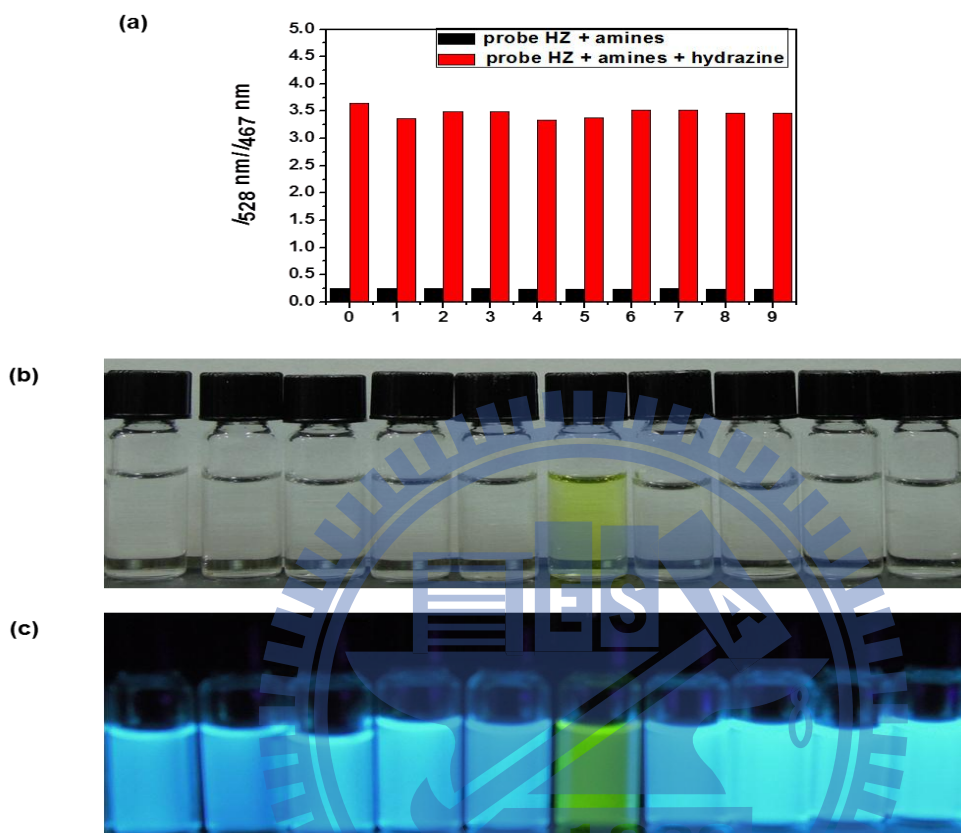


Figure 4.4. (a) Fluorescence responses of probe **HZ** (5 μM) with various primary amines (25 μM) in a mixture of PBS buffer (PBS, pH 7.2, 10 mM) and EtOH (1:9, v/v) solution. Bars represent the fluorescence intensity ratio in the presence and absence of various amines. Black bar represent the addition of primary amines (25 μM) to probe **HZ** (5 μM). Red bars represent the subsequent addition of hydrazine (25 μM) to the solution. 0 = hydrazine, 1 = hydroxyl amine, 2 = urea, 3 = thiourea, 4 = monomethylamine, 5 = ethylenediamine, 6 = 1,4-Diaminobutane, 7 = trans-1,2-Diaminocyclohexane, 8 = aqueous ammonia, and 9 = guanidine nitrate, respectively. (b) and (c) UV-vis and fluorescence color changes under (UV lamp 365 nm) of probe **HZ** (5 μM) with various amines (25 μM) sequentially from left to right hydroxyl amine, urea, thiourea,

monomethylamine, ethylenediamine, hydrazine, 1,4-Diaminobutane, trans-1,2-Diaminocyclohexane, aqueous ammonia, and guanidine nitrate. $\lambda_{\text{ex}} = 405 \text{ nm}$, Slits: 5 nm/ 5 nm.

Taking this vivid spectroscopic clue, we further examined fluorescence responses of the probe **HZ** over the various primary amine sources, such as hydroxylamine, urea, thiourea, monomethylamine, ethylenediamine, 1,4-diaminobutane, trans-1,2-Diaminocyclohexane, ammonia, guanidine nitrate, and hydrazine to substantiate the selectivity of probe **HZ** (**Figure 4. 4**). Upon the addition of 5 equiv of hydrazine, probe **HZ** (5 μM) illustrated a discernible ratiometric red-shift in **Figure 4. 5a**. However, under similar conditions the other primary amine sources merely showed trivial responses in the emission behaviour.

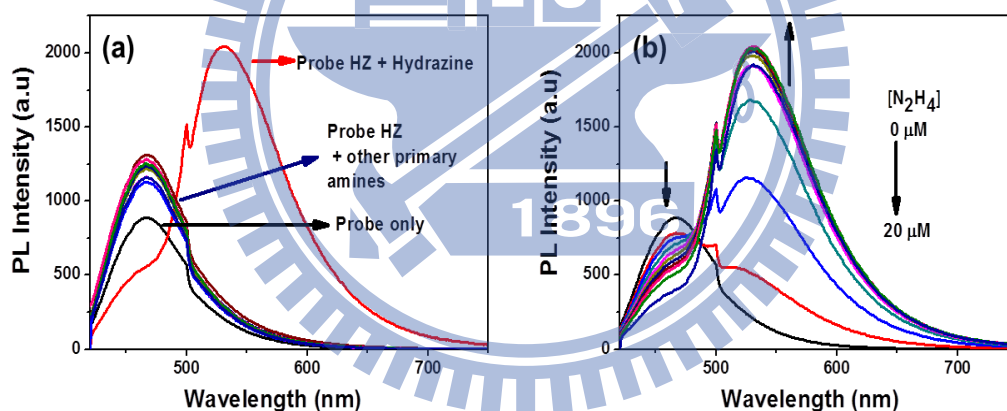


Figure 4. 5. (a) Fluorescence spectra of probe **HZ** in the presence of hydrazine and other representative primary amines. [**HZ**] = (5 μM), [hydrazine], and [primary amines] = (25 μM) in a mixture of PBS buffer solutions (pH 7.2, 10 mM) and EtOH (1:9, v/v); (b) Fluorescence spectra of Probe **HZ** (5 μM) upon the titration of hydrazine (0-20 μM). $\lambda_{\text{ex}} = 405 \text{ nm}$, Slit: 5 nm/ 5 nm.

To evaluate the quantitative analysis of probe **HZ**, we further measured the absorption and fluorescence changes of probe **HZ** (5 μM) by increasing the hydrazine concentrations from 0 to

20 μM . As shown in **Figure 4. 6**, upon the addition of hydrazine we noticed a gradual decline in the absorption band at 344 nm and a simultaneous increase of newly red-shifted absorption band at 439 nm. Likewise, the fluorescence emission band at 467 nm was gradually decreased with a concomitant upturn of a new red-shifted emission band at 528 nm (**Figure 4. 5b**), indicating a lucid colorimetric and ratiometric fluorescence response of probe **HZ**.

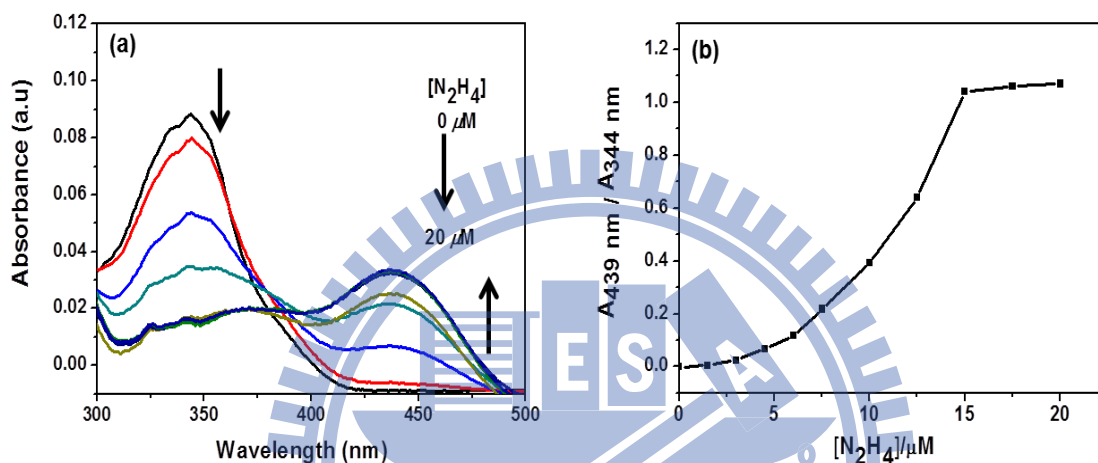


Figure 4.6. (a) UV-vis absorption spectra of probe **HZ** (5 μM) upon titration with hydrazine (0-20 μM) in a mixture of PBS buffer solution (pH 7.2, 10 mM) in EtOH (1:9, v/v). (b) Ratiometric calibration curve $A_{439 \text{ nm}}/A_{344 \text{ nm}}$.

With the addition of hydrazine (20 μM), the emission intensity ratio at the two characteristic wavelengths of 467 and 528 nm increased to 15 fold (from 0.24 to 3.65). Importantly, the fluorescence response of probe **HZ** towards hydrazine showed a clear linear relationship (**Figure 4. 7a**) within the range of 0-7.5 μM , which allowed us to determine the detection limit of probe **HZ** for hydrazine (**Figure 4. 7b**). Thus, the estimated detection limit was as low as 4.2 nM (hydrazine content = 1 ppb) far below than the threshold limit value (TLV) of 10 ppb according to the U. S. Environmental Protection Agency (EPA).¹⁵⁷

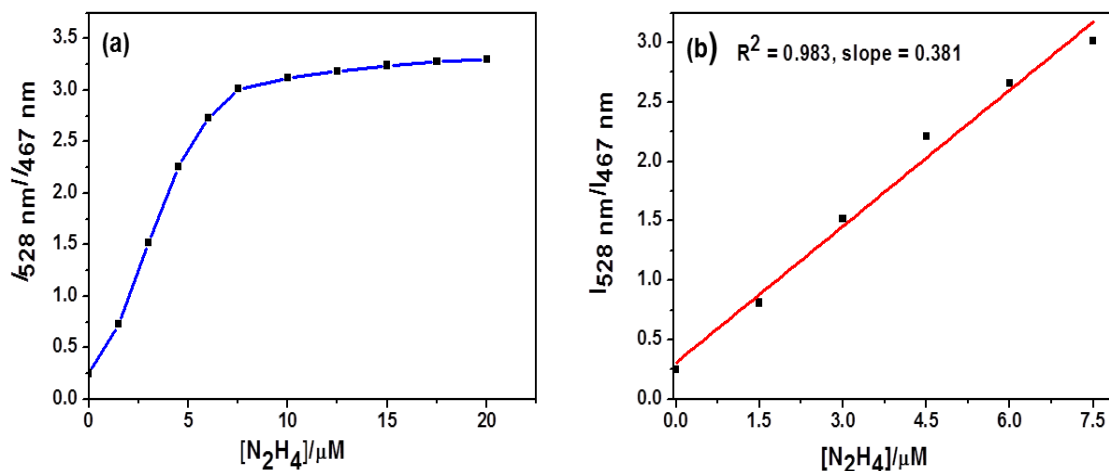


Figure 4. 7. (a) Fluorescent Ratiometric calibration curve $I_{528 \text{ nm}}/I_{467 \text{ nm}}$; (b) plot of fluorescent ratio intensity change at two characteristic wavelengths 467 and 528 nm for the mixture of probe **HZ** (5 μM) and hydrazine in a mixture of PBS buffer solution (pH 7.2, 10 mM) in EtOH (1:9, v/v) in the range of (0-7.5 μM). $\lambda_{\text{ex}} = 405 \text{ nm}$, Slits: 5 nm/5 nm.

4. 3. 2. Studies to realize ratiometric signaling mechanism of probe **HZ**:

To realize the ratiometric signaling mechanism of probe **HZ**, further strides were then made, in which the semi-empirical theoretical calculations of probe **HZ** and compound **HZA** were studied as shown in **Figure 4. 8** and **4. 9**. We observed that both HOMO and LUMO molecular orbital distributions in probe **HZ** were mainly resided on the naphthalimide moiety, which possessed a dihedral angle of $\Phi = 71.8^\circ$ with the distorted phthalimide unit. A further Mulliken charge analysis showed that the phthalimide carbonyl unit had a more electropositive character for carbon $\delta^+ = 0.33 e$ in contrast to $0.31 e$ in the naphthalimide carbonyl unit. Moreover, ^1H NMR spectra and ESI-MS analysis of the free probe **HZ**, probe **HZ**-hydrazine complex and isolated **HZA** in d_6 -DMSO verified the release of phthalhydrazide during the hydrazine mediated phthalimide deprotection (Figure. 10).

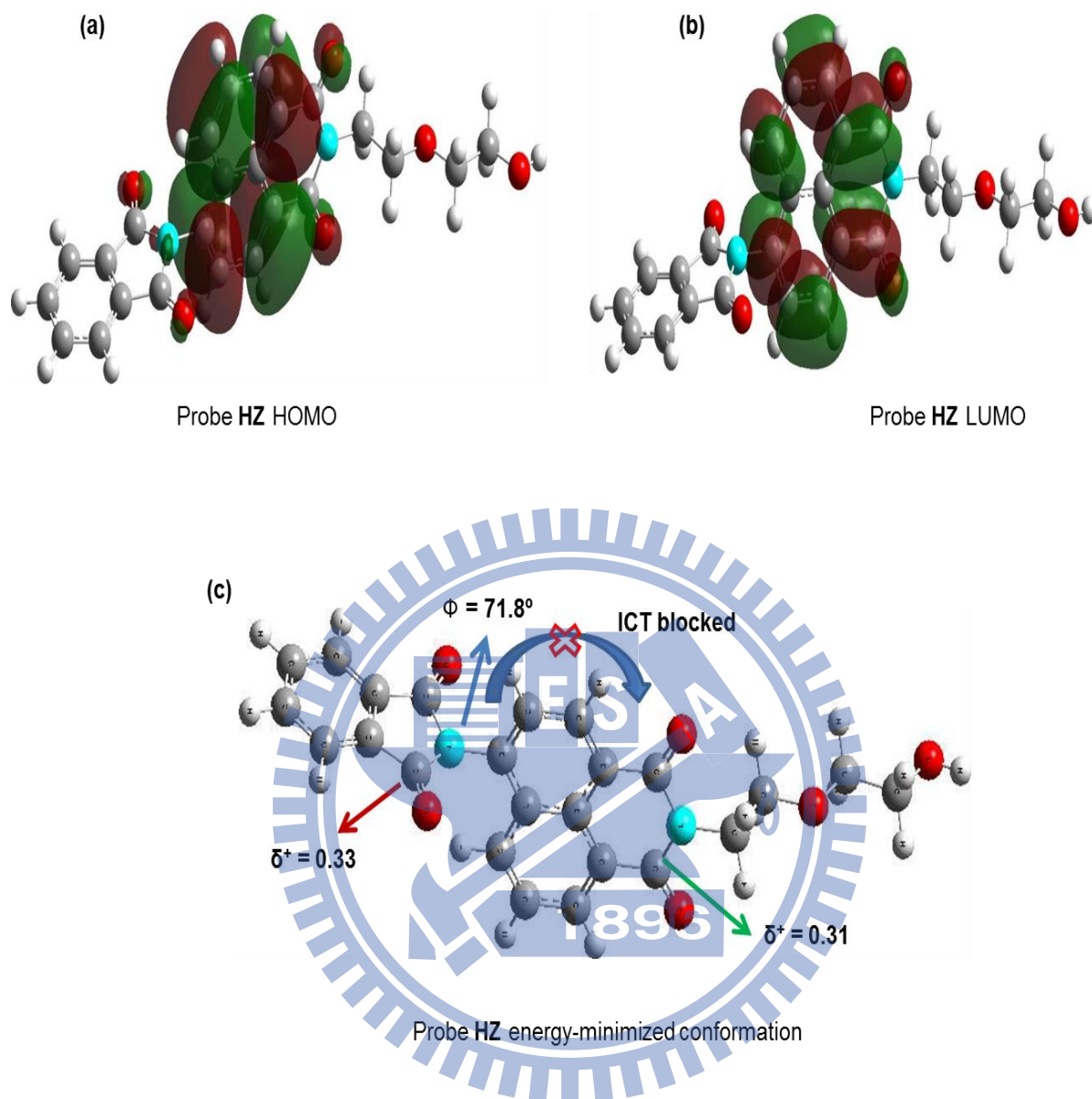


Figure 4. 8. (a) and (b) Semi-empirical PM3 method optimized HOMO and LUMO frontier molecular orbital distributions of probe **HZ**, respectively; (c) energy-minimized geometry of probe **HZ**. Dihedral angle between phthalimide and naphthalimide plane was denoted which effectively blocked the ICT-process. Mulliken charges of phthalimide and naphthalimide carbonyl carbons were denoted in picture (c). Color coding of atoms blue = N, red = O, grey = C and white = H, respectively.

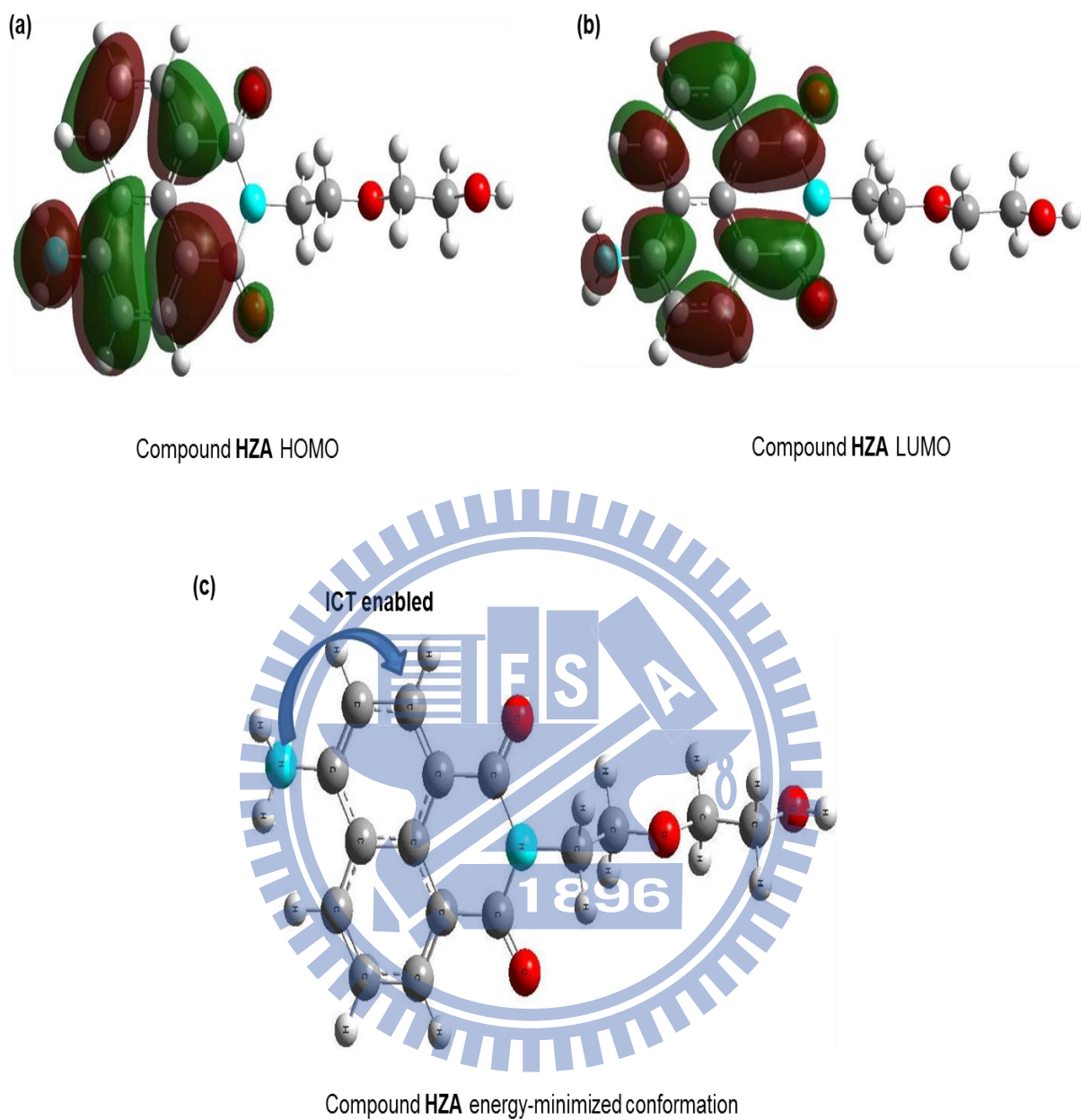


Figure 4. 9. (a) and (b) Semi-empirical PM3 method optimized HOMO and LUMO frontier molecular orbital distributions of compound **HZA**, respectively; (c) energy-minimized geometry of compound **HZA**. Hydrazinolysis released the free amine and eventually enabling the ICT process. Color coding of atoms blue = N, red = O, grey = C and white = H, respectively.

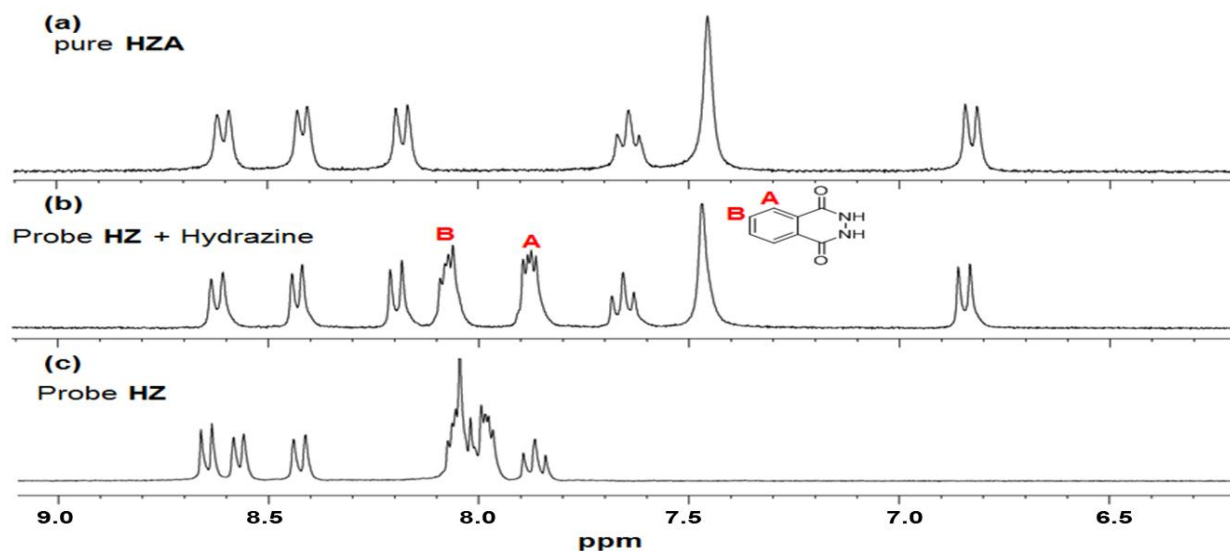


Figure 4. 10. ^1H NMR (d_6 -DMSO, 300 MHz, 25 $^\circ\text{C}$) stock plot. (a) Compound **HZA** (3 mM), (b) probe **HZ** (3 mM) with the addition of hydrazine (2.0 equiv), and (c) probe **HZ** (3 mM).

Based on these concrete experimental and theoretical observations we outlined the plausible signaling mechanism. Deprotection of the phthalimide group of probe **HZ** is proceed first at the carbonyl position of phthalimide by the nucleophilic addition of hydrazine to leave intermediate 2-(hydrazinecarbonyl)-*N*-naphthalimidobenzamide.¹⁵⁸ Further, the subsequent nucleophile attacked on carbonyl to generate phthalhydrazide and 4-amino naphthalimide, which possessed a unique colorimetric and ratiometric response (**Figure 4. 11**).

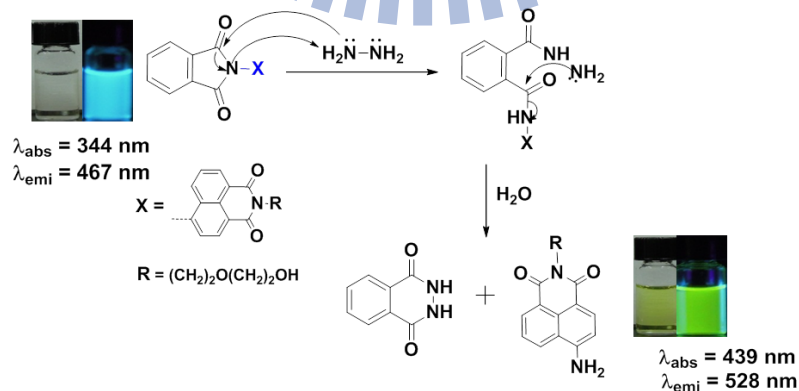


Figure 4. 11. The mechanism for hydrazine selective phthalimide deprotection of probe **HZ**.

4. 3. 3. Time effects on Ratiometric Signaling:

Considering the real time detection of the probe **HZ** (6 μM) towards hydrazine, time-dependent fluorescence ratiometric changes of two characteristic wavelengths at 467 and 528 nm in the presence of hydrazine (30 μM) in a mixture buffer (PBS, pH 7.2, 10 mM) and EtOH (1:9, v/v) solutions (**Figure 4. 12a**) were verified. Delightfully, within 15 min the fluorescence ratiometric intensity ($I_{528 \text{ nm}}/I_{467 \text{ nm}}$) was increased to 5 fold with a perceivable dynamic nature (**Figure 4. 12b**). Obviously, the crossover point at 750 s for the two characteristic wavelengths 467 and 528 nm indicated the release of compound **HZA**, with enabling an effective ICT induced hydrazine selective ratiometric response of the probe **HZ**. Thus, the probe **HZ** could be useful for real-time detection of hydrazine with a trace amounts.

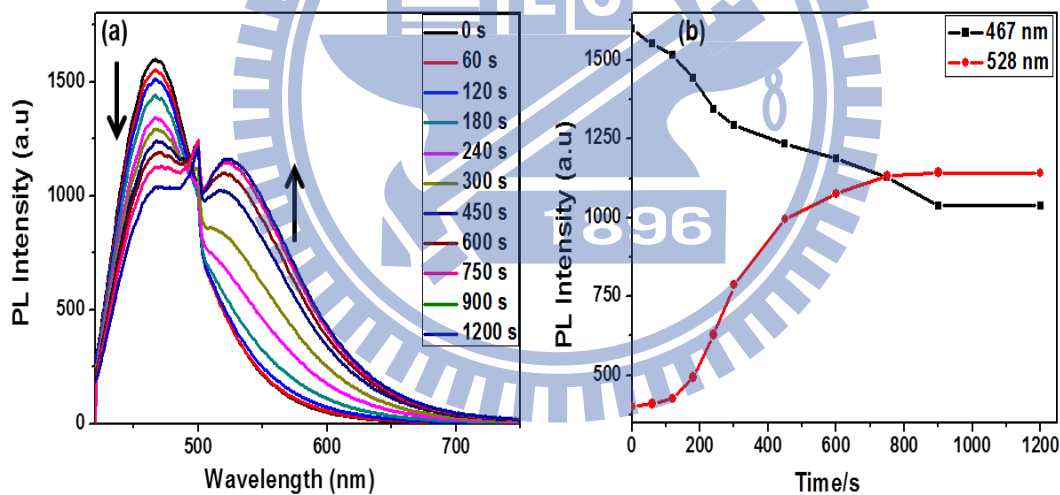


Figure 4. 12. (a) Fluorescent spectral changes of probe **HZ** (6 μM) upon addition of hydrazine (30 μM) in a mixture of PBS buffer (PBS, pH 7.2, 10 mM) and EtOH (1:9, v/v) solution. The fluorescence intensity data were collected after certain time intervals as depicted in the figure (a). (b) Corresponding time dependent fluorescence ratio (I_{528}/I_{467} nm) and two characteristic wavelength changes of probe **HZ**; $\lambda_{\text{ex}} = 405 \text{ nm}$, Slits: 5 nm/ 5 nm.

4. 3. 4. Screening the selectivity of Probe HZ:

To fortify the selectivity of probe **HZ** to other common metal ions and anions (10 equiv), we investigated the fluorescence behavior of probe **HZ**. However, the tested various metal ions, such as Na^+ , Ag^+ , Ca^{2+} , Zn^{2+} , Cu^{2+} , Ni^{2+} , Cd^{2+} , Hg^{2+} , Pb^{2+} , Ag^{2+} , Fe^{3+} and Al^{3+} , on probe **HZ** and probe **HZ**-hydrazine complex could not induce any noticeable changes as shown in **Figure 4. 13**. Similarly, we screened the effect of different anions, such as F^- , Cl^- , Br^- , I^- , AcO^- , NO_3^- , H_2PO_4^- , N_3^- , HCO_3^- , ClO_4^- , SO_4^{2-} and $\text{S}_2\text{O}_8^{2-}$, on probe **HZ** and probe **HZ**-hydrazine complex. As anticipated, none of these above anions could present distinct responses on probe **HZ** as well as probe **HZ**-hydrazine complex as depicted in **Figure 4. 14**. Based on these concrete results, we inferred that probe **HZ** could be selectively and sensitively detect the hydrazine even in the presence of other competing metal ions and anions.

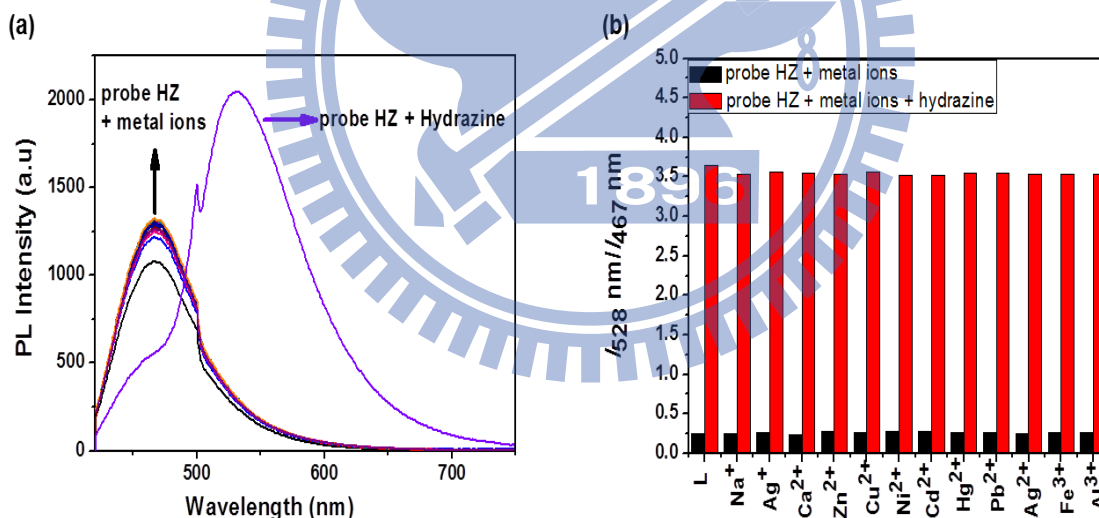


Figure 4. 13. (a) Fluorescence spectra of probe **HZ** in the presence of hydrazine and other representative metal ions. [**HZ**] = (5 μM), [hydrazine] = (25 μM), and [metal ions] = (50 μM) in a mixture of PBS buffer (pH 7.2, 10 mM) and EtOH (1:9), v/v). λ_{ex} = 405 nm, Slit: 5 nm/ 5 nm.

(b) Fluorescence responses of probe **HZ** (5 μM) with various metal ions (50 μM) in a mixture of

PBS buffer (pH 7.2, 10 mM) and EtOH (1:9, v/v) solution. Bars represent the fluorescence intensity ratio in the presence and absence of various metal ions (Na^+ , Ag^+ , Ca^{2+} , Zn^{2+} , Cu^{2+} , Ni^{2+} , Cd^{2+} , Hg^{2+} , Pb^{2+} , Ag^{2+} , Fe^{3+} and Al^{3+}). Black bar represent the addition of metal ions (50 μM) to probe **HZ** (5 μM). Red bars represent the subsequent addition of hydrazine (25 μM) to the solution.

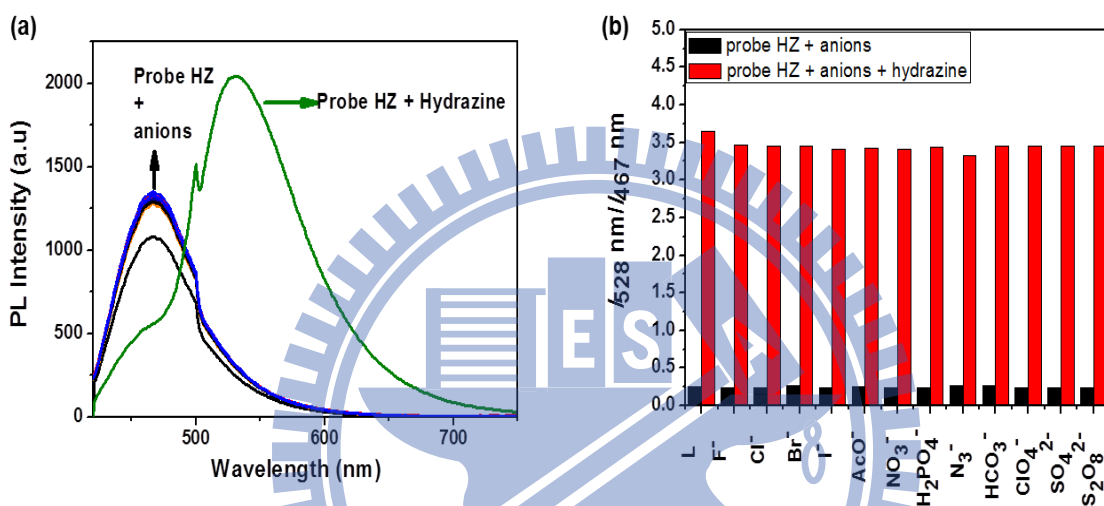


Figure 4. 14. (a) Fluorescence spectra of probe **HZ** in the presence of hydrazine and other representative anions. [**HZ**] = (5 μM), [hydrazine] = (25 μM), and [anions] = (50 μM) in a mixture of PBS buffer (pH 7.2, 10 mM) and EtOH (1:9, v/v). λ_{ex} = 405 nm, Slit: 5 nm/ 5 nm. (b) Fluorescence responses of probe **HZ** (5 μM) with various anions (50 μM) in a mixture of PBS buffer (pH 7.2, 10 mM) and EtOH (1:9, v/v) solution. Bars represent the fluorescence intensity ratio in the presence and absence of various anions (F^- , Cl^- , Br^- , I^- , AcO^- , NO_3^- , H_2PO_4^- , N_3^- , HCO_3^- , ClO_4^- , SO_4^{2-} and $\text{S}_2\text{O}_8^{2-}$). Black bar represent the addition of anions (50 μM) to probe **HZ** (5 μM). Red bars represent the subsequent addition of hydrazine (25 μM) to the solution.

4. 3. 5. pH effects in ratiometric signaling of probe HZ:

Since phthalimide was prone to basic hydrolysis and to further appreciate the probe **HZ** towards biological applications, we investigated the pH effects on fluorescence capabilities of **HZ** and **HZ**-hydrazine complex. The probe **HZ** possessed a stable response over the pH range of 1.0-10.0. Moreover, the **HZ**-hydrazine complex showed a stable ratiometric response within the biological pH range of 5.0-9.0 including acidic media as shown in **Figure 4. 15a** and **4. 15b**. However, both the free probe **HZ** and **HZ**-hydrazine complex displayed a distinct ratiometric response (red color) with a newly instigated fluorescence band at 596 nm in high basic pH range of 12-14 in contrast to the green fluorescence of probe-**HZ**-hydrazine within the pH range of 1-

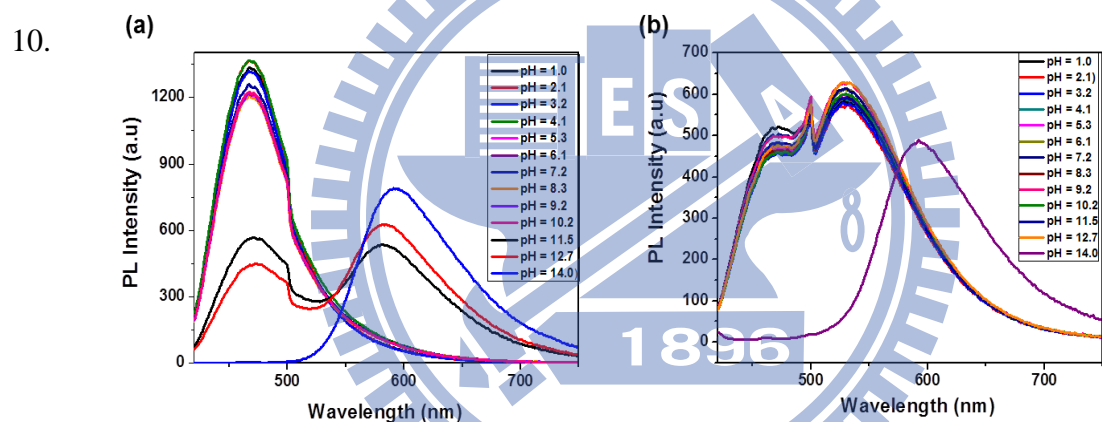


Figure 4. 15. (a) and (b) Fluorescence intensity changes of probe **HZ** (6 μM) and Fluorescence intensity changes of probe **HZ** (6 μM) in the presence of hydrazine (12 μM) as a function of pH in a mixture of PBS buffer (pH 7.2, 10 mM) and EtOH (1:9), v/v), respectively. $\lambda_{\text{exc}} = 405 \text{ nm}$, Slits: 5 nm/5 nm.

Further spectroscopic (^1H NMR & ESI-MS) analyses were confirmed the distinctive ratiometric mode of probe under basic hydrolysis conditions as shown in **Figures. S16-S19**. Based on these evidences we draw out the plausible intermediates in acidic, hydrazinolysis and basic conditions for probe **HZ** as depicted in **Scheme 4. 2**. These results clearly suggested that the current probe could be employed in living cells with better cell permeability without interference from the pH effects within the biological pH

range. Although the probe has a pure aqueous solubility, it gave long-time and trivial responses towards hydrazine and other primary amines owing to the reduced nucleophilicity of amines by the strong water-amine H-bonding in aqueous solutions in contrast to ethanol buffer solutions.

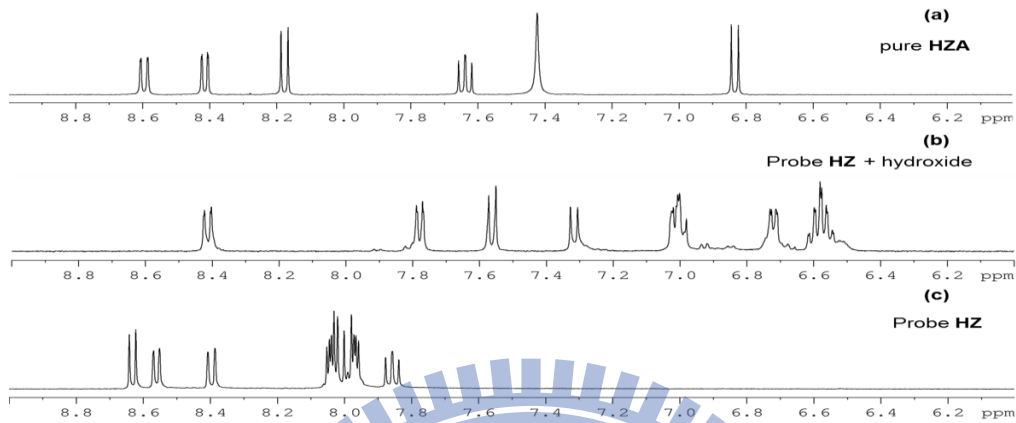


Figure 4. 16. ^1H NMR (d_6 -DMSO, 300 MHz, 25 °C) stock plot. (a) Compound **HZA** (3 mM), (b) probe **HZ** (3 mM) with the addition of hydroxide in D_2O (5.0 equiv), and (c) probe **HZ** (3 mM).

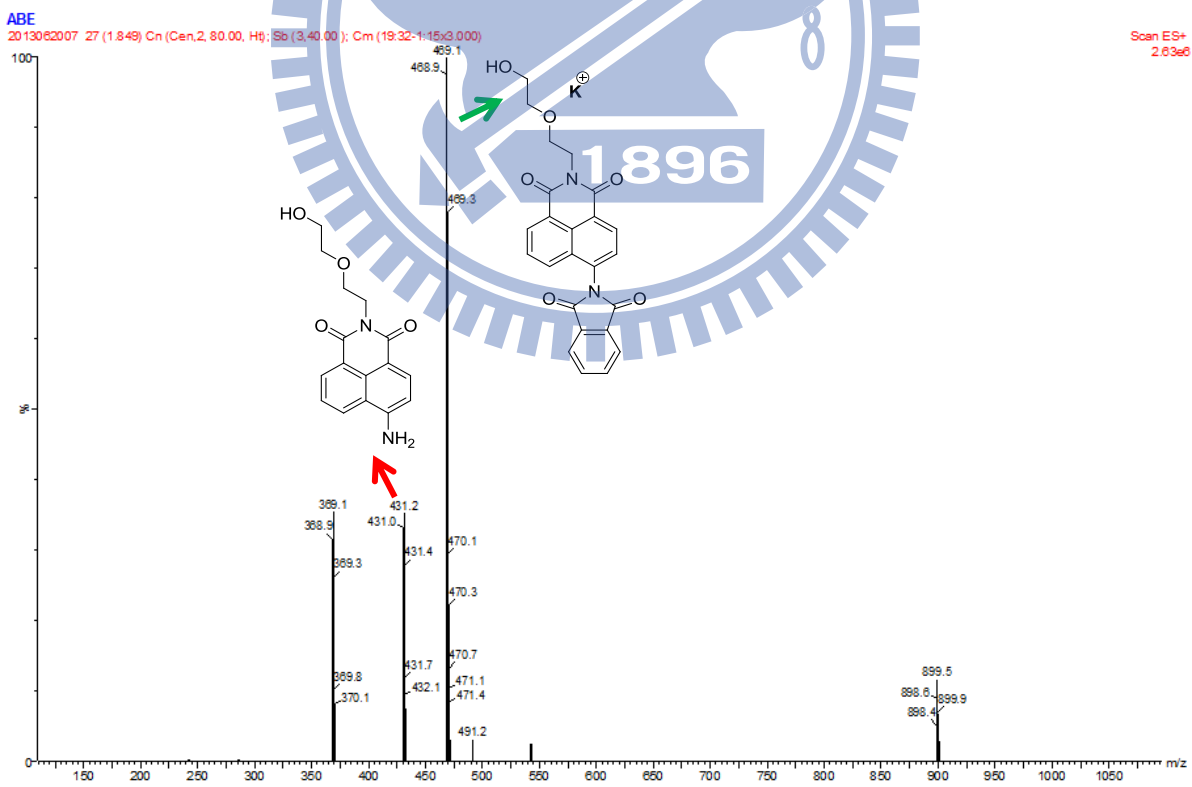


Figure 4. 17. ESI (+)-MS chromatogram of Probe **HZ** in acidic pH = 1.0 solution.

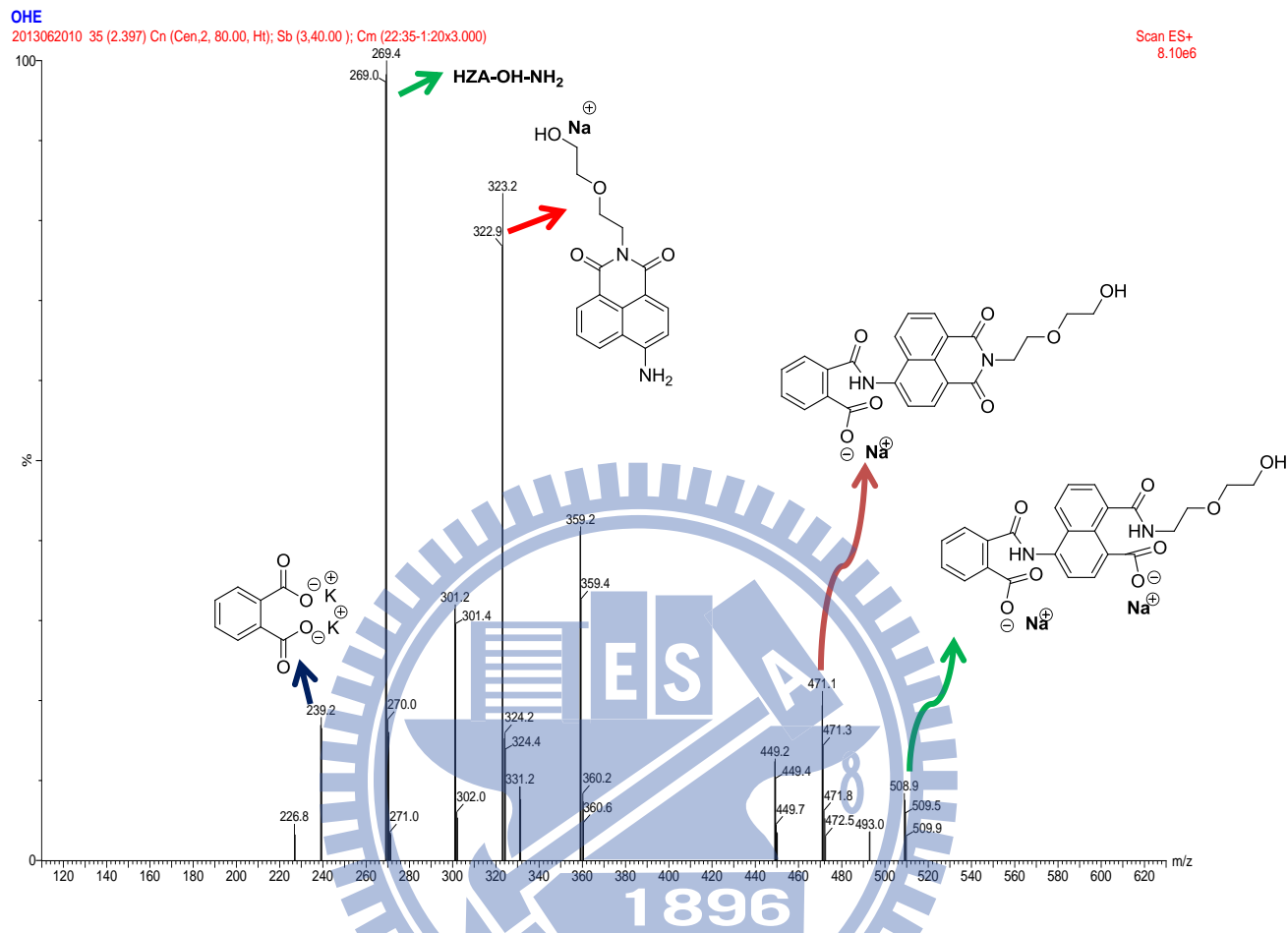


Figure 4. 18. ESI (+)-MS chromatogram of Probe **HZ** in basic pH = 14.0 solution.

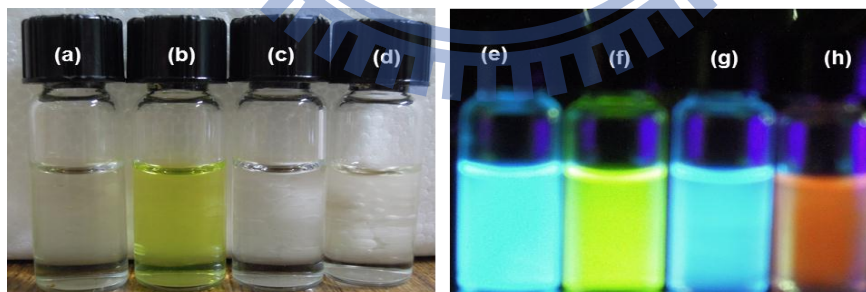
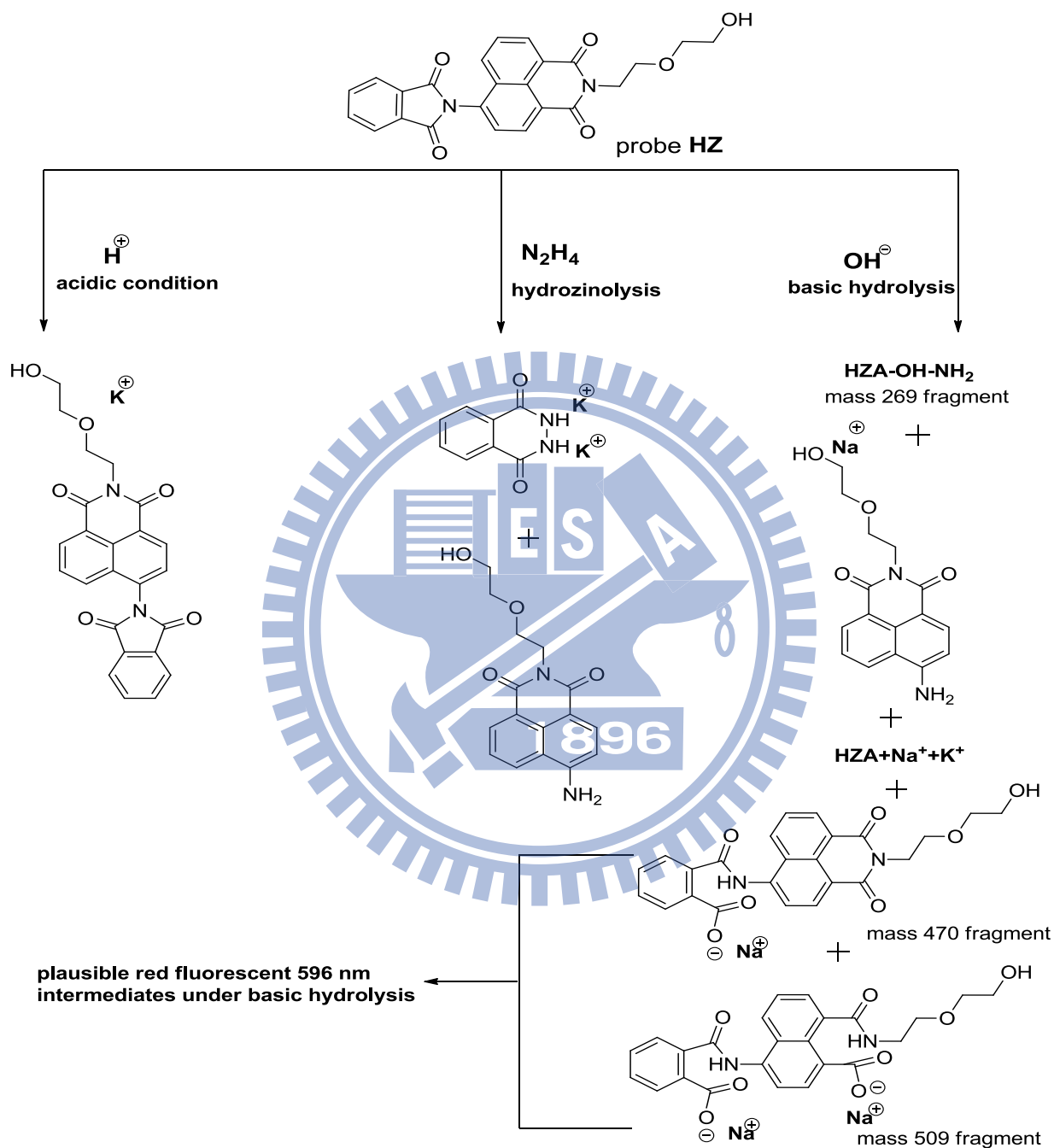


Figure 4. 19. (a), (b), (c) and (d) naked eye color changes of probe **HZ** free (5 μM), in the presence of hydrazine (25 μM), in the presence acidic solution (pH = 1.0), in the presence basic

solution (pH = 14.0), respectively. (e)-(h) fluorescence color changes under UV lamp 365 nm of the respective (a)-(d) solutions.



Scheme 4. 2. Plausible mass fragments during the acidic hydrolysis, hydrazinolysis and basic hydrolysis of probe **HZ**.

4. 3. 6. Confocal imaging of probe HZ in living cells:

Encouraged by all above merits of probe **HZ**, we next sought to apply probe **HZ** for fluorescence ratiometric imaging of hydrazine in living cells. Hydrazine could be detected in the human liver carcinoma cells (Hep G2 cells). The Cells incubated with probe **HZ** (10 μM) alone for 15 min at 37°C showed blue fluorescence (**Figure 4. 20a** and **4. 20b**). However, a perceptible green fluorescence was monitored in the cells after treatment with hydrazine (25 μM) see **Figure 4. 20c** and **4. 20d**. Apparent changes denoted that probe **HZ** was cell membrane permeable and capable of ratiometric imaging of hydrazine in the living cells.

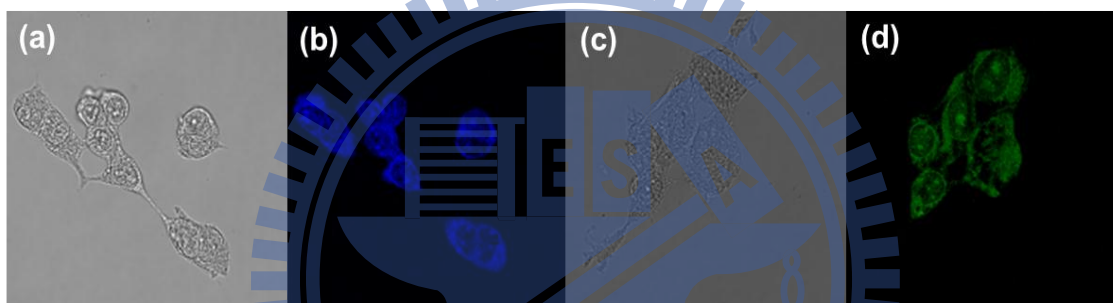


Figure 4. 20. Fluorescence images of Hep G2 cells incubated with 10 μM probe **HZ** for 15 min (b) and then further incubated with 25 μM hydrazine for 15 min (d). (a), (c) Bright-field transmission image of Hep G2 cells in (b) and (d). $\lambda_{\text{ex}} = 405 \text{ nm}$.

4. 4. Conclusions

In summary, we have judiciously developed a facile and sensitive fluorescent probe for hydrazine based on Ing-Manske hydrazinolysis method under mild conditions. Inimitably, the probe **HZ** showed a selective colorimetric and fluorescent ratiometric response towards hydrazine in the semi-aqueous buffer solution with a low detection limit. The unique ratiometric response under basic hydrolysis further differentiated from probe **HZ** hydrazinolysis. Hence, the hydrazinolysis-based ratiometric fluorescent probe was developed for the first time in this report.

Pivotal confocal imaging of hydrazine in living cells also demonstrated that probe **HZ** could be favorable for biological applications.



Chapter-5

Conclusions

In summary, a bright DPP functionalized [2]rotaxane was synthesized and well characterized. The pre-organized cavity formed in rotaxane by virtue of mechanical bond enhanced stimuli-responses towards solvent and F^- via noncovalent interactions. It was demonstrated spectroscopically that the [2]rotaxane **2-R** host could selectively recognize F^- with remarkable chromogenic, fluorogenic, and reversible functions. A Prevaling time resolved fluorescence profile proved the sensitivity of **2-R** in contrast to its precursors. As the complex quenching mechanism was coupled with both charged macrocycle shuttling and chemical stimuli, the electron or energy transfer between macrocycle and fluorophore could not be easily differentiated. Further kinetic and transient absorption studies are currently underway in our laboratory, which will be reported in due course. Hence, this design of functional MIMs could be an ideal for developing future allosteric anion sensors.

In this study, we have developed a novel polymer with the mechanically interlocked polymeric architecture by polymerization of 9-alkylidene-9*H*-fluorene with a diketopyrrolopyrrole tethered with an orthogonally H-bonded macrocycle unit, which successfully illustrated the effects of orthogonal H-bonded unit on the photophysical properties as well as nano-self-assembly process of the conjugated main-chain polymer (**P3**). It was demonstrated spectroscopically and microscopically that the mechanically interlocked nature of polyrotaxane **P3** was well preserved during the polymerization. Benefited from its unique topological cavities formed in **P3**, it showed enriched material properties, such as extended conjugations, narrow bandgaps, and unique self-assembled structures, in contrast to the other polymers in this study. Remarkably, the fluorescence on-off-on reversible acid-base controllable molecular switch ability in NIR region

for the first time has been fruitfully attained by supramolecular electronic energy transfer between the polymeric backbone and pendent topological cavities. We were able to show that the orthogonal H-bonded unit in **P3** induced the hierarchical nanostructures, first into vesicle-shaped particles in its free form, which further morphed into hexagonal nano-sheets and fibers in its protonated form. The formation of vesicle-type nanostructures was mainly governed by π - π stackings and hydrophobic interactions by virtue of its folded geometry. Moreover, this polymer in protonated state was reoriented to elude local electrostatic repulsions, and augmented positive cooperative anion- π interactions between embedded inner layers were also allowed to form hierarchical multilayered hexagonal nano-sheets and fibers. Therefore, we developed the first prototype design of a polyrotaxane architecture and set a stage to realize previously unattainable macromolecular architectures with orthogonally H-bonded topological cavities in a reversible fashion. Hence, this design of functional molecular switchable MIPAs will lead to a new bottom-up approach for the future optoelectronic applications of nano-materials.

In summary, we have judiciously developed a facile and sensitive fluorescent probe for hydrazine based on Ing-Manske hydrazinolysis method under mild conditions. Inimitably, the probe **HZ** showed a selective colorimetric and fluorescent ratiometric response towards hydrazine in the semi-aqueous buffer solution with a low detection limit. The unique ratiometric response under basic hydrolysis further differentiated from probe **HZ** hydrazinolysis. Hence, the hydrazinolysis-based ratiometric fluorescent probe was developed for the first time in this report. Pivotal confocal imaging of hydrazine in living cells also demonstrated that probe **HZ** could be favourable for biological applications.

References

1. Lehn, J.-M. *Angew. Chem. Int. Ed. Engl.* **1988**, *27*, 89.
2. Lehn, J.-M. *Supramolecular Chemistry; Concepts and Perspectives*; VCH: Weinheim, **1995**.
3. Fischer, E. *Ber. Dtsch. Chem. Ges.* **1894**, *27*, 2985.
4. Pedersen, C. J. *J. Am. Chem. Soc.* **1967**, *89*, 2495.
5. Pedersen, C. J. *J. Am. Chem. Soc.* **1967**, *89*, 7017.
6. Lüttringhaus, A.; Cramer, F.; Prinzbach, H.; Henglein, F. M. *Liebigs Ann. Chem.* **1958**, *613*, 185 – 198.
7. Frisch, H. L.; Wasserman, E. *J. Am. Chem. Soc.* **1961**, *83*, 3789.
8. Harrison, I. T.; Harrison, S. *J. Am. Chem. Soc.* **1967**, *89*, 5723.
9. Schill, G.; Zöllenkopf, H. *Nachr. Chem. Techn.* **1967**, *79*, 149.
10. Dietrich-Buchecker, C. O.; Sauvage, J.-P. *Chem. Rev.* **1987**, *87*, 795.
11. Griffiths, K. E.; Stoddart, J. F. *Pure Appl. Chem.* **2008**, *80*, 485.
12. Although various attempts were conducted for head-to-tail poly[2]rotaxane, all attempts were unsuccessful: (a) Ashton, P.; Baxter, I.; Cantrill, S. J.; Fyfe, M. C. T.; Glink, P. T.; Stoddart, J. F.; White, A. J. P.; Williams, D. J. *Angew. Chem. Int. Ed.* **1998**, *37*, 1294. (b) Ashton, P. R.; Parsons, I. W.; Raymo, F. M.; Stoddart, J. F.; White, A. J. P.; Williams, D. J.; Wolf, R. *Angew. Chem. Int. Ed.* **1998**, *37*, 1913. (c) Rowan, S. J.; Cantrill, S. J.; Stoddart, J. F.; White, A. J. P.; Williams, D. J. *Org. Lett.* **2000**, *2*, 759. (d) Fujimoto, T.; Sakata, Y.; Kaneda, T. *Chem. Commun.* **2000**, 2143. (e) Onagi, H.; Easton, C. J.; Lincoln, S. F. *Org. Lett.* **2001**, *3*, 1041. (f) Hoshino, T.; Miyauchi, M.; Kawaguchi, Y.; Yamaguchi, H.; Harada, A. *J. Am. Chem. Soc.* **2000**, *122*, 9876. (g) Rowan, S. J.; Stoddart, J. F. *Polym Adv. Technol.* **2002**, *13*, 777.

13. Head-to-head poly[2]rotaxane has been referred as poly[3]rotaxane: Oku, T.; Furusho, Y.; Takata, T. *J. Polym. Sci. Part A: Polym Sci.* **2003**, *41*, 119.
14. (a) Kohsaka, Y.; Koyama, Y.; Takata, T. *Angew. Chem. Int. Ed.* **2011**, *50*, 10417. (b) Kohsaka, Y.; Nakazono, K.; Koyama, Y.; Asai, S.; Takata, T. *Angew. Chem. Int. Ed.* **2011**, *50*, 4872. (c) Lee, Y.-G.; Koyama, Y.; Yonekawa, M.; Takata, T. *Macromolecules* **2010**, *43*, 4070. (d) Yamabuki, K.; Isobe, Y.; Onimura, K.; Oishi, T. *Chem. Lett.* **2007**, *36*, 1196. (e) Takata, T.; Kawasaki, H.; Kihara, N.; Furusho, Y. *Macromolecules* **2001**, *34*, 5449.
15. (a) Yamaguchi, I.; Osakada, K.; Yamamoto, T. *Macromolecules* **1997**, *30*, 4288. (b) Yamaguchi, I.; Osakada, K.; Yamamoto, T. *Macromolecules* **2000**, *33*, 2315. (c) Takata, T.; Kawasaki, H.; Kihara, N.; Furusho, Y. *Macromolecules* **2001**, *34*, 5449.
16. Fang, L.; Olson, M. A.; Benitez, D.; Tkatchouk, E.; Goddard III, W. A.; Stoddart, J. F. *Chem. Soc. Rev.* **2010**, *39*, 17.
17. Vetter, W.; Schill, G. *Tetrahedron* **1967**, *23*, 3079.
18. Schill, G.; Schweickert, N.; Fritz, H.; Vetter, M. *Chem. Ber.* **1988**, *121*, 961.
19. Dietrich-Buchecker, C. O.; Sauvage, J.-P.; Kintzinger, J.-P. *Tetrahedron Lett.* **1983**, *24*, 5095.
20. Dietrich-Buchecker, C. O.; Sauvage, J.-P.; Kintzinger, J.-P. *J. Am. Chem. Soc.* **1984**, *106*, 3043.
21. Cesario, M.; Dietrich-Buchecker, C. O.; Guilhem, J.; Pascard, C.; Sauvage, J.-P. *J. Chem. Soc. Chem. Commun.* **1985**, 244.
22. (a) The slipping and threading terms were initially coined as ‘threading’, without differentiating the presence or absence of the stopper. Thus, slipping could be viewed as a particular case of the general ‘threading’. (b) Blanco, M. J.; Jimenez, M. C.; Chambron, J. C.;

- Heitz, V.; Linke, M.; Sauvage, J.-P. *Chem. Soc. Rev.* **1999**, 28, 293. (c) Stoddart, J. F. *Chem. Soc. Rev.* **2009**, 38, 1521.
23. Hanman, J. S.; Kidd, T. J.; Leigh, D. A.; Wilson, A. J. *Org. Lett.* **2003**, 11, 1907.
24. Jäger, R.; Vögtle, F. *Angew. Chem., Int. Ed. Engl.* **1997**, 36, 930-944.
25. Leigh, D. A.; Murph, A.; Smart, J. P.; Slawin, A. M. Z. *Angew. Chem. Int. Ed. Engl.* **1997**, 7, 728.
26. (a) Balzani, V.; Credi, A.; Marchioni, F.; Stoddart, J. F. *J. Chem. Soc., Chem. Commun.* **2001**, 1860. (b) Ashton, P. R.; Brown, C. L.; Cao, J.; Lee, J. Y.; Newton, S. P.; Raymo, F. M.; Stoddart, J. F.; White, A. J. P.; Williams, D. J. *Eur. J. Org. Chem.* **2001**, 957. (c) Balzani, V.; Ceroni, P.; Credi, A.; Gomez-Lopez, M.; Hamers, C.; Stoddart, J. F.; Wolf, R. *New J. Chem.* **2001**, 25, 25. (d) Gunter, M. J.; Bampos, N.; Johnstone, K. D.; Sanders, J. K. M. *New J. Chem.* **2001**, 25, 166. (e) Amabilino, D. B.; Ashton, P. R.; Balzani, V.; Brown, C. L.; Credi, A.; Frechet, J. M. J.; Leon, J. W.; Raymo, F. M.; Spencer, N.; Stoddart, J. F.; Venturi, M.; *J. Am. Chem. Soc.* **1996**, 118, 12012.
27. Fyfe, M. C. T.; Stoddart, J. F. *Adv. Supramol. Chem.* **1999**, 5, 1-53.
28. Raymo, F. M.; Stoddart, J. F. *Chem. Rev.* **1999**, 99, 1643-1664.
29. Chang, T.; Heiss, A. M.; Cantrill, S. J.; Fyfe, M. C. T.; Pease, A. R.; Rowan, S. J.; Stoddart, J. F.; White, A. J. P.; Williams, D. J. *Org. Lett.* **2000**, 19, 2947.
30. (a) Ogino, H. *J. Am. Chem. Soc.* **1981**, 103, 1303. (b) Ogino, H.; Ohata, K. *Inorg. Chem.* **1984**, 23, 3312. (c) Ogino, H. *New J. Chem.* **1993**, 17, 683.
31. (a) Allwood, B. L.; Spencer, N.; Shahriari-Zavareh, H.; Stoddart, J. F.; Williams, D. J. *J. Chem. Soc., Chem. Commun.* **1987**, 1061. (b) Ashton, P. R.; Slawin, A. M. Z.; Spencer, N.; Stoddart, J. F.; Williams, D. J. *J. Chem. Soc., Chem. Commun.* **1987**, 1066.

32. Wisner, J. A.; Beer, P. D.; Drew, M. G. B. *A demonstration of anion templation and selectivity in pseudorotaxane formation* *Angew. Chem. Int. Ed.* **2001**, *40*, 3606.
33. Wisner, J. A.; Beer, P. D.; Drew, M. G. B.; Sambrook, M. R. Anion-Templated Rotaxane Formation. *J. Am. Chem. Soc.* **2002**, *124*, 12469.
34. (a) Sambrook, M. R.; Beer, P. D.; Wisner, J. A.; Paul, R. L.; Cowley, A. R.; Szemes, F.; Drew, M. G. B. Anion-Templated Assembly of Pseudorotaxanes: Importance of Anion Template, Strength of ion-pair Association, and macrocycle Ring Size. *J. Am. Chem. Soc.* **2005**, *127*, 2292. (b) Lankshear, M. D.; Beer, P. D. *Acc. Chem. Res.* **2007**, *40*, 657.
35. Aucagne, V.; Hanni, K. D.; Leigh, D. A.; Lusby, P. J.; Walker, D. B.; *J. Am. Chem. Soc.* **2006**, *128*, 2186.
36. Aucagne, V.; Berna, J.; Leigh, D. A.; Lusby, P. J.; Crowley, J. D.; Goldup, S. M.; Hanni, K. D.; Ronaldson, V. E.; Slawin, A. M. Z. *J. Am. Chem. Soc.* **2007**, *129*, 11950.
37. Crowley, J. D.; Goldup, S. M.; Lee, A. L.; Leigh, D. A.; McBurney, R. T. *Chem. Soc. Rev.* **2009**, *38*, 1530.
38. Anelli, P. L.; Spencer, N.; Stoddart, J. F. *J. Am. Chem. Soc.* **1991**, *113*, 5131.
39. Chmielewski, M. J.; Davis, J. J.; Beer, P. D.; *Org. Biomol. Chem.* **2009**, *7*, 415.
40. Wang, Q.-C.; Qu, D. -H.; Tian, H. *Angew. Chem. Int. Ed.* **2004**, *43*, 2661.
41. Perez, E. M.; Dryden, D. T. F.; Leigh, D. A.; Teobaldi, G.; Zerbetto, F.; *J. Am. Chem. Soc.* **2004**, *126*, 12210.
42. Tian, H.; Wang, Q.-C. *Chem. Soc. Rev.* **2006**, *35*, 361.
43. Ma, X.; Tian, H. *Chem. Soc. Rev.* **2010**, *39*, 70.
44. Qu, D.-H.; Wang, Q.-C.; Ren, J.; Tian, H. *Org. Lett.* **2004**, *6*, 2085.
45. Li, Y.; Li, H.; Li, Y. Liu, H.; Wang, S.; He, X.; Wang, N.; Zhu, D. *Org. Lett.* **2005**, *7*, 4835.

46. Baggerman, J.; Jagesar, D. C.; Vallee, R. A. L.; Hofkens, J.; De Schryver, C. F.; Schelhase, F.; Vogtle, F.; Brouwer, A. M. *Chem. Eur. J.* **2007**, *13*, 1291.
47. Arunkumar, E.; Forbes, C. C.; Noll, B. C.; Smith, B. D. *J. Am. Chem. Soc.* **2005**, *127*, 3288.
48. Johnson, J. R.; Fu, N.; Arunkumar, E.; Leevy, W. M.; Gammon, S. T.; Piwnica-Worms, D.; Smith, B. D. *Angew. Chem. Int. Ed.* **2007**, *46*, 5528.
49. Wang, X.; Bao, X.; Mancini, M. M.; Isaacsohn, I.; Drew, A. F.; Smithrud, D. B. *J. Am. Chem. Soc.* **2007**, *129*, 7284.
50. Sakamoto, K.; Takashima, Y.; Hamada, N.; Ichida, H.; Yamaguchi, H.; Yamamoto, H. Harada, A. *Org. Lett.* **2011**, *13*, 672.
51. Jiang, Q.; Zhang, H.-Y.; Han, M.; Ding, Z.-H.; Liu, Y. *Org. Lett.* **2010**, *12*, 1728.
52. Kwan, P. H.; Swager, T. M. *J. Am. Chem. Soc.* **2005**, *127*, 5902.
53. Onagi, H. Rebeck, J. Jr. *Chem. Commun.* **2005**, 4604.
54. Alonso, A. M.; Ehil, C.; Rahman, A.; Guldi, D. M.; Fioravanti, G.; Marcaccio, M.; Paolucci, F.; Prato, M. *Angew. Chem. Int. Ed.* **2007**, *46*, 3521.
55. (a) Lee, C. H.; Miyaji, H.; Yoon, D. W.; Sessler, J. L. *Chem. Commun.* **2008**, 24. (b) Kim, J. S.; Quang, D. T., *Chem. Rev.* **2007**, *107*, 3780. (c) Wright, A.T.; E. V. Anslyn, E. V. *Chem. Soc. Rev.* **2006**, *35*, 14.
56. (a) Yoon, J.; Kim, S. K.; Singh, N. J.; Kim, K. S. *Chem. Soc. Rev.* **2006**, *35*, 355. (b) Gunnlaugsson, T.; Glynn, M.; Tocci, G. M.; Kruger, P. E.; Pfeffer, F. M. *Coord. Chem. Rev.* **2006**, *250*, 3094. (c) Callan, J. F.; de Silva, A. P.; Magri, D. C., *Tetrahedron* **2005**, *61*, 8551. (d) Zhao, J.; Davidson, M. G.; Mahon, M. F.; Kociok-Kohn, G.; James, T. D. *J. Am. Chem. Soc.* **2004**, *126*, 16179.

57. (a) Cao, H.; Heagy, M. D. *J. Fluoresc.* **2004**, *14*, 569. (b) Sessler, J. L.; Seidel, D. *Angew. Chem., Int. Ed.* **2003**, *42*, 5134. (c) Czarnik, A. W. *Acc. Chem. Res.* **1994**, *27*, 302.
58. McDonagh, C.; Burke, C. S.; MacCraith, B. D. *Chem. Rev.* **2008**, *108*, 400.
59. Doussineau, T.; Schulz, A.; Lapresta-Fernandez, A.; Moro, A.; Kçrsten, S.; Sabine Trupp, Mohr, G. J. *Chem. Eur. J.* **2010**, *16*, 10290.
60. De Silva, A.P.; Gunaratne, H. Q. N.; Gunnlaugsson, T.; Huxley, A.J.M.; McCoy, C. P.; Rademacher, J.T.; Rice, T.E. *Chem. Rev.* **1997**, *97*,1515.
61. De Silva, A. P.; Moody, T. S.; Wright, G. D. *Analyst* **2009**, *134*, 2385.
62. (a) Valeur, B.; Schulman, (Ed.) S. G. *Molecular Luminescence Spectroscopy*, Part 3, Wiley, New York, **1993**, p. 25. (b) Valeur, B.; Bourson, J.; Pouget, J.; Czarnik (Ed.), A. W. *Fluorescent Chemosensors for Ion and Molecule Recognition*, ACS Symposium Series 538, American Chemical Society, Washington, DC, **1993**, p. 25.
63. Wagner, R. W.; Lindsey, J. S.; Seth, T.; Palaniappan, V.; Bocian, D. F. *J. Am. Chem. Soc.* **1996**, *118*, 3996.
64. (a) Forester, T. *Discuss. Faraday Soc.* 1959, *27*, 7. (b) Forster, T. *Naturwissenschaften* **1946**, *33*, 166. (c) Galanin, M. D. *JETP*.**1955**, *28*,485. (c) Dexter, D. L. *J. Chem. Phys.***1953**, *21*, 836.
65. Tsien, R. Y.; Poenie, M. *Trends Biochem. Sci.* **1986**, *11*, 450-455.
66. (a) J. Du.; M. Hu.; J. Fan.; X. Peng. *Chem. Soc. Rev.* **2012**, *41*, 4511. (b) Y. Yang.; Q. Zhao.; W. Feng.; F. Li. *Chem. Rev.* **2013**, *113*, 192.
67. Srikun, D.; Miller, E. W.; Domaille, D. W.; Chang, C. J. *J. Am. Chem. Soc.* **2008**, *130*, 4596.
68. Lane, A. S.; Leigh, D. A. *J. Am. Chem. Soc.* **1997**, *119*, 11092.
69. Zhang, Z.; Han, C.; Yu, G.; Huang, F. *Chem. Sci.* **2012**, *3*, 3026.

70. Mateo-Alonso, A.; Ehil, C.; Guldi, D. M.; Prato, M. *Org. Lett.* **2013**, *15*, 84.
71. Keaveney, C. M.; Leigh, D. A. *Angew. Chem. Int. Ed.* **2004**, *43*, 1222.
72. Gassensmith, J. J.; Matthys, S.; Lee, J.-J.; Wojcik, A.; Kamat, P. V.; Smith, B. D. *Chem. Eur. J.* **2010**, *16*, 2916.
73. Hancock, L. M.; Marchi, E.; Ceroni, P.; Beer, P. D. *Chem. Eur. J.* **2012**, *18*, 11277.
74. Langton, M. J.; Beer, P. D. *Chem. Eur. J.* **2012**, *18*, 14406.
75. Chuang, C. -J.; Lai, C. -C.; Liu, Y. -H.; Peng, S.-M.; Chiu, S. -H. *Chem. Eur. J.* **2012**, *18*, 16698.
76. Chuang, C.-J.; Li, W. -S.; Lai, C. -C.; Liu, Y. -H.; Peng, S.-M.; Chao, I.; Chiu, S. -H. *Org. Lett.* **2009**, *11*, 385.
77. Zhang, H.; Hu, J. Qu, D. -H. *Org. Lett.* **2012**, *14*, 2334.
78. Kwan, P. H.; MacLachlan, M. J.; Swager, T. W. *J. Am. Chem. Soc.* **2004**, *126*, 8638.
79. Yamashita, A.; Kanda, D.; Katoono, R.; Yui, N.; Ooya, T.; Maruyama, A.; Akita, H.; Kogure, K.; Harashima, H. *J. Controlled Release* **2008**, *131*, 137.
80. Ogoshi, T.; Takashima, Y.; Yamaguchi, H.; Harada, A. *Chem. Commun.* **2006**, 3702.
81. Ji, X.; Yao, Y.; Li, J.; Yan, X.; Huang, F. *J. Am. Chem. Soc.* **2013**, *135*, 74.
82. Hwang, M. J.; Bae, H. S.; Kim, S. J.; Jeong, B. *Macromolecules* **2004**, *37*, 8820.
83. Wakabayashi, R.; Kubo, Y.; Kaneko, K.; Takeuchi, M.; Shinkai, S. *J. Am. Chem. Soc.* **2006**, *128*, 8744.
84. Olson, M. A.; Braunschweig, A. B.; Fang, L.; Ikeda, T.; Klajin, R.; Trabolsi, A.; Wesson, P. J. Benitez, D.; Mirkin, C. A.; Grazybowski, B. A.; Stoddart, J. F. *Angew. Chem. Int. Ed.* **2009**, *48*, 1792.
85. Sun, R.; Xue, C, Ma, X.; Gao, M. Tian, H.; Li, Q. *J. Am. Chem. Soc.* **2013**, *135*, 5990.

86. Choi, M. G.; Hwang, J.; Moon, J. K.; Sung, J.; Chang, S. -K. *Org. Lett.* **2011**, *13*, 5260.
87. (a) Fan, J.; Sun, W.; Hu, M.; Cao, J.; Cheng, G.; Dong, H.; Song, K.; Liu, Y.; Sun, S.; Peng, X.; *Chem. Commun.* **2012**, *48*, 8117. (b) Hu, C.; Sun, W.; Cao, J.; Gao, P.; Wang, J.; Fan, J.; Song, F.; Sun, S. Peng, X. *Org. Lett.* **2013**, *15*, 4022.
88. Li, K.; Xu, H. -R.; Yu, K. -K, Hou, J. -T.; Yu, X. -Q. *Anal. Methods* **2013**, *5*, 2653.
89. Choi, M. G.; Moon, J. K.; Bae, J.; Lee, J. W.; Chang, S. -K. *Org. Biomol. Chem.* **2013**, *11*, 2961.
90. C. Hu.; W. Sun.; J. Cao.; P. Gao.; J. Wang.; J. Fan.; F. Song.; S. Sun.; X. Peng. *Org. Lett.* **2013**, *15*, 4022.
91. (a) Lehn, J.-M. *Supramolecular chemistry: Concepts and Perspectives*; Wiley-VCH: New York, 1995. (b) Schmidtchen, F. P.; Berger, M. *Chem. Rev.* **1997**, *97*, 1609. (c) *Supramolecular chemistry of Anions*; Wiley-VCH: New York, 1997. (d) Martínez-Máñez.; Sancenón, F. *Chem. Rev.* **2003**, *103*, 4419.
92. (a) Weatherall, A. *Pharmacology of Fluorides in Handbook of Experimental Pharmacology XX/1*, Part 1, Springer, Berlin, 1969, pp. 141. (b) Kirk, K. L. *Biochemistry of the Halogens and Inorganichalides*, plenum, new York, 1991, p. 58.
93. (a) Pflugrath, J. W.; Quioco, F. A. *Nature* **1985**, *314*, 257. (b) Sessler, J. L.; Camiolo, S.; Gale, P. A. *Coord. Chem. Rev.* **2003**, *240*, 17.
94. (a) Altieri, A.; Bottari, G.; Dehez, F.; Leigh, D. A.; Wong, J. K. Y.; Zerbetto, F. *Angew. Chem. Int. Ed.* **2003**, *42*, 2296. (b) Lin. C.-F.; Liu, Y.-H.; Peng, S.-M.; Lai, C.-C.; Chiu, S.-H. *Chem. Eur. J.* **2007**, *13*, 4350. (c) Zhou, W.-D.; Li, J.-B.; He, X.-R.; Li, C.-H.; Lv, J.; Li, Y.-L.; Wang, S.; Liu, H.-B.; Zhu, D.-B. *Chem. Eur. J.* **2008**, *14*, 754. (d) Megiatto, J. D.; Schuster, D. I. *Org. Lett.* **2011**, *13*, 1808. (e) Li, H.; Zhang, H.; Zhang, Q.; Qu, D.-H. *Org. Lett.* **2012**, *14*, 5900.

95. (a) Huang, Y.-L.; Hung, W.-C.; Lai, C.-C.; Liu, Y.-H.; Peng, S.-M.; Chiu, S.-H. *Angew. Chem. Int. ed.* **2007**, *46*, 6629. (b) Lin, T.-Z.; Lai, C.-C.; Chiu, S.-H. *Org. Lett.* **2009**, *11*, 613. (c) Evans, N. H.; Serpell, C. J.; Beer, P. D. *Chem. Commun.* **2011**, *47*, 8775.
96. Lakowicz, J. R. *Principles of Fluorescence Spectroscopy*; Kluwer Academic/Plenum: New York, 1999.
97. Hao, Z.; Iqbal, A. *Chem. Soc. Rev.* **1997**, *26*, 203.
98. (a) Korendovych, I. V.; Cho, M.; Butler, P. L.; Staples, R. J.; Rybak-Akimova, E. V. *Org. Lett.* **2006**, *8*, 3171. (b) Kaewtong, C.; Fuangswasdi, S.; Muangsin, N.; Chaichit, N.; Vicens, J.; Pulpoka, B. *Org. Lett.* **2006**, *8*, 1561. (c) Kim, J. S.; Quang, D. T. *Chem. Rev.* **2007**, *107*, 3780. (d) Sessler, J. L.; Kim, S. K.; Gross, D. E.; Lee, C. H.; Kim, J. S.; Lynch, V. M. *J. Am. Chem. Soc.* **2008**, *130*, 13162. (e) Kim, S. K.; Lynch, V.; Young, N. J.; Hay, B. P.; Lee, C. H.; Kim, J. S.; Moyer, B. A.; Sessler, J. L. *J. Am. Chem. Soc.* **2012**, *134*, 20837. (f) Thiampanya, P.; Muangsin, N.; Pulpoka, B. *Org. Lett.* **2012**, *14*, 4050.
99. Barrell, M. J.; Leigh, D. A.; Lusby, P. J.; Slawin, A. M. Z. *Angew. Chem. Int. Ed.* **2008**, *47*, 8036.
100. Cheng, T. P.; Pratic, D.; Yoon, J.; Hao, Z. U.S. 2002, US6414002B1, 20020702.
101. Sabah, A.; Alexandre, L.; Mourard, E.; Charbonniere, J. L. *Dalton Trans.* **2010**, *29*, 9055.
102. Gibson, H. W.; Lee, S. H.; Engen, P. T.; Lecavalier, P.; Sze, J.; Shen, Y. X.; Bheda, M. J. *Org. Chem.* **1993**, *58*, 3748.
103. Fuller, A.-M.; Leigh, D. A.; Lusby, P. J.; Slawin, A. M. Z.; Walker, D. B. *J. Am. Chem. Soc.* **2005**, *127*, 12612.
104. Huo, L.; Hou, J.; Chen, H. Y.; Zhang, S.; Yang, Y. *Macromolecules* **2009**, *42*, 6564.

105. (a) Furusho, Y.; Matsuyama, T.; Takata, T.; Moriuchi, T.; Hirao, T. *Tetrahedron Lett.* **2004**, *45*, 9593. (b) Fuller, A. M.; Leigh, D. A.; Lusby, P. J.; Oswald, I. D. H.; Parsons, S.; Walker, D. B. *Angew. Chem. Int. Ed.* **2004**, *43*, 3914. (c) Leigh, D. A.; Lusby, P. J.; Slawin, A. M. Z.; Walker, D. B. *Angew. Chem. Int. Ed.* **2005**, *44*, 4557. (d) Crowley, J. D.; Leigh, D. A.; Lusby, P. J.; MaBurney, R. T.; Perret-Aebi, L.-E.; Petzold, C.; Slawin, A. M. Z.; Symes, M. D. *J. Am. Chem. Soc.* **2007**, *129*, 15085. (e) Fuller, A. M.; Leigh, D. A.; Lusby, P. J. *J. Am. Chem. Soc.* **2010**, *132*, 4954.
106. (a) Lane, A. S.; Leigh, D. A.; Murphy, A. *J. Am. Chem. Soc.* **1997**, *119*, 11092. (b) Chiang, P.-T.; Cheng, P.-N.; Lin, C.-F.; Liu, Y.-H.; Lai, C.-C.; Peng, S.-M.; Chiu, S.-H. *Chem.-Eur. J.* **2006**, *12*, 865.
107. Strutt, N. L.; Forgan, R. S.; Spruell, J. M.; Batros, Y. Y.; Stoddart, J. F. *J. Am. Chem. Soc.* **2011**, *133*, 5668.
108. Connors, K. A. *Binding Constants*; Wiley: New York, 1987.
109. Fukuzumi, S.; Ohukubo, K.; D'Souza, F.; Sessler, J. L.; *Chem. Commun.* **2012**, *48*, 9801.
110. Collier, C. P.; Mattersteig, G.; Wong, E. W.; Luo, Y.; Beverly, K.; Sampaio, J.; Raymo, F. M.; Stoddart, J. F.; Heath, J. R. *Science* **2000**, *289*, 1172-1175.
111. (a) Frampton, M. J.; Anderson, H. L. *Angew. Chem. Int. Ed.* **2007**, *46*, 1028-1064. (b) Terao, J.; Tanaka, Y.; Tsuda, S.; Kambe, N.; Taniguchi, M.; Kawai, T.; Saeki, A.; Seki, S. *J. Am. Chem. Soc.* **2009**, *131*, 18046-18047. (c) Terao, J. *Polym. Chem.* **2011**, *2*, 2444-2452.
112. (a) Ooya, T.; Choi, H. K.; Yamashita, A.; Yui, N.; Sugaya, Y.; Kano, A.; Maruyama, A.; Akita, H.; Ito, R.; Kogure, K.; Harashima, H. *J. Am. Chem. Soc.* **2006**, *128*, 3852-3853. (b) Seo, J. H.; Kakinoki, S.; Inoue, Y.; Yamaoka, T.; Ishihara, K.; Yui, N. *J. Am. Chem. Soc.* **2013**, *135*, 5513-5516.

113. (a) Anderson, H. L.; Anderson, S.; Sanders, J. K. M. *Acc. Chem. Res.* **1993**, *26*, 469-475. (b) Werts Michel, P. L.; Boogaard, M. V. D.; Tsivgoulis, G. T.; Hadziioannou, G. *Macromolecules* **2003**, *36*, 7004-7013. (c) Hawker, C. J.; Wooley, K. L. *Science* **2005**, *309*, 1200-1205.
114. (a) Zhu, S. S.; Carroll, P. J.; Swager, T. M. *J. Am. Chem. Soc.* **1996**, *118*, 8713-8714. (b) Gong, C.; Ji, Q.; Subramaniam, C.; Gibson, H. W. *Macromolecules* **1998**, *31*, 1814-1818. (c) Liu, Y.; Zhao, Y. L.; Zhang, H. Y.; Song, H. B. *Angew. Chem. Int. Ed.* **2003**, *42*, 3260-3263. (d) Terao, J.; Tsuda, S.; Tanaka, Y.; Okoshi, K.; Fujihara, T.; Tsuji, Y.; Kambe, N. *J. Am. Chem. Soc.* **2009**, *131*, 16004-16005. (e) Tzeng, B. C.; Wei, S. L.; Chang, T. Y. *Chem. Eur. J.* **2012**, *18*, 16443-16449.
115. (a) Weidmann, J. L.; Kern, J. M.; Sauvage, J. P.; Geerts, Y.; Muscat, D.; Mullen, K. *Chem. Commun.* **1996**, 1243-1244. (b) Weidmann, J. L.; Kern, J. M.; Sauvage, J. P.; Muscat, D.; Mullins, S.; Kohler, W.; Rosenauer, C.; Radar, H. J.; Martin, K.; Geerts, Y. *Chem. Eur. J.* **1999**, *5*, 1841-1851. (c) Taura, D.; Li, S.; Hashidzume, A.; Harada, A. *Macromolecules* **2010**, *43*, 1706-1713.
116. (a) Michels, J. J.; O'Connell, M. J.; Taylor, P. N.; Wilson, J. S.; Cacialli, F.; Anderson, H. L. *Chem. Eur. J.* **2003**, *9*, 6167-6176. (b) Yamaguchi, I.; Kashiwagi, K.; Yamamoto, T. *Macromol. Rapid Commun* **2004**, *25*, 1163-1166.
117. (a) Fluery, G.; Schlatter, G.; Brochon, C.; Travelet, C.; Lapp, A.; Lindener, P.; Hadziioannou, G. *Macromolecules* **2007**, *40*, 535-543. (b) Ren, L.; Ke, F.; Chen, Y.; Liang, D.; Huang, J. *Macromolecules* **2008**, *41*, 5295-5300. (c) De Bo, G.; Winter, J. D.; Gerbaux, P.; Fustin, C. A. *Angew. Chem. Int. Ed.* **2011**, *50*, 9093-9096.

118. (a) Ball, P. *Nature* **2000**, *406*, 118-120. (b) Scarff, C. A.; Snelling, J. R.; Knust, M. M.; Wilkins, C. L.; Scrives, J. H.; *J. Am. Chem. Soc.* **2012**, *134*, 9193–9198.
119. MacLachlan, M. J.; Rose, A.; Swager, T. M. *J. Am. Chem. Soc.* **2001**, *123*, 9180-9181.
120. Green, J. E.; Choi, J. W.; Boukai, A.; Bunimovich, Y.; Happerin, E. J.; DiIonno, E.; Luo, Y.; Sheriff, B. A.; Xu, K.; Shin, Y. S.; Tseng, R.; Stoddart, J. F.; Heath, J. R. *Nature* **2007**, *445*, 414-417.
121. (a) Wenz, G.; Han, B. H.; Muller, A. *Chem. Rev.* **2006**, *106*, 782-817. (b) Harada, A.; Hashidzume, A.; Yamaguchi, H.; Takashima, Y. *Chem. Rev.* **2009**, *109*, 5974-6023.
122. (a) Kim, K. *Chem. Soc. Rev.* **2002**, *31*, 96-107. (b) Ko, Y. H.; Kim, E.; Hwang, I.; Kim, K. *Chem. Commun.* **2007**, 1305-1315.
123. Momcilovic, N.; Clark, P. G.; Boydston, A. J.; Grubbs, R. H. *J. Am. Chem. Soc.* **2011**, *133*, 19087-19089.
124. (a) Li, J.; Loh, X. J.; *Advanced Drug Delivery Reviews* **2008**, *60*, 1000-1017. (b) Dam, H. H.; Caruso, F. *Adv. Mater.* **2011**, *23*, 3026-3029. (c) Yamada, Y.; Nomura, T.; Harashima, H.; Yamashita, A.; Yui, N. *Biomaterials* **2012**, *33*, 3952-3958.
125. Ghadari, M. R.; Granja, J. R.; Buehler, L. K. *Nature* **1994**, *369*, 301-304.
126. Raju, M. V. R.; Lin, H. C. *Org. Lett.* **2013**, *15*, 1274-1277.
127. Heeney, M.; Bailey, C.; Giles, M.; Shkunov, M.; Sparrowe, D.; Tierney, S.; Zhang, W.; McCulloch, I. *Macromolecules* **2004**, *37*, 5250-5256.
128. Tamayo, A. B.; Tantiwivat, M.; Walker, B.; Nguyen, T. Q. *J. Phys. Chem. C* **2008**, *112*, 15543-15552.
129. Frisch, M. J. *et al.* Gaussian 09; Gaussian, Inc.: Wallingford CT, **2009**.
130. Boese, A. D.; Handy, N. C.; *J. Chem. Phys.* **2002**, *116*, 9559–9569.

131. (a) Hamprecht, F. A.; Cohen, A. J.; Tozer, D. J.; Handy, N. C. *J. Chem. Phys.* **1998**, *109*, 6264-6271. (b) Boese, A. D.; Doltsinis, N. L.; Handy, N. C.; Sprik, M. *J. Chem. Phys.* **2000**, *112*, 1670-1678.
132. (a) Stewart, J. J. P. *J. Comp. Chem.* **1989**, *10*, 209-220. (b) Stewart, J. J. P. *J. Comp. Chem.* **1989**, *10*, 221-264.
133. Qu, S.; Tian, H. *Chem. Commun.* **2012**, *48*, 3039-3051.
134. Du, C.; Li, C.; Li, W.; Chen, X.; Bo, Z.; Veit, C.; Ma, Z.; Wuerful, U.; Zhu, H.; Hu, W.; Zhang, F. *Macromolecules* **2011**, *44*, 7617-7624.
135. Zhang, W.; Dichtel, W. R.; Stieg, A. Z.; Benitez, D.; Glimzewski, J. K.; Heath, J. R.; Stoddart, J. F. *Proc. Natl. Acad. Sci.* **2008**, *105*, 6514-6519.
136. (a) Jang, Y. H.; Hwang, S.; Kim, Y. H.; Jang, S. S.; Goddard, W. A. *J. Am. Chem. Soc.* **2004**, *126*, 12636-12645. (b) Benitez, D.; II Yoon, T.; Stoddart, J. F.; Goddard III, W. A. *J. Am. Chem. Soc.* **2008**, *130*, 14928-14929.
137. (a) Wu, J.; Gao, C. *Macromolecules* **2010**, *43*, 7139-7146. (b) Chen, Y.; Zhang, Y. M.; Liu, Y. *Chem. Commun.* **2010**, *46*, 5622-5633.
138. (a) Martinez, C. R.; Iverson, B. L. *Chem. Sci.* **2012**, *3*, 2191-2201. (b) Tzeng, B. C.; Wei, S. L.; Chang, T. Y. *Chem. Eur. J.* **2012**, *18*, 5105-5112. (c) Mitra, A.; Panda, D. K.; Carson, L. J.; Saha, S. *Chem. Commun.* **2013**, *49*, 4601-4603.
139. (a) Magonov SN (2001) Visualization of polymers at surfaces and interfaces with atomic force microscopy. *Handbook of Surfaces and Interfaces of Materials*, ed Nalwa HR (Academic, New York), Vol 2, pp 393-429. (b) Moulin, J.-F.; Kengne, J. C.; Kshirsagar, R.; Cavallani, M.;

- Biscarini, F.; Leon, S.; Zerbetto, F.; Bottari, G.; Leigh, D. A. *J. Am. Chem. Soc.* **2006**, *128*, 526-532.
140. Fialkowski, M.; Bitner, A.; Grzybowski, B. A. *Nat. Mater.* **2005**, *4*, 93 – 97.
141. Seo, S. H.; Chang, J. Y.; Tew, G. N. *Angew. Chem. Int. Ed.* **2006**, *45*, 7526-7530.
142. Shapira, A.; Livney, Y. D.; Broxterman, H. J.; Assaraf, Y. G. *Drug Resistance Updates* **2011**, *14*, 150-163.
143. Schiessl, H. W. *Kirk-Othmer Encyclopedia of Chemical Technology*, John Wiley & Sons, Inc., **2000**, pp. 562-607.
144. Ragnarsson, U. *Chem. Soc. Rev.* **2001**, *30*, 205–213.
145. Wang, J.; Chen, L. *Anal. Chem.* **1995**, *67*, 3824-3927.
146. International Agency for Research on Cancer: Re-evaluation of some organic chemicals, hydrazine, and hydrogen peroxide. IARC monographs on the evaluation of carcinogenic risk of chemicals to humans. Lyon, IARC, **1999**, Vol. 71, pp 991_1013. <http://monographs.iarc.fr/ENG/Monographs/vol71/mono71-43.pdf>.
147. Batchelor-McAuley, C.; Banks, C. E.; Simm, A. O.; Jones, T. G. J.; Compton, R. G. *Analyst* **2006**, *131*, 106-110.
148. Liu, Y. Y.; Schmeltz, I.; Hoffmann, D. *Anal. Chem.* 1974, *46*, 885-889.
149. (a) Chen, X.; Tian, X.; Shin, I.; Yoon, J. *Chem. Soc. Rev.* **2011**, *40*, 4783-4804. (b) Zhang, J. F.; Zhou, Y.; Yoon, J.; Kim, J. S. *Chem. Soc. Rev.* **2011**, *40*, 3416-3429.
150. Jiang, J.; Liu, W.; Cheng, J.; yang, L.; Jiang, H.; Bai, D.; Liu, W. *Chem. Commun.* **2012**, *48*, 8371-8373.

151. (a) Song, F.; Watanabe, S.; Foreancig, P. A.; Koide, K. *J. Am. Chem. Soc.* **2008**, *130*, 16460-16461. (b) Maity, D.; Govindaraju, T. *Chem. Commun.* **2012**, *48*, 1039-1041. (c) Xu, Y.; Li, B.; Li, W.; Zhao, J.; Sun, S.; Pang, Y. *Chem. Commun.* **2013**, *49*, 4764-4766.
152. Khan, M. N. *J. Org. Chem.* **1995**, *60*, 4536-4541.
153. Duke, M. R.; Veale, E. B.; Pfeffer, M.; Kruger, P. E.; Gunnlaugsson, T. *Chem. Soc. Rev.* **2010**, *39*, 3936-3953.
154. March, J. *Advanced Organic Chemistry: Reactions, Mechanisms and Structures*, 2nd ed.; McGraw-Hill Kogakusha, Ltd.: Tokyo, **1977**; p 388.
155. (a) Bolhofer, W. A.; Sheehan, J. C. *J. Am. Chem. Soc.* **1950**, *72*, 2786-2788. (b) Gibson, M. S.; Bradshaw, R. W. *Angew. Chem. Int. Ed.* **1968**, *7*, 919-930.
156. Tian, H.; Gan, J.; Chen, K.; He, J.; Song, Q. L.; Hou, X. Y. *J. Mater. Chem.* **2012**, *12*, 1262-1277.
157. (a) Shortreed, M.; Kopelman, R.; Kuhn, M. Hoyland, B. *Anal. Chem.* **1996**, *68*, 1414-1418. (b) Umar, A.; Rahman, M. M.; Kim, S. H.; Hahn, Y.-B. *Chem. Commun.* **2008**, 166-168.
158. (a) Ing, H. R.; Manske, R. H. F. *J. Chem. Soc.* **1926**, 2348-2351. (b) Ariffin, A.; Khan, M. N.; Lan, L. C.; May, F. Y.; Yun, C. S. *Synth Commun.* **2004**, *34*, 4439-4445.

CURRICULUM VITAE

PERSONAL DETAILS

Name : **M. V. P. S. K. R. Raju**
Gender : **Male**
Marital Status : **Unmarried**
Date of Birth : **06.08.1983**
E-mail : raju_drl81@yahoo.co.in
Permanent Address : **H-No. 5/48 New colony Street,
Gantiyada (post, Vil, and Mandal),
Vizianagaram District. Pin- 535215.
Andhara Pradesh, India. Phone No.: +919963399938.**

EDUCATIONAL DETAILS

- ☉ **Ph. D. in Materials Science and Engineering** [2010, Feb – 2013, Aug], Department of Materials Science and Engineering, National Chiao Tung University, Hsinchu, Taiwan.
- ☉ **M. Sc. in General Chemistry** [2003 – 2005], Department of Chemistry, M. V. R Post Graduate College, Andhra University, Visakhapatnam-530 003, India.
- ☉ **B. Sc. in Chemistry** [2000 – 2003], Department of Chemistry, M. R. (A) College, Andhra University, Vizianagaram-535 001, India.

EXPERIENCE

- ☉ [2005 – 2007]: **Research Associate** in “Dr. REDDY’S Laboratories”, Hyderabad, Andhra Pradesh,
Area of work: Cost-effective novel synthetic routes and protocols for **Oncology molecules** and **Taxol** side-chain.
- ☉ [2007 – 2010]: **Senior Research Associate** in “Jubilant Chemsys Ltd”, Noida, Uttar Pradesh,
Area of work: Library based New Chemical Entities (NCEs) synthesis to find novel drug candidates for **Eli Lilly** (USA) & **MERCK** (Germany) clients.

List of publications

- 1. Mandapati V. Ramakrishnam Raju** and Hong-Cheu Lin*, “A Novel Diketopyrrolopyrrole (DPP)-Based [2]Rotaxane for Highly Selective Optical Sensing of Fluoride”, *Org. Lett.*, **2013**, *15*, 1274-1277.
- 2. Mandapati V. Ramakrishnam Raju**, P. Raghunath, Ming-Chang Lin and Hong-Cheu Lin , “An Acid-Base Controllable Hierarchical Nanostructure from a NIR-Absorbing Conjugated Polyrotaxane-Based Optical Molecular Switch ”, *Macromolecules.*, **2013**, (Just Accepted, ASAP) DOI: 10.1021/ma401485b.
- 3. Mandapati V. Ramakrishnam Raju** and Hong-Cheu Lin*, “A Facile Ratiometric Fluorescent Chemodosimeter for Hydrazine and its Application in Living Cells”, *Chem. Eur. J.* (To be submitted).
- 4. Muthaiah Shellaiah**, Yen-Hsing Wu, Ashutosh Singh, **Mandapati V. Ramakrishnam Raju** and Hong-Cheu Lin*, “Novel Pyrene- and Anthracene-Based Schiff Base Derivatives as Cu²⁺ and Fe³⁺ Fluorescence Turn-On Sensors and for Aggregation Induced Emissions”, *J. Mater. Chem. A*, **2013**, *1*, 1310-1318.